

Measurement of Something

by

Kiyotaka Akabori

Submitted in partial fulfillment of the

requirements for the degree of

Doctor of Philosophy

at

Carnegie Mellon University

Department of Physics

Pittsburgh, Pennsylvania

Advised by Professor John F. Nagle
and Professor Stephanie Tristram-Nagle

July 21, 2014

Contents

1	Introduction	1
2	Structural Perturbation of Lipid Bilayers Due to Tat Peptide	5
2.1	Introduction	5
2.2	Materials and Methods	8
2.2.1	Stock Solutions	8
2.2.2	Thin Film Samples	8
2.2.3	Volume Measurements	9
2.2.4	X-ray setup	11
2.2.5	Data reduction of diffuse scattering data	12
2.2.6	Analysis of Diffuse Scattering	12
2.2.7	Modeling the Bilayer Structure	15
2.2.8	Molecular Dynamics Simulation	21
2.3	Analysis of Molecular Dynamics Simulation Data	24
2.3.1	SIMtoEXP program	24
2.3.2	Local Thinning of Membranes	24
2.3.3	Lateral Decay Length of Membrane Thinning	26
2.4	Results	28
2.4.1	Bending and Bulk Modulus	28
2.4.2	Volume results	30
2.4.3	Electron Density Profile Modeling	31
2.4.4	Molecular Dynamics Simulations	44
2.5	Discussion	53
2.6	Conclusion	56

3 Ripple Phase	58
3.1 Introduction	58
3.2 Materials and Methods	62
3.2.1 Sample Preparation	62
3.2.2 Instrumental Resolution	63
3.2.3 Low Angle X-ray Scattering Experiment	71
3.2.4 Near Grazing Incidence Wide Angle X-ray Scattering Experiment	72
3.2.5 Transmission Wide Angle X-ray Scattering Experiment	72
3.3 LAXS: analysis	77
3.3.1 Lattice Structure	77
3.3.2 Sample q-space	78
3.3.3 Lorentz Correction	80
3.3.4 Absorption Correction for LAXS	85
3.3.5 Correction due to mosaic spread	89
3.4 LAXS: model	94
3.4.1 Contour Part of the Form Factor	94
3.4.2 Transbilayer Part of the Form Factor	94
3.5 LAXS: results	97
3.6 nGIWAXS: results	110
3.6.1 Fluid and gel phase	110
3.6.2 Ripple phase	113
3.7 TWAXS: results	119
3.8 Discussion	124
3.8.1 Major arm	124
3.8.2 Minor arm	126
3.9 Conclusion	131
Appendices	133
A	134
A.1 More results from chapter 2	134
A.2 Mosaic Spread for NFIT analysis	134
A.2.1 Mosaic Spread: Calculation	134
A.2.2 Mosaic Spread: Near Equivalence of Two Methods	141
A.2.3 NFIT	144

A.3	More results from LAXS models	146
A.4	Derivation of the contour part of the form factor	150
A.5	Rotation of a Two-Dimensional Function	153
A.6	Derivation of the transbilayer part of the form factor in the 2G hybrid model	154
A.7	Correction due to refractive index	156
A.8	Thin Rod Model of the ripple phase	157

List of Tables

2.1	Some Amino Acids Data	10
2.2	Number of electrons per lipid and volume per lipid.	20
2.3	Some structural parameters for each component. n_i^e is the number of electrons and ρ_i is the average electron density.	20
2.4	Tat basic structural parameters. The notations are the same as in Table 2.3. $x_{\text{Tat}} = \text{Tat}/(\text{Tat}+\text{Lipid})$	20
2.5	Volume results at 37 °C	31
2.6	Fitting Results for DOPC membranes for the THG (Tat in headgroup) model. $z_{\text{PC}} - z_{\text{CG}} = 3.1 \text{ \AA}$ and $z_{\text{CG}} - z_{\text{HC}} = 1.3 \text{ \AA}$ in all fits.	32
2.7	Fitting Results for DOPC:DOPE (3:1) membranes for the THG model. $z_{\text{PC}} - z_{\text{CG}} = 3.1 \text{ \AA}$ and $z_{\text{CG}} - z_{\text{HC}} = 1.3 \text{ \AA}$ in all fits.	37
2.8	(Numbers are wrong) Fitting Results for DOPC:DOPE (1:1) membranes for the THG model. $\Delta z_1 = z_{\text{PC}} - z_{\text{CG}}$ and $\Delta z_2 = z_{\text{CG}} - z_{\text{HC}}$	37
2.9	Fitting Results of the bound THG model for DOPC membranes. $z_{\text{PC}} - z_{\text{CG}} = 3.1$ and $z_{\text{CG}} - z_{\text{HC}} = 1.3$ in all fits.	42
2.10	Comparison of the simulated form factors to the experimental form factors.	49
2.11	Summary of simulation results. $\langle D_{\text{PP}} \rangle$, phosphorus-phosphorus distance averaged over all lipids; D_{PP} , Tat-perturbed phosphorus atoms; x , thickness away from Tat; Δt , $\langle D_{\text{PP}}^{\text{DOPC}} \rangle - D_{\text{PP}}$; H_{Tat} , Tat height; R_{Tat} , radius of Tat cylinder; R_2 , radius of the calculated in-plane Tat-perturbed region; R_3 , effective radius of the simulation box.	50
2.12	Summary of weighted average results. The caption is the same as Table 2.11.	50

3.1	Lattice constants for DMPC at $T = 18.0$ °C reported by Wack and Webb [8] except the one colored in blue. The data collected and analyzed in this thesis are colored blue.	61
3.2	Beam divergence	63
3.3	Energy dispersion	64
3.4	Geometric broadening	70
3.5	Add caption	93
3.6	Definitions of Z_{CH_2} and Z_{W}	95
3.7	Observed intensity for $h = 1$ to 4 at $D = 57.8$, $\lambda_r = 145$, and $\gamma = 98.2^\circ$	98
3.8	Observed intensity for $h = 5$ to 9 at $D = 57.8$, $\lambda_r = 145$, and $\gamma = 98.2^\circ$ (continued from Table 3.7).	99
3.9	Comparison of form factor obtained in two different methods. *Unoriented data are from Wack and Webb [8].	100
3.10	Model parameters. Fit1 and Fit2 were performed with the M1G model while Fit3 to 7 were with the M2G model. *Parameters were fixed to the values shown.	101
3.11	Ripple structural quantities. I: Results from Sun <i>et al.</i> II: Used only up to $(h, k) = (3, 4)$ III: Replaced lower order $ F(h, k) $ with those from Wack and Webb, keeping the same relative error	103
3.12	Estimated structural quantities	109
3.13	Summary of peak properties	118
A.1	Form factors for $h = 1$ to 4	146
A.2	Form factors for $h = 5$ to 9	147

List of Figures

1.1	Experimental phase diagram of DMPC from Ref. [11]. $L_{\beta I}$, $L_{\beta L}$, and $L_{\beta F}$ belong to the gel $L_{\beta'}$ phase. $P_{\beta'}$ is the ripple phase and L_{α} is the fluid phase.	2
1.3	Chain tilt direction in $L_{\beta I}$ (left), $L_{\beta F}$ (middle), and $L_{\beta L}$ (right) phases. Black dots are orthorhombic lattice points. Unit cells are shown in dashed lines. Chains are drawn as solid lines. Chains are tilted toward the nearest neighbor in $L_{\beta I}$ phase with $\phi = \pi/2$. In $L_{\beta F}$ phase, they are titled toward the next-next nearest neighbor ($\phi = 0$). In $L_{\beta L}$ phase, ϕ can be anywhere between 0 and $\pi/2$.	3
1.4	Schematic of the $P_{\beta'}$ ripple phase. In this phase, bilayers assume periodic height modulation with a sawtooth shape. The longer side of a sawtooth is called major arm and the shorter side is called minor arm. It is generally assumed that chains are in all trans conformation in the major arm, but the molecular packing in the minor arm is not known.	4
2.2	LAXS of DOPC:DOPE (1:1) with $x_{\text{Tat}} = 0.034$ at 37 °C. White lobes of diffuse scattering intensity have large grey numbers, while lamellar orders and beam are shown to the left of the molybdenum beam attenuator (short, dark rectangle). q_z and q_r are the cylindrical coordinates of the sample q -space, where q_z -axis is along the bilayer normal and q_r -axis is along the in-plane direction. The lamellar repeat spacing was $D = 66.2$ Å.	12

2.3	Schematic of an oriented stack of lipid bilayers. Thick green curves represent an instance of thermally fluctuating bilayers. The dashed lines show the thermally averaged positions $z = nD$ of the centers of each bilayer and $u_n(x, y)$ gives the instantaneous deviation from the average. Each bilayer extends in the $\mathbf{r} = (x, y)$ plane.	14
2.4	Schematic of DOPC showing each lipid component. The dash lines show where the lipid is divided into different components. The lipid headgroup is divided into two components, phophate-choline (PC) and carbonyl-glycerol (CG). The hydrocarbon chain region is also divided into two components, methylene+methine (CH_2+CH) and terminal methyl groups (CH_3).	16
2.5	A model electron density profile for DOPC with Tat.	17
2.6	Our simple model to extract the local bilayer thickness from simulation trajectories. Tat is modeled as a cylinder with its height H_{Tat} and radius R_{Tat} . The local thickness is defined as $D'_{\text{phos-phos}}$. The thickness of the unperturbed DOPC bilayer is $D_{\text{phos-phos}}$. Blue highlighted lipids fall within the imaginary cylinder extended from the Tat. Unperturbed lipids are highlighted in green.	25
2.7	Simple model of the lateral decay of the membrane thickness perturbation due to Tat.	27
2.8	Bilayer bending modulus, K_c , vs. Tat mole fraction x_{Tat} . D -spacings for DOPC/Tat mixtures varied from 64 to 68 Å, for DOPC/DOPE/Tat mixtures from 64 to 69 Å, for DOPC/DOPS/Tat (3:1) mixtures from 57 Å to 100 Å (pure DOPS was unbound), and for nuclear mimic/Tat mixtures from unbound (nuclear mimic) to 64 Å. Estimated uncertainty in all values is about ± 2	29
2.9	Form factors of lipid mixtures (arbitrarily scaled and vertically displaced) with increasing Tat mole fractions x_{Tat} indicated on figure legends. Lipid mixtures: A. DOPC B. DOPC/DOPE (3:1) C. DOPC/DOPE (1:1) D. DOPC/DOPS (3:1) E. Nuclear mimic. The entire q_z range is shown in C, while others show partial ranges. Solid vertical lines indicate the q_z values where the form factors equal zero between the lobes of diffuse data.	30

2.10 The best fits to DOPC form factors (left) and the corresponding electron density profiles (right) with $x_{\text{Tat}} = 0, 0.016, 0.034$, and 0.059 (from top to bottom).	33
2.13 Difference between total electron density profiles of DOPC with Tat and that of DOPC	36
2.15 Bilayer thickness, D_{HH} (left) and D_{PP} (right) plotted against Tat mole fraction x_{Tat} . Black squares (DOPC), red circles (DOPC:DOPE (3:1)), and green triangles (DOPC:DOPE (1:1)). Error bars are standard deviations from imposing Tat Gaussian widths, $\sigma_{\text{Tat}} = 2.5, 3.0$ or 3.5 \AA .	39
2.16 Bilayer thickness, D_{PP} (left) and twice Tat position $2z_{\text{Tat}}$ (right) plotted against Tat mole fraction x_{Tat} . Black squares (DOPC), red circles (DOPC:DOPE (3:1)), and green triangles (DOPC:DOPE (1:1)). Error bars are standard deviations from imposing Tat Gaussian widths, $\sigma_{\text{Tat}} = 2.5, 3.0$ or 3.5 \AA . The data points of D_{PP} (left) is identical to those in Fig. 2.15, but the left axis is adjusted to facilitate comparison against $2z_{\text{Tat}}$	40
2.17 Area per lipid plotted against Tat mole fraction x_{Tat} . Black squares (DOPC), red circles (DOPC:DOPE (3:1)), and green triangles (DOPC:DOPE (1:1)). Error bars are standard deviations from imposing Tat Gaussian widths, $\sigma_{\text{Tat}} = 2.5, 3.0$ or 3.5 \AA	40
2.18 χ^2 as a function of z_{Tat} for DOPC, DOPC:DOPE (3:1), and DOPC:DOPE (1:1) (from left to right) with $x_{\text{Tat}} = 0.016, 0.034$, and 0.059 (from top to bottom). $\sigma_{\text{Tat}} = 3.0$. The THG model (black squares) and the THC model (red circles).	41
2.19 z_{Tat} as a function of Tat mole fraction x_{Tat} for fits with lower bounds on the headgroup widths (red circles) and without lower bounds (black squares)	43
2.20 MD simulated form factors for DOPC at $A_{\text{L}} = 68 \text{ \AA}^2$ (blue solid line), 70 \AA^2 (red solid line), and 72 \AA^2 (green solid line) compared to the experimental form factor (open circles) scaled vertically to best match the form factor for 70 \AA^2	45

2.21 The simulated, symmetrized electron density profile for DOPC at $A_L = 70 \text{ \AA}^2$ as a function of the distance away from the bilayer center. Each component profile is labeled with its name: PC (phosphate-choline), CG (carbonyl-glycerol), CH ₂ +CH (methylene-methine combination), CH ₃ (terminal methyl). The sum of all the components is labeled as total.	46
2.22 MD simulated form factors for DOPC with $x_{\text{Tat}} = 0.015$ at $A_L = 72 \text{ \AA}^2$ (top) and 74 \AA^2 (bottom), with $z_{\text{Tat}} = 18 \text{ \AA}$ (red solid lines), 16 \AA (green solid lines), and 14 \AA (blue solid lines) compared to the experimental form factor (open circles) scaled vertically to best match the form factor for $z_{\text{Tat}} = 18 \text{ \AA}$	47
2.23 MD simulated form factors for DOPC with $x_{\text{Tat}} = 0.030$ at $A_L = 74 \text{ \AA}^2$ (top) and 76 \AA^2 (bottom), with $z_{\text{Tat}} = 18 \text{ \AA}$ (red solid lines), 16 \AA (green solid lines), and 14 \AA (blue solid lines) compared to the experimental form factor (open circles) scaled vertically to best match the form factor for $z_{\text{Tat}} = 18 \text{ \AA}$	48
2.24 Electron density profiles of guanidinium groups from the four best matched simulations for DOPC with $x_{\text{Tat}} = 0.015$ (one Tat on each leaflet). Tat on the lower and upper leaflets are shown on the left and right plots, respectively.	51
2.25 MD simulated form factors (red solid lines in A and C) of Tat/(DOPC+Tat), $x_{\text{Tat}}=0.030$, with Tat fixed at $z_{\text{Tat}}= 18 \text{ \AA}$ (panel A) and 5 \AA (panel C) from the bilayer center compared to experimental form factors (open circles) scaled vertically to provide the best fit to the simulations. Corresponding snapshots are shown in Panels B and D in which the lipid chains are represented as grey sticks on a white background, Tats are yellow, phosphate groups are red and water is blue.	52
2.26 Location of Tat in DOPC bilayer. Tat is represented as a cylinder, z is the distance from the bilayer center, and R is the in-plane distance from the center of Tat. The average z of the lipid phosphates as a function of R and the arginine guanidiniums are shown in red and blue, respectively.	53

3.1 Lattice structure of the asymmetric ripple phase. Unit cells are shown in dash lines. Center of bilayers are shown by thick, solid lines. Notations in the figure are (a and b : lattice unit vectors), (D : D -spacing along z), ($\lambda_r = \mathbf{b} $: ripple wavelength), (γ : oblique tilt angle), (A : ripple amplitude), (ψ : chain tilt angle with respect to the z direction), and (x_M : projected length of the major arm).	59
3.2 Pictures of an annealing chamber	62
3.3 The horizontal profile of the beam used in the 2013 low resolution study. Each pixel was 0.07113 mm, which gave a CCD angular resolution $\Delta\theta$ of 0.0057°, corresponding to $\Delta q = 0.0011 \text{ \AA}^{-1}$ at the sample to detector distance of 359.7 mm. The beam FWHM = 1.7 pixels, giving $\Delta\theta = 0.010^\circ$ or $\Delta q = 0.0019 \text{ \AA}^{-1}$	65
3.4 The vertical profile of the beam used in the 2013 low resolution study. The beam height = 15 pixels = 1.1 mm.	65
3.5 In-plane geometric broadening due to the sample width w_s and the beam width Δx_{beam} . A top view of the sample (green) on the Si wafer (gray) and the incoming and diffracted X-rays (bounded by red solid lines) are shown. The total in-plane scattering angle for a lipid chain-chain correlation is labeled as 2θ , and the geometric broadening as Δx	67
3.6 The horizontal profile of the beam used in the 2013 high resolution experiment. The CCD angular resolution $\Delta\theta = 0.0092^\circ$ corresponding to $\Delta q = 0.0017 \text{ \AA}^{-1}$, at the sample to detector distance of 220.6 mm. The beam FWHM = 3.7 pixels = 0.26 mm, giving $\Delta\theta = 0.034^\circ$ or $\Delta q = 0.0063 \text{ \AA}^{-1}$	67
3.7 The vertical profile of the beam used in the 2013 high resolution experiment. The beam height = 9 pixels = 0.64 mm.	68
3.8 Geometric broadening in TWAXS	69
3.9 Top and side view of the beam on the sample in TWAXS	70
3.10 Projection of rectangular beam on the detector. Scattered beam appears as a parallelogram on the CCD.	70

3.11 (top panels) CCD images of X-ray scattering taken with (left) and without (right) a nominally 25 μm thick Mo attenuator. These data were taken at a fixed angle of incidence $\omega = 0.8^\circ$. The sample was an oriented film of DOPC:DOPE (3:1) in the fluid phase at 37 °C. The wavelength was 1.175 Å, the same as the one used for the ripple phase experiment. The same gray scale is used in both images. 100 pixel = 0.11 \AA^{-1} in q . A small dot located about $(p_x, p_z) = (520, 170)$ between the first and second orders is a specular reflection from the substrate. The exposure times were 1 second. (bottom panels) Vertical p_z slices of the X-ray images shown in the top panels (left). The scattering intensity measured with the attenuator (red solid circles) was multiplied by a factor of 6.9 and compared to the intensity measured without the attenuator (black solid circles, right).	73
3.12 1 second exposure (left) and 60 second exposure (right) of the low angle X-ray scattering from the DMPC ripple phase in gray log scales. The index h is labeled in green. $(3, k)$ reflections are identified in cyan. The shadow cast by 100 μm thick molybdenum attenuator blocking strong $(1,0)$ and $(2,0)$ orders in the right image is labeled as attenuator and extends from $q_z = 0 \text{ \AA}^{-1}$ to 0.2 \AA^{-1} . $D = 57.8 \text{ \AA}$, $\lambda_r = 145.0 \text{ \AA}$, and $\gamma = 98.2^\circ$	74
3.13 Schematics of the sample holder in the transmission mode. Side (left) and top (right) views are shown. The thickness of the Si wafer = 35 μm . The thickness of the sample $\approx 10 \mu\text{m}$. The distance between the axis of rotation and sample = 21.1 mm.	75
3.14 Circular path followed by the sample as the angle of incidence ω was changed. The sample to detector distance and D -spacing of the sample were measured in the LAXS mode, where $\omega = 1^\circ$. WAXS images were collected at the transmission mode, where $\omega = -45^\circ$. The z position of the sample was slightly higher at the LAXS mode than at the transmission mode, so the sample holder was vertically shifted for different modes.	76

3.15 Picture of the sample holder looking from above. A lead tape was attached to the back of the sample holder to help reduce the background scattering, typically coming from the air gap between the flightpath snout and the mylar window of the chamber.	76
3.16 Experimental reflectivity geometry.	79
3.17 Ewald sphere construction for the ripple phase diffraction in the low angle regime. A ripple $k = 0$ peak is the solid, black circle on the q_z -axis. A ripple $k \neq 0$ ring is the black ring centered about the q_z -axis. The portion of the ring that is inside the Ewald sphere is shown as a red dashed line and the portion of the ring that is outside but behind the Ew here to sayald sphere is shown as a black dotted line. The magnitude of the total scattering angle is exaggerated. With a wavelength of 1.175 Å, the magnitude $ \mathbf{k}_{\text{in}} = 5.35 \text{ \AA}^{-1}$. For a $h = 5$ peak, $q_{50}^z = 0.54 \text{ \AA}^{-1}$, one tenth of k_{in}	81
3.18 Side view of an arc of $k = 0$ peak shown as a thick blue line.	82
3.19 q -space representations of Bragg peaks and Bragg rings for $h = 1$ and 2 and $k = 0, 1$, and 2 in q_{hk}^z planes. The intersection between the Ewald sphere and a Bragg peak/ring is indicated in red. The observed intensity for the $k \neq 0$ orders is proportional to the fraction of the length of red arcs in the circumference. This fraction is equal to one for $k = 0$ reflections. Because the reflections are not in the same q_z plane, the range of q_y integration indicated by the height of the gray rectangle is different for different h orders. For $\gamma \neq 90^\circ$, the range of q_y integration is slightly different for different k reflections with the same h . The values shown are for $D = 58 \text{ \AA}$, $\lambda_r = 145 \text{ \AA}$, $\gamma = 90^\circ$, and $\lambda = 1.175 \text{ \AA}$. The magnitude of curvature of arcs is exaggerated.	83
3.20 The path of X-rays within the sample. The incident angle is ω and the total scattering angle is 2θ . An X-ray with a penetration depth of z is shown. The total thickness of the sample is t . Refraction correction is smaller than what? for $\theta > 0.5^\circ$ ($h = 1$).	86
3.21 Absorption factors as a function of $q_z \approx 4\pi\theta/\lambda$. Values at $q_z = 2\pi h/D$ corresponding to $D = 57.8 \text{ \AA}$ are shown as squares. $\mu = 2600 \text{ \mu m}$, $t = 10 \text{ \mu m}$, and $\lambda = 1.175 \text{ \AA}$	88
3.22 Eq. (3.30) plotted as a function of ω for $\theta = \theta_B$	89

3.23	Contours of a mosaic spread distribution projected on the $\omega\chi$ -plane, where $\chi - \chi_{hk}$ is an angle measured from a (h, k) reflection on the detector ($\chi = \pi/2 - \phi$ in Fig. 3.16) and θ_{hk} is the Bragg angle for a (h, k) reflection. The distribution function takes a form of Lorentzian centered at $\alpha = 0$. Domains with $\alpha = 0$ are probed at $\omega = \theta_{hk}$ and $\chi = \chi_{hk}$. Integrated intensity of $(1, k)$ reflection arises from domains in the green shaded area while that of $(3, k)$ reflection is from the blue shaded area, which is three times larger.	90
3.24	Mosaic factor given by Eq. (3.37) as a function of $q_z \approx 4\pi\theta/\lambda$	92
3.25	Two dimensional map of F_C	102
3.26	Two dimensional electron density profile calculated using the phases predicted by the 2G hybrid model (Fit5)	104
3.27	Electron density profiles along Slice A shown in Fig. 3.26, calculated using the phases predicted by different fits. The distance r is measured from the bilayer center. A cartoon of lipids is shown at the top, designating different parts of the profile as the lipid headgroup and chains. The fit from which each profile was calculated is shown in the figure legend.	105
3.28	Electron density profiles along Slice B shown in Fig. 3.26, calculated using the phases predicted by different fits. The distance r is measured from the bilayer center. The fit from which each profile was calculated is shown in the figure legend.	106
3.29	Two dimensional electron density profile calculated using the phases predicted by the 2G hybrid model (Fit2)	107
3.30	Variation in the electron density profile along Slice A. Reversing the sign of the $(3, 0)$ phase in Fit5 resulted in the red dashed profile (Fit5a). Reversing the sign of the $(1, 3)$, $(3, 0)$, $(6, 0)$, and $(9, 0)$ resulted in the green dash-dotted profile (Fit5b). The distance r is measured from the bilayer center.	108
3.31	Variation in the electron density profile along Slice B. Reversing the sign of the $(3, 0)$ phase in Fit5 resulted in the red dashed profile (Fit5a). Reversing the sign of the $(1, 3)$, $(3, 0)$, $(6, 0)$, and $(9, 0)$ resulted in the green dash-dotted profile (Fit5b). The distance r is measured from the bilayer center.	109

3.32 Transformation of wide angle scattering data from the CCD to q -space	111
3.33 Fluid phase WAXS plotted along q_r at $q_z = 0.012 \text{ \AA}^{-1}$. The red solid line is a Lorentzian fit with its FWHM equal to 0.288 \AA^{-1} , centered at $q_r = 1.408$. Extra intensity at larger q_r was due to water scattering, which led to a slightly asymmetric profile.	112
3.34 nGIWAXS of the DMPC gel phase	113
3.35 High resolution nGIWAXS of the DMPC ripple phase for $D = 60.8 \text{ \AA}$. The angle of incidence ω was 0.2° . The stronger peak was at $(q_r, q_z) \approx (1.478 \text{ \AA}^{-1}, 0.20 \text{ \AA}^{-1})$. The weaker peak was at $(q_r, q_z) \approx (1.452 \text{ \AA}^{-1}, 0.12 \text{ \AA}^{-1})$. The scattered intensity along the line slightly above $q_z = 0 \text{ \AA}^{-1}$ is the Vineyard-Yoneda peak [106, 107].	115
3.36 q_r swaths of the ripple WAXS, each averaged over 0.02 \AA^{-1} in q_z . Each curve is shifted by 100 vertically. The central q_z values of swaths are shown in the figure legend.	116
3.37 nGIWAXS of the DMPC ripple phase for $D = 59.2 \text{ \AA}$ (left) and difference between $D = 59.2 \text{ \AA}$ and 60.8 \AA (right). The difference shows no obvious feature, indicating that the ripple WAXS patterns at the two D-spacing were identical within an error. The angle of incidence ω was 0.2° . The data were taken with the high resolution setup.	117
3.38 Peak profile in q_r at $q_z = 0.2 \text{ \AA}^{-1}$ fitted to double Lorentzian functions	117
3.39 Peak profile in q_r at $q_z = 0.12 \text{ \AA}^{-1}$ fitted to double Lorentzian (left) and double pseudo Voigtian functions (right)	118
3.40 Transmission WAXS of the DMPC gel phase	120
3.41 TWAXS image of the DMPC ripple phase	121
3.42 q_r swath of the ripple TWAXS averaged between 0.11 \AA^{-1} and 0.13 \AA^{-1} in q_z . Asymmetric shape of the profile is due to two Bragg rods centered at different q_r values as discussed in Sec. 3.6.	122
3.44 q_z swath averaged between 1.465 \AA^{-1} and 1.481 \AA^{-1} (left) and between 1.465 \AA^{-1} and 1.51 \AA^{-1} (right) in q_r . The left plot is approximately the q_z profile along the weaker peak while the right profile extends over the entire ripple WAXS pattern.	123

3.45 Comparison of the electron density profiles of the DMPC gel phase (left) and the major arm in the ripple phase (right). The DMPC profile is taken from Ref. [53]. The ripple major arm profiles were calculated using the phases predicted by Fit2, 5, and 7 (black, red, and green, respectively). The ripple profiles are scaled to match with the gel phase profile.	125
3.46 Comparison of the electron density profiles of the DMPC fluid phase (left) and the minor arm in the ripple phase (right). The DMPC profile is taken from Ref. [68]. The ripple minor arm profiles were calculated using the phases predicted by Fit2, 5, and 7 (black, red, and green, respectively). The ripple profiles are scaled to match approximately with the fluid phase profile.	128
3.47 Comparison of the ripple (black) and fluid (red) phase WAXS at $q_z = 0.012 \text{ \AA}^{-1}$. The fluid phase data were taken with the low resolution setup and scaled vertically to enable visual comparison.	128
3.48 Comparison of the electron density profiles of the DHPC $L_\beta I$ interdigitated phase (left) and the minor arm in the ripple phase (right). The DHPC profile is taken from Ref. [?]. The ripple minor arm profiles were calculated using the phases predicted by Fit2, 5, and 7 (black, red, and green, respectively). The ripple profiles are scaled to match approximately with the $L_\beta I$ phase profile.	129
3.49 Comparison of the wide angle (WAXS) pattern predicted by the ripple phase structure proposed in Ref. [98] (left) and our measured WAXS (right). In the left, the interdigitated chains scatter coherently, giving rise to a Bragg peak at $q_z \approx 0.4 \text{ \AA}^{-1}$, while q_z values of the observed peaks in our data were 0.12 \AA^{-1} and 0.2 \AA^{-1}	130
A.1 The best fits to DOPC:DOPE (3:1) form factors (left) and the corresponding electron density profiles (right) with $x_{\text{Tat}} = 0, 0.016, 0.034,$ and 0.059 (from top to bottom).	135
A.2 The best fits to DOPC:DOPE (1:1) form factors (left) and the corresponding electron density profiles (right) with $x_{\text{Tat}} = 0, 0.016, 0.034,$ and 0.059 (from top to bottom).	136

A.3	Two dimensional view of mosaic spread (left) and notations used in this section (right). The stacking direction of an ideal domain is \mathbf{n} and that of a tilted domain \mathbf{n}' . The deviation of \mathbf{n}' from \mathbf{n} denoted as α quantifies the degree of misorientation of a domain. The x , y , and z -axes are the sample coordinates.	137
A.4	Example of a two dimensional sample consisting of an ideal and tilted domains. $\mathbf{q} = (q_x, q_z)$ is the sample q -space and $\mathbf{q}' = (q'_x, q'_z)$ is the domain q -space. The two q -spaces are related by a rotation of α about the y -axis, which is into the page.	139
A.5	Notations used in this section. The arc originating from the Z -axis is the mosaic arc due to the mosaic spread distribution.	142
A.6	Rocking scan trace in q -space.	143
A.10	Unit cell for chain packing in the major arm	158

Chapter 1

Introduction

Lipids are amphiphilic molecules, consisting of a hydrophilic headgroup and hydrophobic chains. There are various kinds of lipids. These can be categorized in terms of headgroup, chain length, and chain saturation.

In water lipids self-assemble into lipid bilayers to shield their hydrophobic cores. Lipid bilayers are the building blocks of cell membranes. Lipid bilayers display a wide variety of thermodynamic phases as a function of temperature and hydration. Figure 1.1 shows a phase diagram of dimyristoylphosphatidylcholines (DMPC). At full hydration, a lamellar phase coexists with excess water. PC lipids constitute a substantial fraction of cell membranes and have been studied for many decades. In the high temperature, fluid L_α phase, the hydrocarbon chains are conformationally disordered, and intra-membrane molecular correlations are liquid-like [1] (Fig. 1.2). In the low temperature, gel $L_{\beta'}$ phase, hydrocarbon chains are stiff and tilted with respect to the membrane normal [2], and are organized in either hexagonal or orthorhombic lattice. The $L_{\beta'}$ is further categorized into three phases according to the chain tilt direction [11]. In the $L_{\beta I}$ phase, chains are tilted toward the nearest neighbor as shown in Fig. 1.3, and in the $L_{\beta F}$ phase, chains are tilted toward the next-nearest neighbor. In the $L_{\beta L}$ phase, chains are tilted toward an intermediate direction.

Between the fluid and gel phases appears a height modulated phase where bilayers are no longer flat (Fig. 1.4). The low angle diffraction pattern of this phase conforms to the symmetry of a two dimensional monoclinic lattice. This phase was termed P'_{β} and is commonly called the ripple phase. The $P_{\beta'}-L_{\beta'}$ transition is often called the pre-transition. The topography of the membrane ripples has been directly visual-

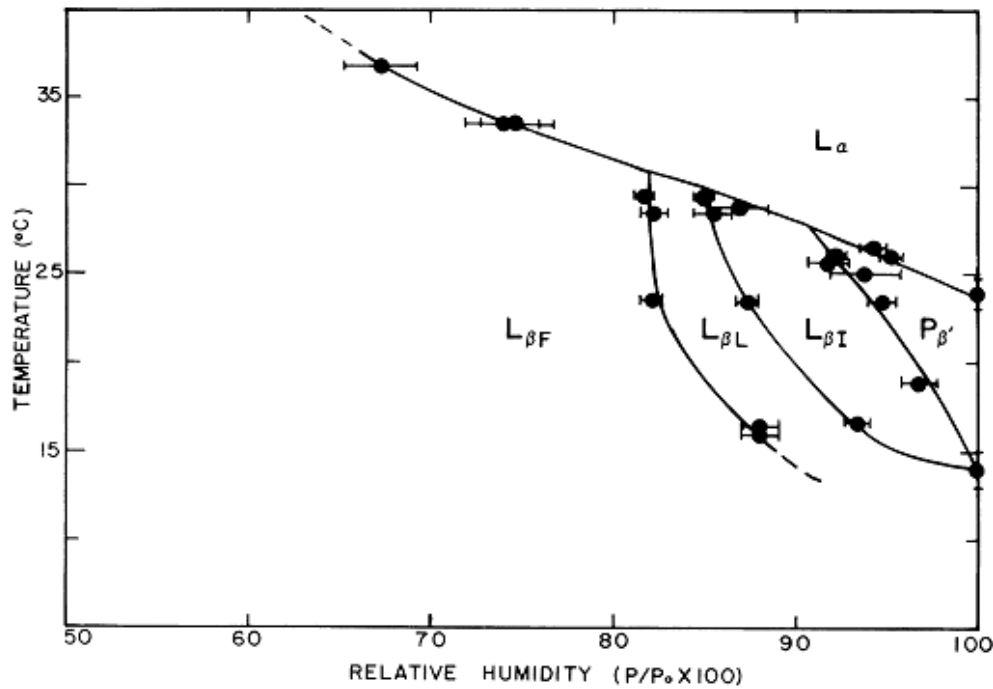


Figure 1.1: Experimental phase diagram of DMPC from Ref. [11]. $L_{\beta'I}$, $L_{\beta'L}$, and $L_{\beta'F}$ belong to the gel $L_{\beta'}$ phase. $P_{\beta'}$ is the ripple phase and L_α is the fluid phase.

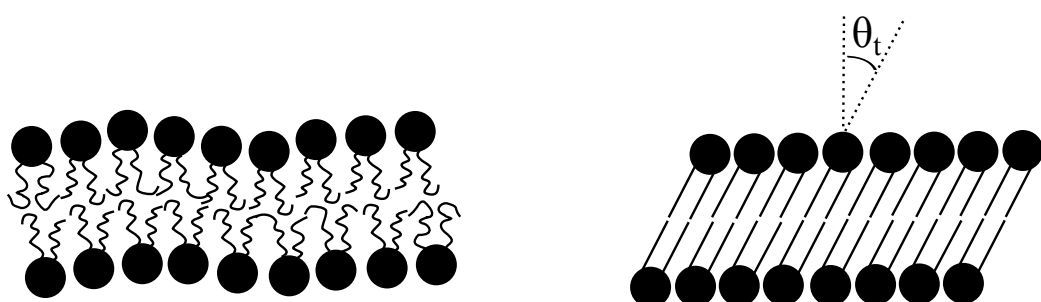


Figure 1.2: Schematics of the structure of fluid L_α phase (left) and gel $L_{\beta'}$ phase (right). Black solid circles are lipid headgroups and solid lines are lipid chains. θ_t is the chain tilt angle.

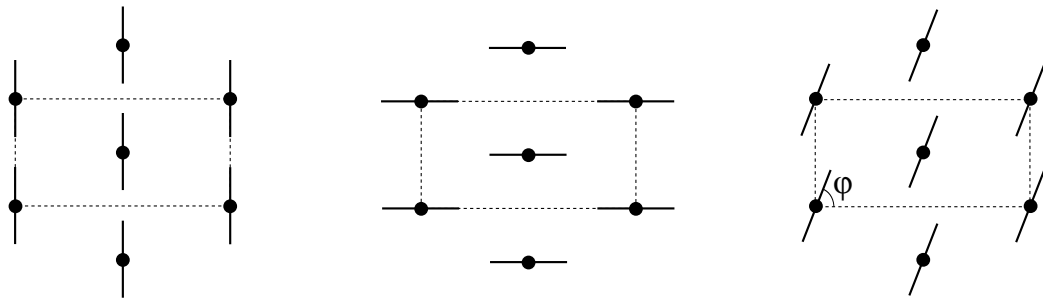


Figure 1.3: Chain tilt direction in $L_{\beta I}$ (left), $L_{\beta F}$ (middle), and $L_{\beta L}$ (right) phases. Black dots are orthorhombic lattice points. Unit cells are shown in dashed lines. Chains are drawn as solid lines. Chains are tilted toward the nearest neighbor in $L_{\beta I}$ phase with $\phi = \pi/2$. In $L_{\beta F}$ phase, they are titled toward the next-next nearest neighbor ($\phi = 0$). In $L_{\beta L}$ phase, ϕ can be anywhere between 0 and $\pi/2$.

ized by freeze fracture electron microscopy experiments [3–7]. The wavelength of the modulation is about 140 Å for dimyristoylphosphatidylcholine (DMPC), which has 14 carbons in the hydrocarbon chains [8]. There has been evidence that molecular conformation in the ripple phase is not unique. NMR signals in the ripple phase [9] were consistent with a superposition of signals observed in the fluid and gel phases. Lateral diffusion measurements found two distinct populations, with diffusion coefficients characteristic of fluid and gel phases [10].

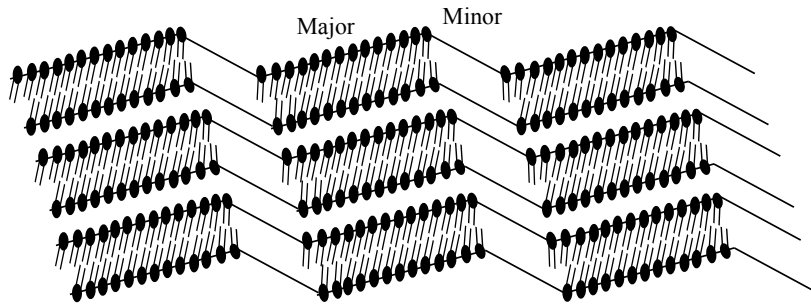


Figure 1.4: Schematic of the $P_{\beta'}$ ripple phase. In this phase, bilayers assume periodic height modulation with a sawtooth shape. The longer side of a sawtooth is called major arm and the shorter side is called minor arm. It is generally assumed that chains are in all trans conformation in the major arm, but the molecular packing in the minor arm is not known.

In this thesis, we focus on the fluid and ripple phases. In the former phase, we investigated the interaction of Tat peptide with lipid bilayers. This study is discussed in chapter 2. Regarding the ripple phase, we measured the electron density profile of the lipid bilayers using a stack of oriented bilayers. Using wide angle x-ray scattering technique, we also investigated the chain packing within a bilayer. The ripple phase is discussed in chapter 3. The appendix includes details that are not essential in understanding this thesis, but allow other researchers to reproduce most of the results shown in this thesis.

Chapter 2

Structural Perturbation of Lipid Bilayers Due to Tat Peptide

2.1 Introduction

The name cell-penetrating peptide (CPP) connotes a peptide that easily penetrates cell membranes (for Reviews see [12–14]).

This thesis focuses on the transactivator of translation, Tat, from the HIV-1 virus, which plays a role in AIDS progression. Earlier work showed that the HIV-Tat protein (86 amino acids) was efficiently taken up by cells, and concentrations as low as 1 nM were sufficient to transactivate a reporter gene expressed from the HIV-1 promoter [15, 16]. It has been reported that Tat protein uptake does not require ATP [17]. Studies using inhibitors of different types of endocytosis, including clathrin and caveolae-mediated, or receptor-independent macropinocytosis reached the same conclusion that ATP mediated endocytosis is not involved in Tat protein permeation [?, 18–20]. However, this issue is controversial, as other studies found evidence for endocytosis in Tat protein import [21–29]. Still other studies have concluded that an ATP requirement for Tat protein entry depends on the size of the cargo attached to Tat protein, or on the specific cell type [30–32]. The part of the Tat protein responsible for cellular uptake was assigned to a short region Tat (48–60), G₄RKKRRQRRRPPQ₆0, which is particularly rich in basic amino acids [17]. Deletion of three out of eight positive charges in this region caused loss of its ability to translocate [17]. In this chapter, short basic regions will be called Tat, while the entire

86 amino acid protein will be called Tat protein. Tat was shown to be responsible for the Tat proteins permeation into the cell nucleus and the nucleoli [17], and this was confirmed using live cell fluorescence in SVGA cells [33]. Tat (48-60) was shown to have little toxicity on HeLa cells at 100 μM concentration [17], but the longer Tat protein (2-86) was toxic to rat brain glioma cells at 1-10 μM [34]. Interestingly, no hemolytic activity was found when human erythrocytes were incubated with a highly neurotoxic concentration (40 μM) of Tat (2-86) [34]. These results prompt the question, what is the mechanism of Tats translocation through membranes? To address this question, many biophysical studies have used simple models of biological membranes composed of a small number of lipid types. These studies are valuable because there is no possibility for ATP-dependent translocation, thus ruling out endocytosis if translocation occurs. For example, Mishra et al. reported that the rate of entry into giant unilamellar vesicles (GUVs) composed of PS/PC (1:4 mole ratio) lipids of rhodamine-tagged Tat is immeasurably slow, but it crosses a GUV composed of PS/PC/PE (1:2:1) lipids within 30 seconds [35]. This study suggests that negative curvature induced by the inclusion of PE facilitates translocation. In a subsequent study using much smaller unilamellar vesicles (LUVs), Tat did not release an encapsulated fluorescent probe in LUVs composed of lipids modeling the outer plasma membrane, PC/PE/SM/Chol (1:1:1:1.5), but did release the probe in LUVs composed of BMP/PC/PE (77:19:4) [36]; BMP (bis(monoacylglycero)-phosphate) is an anionic lipid specific to late endosomes. In that study [36], the inclusion of PE did not suffice to cause leaky fusion in LUVs in the absence of a negatively charged lipid. The contrasting results in these two experiments may also be due to the use of LUVs instead of GUVs since it was reported that Tat does not translocate across LUVS of PC/PG (3:2) but does translocate across GUVs of the same lipid composition [37]. In a similar experiment, Tat did not translocate into egg PC LUVs [38]. In another experiment confirming these results, Tat did not translocate into GUVs containing only PC with 20 mol% cholesterol, but when PS or PE was included with PC, then rapid translocation of Tat was observed [39]. These experiments demonstrate that the choice of lipids and model systems influences Tat translocation.

Is a pore formed during Tat translocation? Although direct conductance measurements of Tat and lipid membranes have not been carried out, two studies measured conductance with the somewhat similar CPP oligoarginine R₉C peptide. Using single-channel conductance of gramicidin A in planar lipid membranes consisting of anionic,

neutral or positively charged lipids, R₉C did not increase conductance, even in anionic lipid membranes [40]. By contrast, in a similar experiment using planar lipid membranes, a current was induced by R₉C in PC/PG (3:1) membranes, with increasing destabilization over time [41]. Thus questions remain about pore formation of Tat in membranes. In the GUV experiment with Tat mentioned above [39], Ciobanasu *et al.*, using size exclusion methods, suggested a pore in the nanometer range, which could only be passed by small dye tracer molecules. Thus, if a true pore forms, it is likely to be small and transitory.

The secondary structure of Tat has been characterized by many researchers. Ref. [37] carried out Circular dichroism (CD) spectroscopy on a variation of Tat where the penultimate proline on Tat (48-60) was replaced by a tryptophan [37]. Their study found a random coil secondary structure in aqueous solution as well as when Tat was mixed with PC/PG/PE (65:35:5) LUVs. Ziegler *et al.* [20] obtained the same result using CD in PC/PG (3:1) vesicles. In addition, solid state NMR has identified a random coil structure of Tat in DMPC/DMPG (8:7 mole ratio) multibilayers [42]. In the larger Tat-(1-72)-protein NMR measurements at pH 4 have determined there is no secondary structure, with a dynamical basic region [43]. Similarly, NMR was used to study the full Tat protein and found a highly flexible basic region [44]. These previous studies indicate that an alpha helix is not required for Tats translocation ability.

Regarding the mechanism of translocation of this randomly structured, short basic peptide, many models have been proposed based on the conflicting results listed above. Molecular dynamics simulations offer some insight into the molecular details of translocation. Herce and Garcia simulated the translocation of Tat (Y₄₇GRKKRRQRRR₅₇) across DOPC at various lipid:peptide molar ratios [45]. Their simulations indicated that Tat binds to the phosphate headgroups, with 1 Tat binding with 14 lipids, each positive charge on Tat associated with nearly 2 phosphate groups [45]. Translocation involved a localized thinning, and snorkeling of arginine side chains through the hydrophobic layer to interact with phosphates on the other side of the membrane. This allowed some water molecules to penetrate the membrane along with Tat, forming a pore [45]. In this simulation, performed without inclusion of counterions, pore formation was only observed at high ratios of peptide:lipid (1:18) or at elevated temperature. However, a subsequent Gromacs simulation with counterions found no thinning and no pore formation when Tat was added to DOPC

membranes [46]. Instead it found a membrane invagination associated with a cluster of Tat peptides. From their findings, the authors suggested that micropinocytosis could be the model for Tat translocation across membranes [46].

In this thesis, I combine experimental low-angle X-ray scattering (LAXS) data with MD simulations to obtain the structure of fully hydrated, oriented lipid bilayers with Tat (47-57) added at several mole ratios. The lipid systems were DOPC, DOPC/DOPE (3:1 mole ratio), DOPC/DOPS (3:1), DOPC/DOPE (1:1) and a mimic of the nuclear membrane (POPC/POPE/POPS/SoyPI/Chol, 69:15:2:4:11).

2.2 Materials and Methods

2.2.1 Stock Solutions

Synthesized lipids were purchased from Avanti Polar Lipids (Alabaster, AL). Membrane mimics for Tat experiments were prepared by first dissolving lyophilized lipids in chloroform and then mixing these stock solutions to create the lipid compositions DOPC, DOPC:DOPE (3:1), DOPC:DOPE (1:1), DOPC:DOPS (3:1) and nuclear membrane mimic (POPC:POPE:POPS:SoyPI:Cholesterol, 69:15:2:4:11) (based on Ref. [37] []). Peptide ($\text{Y}_{47}\text{GRKKRRQRRR}_{57}$) was purchased in two separate lots from the Peptide Synthesis Facility (University of Pittsburgh, Pittsburgh, PA); mass spectroscopy revealed greater than 95% purity. This Tat peptide corresponds to residues (47-57) of the 86 residues in the Tat protein [6] []. Tat was dissolved in HPLC trifluoroethanol (TFE) and then mixed with lipid stock solutions in chloroform to form mole fractions between 0.0044 and 0.108. Weight of Tat in these mole fractions was corrected for protein content (the remainder being 8 trifluoroacetate counter-ions from the peptide synthesis). Solvents were removed by evaporation in the fume hood followed by 2 hours in a vacuum chamber at room temperature.

2.2.2 Thin Film Samples

For Tat experiments, four mg dried lipid/peptide mixture was re-dissolved in HPLC chloroform:TFE (2:1 v:v) for most of the lipid compositions. DOPC:DOPS (3:1) mixtures required chloroform:HFP (1:1 v:v) in order to solubilize the negatively charged DOPS. 200 μl of 4 mg mixtures in solvents were plated onto silicon wafers ($15 \times 30 \times 1$

mm) via the rock and roll method [38] to produce stacks of \sim 1800 well-aligned bilayers; solvents were removed by evaporation in the fume hood, followed by two hours under vacuum. Samples were prehydrated through the vapor in polypropylene hydration chambers at 37 °C for two to six hours directly before hydrating in the X-ray hydration chamber [39] for 0.5 to 1 hour.

2.2.3 Volume Measurements

Multilamellar vesicles (MLVs) were prepared by mixing dried lipid mixtures with MilliQ water to a final concentration of 2-5 wt% in nalgene vials and cycling three times between 20 °C and 60 °C for ten minutes at each temperature with vortexing. Pure Tat was dissolved in water at 0.4 wt%.

Volumes of lipid mixtures with and without peptides in fully hydrated multilamellar vesicles (MLV) were determined at 37 ± 0.01 °C using an Anton-Paar USA DMA5000M (Ashland, VA) vibrating tube densimeter. This instrument measures the average density of a solution and compares it to the density of air using $\rho_s - \rho_0 = k(\tau_s - \tau_0)^2$ where k is an instrumental ??? that depends on the atmospheric pressure.

The Tat peptide sequence used in X-ray experiments and MD simulations was Y₄₇GRKKRRQRRR₅₇. Table 2.1 lists the chemical formulas and molecular weights of these amino acids for convenience. The molecular weight of this sequence is $181.2 + 75.1 + 146.1 + 2 \times 146.2 + 6 \times 174.2 - 10 \times 18 = 1560$. The Tat peptides were synthesized in trifluoroacetic acid, which has the chemical formula CF₃CO₂H, and is made into a powder form by the freeze-dry method. Therefore, each positively charged amino acid such as an arginine and lysine was counter-balanced by a trifluoroacetate (TFA) (C₂F₃O₂). Since Tat has six arginines and two lysines, it came with eight trifluoroacetates. This complex has a molecular weight of $1560 + 113 \times 8 = 2464$. We used the molecular weight of this complex in order to calculate the molarity of Tat correctly. The same molecular weight was also used in preparing oriented samples.

The Tat volume V_{Tat} was calculated from the measured average density of a Tat-water solution in the following way. Assuming that Tat molecules in water do not change the volume of water molecules, the density of Tat-water solution is equal to the mass of Tat-water solution divided by the sum of volumes of water and Tat,

$$\rho_{\text{sol}} = \frac{m_w + m_c}{V_w + V_c N_c}, \quad (2.1)$$

Code	Amino acid	Chemical Formula	Molecular weight (g/mol)
K	Lysine	C ₆ H ₁₄ N ₂ O ₂	146.2
R	Arginine	C ₆ H ₁₄ N ₄ O ₂	174.2
G	Glycine	C ₂ H ₅ NO ₂	75.1
Y	Tyrosine	C ₉ H ₁₁ NO ₃	181.2
Q	Glutamine	C ₅ H ₁₀ N ₂ O ₃	146.1

Table 2.1: Some Amino Acids Data

where m_w and m_c are the total masses of water and Tat-TFA complex, respectively, V_w is the total volume of water, V_c is the molecular volume of a Tat-TFA complex, and N_c is the total number of this complex in the solution. Denoting $V_w = m_w/\rho_w$ and $N_c = N_A m_c/W_c$, where W_c is the molecular weight of the complex, N_A is the Avogadro's number, and ρ_w is the density of water, we have

$$V_c = \frac{W_c}{\rho_{\text{sol}} N_A} \left(1 + \frac{m_w}{m_c} \left(1 - \frac{\rho_{\text{sol}}}{\rho_w} \right) \right), \quad (2.2)$$

which allows us to calculate the molecular volume of a Tat-TFA complex from the experimentally measured quantities. Assuming that the molecular volume scales with the molecular weight gives the volume of Tat, $V_{\text{Tat}} = 1560/2464 \times V_c \text{ \AA}^3$.

2.2.4 X-ray setup

Figure 2.1 shows a schematic of the X-ray setup.

The hydration chamber is described in detail in [?]. The sample holder was mounted on a servo motor, which allowed continuous rotation of the sample between -1.6° and 7° . A Peltier cooling/heating element was attached to the sample holder and the sample was situated on this Peltier element, with which hydration level of the sample could be easily adjusted. This ability of the chamber was important especially in the ripple phase experiment, which is described in chapter 3. Hydration level of a sample was estimated by measuring the average interbilayer distance, D -spacing, which was easily calculated by indexing the diffraction peaks using the tview software developed by Dr. Yufeng Liu. The semitransparent beam stop was set to always cover the direct beam, which would otherwise saturate the charge coupled device (CCD) detector. The beam profile was measured through this semitransparent beam stop. Data reduction and correction for a CCD detector are described in detail in [47].

Figure 2.1: X-ray setup for LAXS experiments.

2.2.5 Data reduction of diffuse scattering data

2.2.6 Analysis of Diffuse Scattering

Figure 2.2 shows our typical low angle X-ray scattering (LAXS) data from oriented stacks of fluctuating bilayers in the fluid phase. Analysis of diffuse scattering intensity patterns like the one shown in Fig. 2.2 results in material parameters such as the bending modulus K_c and bulk modulus B as well as the absolute form factor $|F(q_z)|$. The form factor is the Fourier transform of the bilayer electron density profile $\rho(z)$ and directly related to the internal structure of the bilayers including Tat peptides.

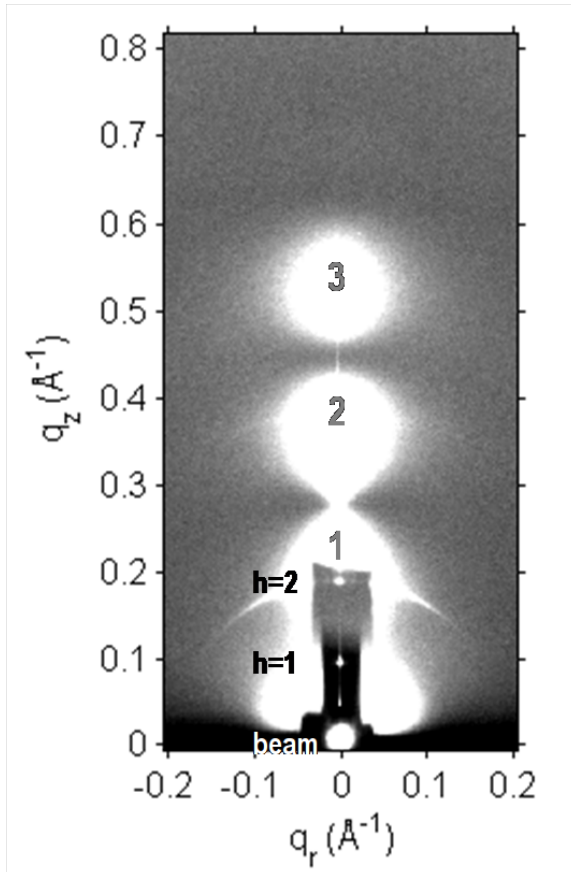


Figure 2.2: LAXS of DOPC:DOPE (1:1) with $x_{\text{Tat}} = 0.034$ at 37 °C. White lobes of diffuse scattering intensity have large grey numbers, while lamellar orders and beam are shown to the left of the molybdenum beam attenuator (short, dark rectangle). q_z and q_r are the cylindrical coordinates of the sample q -space, where q_z -axis is along the bilayer normal and q_r -axis is along the in-plane direction. The lamellar repeat spacing was $D = 66.2 \text{ \AA}$.

The form factor $F(q_z)$ is obtained by realizing that the diffuse scattering intensity pattern $I(\mathbf{q})$ is a product of the structure factor $S(\mathbf{q})$ and the form factor; $I(\mathbf{q}) = S(\mathbf{q})|F(q_z)|^2$, where $\mathbf{q} = (q_r, q_z)$, indicating that the system is in-plane isotropic. In fully hydrated multilamellar samples, $S(\mathbf{q})$ is not simple delta functions because of thermal fluctuations of bilayers. Calculating $S(\mathbf{q})$ requires a model free energy for bilayer fluctuations, from which the scattering pair correlation function is derived. A basic scattering theory, then, relates the scattering intensity $I(\mathbf{q})$ to the pair correlation function. For modeling the membrane fluctuations of a multilamellar system, the smectic liquid crystal free energy functional in the discrete form,

$$F = \frac{1}{2} \int d\mathbf{r} \sum_{n=0}^{N-1} \left\{ K_c [\nabla_r^2 u_n(\mathbf{r})]^2 + B [u_{n+1}(\mathbf{r}) - u_n(\mathbf{r})]^2 \right\}, \quad (2.3)$$

has been shown to be adequate [48]. Here, $u_n(\mathbf{r})$ is the spatial deviations of the center of the n -th bilayer from its average position in the z direction at the in-plane location $\mathbf{r} = (x, y)$ (Fig. 2.3). The first term is the bending free energy proportional to the curvature squared with the proportionality given by a bending modulus K_c and the second term is a harmonic approximation to the interactions between membranes with a modulus B . Once the two dimensional structure factor map $S(\mathbf{q})$ is calculated from Eq. (2.3), the form factor can be calculated by dividing the intensity by the structure factor. Getting the best fit of a model structure factor to the intensity results in the material parameters, K_c and B .

We used a software called NFIT developed by Dr. Yufeng Liu [48–50] to analyze the diffuse scattering and obtain the bending modulus, bulk modulus, and form factor. Details of the analysis, including the theoretical derivation of the structure factor from Eq. (2.3) and its numerical computation, are found in Dr. Yufeng Liu’s thesis [50].

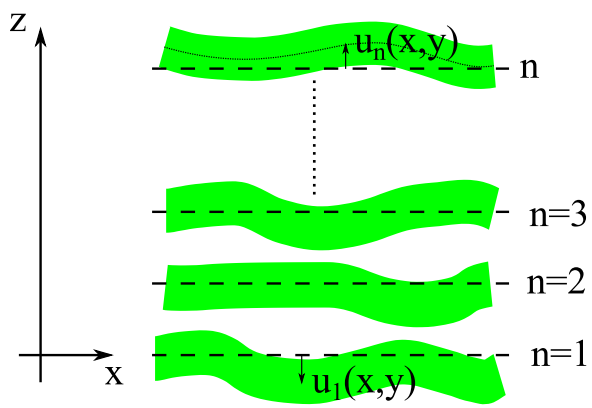


Figure 2.3: Schematic of an oriented stack of lipid bilayers. Thick green curves represent an instance of thermally fluctuating bilayers. The dashed lines show the thermally averaged positions $z = nD$ of the centers of each bilayer and $u_n(x, y)$ gives the instantaneous deviation from the average. Each bilayer extends in the $\mathbf{r} = (x, y)$ plane.

2.2.7 Modeling the Bilayer Structure

In the case of X-rays, the features with the most contrast are the electron-dense headgroups, providing the head-head spacing D_{HH} , and also the terminal methyl groups in the bilayer center with the least electron density. Modeling of the bilayer structure was done similarly to the SDP model written by Dr. Norbert Kucerka when he was a postdoc in the Nagle/Tristram-Nagle lab [52].

Parsing of DOPC into lipid components is shown in Fig. 2.4. The phosphate/choline (PC) and carbonyl/glycerol (CG) components together make up the lipid headgroup whereas the hydrocarbon chain region (HC) is divided into two components, the methylene (CH_2) and methine (CH) group combination (denoted as CH_2+CH) and terminal methyl groups (CH_3). We combine methylene (CH_2) and methine groups (CH) in order to avoid proliferation of fitting parameters.

2.2.7.1 Functional forms

Our model for the electron density profile (EDP) of Tat/lipid bilayer system consists of five structural subgroups: PC, CG, CH_2+CH , CH_3 , and Tat (see Fig. 2.5). The volume probability distributions of components PC, CG, CH_3 , and Tat are described by Gaussian functions,

$$P_i(z) = \frac{c_i}{\sqrt{2\pi}} \left(\exp\left\{-\frac{(z+z_i)^2}{2\sigma_i^2}\right\} + \exp\left\{-\frac{(z-z_i)^2}{2\sigma_i^2}\right\} \right), \quad (2.4)$$

where c_i is an integrated area underneath the curve and the two parts of the expression describe the two bilayer leaflets.

The hydrocarbon chain region (HC) is represented by error functions,

$$P_{\text{HC}}(z) = \frac{1}{2} [\text{erf}(z, -z_{\text{HC}}, \sigma_{\text{HC}}) - \text{erf}(z, z_{\text{HC}}, \sigma_{\text{HC}})], \quad (2.5)$$

where

$$\text{erf}(z, z_i, \sigma_i) = \frac{2}{\sqrt{\pi}} \int_0^{\frac{z-z_i}{\sqrt{2}\sigma}} dx e^{-x^2}. \quad (2.6)$$

The volume probability distribution for the methylene and methine group combination can then be expressed as

$$P_{\text{CH}_2+\text{CH}}(z) = P_{\text{HC}}(z) - P_{\text{CH}_3}(z). \quad (2.7)$$

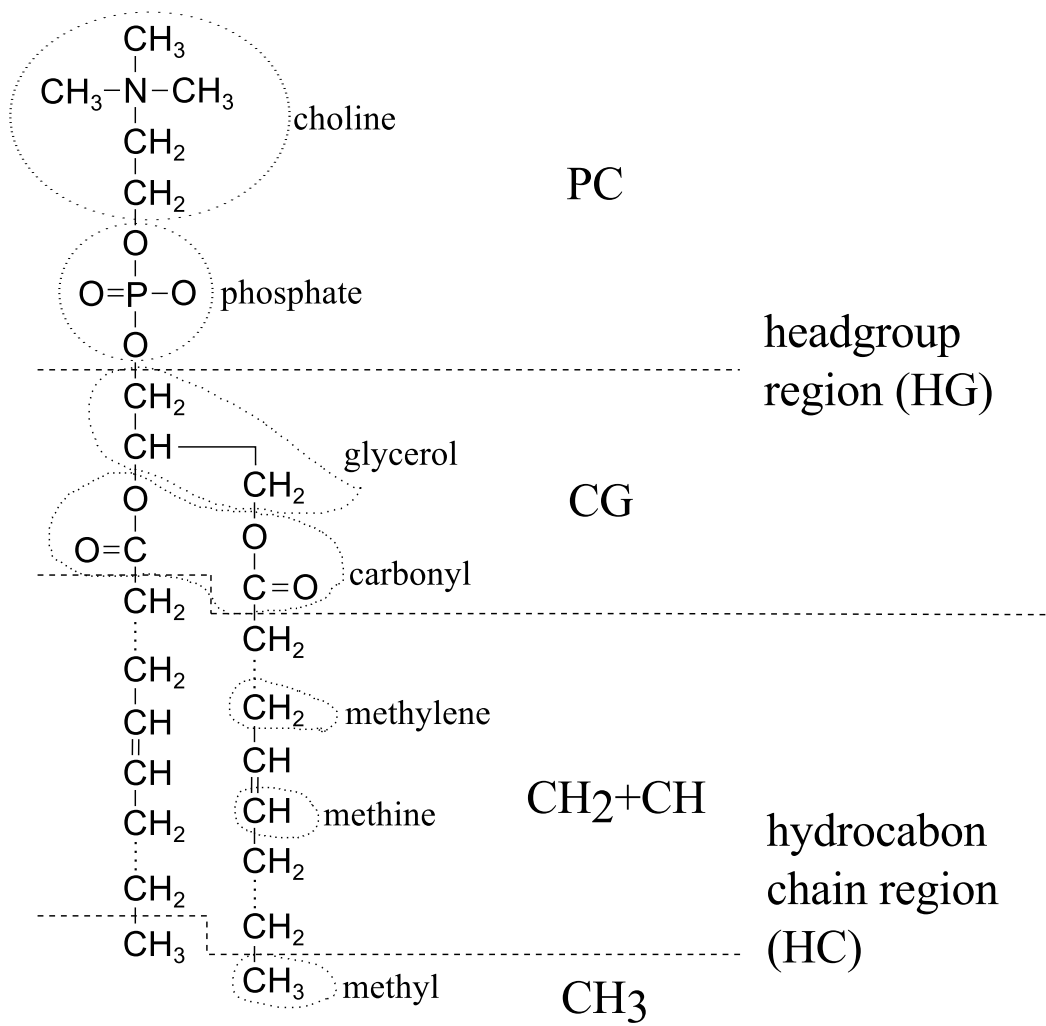


Figure 2.4: Schematic of DOPC showing each lipid component. The dash lines show where the lipid is divided into different components. The lipid headgroup is divided into two components, phosphate-choline (PC) and carbonyl-glycerol (CG). The hydrocarbon chain region is also divided into two components, methylene+methine (CH_2+CH) and terminal methyl groups (CH_3).

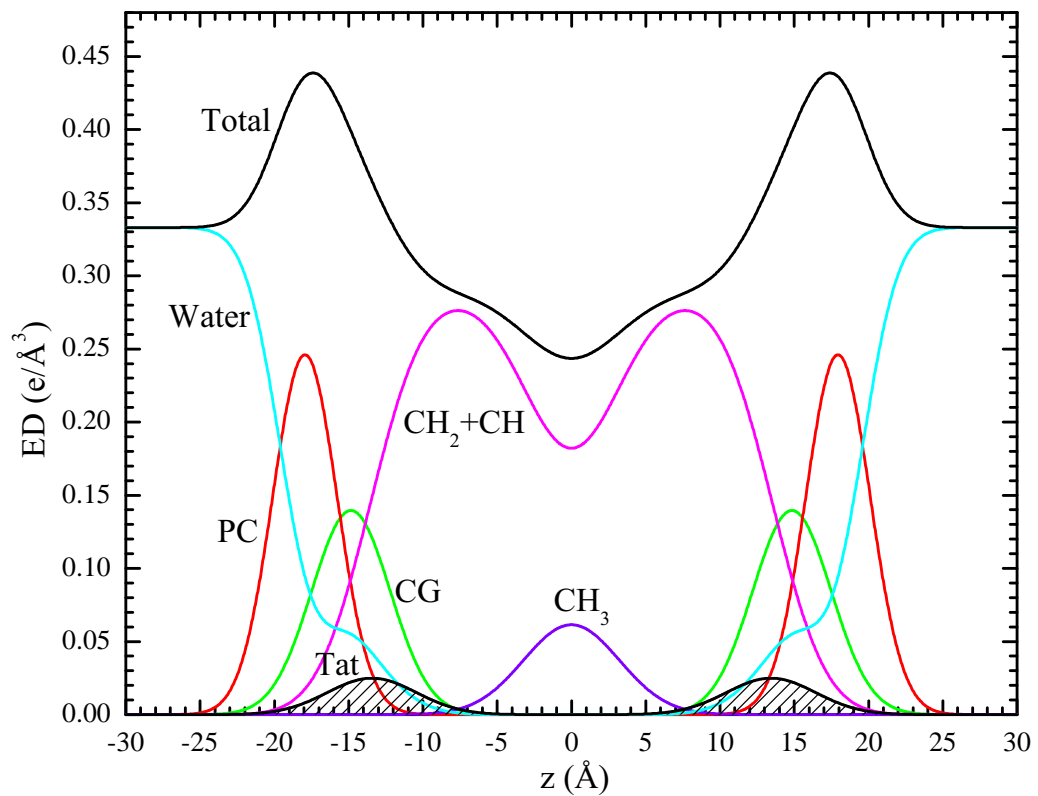


Figure 2.5: A model electron density profile for DOPC with Tat.

This definition enforces the total probability P_{HC} in the hydrocarbon chain region to equal one, which in turn means that placement of Tat in the chain region is prohibited. We call the model defined by Eq. (2.7) model A. To allow Tat to be placed inside the hydrocarbon chain region, we also consider an alternative definition,

$$P_{\text{CH}_2+\text{CH}}(z) = P_{\text{HC}}(z) - P_{\text{CH}_3}(z) - P_{\text{Tat}}(z), \quad (2.8)$$

where the volume probability of CH_2+CH combined component is reduced by the Tat volume probability distribution. We call this model B. The spatial conservation requires the water volume probability distribution to be

$$P_{\text{W}}(z) = 1 - P_{\text{PC}}(z) - P_{\text{CG}}(z) - P_{\text{Tat}}(z) - P_{\text{HC}}(z) \quad (2.9)$$

for model A and

$$P_{\text{W}}(z) = 1 - P_{\text{PC}}(z) - P_{\text{CG}}(z) - P_{\text{HC}}(z) \quad (2.10)$$

for model B.

Because X-rays measure the contrast between the bilayer and surrounding solvents, water, the experimental form factor is compared to the water subtracted model form factor,

$$F(q_z) = 2 \int_0^{\frac{D}{2}} dz \left(\sum_i (\rho_i - \rho_{\text{W}}) P_i(z) \right) \cos(q_z z), \quad (2.11)$$

where $i = \text{PC}, \text{CG}, \text{Tat}, \text{CH}+\text{CH}_2$, and CH_3 .

2.2.7.2 Constraints

The height of the hydrocarbon chain error function is fixed to one by imposing spatial conservation, whereas the mean position of the terminal methyls is fixed to $z_{\text{CH}_3} = 0$ by symmetry arguments. The total lipid volume V_L is fixed to the experimentally measured value. The headgroup volume V_{HL} was determined to be 331 \AA^3 for gel phase phosphatidylcholine (PC) bilayers [53], and we assume the same volume for the fluid phase PC bilayers. The volumes of PC and CG components satisfy

$$V_{\text{PC}} + V_{\text{CG}} = V_{\text{HL}}, \quad (2.12)$$

and the volumes of CH_3 and CH_2+CH components satisfy

$$2(16V_{\text{CH}_2+\text{CH}} + V_{\text{CH}_3}) = V_L - V_{\text{HL}}. \quad (2.13)$$

These component volumes constrain the height of the Gaussians as

$$c_{\text{PC}} = \frac{V_{\text{PC}}}{A_L \sigma_{\text{PC}}} \quad (2.14)$$

$$c_{\text{CG}} = \frac{V_{\text{CG}}}{A_L \sigma_{\text{CG}}} \quad (2.15)$$

$$c_{\text{CH}_3} = \frac{2V_{\text{CH}_3}}{A_L \sigma_{\text{CH}_3}} \quad (2.16)$$

$$c_{\text{Tat}} = \frac{V_{\text{Tat}}}{A_L \sigma_{\text{Tat}}} \quad (2.17)$$

where A_L is area per lipid.

The ratio of the carbonyl/glycerol volume to the headgroup volume V_{HL} was reported to be 0.41 [54], so we constrain the CG component volume to 135.7 \AA^3 and the PC component volume to 195.3 \AA^3 .

The most detailed structural study on DOPC to date was published by Braun *et al.* [54], and many of constraints on our model parameters can be derived from their study. However, in that work, the authors used the SDP model [52], which is specifically tailored for combined analysis of neutron and X-ray form factors. Therefore, we need to convert their structural results to the corresponding parameters in our simpler model. For example, from the reported values of the ratio of the volumes of the chain terminal methyl (CH_3) to the chain methylenes (CH_2) and the ratio of the volumes of the chain methines (CH) to the chain methylenes, we can calculate the ratio r_{CH_3} of the volumes of CH_3 to the CH_2 and CH combined component. Furthermore, the study by Braun *et al.* was at 30°C while our study was at 37°C , so our measured volume of DOPC was slightly higher.

At 30°C , the volume of DOPC was reported to be 1303 \AA^3 , so the volume of hydrocarbon chain region at the same temperature is $1303 - 331 = 972 \text{ \AA}^3$. The ratio r of the volumes of the chain terminal methyl (CH_3) to the chain methylenes (CH_2) was reported to be 1.95, and the ratio r_{12} of the volumes of the chain methines (CH) to the chain methylenes 0.91 at 30°C . Because there are 14 CH_2 groups, 2 CH groups, and 1 CH_3 group in each DOPC hydrocarbon chain, we have $2 \times (14V_{\text{CH}_2} + 2V_{\text{CH}} +$

$V_{\text{CH}_3}) = 972 \text{ \AA}^3$. Using $r = V_{\text{CH}_3}/V_{\text{CH}_2} = 1.95$ and $r_{12} = V_{\text{CH}}/V_{\text{CH}_2} = 0.91$, we get $V_{\text{CH}_2} = 27.3 \text{ \AA}^3$, $V_{\text{CH}} = 24.9 \text{ \AA}^3$, and $V_{\text{CH}_3} = 53.3 \text{ \AA}^3$. These calculated volumes lead to $V_{\text{CH}_3}/V_{\text{CH}_2+\text{CH}} = 1.97$ for 30 °C.

At 37 °C, the volume of DOPC was measured to be 1313.5 \AA^3 , so we have $2 \times (16V_{\text{CH}_2+\text{CH}} + V_{\text{CH}_3}) = 1313.5 - 331$. Assuming that the ratio $V_{\text{CH}_3}/V_{\text{CH}_2+\text{CH}}$ at 37 °C is the same as that at 30 °C gives $V_{\text{CH}_2+\text{CH}} = 27.3 \text{ \AA}^3$ and $V_{\text{CH}_3} = 53.9 \text{ \AA}^3$. We constrain the components for the hydrocarbon chain region in our model to these calculated values.

lipid	number of electrons	volume (\AA^3)
DOPC	434	1313.5
DOPE	410	1212.3
DOPC:DOPE (3:1)	428	1288.2

Table 2.2: Number of electrons per lipid and volume per lipid.

component	n_i^e	$V_i (\text{\AA}^3)$	$\rho_i (\text{e}/\text{\AA}^3)$
PC	97	195.3	0.497
PE	73	94.1	0.776
PC:PE (3:1)	91	170	0.535
CG	67	135.7	0.494
CH_2+CH	7.875	27.3	0.288
CH_3	9	53.9	0.167

Table 2.3: Some structural parameters for each component. n_i^e is the number of electrons and ρ_i is the average electron density.

number of electrons	838	mole fraction (x_{Tat})	n_{Tat}^e	$V_{\text{Tat}} (\text{\AA}^3)$
volume (\AA^3)	1877	0.016	13.6	30.5
$\rho_{\text{Tat}} (\text{e}/\text{\AA}^3)$	0.446	0.034	29.5	66.1
		0.059	53.0	118.8

Table 2.4: Tat basic structural parameters. The notations are the same as in Table 2.3. $x_{\text{Tat}} = \text{Tat}/(\text{Tat}+\text{Lipid})$.

2.2.7.3 Fits with Lower Bounds

Non-linear least squared fits with upper and lower bounds for the model parameters are implemented using an internal-external parameter transformation method. This

method is described in MINUIT User's Guide, section 1.3 [55]. This section briefly describes the method. The details can be found in the MINUIT website [56].

Basically, instead of a model parameter, which is also called the external variable, the minimization procedure varies a related variable called the internal variable. This internal variable can take any values between $-\infty$ to $+\infty$. At every χ^2 calculation, the internal variable is transformed to the external variable, which can take values only between the lower and upper bounds (a and b). This non-linear transformation allows an existing minimization algorithm that was developed for fits with no bounds to work for fits with bounds. This point was important because it allowed us to implement bound fits in the model fitting program called the SDP program, fully developed by Dr. Norbert Kucerka, without too many additional changes. Downsides of the transformation method include turning a linear problem into a non-linear one and some computational overhead, neither of which is particularly problematic in this study.

For variables with both lower and upper bounds (a and b , respectively), the transformation between the internal and external variables is

$$P_{\text{int}} = \arcsin\left(2\frac{P_{\text{ext}} - a}{b - a} - 1\right) \quad (2.18)$$

$$P_{\text{ext}} = a + \frac{b - a}{2}(\sin P_{\text{int}} + 1). \quad (2.19)$$

For variables with a lower bound a only, the transformation is

$$P_{\text{int}} = \sqrt{(P_{\text{ext}} - a + 1)^2 - 1} \quad (2.20)$$

$$P_{\text{ext}} = a - 1 + \sqrt{P_{\text{int}}^2 + 1}, \quad (2.21)$$

and for variables with an upper bound b only,

$$P_{\text{int}} = \sqrt{(b - P_{\text{ext}} + 1)^2 - 1} \quad (2.22)$$

$$P_{\text{ext}} = b + 1 - \sqrt{P_{\text{int}}^2 + 1}. \quad (2.23)$$

2.2.8 Molecular Dynamics Simulation

This section describes the MD simulations performed by Dr. Kun Huang, who was a graduate student of Prof. Angel Garcia at Rensselaer Polytechnic Institute.

Systems with different DOPC/Tat mole ratios (128:0, 128:2 and 128:4, corresponding to 0, 0.015 and 0.030 mole fractions) were simulated atomistically using the Gromacs 4.6.1 package [57]. DOPC was modeled by the Slipid force field [58, 59] and HIV Tat was modeled by Amber 99SB [60]. Tip3p water was used [61]. The number of Tats was divided equally on each side of the bilayer to mimic experimental conditions. All systems were simulated at 310 K with a constant area in the x - y plane and 1 atm constant pressure in the z direction. Each system was simulated for 100 ns and the last 50 ns was used as the production run. At each DOPC/Tat mole ratio, we studied systems with three different area/lipid (A_L). For the DOPC system, we fixed $A_L = 68, 70, 72 \text{ \AA}^2$; DOPC/Tat (128:2), we fixed the $A_L = 72, 74, 76 \text{ \AA}^2$; DOPC/Tat (128:4), we fixed the $A_L = 72, 74, 76 \text{ \AA}^2$. These values were based on the analysis of experimentally obtained form factors, which is discussed in Sec. 2.4.3. For each DOPC/Tat system at fixed A_L , we then conducted seven independent simulations with the center of mass (COM) of each Tat constrained at different bilayer depths from the bilayer center (18, 16, 14, 12, 10, 8 and 5 \AA). In total, 45 independent simulations were conducted. The goal of constrained simulations is to find the best match between experimental and MD simulation form factors. Comparison to the X-ray form factors was performed using the SIMtoEXP software written by Dr. Norbert Kucerka [62].

All simulations were conducted with a 2 fs time integration step. SETTLE [63] was used to constrain water molecules and LINCS [64] was used to constrain all other bond lengths in the system. VdW interactions were truncated at 1.4 nm with a twin-range cutoff scheme and a dispersion correction was applied to both energy and pressure. Electrostatics interactions were treated with the particle-mesh Ewald (PME) method [65]. The direct term for electrostatics was evaluated within 1.0 nm cutoff and the Fourier term was evaluated with a 0.12 nm grid spacing and a 4th order interpolation. Each system was simulated at 310 K using the V-rescale algorithm [66] with a 0.2 ps time coupling constant. The semi-isotropic parrinello-rahman barostat [67] was used to couple the system at 1 atm in the z direction with a 5 ps time coupling constant, while the projected area at the x - y plane was fixed by setting the system compressibility to 0. We inserted the Tats into the system by initially turning off all interactions between Tats and the rest of the system, with Tats constrained at different depths. Then we slowly turned on the interactions to normal strength through thermodynamics integrations. We used umbrella potentials

to constrain Tats at desired depths with a force constant of 3000 kJ/mol/nm².

The center of mass (COM) distance between each peptide and the bilayer was constrained by an umbrella potential with a force constant k of 3000 kJ/mol/nm². Essentially, this potential acts as a spring, where its potential energy depends on the deviation of the distance between the center of mass of Tat and DOPC from a preferred value, z_0 ,

$$U(z_1^{\text{Tat}}, \dots, z_1^{\text{DOPC}}, \dots) = -\frac{1}{2}k(z_{\text{cm}}^{\text{Tat}} - z_{\text{cm}}^{\text{DOPC}} - z_0)^2.$$

Then, $-\partial U / \partial z_i$ is the external force acting on atom, i .

2.3 Analysis of Molecular Dynamics Simulation Data

2.3.1 SIMtoEXP program

This section briefly describes the SIMtoEXP program developed by Dr. Norbert Kucerka [62]. Essentially, for each snapshot, positional distribution of each atom averaged over the xy plane is calculated. Then, the distribution is averaged over snapshots. The product of this distribution and the average electron density gives the electron density profile of the atom. The sum over all the atoms provide the total electron density profile. This total electron density profile minus the average electron density of water is Fourier transformed to provide the X-ray form factor.

$$F^{\text{sim}}(q_z) = \int_0^\infty dz(\rho(z) - \rho_W) \cos(q_z z). \quad (2.24)$$

Electron density profiles were symmetrized and then X-ray form factors were calculated with $\rho_W = 0.326 \text{ e}/\text{\AA}^3$, which was the average electron density of water molecules in the MD simulations. Because $\rho(z)$ is equal to ρ_W outside the bilayer, the upper integration limit takes on a finite value.

Because the experimental form factor is on arbitrary units, it is scaled by a single constant a to produce the best fit to the simulated form factor through a linear least squared fit that minimizes the following goodness of fit

$$\chi^2 = \sum_i \left(\frac{1}{\sigma_i} (a|F_i^{\text{exp}}| - |F^{\text{sim}}(q_{z,i})|) \right)^2 \quad (2.25)$$

where σ_i is the input experimental uncertainties and F_i^{exp} is the experimental form factor measured at $q_z = q_{z,i}$. The SIMtoEXP program does not scale the input uncertainties, so the relative errors ($\sigma_i/|F_i^{\text{exp}}|$) depend on the value of the overall scaling factor a . Consequently, the χ^2 values calculated by the program had to be multiplied by $1/a^2$. These corrected χ^2 are reported in this chapter.

2.3.2 Local Thinning of Membranes

My contribution to the MD simulations was to help analyze the results.

The SIMtoEXP program only gives the average quantities for each leaflet. While our X-ray data are sensitive to the bilayer average electron density, local information

of Tat-bilayer interactions can be obtained from MD simulations. In this section, we discuss a method to extract a local membrane thickness around the Tat peptides from the MD simulation trajectories.

One of the expected effects of Tat interacting with a bilayer is compression of the lipid bilayer along the z -direction. It is reasonable to assume that this compression is greater near Tat and weaker far from Tat. If this is the case, the distance between phosphorus atoms in opposite leaflets near Tat should be different from the distance between phosphorus atoms away from Tat. For a small Tat concentration, $D_{\text{phos-phos}}$ is the same as that of pure DOPC if the distance from all Tats is large enough. For our experimental concentrations, the thinning effect may extend throughout the bilayer because the lateral effect of Tat might have a larger lateral decay length than the distance between Tats. Whether that is the case or not, we expect that the thickness near the Tats is smaller than the average thickness, so $D'_{\text{phos-phos}}$ is what we want to measure.

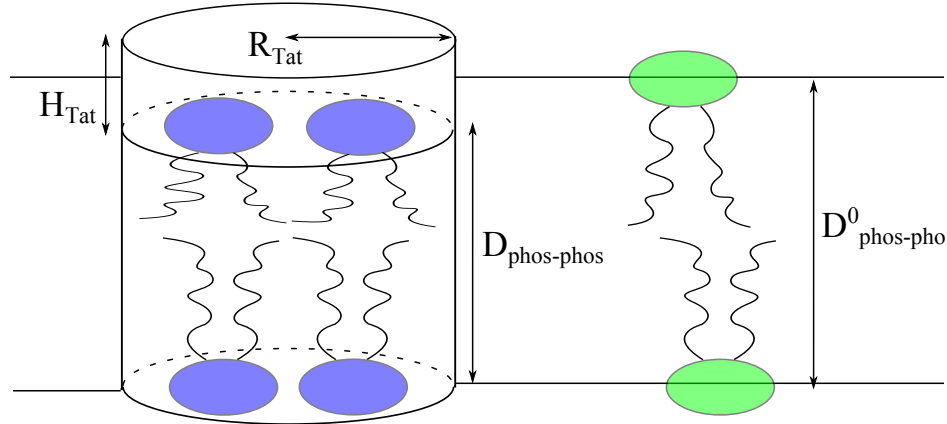


Figure 2.6: Our simple model to extract the local bilayer thickness from simulation trajectories. Tat is modeled as a cylinder with its height H_{Tat} and radius R_{Tat} . The local thickness is defined as $D'_{\text{phos-phos}}$. The thickness of the unperturbed DOPC bilayer is $D_{\text{phos-phos}}$. Blue highlighted lipids fall within the imaginary cylinder extended from the Tat. Unperturbed lipids are highlighted in green.

First, let us define what we mean by lipids close to Tat. As in Fig. 2.6, we imagine a cylinder around Tat and find all the phosphorus atoms within it. Approximating Tat as a cylinder with its height given by the FWHM of its electron density distribution, its radius $R_{\text{Tat}} = 9 \text{ \AA}$ comes from the experimentally determined volume $V_{\text{Tat}} = 1876$

\AA^3 and $H_{\text{Tat}} = 7.6 \text{ \AA}$ measured from one of the simulations (see Sec. ??). Let us define the lateral center of the cylinder as the center of mass of each Tat. Then we define $D'_{\text{phos-phos}}$ using only those lipids whose phosphorus atoms lie within these 9 \AA cylinders around the Tats. Then $D_{\text{phos-phos}} = z_{\text{phos}}^+ - z_{\text{phos}}^-$ where z_{phos}^+ and z_{phos}^- are the average z of the n_1 (n_2) lipids in the upper and lower monolayer, respectively.

The algorithm for doing the above was straightforward. For each time frame, the positions (x_i, y_i, z_i) of each Tat, i , are listed. We chose phosphorus atoms whose (x, y) lateral position lied within 9 \AA of any one of the Tat's lateral position. Then, z positions of the chosen phosphorus atoms were placed in a list. Then, z_{phos} were calculated from the list. We averaged over many snapshots to gain better statistics.

2.3.3 Lateral Decay Length of Membrane Thinning

This section describes a method to measure the lateral decay length of membrane thinning due to Tat-lipid interactions. As in the previous section, Tat is modeled here as a cylinder with its radius equal to R_1 , height H_{Tat} , and volume V_{Tat} such that $R_1 = \sqrt{V_{\text{Tat}}/(\pi H_{\text{Tat}})}$. Let $h(r)$ represent the phosphorus height profile of a leaflet as in Fig. 2.7. The two leaflets are assumed to be decoupled. In our model, lipids are separated into three regions: suppressed, boundary, and unperturbed region. The suppressed region extends from $r = 0$ to R_1 and is directly beneath (above) Tat in the top (bottom) leaflet. In this region, lipids are uniformly compressed by Tat toward the center of the bilayer, so that $h(r)$ is a constant equal to z_{phos} . From $r = R_1$ to R_2 is the boundary region, where $h(r)$ is assumed to linearly increase with the lateral distance r . The lateral decay length of membrane thinning is given by $R_2 - R_1$. In the unperturbed region ($r > R_3$), lipids do not interact with Tat, behaving identically to DOPC, so the phosphorus position is the same as that of DOPC. A continuous $h(r)$ that satisfies the above criteria is

$$h(r) = \begin{cases} z_{\text{phos}} & \text{if } 0 \leq r < R_1 \\ mr + b & \text{if } R_1 \leq r < R_2 \\ z_{\text{phos}}^0 & \text{if } R_2 \leq r < R_3 \end{cases} \quad (2.26)$$

with $m = (z_{\text{phos}} - z_{\text{phos}}^0)/(R_1 - R_2)$ and $b = (z_{\text{phos}}^0 R_1 - z_{\text{phos}} R_2)/(R_1 - R_2)$. Approximating the simulation box as a cylinder gives $R_3 = \sqrt{N A_L / \pi}$, where N is the number of lipids in a leaflet. z_{phos} can be measured directly from simulation trajectories. z_{phos}^0

is a half of the average phosphorus-phosphorus distance in a DOPC simulation, which can be easily obtained from the SIMtoEXP program. The average height profile over the monolayer, $\langle h(r) \rangle$, can be also obtained from the program in the same manner. The only unknown is R_2 .

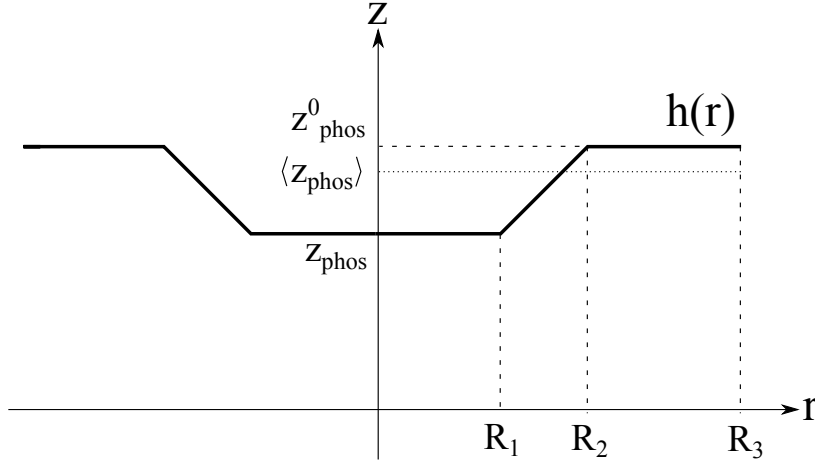


Figure 2.7: Simple model of the lateral decay of the membrane thickness perturbation due to Tat.

Let us calculate $\langle h(r) \rangle$. In cylindrical coordinates,

$$\langle h(r) \rangle = \frac{1}{\pi R_3^2} \int_0^{2\pi} d\phi \int_0^{R_3} dr r h(r) \quad (2.27)$$

The ϕ integration is trivial. The r integration is

$$\begin{aligned} & \int_0^{R_3} dr r h(r) \\ &= \int_0^{R_1} dr z_{\text{phos}} r + \int_{R_1}^{R_2} dr (mr + b)r + \int_{R_2}^{R_3} dr z_{\text{phos}}^0 r \\ &= \frac{1}{2} [z_{\text{phos}} R_1^2 + z_{\text{phos}}^0 (R_3^2 - R_2^2)] + \frac{1}{3} m (R_2^3 - R_1^3) + \frac{1}{2} b (R_2^2 - R_1^2) \\ &= \frac{1}{2} [z_{\text{phos}} R_1^2 + z_{\text{phos}}^0 (R_3^2 - R_2^2)] + \frac{1}{3} (z_{\text{phos}}^0 - z_{\text{phos}}) (R_2^2 + R_1 R_2 + R_1^2) \\ &\quad + \frac{1}{2} (z_{\text{phos}} R_2 - z_{\text{phos}}^0 R_1) (R_1 + R_2) \end{aligned} \quad (2.28)$$

Using Eq. (2.28), we get

$$\langle h(r) \rangle = \frac{(z_{\text{phos}} - z_{\text{phos}}^0)(R_1^2 + R_1 R_2 + R_2^2) + 3z_{\text{phos}}^0 R_3^2}{3R_3^2} \quad (2.29)$$

Eq. 2.29 is a quadratic equation in terms of R_2 . Solving for R_2 gives

$$R_2 = \frac{-R_1 + \sqrt{R_1^2 + 4C}}{2} \quad (2.30)$$

with

$$C = \frac{3R_3^2(z_{\text{phos}}^0 - \langle h(r) \rangle)}{z_{\text{phos}}^0 - z_{\text{phos}}} - R_1^2 \quad (2.31)$$

2.4 Results

2.4.1 Bending and Bulk Modulus

(Under construction) Show X-ray data. Show fitting boxes. Show the Kc values. Also, show the resultant form factors, which qualitatively show the membrane thinning. Also describe how I got error bars.

Fig. 2.2 shows the scattering intensity pattern from DOPC/DOPE (1:1) with mole fraction $x_{\text{Tat}} = 0.034$. The diffuse lobes are due to equilibrium fluctuations that occur in these fully hydrated, oriented lipid/peptide samples. The intensity $I(\mathbf{q})$ in the diffuse patterns provide the absolute values of the form factors $F(q_z)$, which are the Fourier transforms of the electron density profile, through the relation $I(\mathbf{q}) = S(\mathbf{q})|F(q_z)|^2/q_z$, where $\mathbf{q} = (q_r, q_z)$, $S(q)$ is the structure interference factor, and q_z^1 is the usual LAXS approximation to the Lorentz factor [68–70]. The first step in the analysis takes advantage of the q_r dependence of the scattering to obtain the bending modulus K_c with results shown in Fig. 2.8. As positively charged Tat concentration was increased, the lamellar repeat spacing D generally increased in neutral lipid bilayers and decreased in negatively charged bilayers, consistent with changes in electrostatic repulsive interactions. With few exceptions, the water space between bilayers exceeded 20 Å.

The analysis that obtains K_c also obtains the structure factor $S(\mathbf{q})$ and then the unsigned form factors $|F(q_z)|$ are obtained from the intensity $I(\mathbf{q})$ by division. Results for five different membrane mimics are shown in Fig. 2.9. Vertical lines indicate the

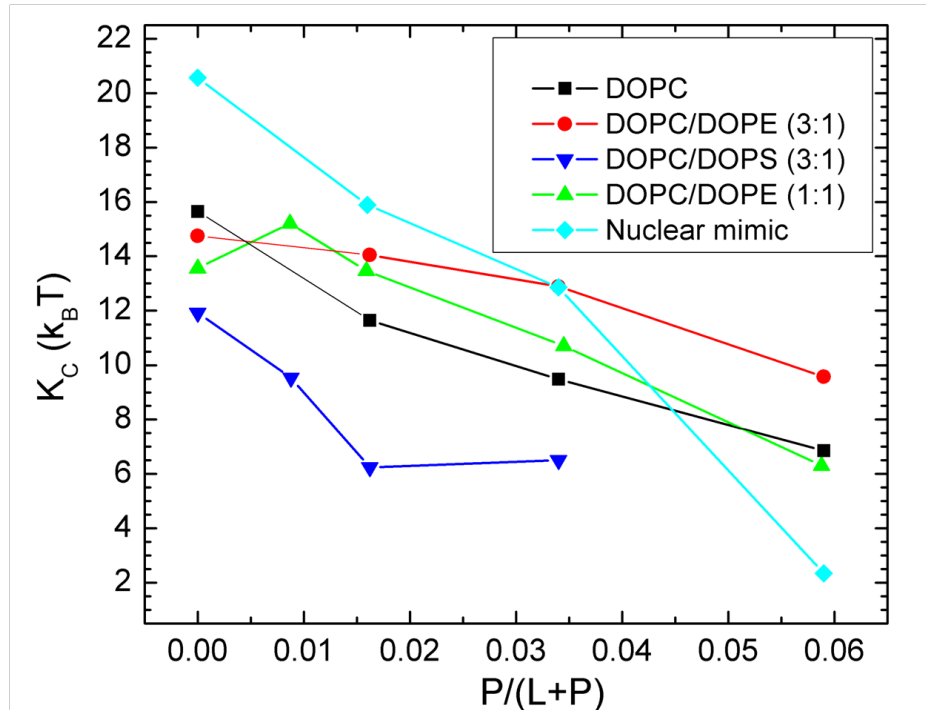


Figure 2.8: Bilayer bending modulus, K_c , vs. Tat mole fraction x_{Tat} . D -spacings for DOPC/Tat mixtures varied from 64 to 68 Å, for DOPC/DOPE/Tat mixtures from 64 to 69 Å, for DOPC/DOPS/Tat (3:1) mixtures from 57 Å to 100 Å (pure DOPS was unbound), and for nuclear mimic/Tat mixtures from unbound (nuclear mimic) to 64 Å. Estimated uncertainty in all values is about ± 2 .

zero position between the lobes of diffuse data where $F(q_z)$ change sign. In every sample, the zero positions shift to larger q_z , indicating a thinning of the membranes.

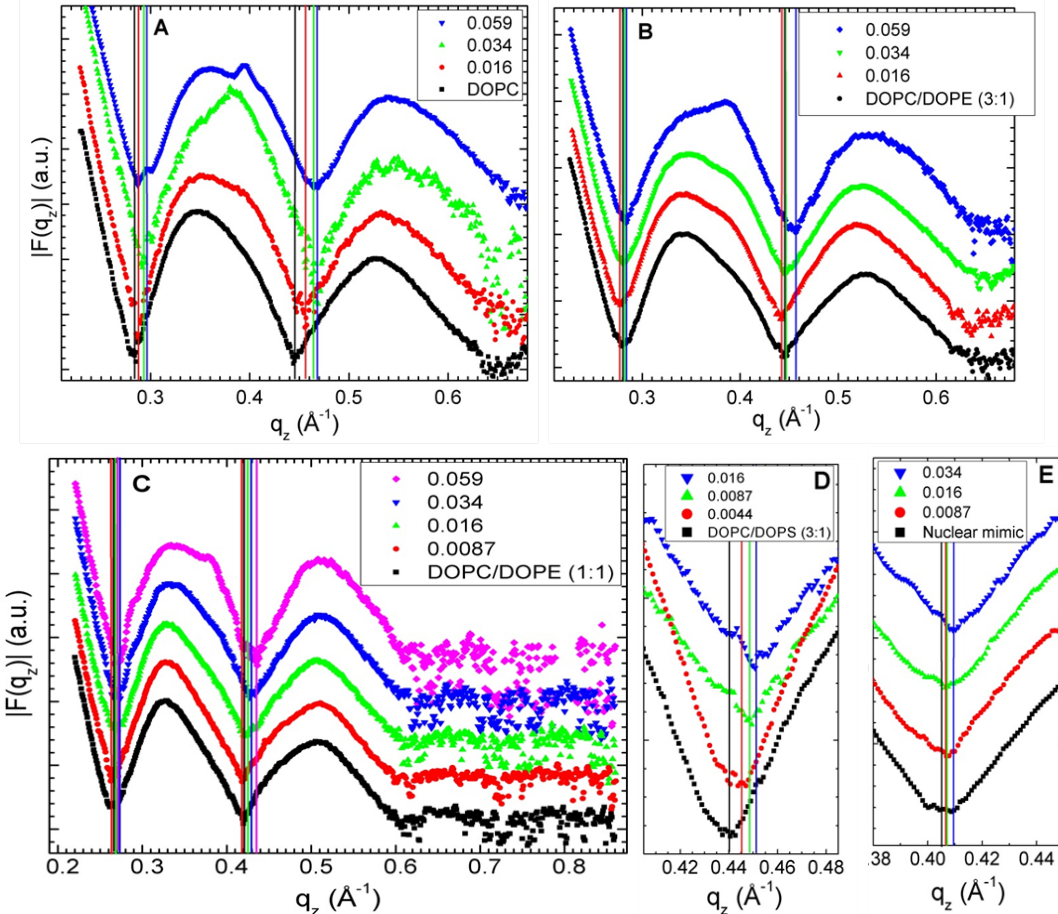


Figure 2.9: Form factors of lipid mixtures (arbitrarily scaled and vertically displaced) with increasing Tat mole fractions x_{Tat} indicated on figure legends. Lipid mixtures: A. DOPC B. DOPC/DOPE (3:1) C. DOPC/DOPE (1:1) D. DOPC/DOPS (3:1) E. Nuclear mimic. The entire q_z range is shown in C, while others show partial ranges. Solid vertical lines indicate the q_z values where the form factors equal zero between the lobes of diffuse data.

2.4.2 Volume results

Experimental and simulated volumes are given in Table 2.5. The simulated volume was obtained using the volume app in the SIMtoEXP program. The experimental Tat volume was calculated from the measured density assuming that the lipid volume was

the same as with no Tat. In general, there may be an interaction volume between the peptide and the lipid membrane as previously reported for bacteriorhodopsin [71]. As lipid was present in excess to Tat, the partial molecular volume of the lipid should be the same as with no Tat, so this way of calculating includes all the interaction volume in V_{Tat} . Comparison of V_{Tat} in water with the result for 5:1 Lipid:Tat suggests that the interaction volume may be negative, consistent with a net attractive interaction with lipid. Understandably, values of V_{Tat} were unreliable for small mole ratios of Tat:Lipid. Therefore we used simple additivity for those mimics not shown in Table 2.5 for the volumes used in the electron density profile modeling. All volumes obtained from the Gromacs MD simulations were somewhat smaller than the measured volumes, but it supports the Tat volume being closer to 1877 \AA^3 than the outlying values obtained experimentally at small Tat concentrations. The measured volume was in a good agreement with the value calculated from a peptide calculator website [72], which gave 1888 \AA^3 .

Experiments			
Tat in:	$V_{\text{lipid}} (\text{\AA}^3)$	Lipid:Tat	$V_{\text{Tat}} (\text{\AA}^3)$
water		1877	
DOPC:DOPE (3:1)	1288	5:1	1822
DOPC	1314	39.6:1	676
DOPC:DOPS (3:1)	1298	39.6:1	2613

Simulations			
Tat in:	$V_{\text{lipid}} (\text{\AA}^3)$	Lipid:Tat	$V_{\text{Tat}} (\text{\AA}^3)$
DOPC	1283	128:2	1694
DOPC	1294	128.4	1699

Table 2.5: Volume results at $37 \text{ }^\circ\text{C}$

2.4.3 Electron Density Profile Modeling

We fitted our measured X-ray form factors to the Tat-in-headgroup (THG) model described in Sec. 2.2.7. In all fits, the positions of component groups were free parameters, but we assumed that the lipid headgroup is somewhat rigid so that it cannot compress or expand. This assumption led to fixing the distance $z_{\text{PC}} - z_{\text{CG}}$ between the PC and CG components as well as the distance $z_{\text{CG}} - z_{\text{HC}}$ between the CG component and the Gibbs dividing surface for the hydrocarbon chains. We also constrained the

width of Tat Gaussian σ_{Tat} . We fitted with three different values of widths, 2.5, 3.0, and 3.5, to study the range of variation due to the Tat width. We constrained the Tat width because this parameter tended to become too small to be physical when it was set free. Without higher q_z data points, a very narrow feature in an electron density profile, which resulted in large form factors, did not get penalized.

Figure 2.10 shows the best fits and corresponding electron density profiles for DOPC with Tat, and Table 2.6 shows the best fit parameters for these fits. In most cases, a better χ^2 was obtained for smaller σ_{Tat} , consistent with its tendency to become too small to be physical as noted in the previous paragraph. The widths of the headgroups σ_{PC} and σ_{CG} decreased from those of pure DOPC when Tat was added. It is also seen from Table 2.6 that the area per lipid A_L increased as the Tat concentration was increased. An increase in A_L implies thinning of a bilayer because a lipid bilayer is an incompressible fluid membrane. Another observed trend was that z_{Tat} increased as x_{Tat} was increased.

x_{Tat}	0	0.016	0.016	0.016	0.034	0.034	0.034	0.059	0.059	0.059
χ^2	2961	1554	1570	1581	1563	1587	1607	2342	2338	2363
z_{PC}	18.1	18.0	17.9	17.9	17.8	17.7	17.6	17.8	17.8	17.7
σ_{PC}	2.52	2.14	2.17	2.18	1.86	1.92	1.93	2.02	1.97	1.93
z_{CG}	15.0	14.9	14.8	14.8	14.7	14.6	14.5	14.7	14.7	14.6
σ_{CG}	3.00	2.62	2.64	2.66	2.22	2.30	2.31	2.58	2.27	2.14
z_{HC}	13.7	13.6	13.5	13.5	13.4	13.3	13.2	13.4	13.4	13.3
σ_{HC}	3.00	2.69	2.84	2.95	2.65	2.82	3.01	2.47	2.58	2.83
σ_{CH_3}	3.20	3.19	3.22	3.24	3.37	3.43	3.47	2.70	2.70	2.74
z_{Tat}	NA	12.9	13.4	14.2	13.1	13.8	14.4	15.2	15.2	15.7
σ_{Tat}	NA	2.5	3.0	3.5	2.5	3.0	3.5	2.5	3.0	3.5
A_L	71.5	72.4	72.5	72.7	73.6	74.0	74.4	73.6	73.5	73.9

Table 2.6: Fitting Results for DOPC membranes for the THG (Tat in headgroup) model. $z_{\text{PC}} - z_{\text{CG}} = 3.1 \text{ \AA}$ and $z_{\text{CG}} - z_{\text{HC}} = 1.3 \text{ \AA}$ in all fits.

As shown in Fig. 2.10, the membrane thickness can be defined as the distance D_{PP} between the PC components in the opposing leaflets or the distance D_{HH} between the maxima in the opposing leaflets. D_{HH} is more reliable than D_{PP} because it is a property of the total electron density of a bilayer and, therefore, does not depend strongly on the specific model employed for fitting the data. This point is illustrated in Fig. 2.11, which compares total electron density profiles resulted from best fits with three different Tat widths σ_{Tat} . While positions of Tat were sensitive to values

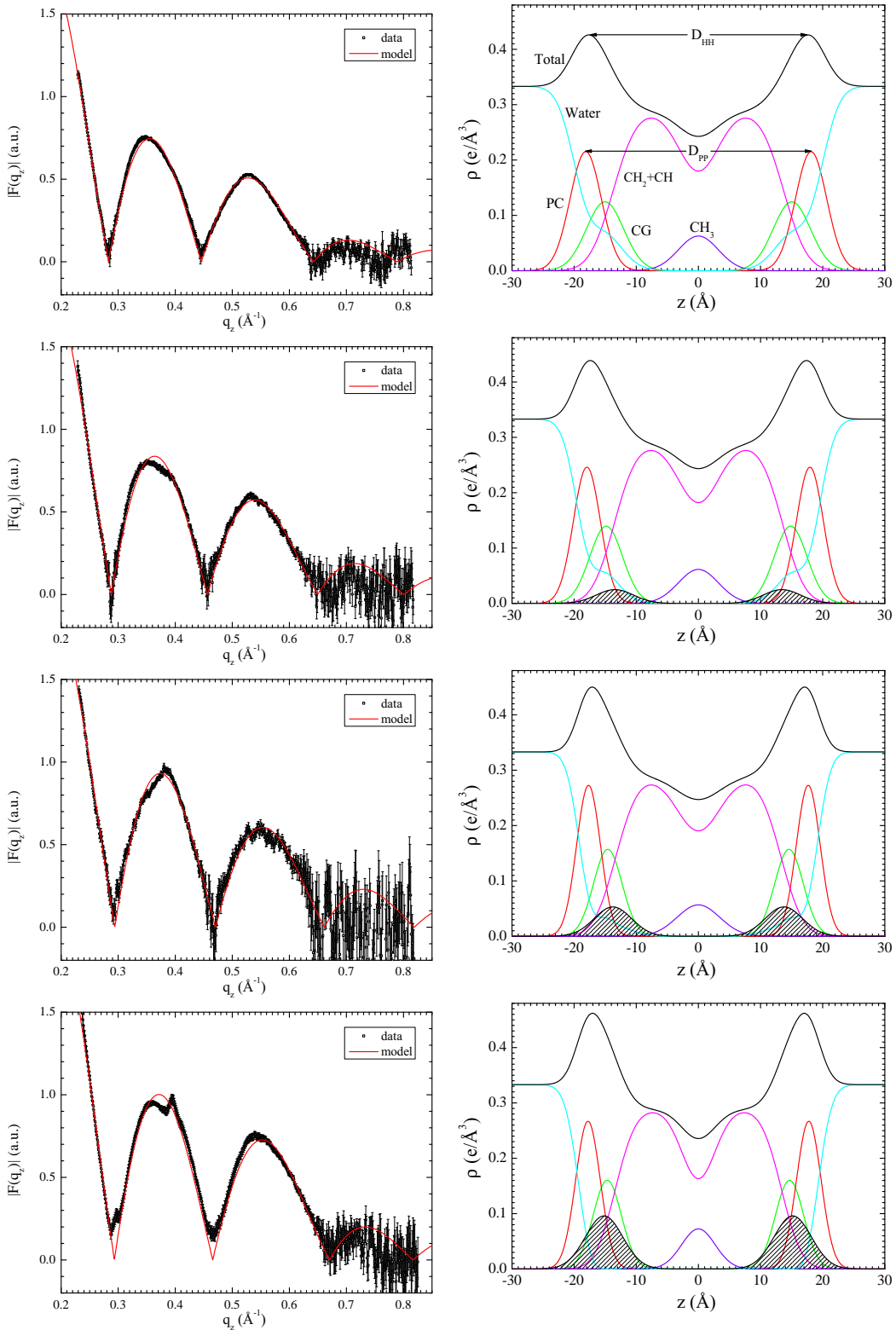


Figure 2.10: The best fits to DOPC form factors (left) and the corresponding electron density profiles (right) with $x_{\text{Tat}} = 0, 0.016, 0.034$, and 0.059 (from top to bottom).

of σ_{Tat} , the total electron density profiles were almost independent of σ_{Tat} . Essentially, other components, namely headgroups, adjusted their widths and positions so that the total electron density profile was about the same. In other words, the model was over parameterized. While the precise values of each parameter was less trustworthy, the total electron density profiles plotted in Fig. 2.11, when Fourier transformed, reproduced the experimental form factors very well and therefore were robust.

In contrast to D_{HH} , D_{PP} is a property that depends on lipid components, which are influenced by how the lipid is parsed and what assumptions and constraints go into the specific model. A disadvantage of using D_{HH} as a measure of the membrane thickness is that D_{HH} is influenced by the electron density of Tat because the total electron density profile includes a contribution from the electron density of Tat. Especially when the mole fraction of Tat in a system becomes large, the Tat electron density contributes significantly to the total electron density profile. If the Tat resided slightly outside of the PC component, the apparent membrane thickness measured by D_{HH} would be larger than D_{PP} . Then, even if the actual bilayer thickness defined by D_{PP} were reduced by the presence of Tat, the effect of thinning might not be obvious. With the above caveat in mind, we report both quantities in what follows since they can be easily calculated from the model.

As described in the previous paragraph, the model parameters were sensitive to specific constraints and assumptions on the model, and as Fig. 2.11 shows, the position of Tat depended on σ_{Tat} . On the other hand, the total electron density profiles were seen to be less sensitive. Figure 2.12 compares the total electron density profiles at different Tat concentrations. Consistent with the form factors shifting to larger q_z as x_{Tat} increased, D_{HH} decreased as x_{Tat} increased. As argued earlier, decrease in D_{HH} does not necessarily indicate decrease in the bilayer thickness, and it could instead be attributed to deeper insertion of Tat into the bilayer. However, compared to the profile of DOPC alone, all three profiles with Tat deviate from the electron density of water at smaller $|z|$ when approached from the water region. This is illustrated in Fig. 2.13 that plots the difference between the total electron density profile of DOPC and those of DOPC with Tat. Negative values of $\Delta\rho = \rho_{\text{DOPC+Tat}} - \rho_{\text{DOPC}}$ indicates that the headgroup, which has excess electron density relative to water, shifted toward the bilayer center as Tat was added to the system, which implies bilayer thinning.

Fitting results for DOPC:DOPE (3:1) and DOPC:DOPE (1:1) are summarized in Table 2.7 and Table 2.8, respectively, and the best fits and corresponding electron

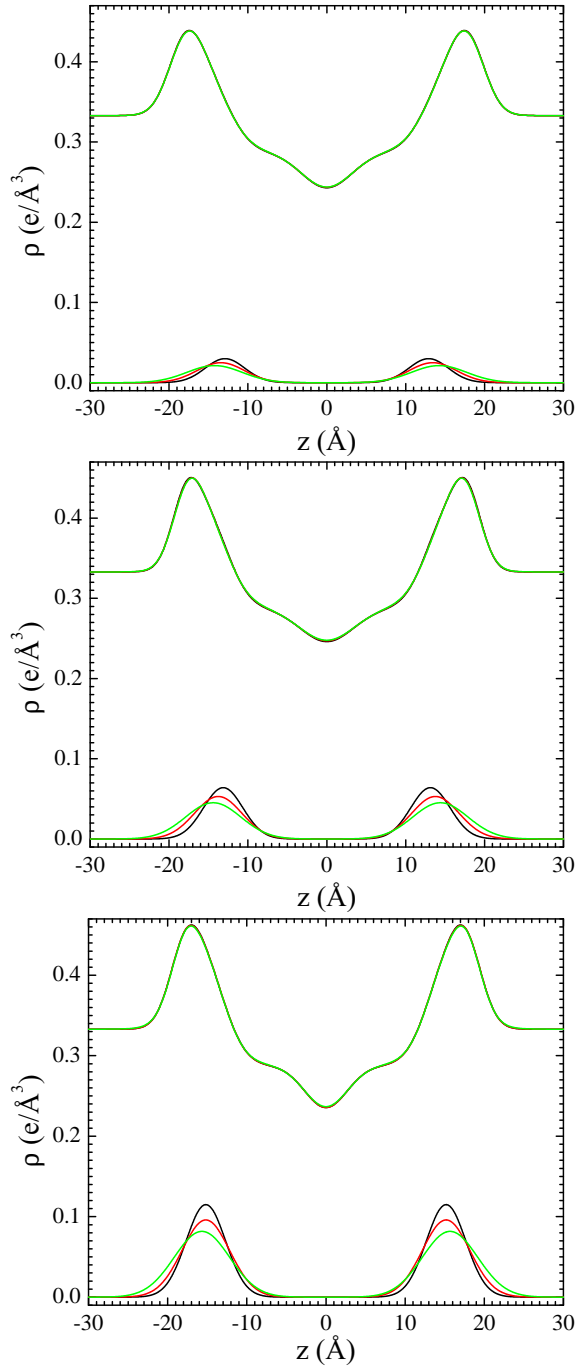


Figure 2.11: Comparison of total electron density profiles corresponding to best fits using different Tat widths σ_{Tat} , 2.5 (red), 3.0 (black), and 3.5 (green). The mole fraction of Tat x_{Tat} was 0.016 (top), 0.034(middle), and 0.059 (bottom). While different values of σ_{Tat} resulted in different positions of Tat, the total electron density profiles were almost identical and independent of σ_{Tat} .

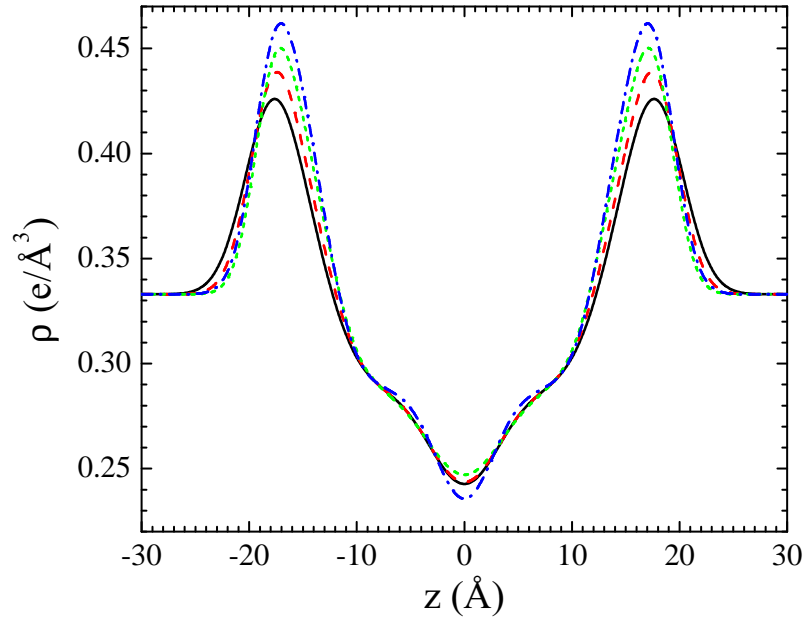


Figure 2.12: Comparison of total electron density profiles at $x_{\text{Tat}} = 0$ (black solid), 0.016 (red dash), 0.034 (green short dash), and 0.059 (blue dash dot).

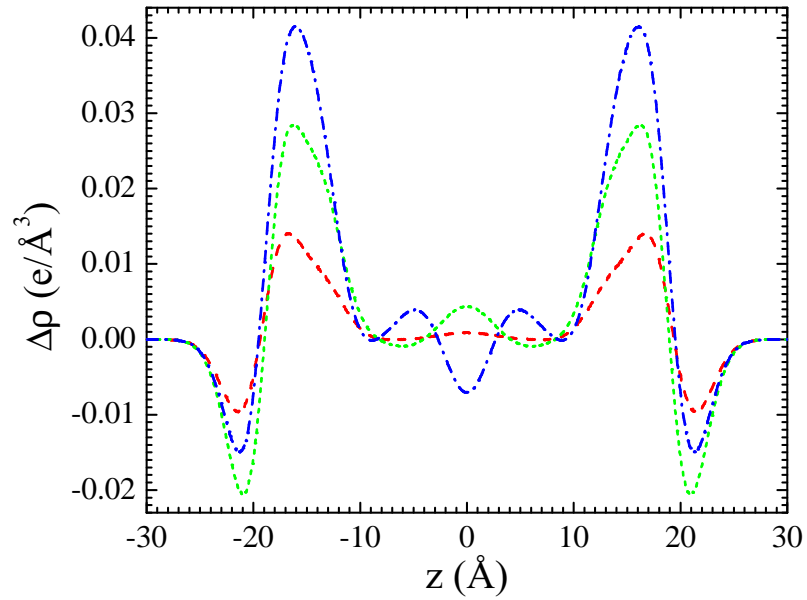


Figure 2.13: Difference between total electron density profiles of DOPC with Tat and that of DOPC. $x_{\text{Tat}} = 0.016$ (red dash), 0.034 (green short dash), and 0.059 (blue dash dot). Positive $\Delta\rho$ means excess electron density due to presence of Tat.

density profiles are shown in Fig. A.1 and Fig. A.2. Figure 2.14 plots total electron density profiles, showing increase of electron density at the headgroup region as Tat concentration increased, similarly to DOPC/Tat systems shown in Fig. 2.12.

x_{Tat}	0	0.016	0.016	0.016	0.034	0.034	0.034	0.059	0.059	0.059
χ^2	924.5	4972	4985	4994	6758	6826	6863	2293	2280	2296
z_{PC}	18.3	18.5	18.5	18.4	18.5	18.4	18.3	18.2	18.2	18.1
σ_{PC}	2.66	2.23	2.26	2.27	2.25	2.31	2.34	2.31	2.19	2.11
z_{CG}	15.2	15.4	15.4	15.3	15.4	15.3	15.2	15.1	15.1	15.0
σ_{CG}	2.92	2.63	2.65	2.69	2.52	2.58	2.63	2.40	2.20	2.01
z_{HC}	13.9	14.1	14.1	14.0	14.1	14.0	13.9	13.8	13.8	13.7
σ_{HC}	2.73	2.70	2.83	2.91	2.86	2.79	2.84	2.25	2.38	2.60
σ_{CH_3}	3.24	2.94	2.97	2.98	2.87	2.90	2.91	2.63	2.61	2.65
z_{Tat}	NA	13.5	14.0	15.0	14.3	14.9	16.0	16.3	16.4	16.9
σ_{Tat}	NA	2.5	3.0	3.5	2.5	3.0	3.5	2.5	3.0	3.5
A_L	70.9	69.8	69.9	70.1	69.5	70.0	70.6	71.3	71.4	71.7

Table 2.7: Fitting Results for DOPC:DOPE (3:1) membranes for the THG model. $z_{\text{PC}} - z_{\text{CG}} = 3.1 \text{ \AA}$ and $z_{\text{CG}} - z_{\text{HC}} = 1.3 \text{ \AA}$ in all fits.

x_{Tat}	0	0.016	0.016	0.016	0.034	0.034	0.034	0.059	0.059	0.059
χ^2	2961	1554	1570	1581	1563	1587	1607	2342	2338	2363
z_{PC}	18.1	18.0	17.9	17.9	17.8	17.7	17.6	17.8	17.8	17.7
σ_{PC}	2.52	2.14	2.17	2.18	1.86	1.92	1.93	2.02	1.97	1.93
z_{CG}	15.0	14.9	14.8	14.8	14.7	14.6	14.5	14.7	14.7	14.6
σ_{CG}	3.00	2.62	2.64	2.66	2.22	2.30	2.31	2.58	2.27	2.14
z_{HC}	13.7	13.6	13.5	13.5	13.4	13.3	13.2	13.4	13.4	13.3
σ_{HC}	3.00	2.69	2.84	2.95	2.65	2.82	3.01	2.47	2.58	2.83
σ_{CH_3}	3.20	3.19	3.22	3.24	3.37	3.43	3.47	2.70	2.70	2.74
z_{Tat}	NA	12.9	13.4	14.2	13.1	13.8	14.4	15.2	15.2	15.7
σ_{Tat}	NA	2.5	3.0	3.5	2.5	3.0	3.5	2.5	3.0	3.5
A_L	71.5	72.4	72.5	72.7	73.6	74.0	74.4	73.6	73.5	73.9

Table 2.8: (Numbers are wrong) Fitting Results for DOPC:DOPE (1:1) membranes for the THG model. $\Delta z_1 = z_{\text{PC}} - z_{\text{CG}}$ and $\Delta z_2 = z_{\text{CG}} - z_{\text{HC}}$.

Figure 2.15 summarizes the results for bilayer thickness as a function of Tat mole fraction x_{Tat} . In all cases, D_{HH} was smaller than D_{PP} , consistent with the results that the value of Tat position z_{Tat} from the bilayer center was smaller than that of PC headgroup position z_{PC} . The CG headgroup also carries high average electron density and is located closer to the bilayer center than the PC headgroup is. Therefore, in

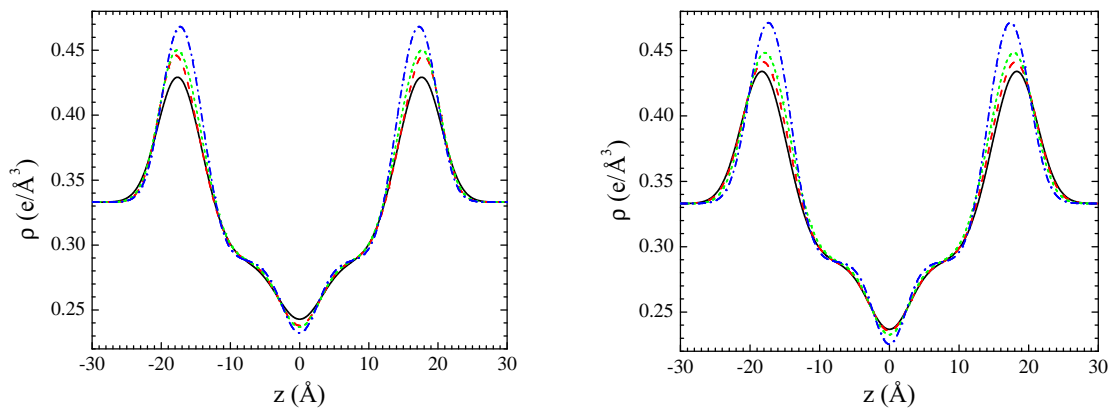


Figure 2.14: Total electron density profiles for DOPC:DOPE (3:1) (left) and DOPC:DOPE (1:1) (right) with Tat mole fraction $x_{\text{Tat}} = 0$ (black solid), 0.016 (red dash), 0.034 (green short dash), and 0.059 (blue dash dot).

general, D_{HH} is smaller than D_{PP} even without presence of Tat. Figure 2.16 compares Tat position to the PC headgroup position, reemphasizing a result that Tat is located inside the PC headgroup. We note, however, that D_{PP} in our models is the average PC-PC distance and not necessarily the same as local bilayer thickness near a Tat peptide. It is reasonable to expect that perturbation of bilayer structure due to Tat is largest near Tat and decays as a function of lateral distance from Tat. In Sec. 2.4.4, we discuss local perturbation of a DOPC bilayer measured in MD simulations. Finally, Fig. 2.17 plots area per lipid as a function of Tat mole fraction. Consistent with bilayer thinning, area per lipid was found to increase in most cases. We could not obtain electron density profiles for DOPC/DOPS (3:1) and the nuclear membrane mimic, due to loss of diffuse scattering by Tats charge neutralization of these negatively charged membranes, which rendered extraction of X-ray form factors unreliable, as described in section 2.4.1.

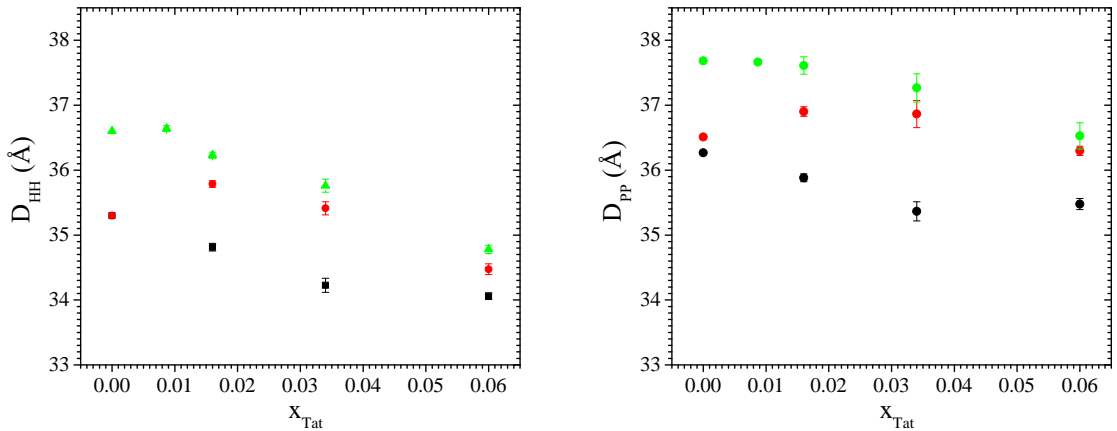


Figure 2.15: Bilayer thickness, D_{HH} (left) and D_{PP} (right) plotted against Tat mole fraction x_{Tat} . Black squares (DOPC), red circles (DOPC:DOPE (3:1)), and green triangles (DOPC:DOPE (1:1)). Error bars are standard deviations from imposing Tat Gaussian widths, $\sigma_{Tat} = 2.5, 3.0$ or 3.5 \AA .

We also studied how the goodness of fit varied as the position of the Tat Gaussian was varied. Figure 2.18 plots χ^2 as a function of the fixed Tat position z_{Tat} . We found that the two models, THG (Tat-in-headgroup region) and THC (Tat-in-hydrocarbon-chain region), resulted in similar electron density profiles, yielding similar χ^2 values when Tat was placed near the hydrocarbon-water interface region. In the THC model, the error function representing the hydrocarbon chain region became wider as Tat was placed closer to the interface region such that the total density profile calculated from

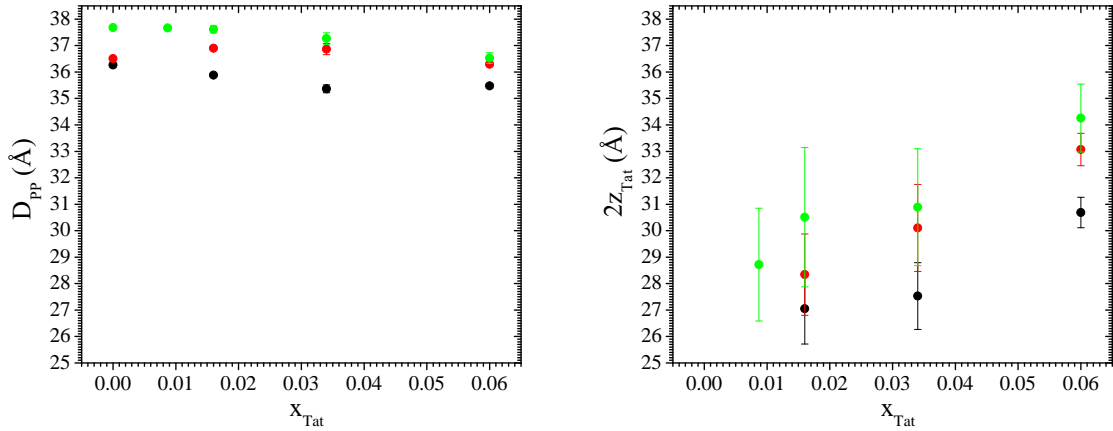


Figure 2.16: Bilayer thickness, D_{PP} (left) and twice Tat position $2z_{\text{Tat}}$ (right) plotted against Tat mole fraction x_{Tat} . Black squares (DOPC), red circles (DOPC:DOPE (3:1)), and green triangles (DOPC:DOPE (1:1)). Error bars are standard deviations from imposing Tat Gaussian widths, $\sigma_{\text{Tat}} = 2.5, 3.0 or 3.5 \AA . The data points of D_{PP} (left) is identical to those in Fig. 2.15, but the left axis is adjusted to facilitate comparison against $2z_{\text{Tat}}$.$

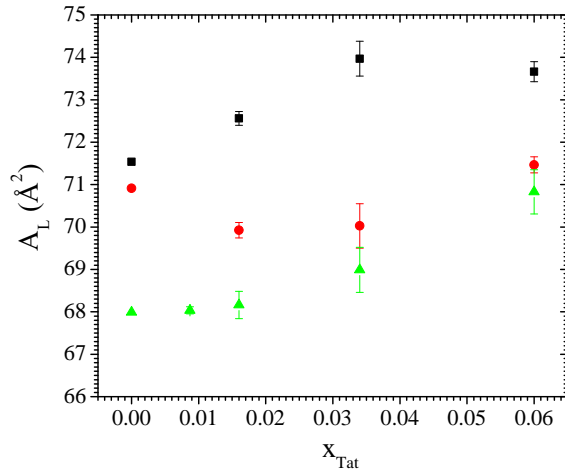


Figure 2.17: Area per lipid plotted against Tat mole fraction x_{Tat} . Black squares (DOPC), red circles (DOPC:DOPE (3:1)), and green triangles (DOPC:DOPE (1:1)). Error bars are standard deviations from imposing Tat Gaussian widths, $\sigma_{\text{Tat}} = 2.5, 3.0 or 3.5 \AA .$

the THC model was very similar to that calculated from the THG model. In general, while the total electron density profile is well determined by our modeling procedures, the values of the parameters for the components are not as well determined as the agreement of the fit to the data may suggest. In many cases, we found multiple local minima in the fitting landscape, including one with Tat closer to the center of the bilayer as shown in Fig. 2.18. χ^2 calculated at these local minima tended to be smaller for larger concentration of Tat. We also found that χ^2 with z_{Tat} in the hydrocarbon chain region and headgroup region was almost equal for the smallest value of x_{Tat} for DOPC:DOPE (1:1) bilayer. The MD simulations performed by Dr. Kun Huang suggested that the interior positions of Tat were artifacts of our model, at least for DOPC bilayers. The simulation results are found in Sec. 2.4.4.

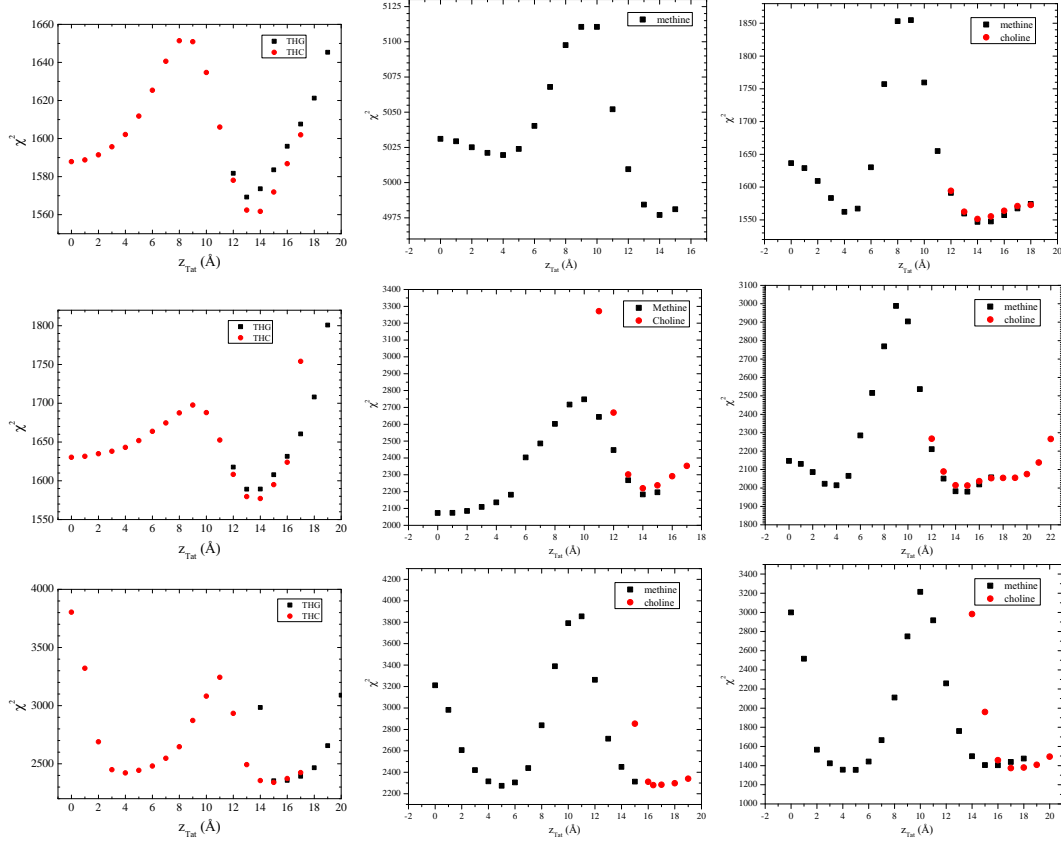


Figure 2.18: χ^2 as a function of z_{Tat} for DOPC, DOPC:DOPE (3:1), and DOPC:DOPE (1:1) (from left to right) with $x_{\text{Tat}} = 0.016, 0.034$, and 0.059 (from top to bottom). $\sigma_{\text{Tat}} = 3.0$. The THG model (black squares) and the THC model (red circles).

As seen from Table 2.6, the widths of the headgroup components became smaller as Tat concentration increased. This decrease seemed somewhat unreasonable; if Tat causes a bilayer to locally become thinner, we would expect that the headgroup components to become wider. Therefore, we also fitted a model with lower bounds on these headgroup widths. Namely, the minimum values of the widths of the headgroup components, PC and CG, were constrained to be greater than or equal to the corresponding values for pure bilayers without Tat. Table 2.9 shows results from fitting the data with lower bounds on the widths of the headgroup components for DOPC/Tat systems. In all cases, both headgroup widths, σ_{PC} and σ_{CG} , resulted in the same value as the value of their corresponding lower bounds. Similarly to fits with unbound widths, $D_{\text{PP}} = 2z_{\text{PC}}$ decreased as Tat concentration increased. The biggest difference between these bound fits and the unbound fits is in Tat position z_{Tat} . Figure 2.19 plots z_{Tat} as a function of Tat mole fraction x_{Tat} for both fits with and without lower bounds. While z_{Tat} increased as x_{Tat} increased for fits without bounds, z_{Tat} stayed more or less constant for fits with the bounds. Moreover, Tat was located closer to the PC headgroup than the CD headgroup. Thus, depth of Tat insertion was affected strongly by the headgroup widths. This again emphasizes the point that model parameters are not as well determined as the total electron density profiles are. In order to gain better understanding of location of Tat in DOPC bilayers, we now turn to MD simulations.

x_{Tat}	0	0.016	0.016	0.016	0.034	0.034	0.034	0.059	0.059	0.059
χ^2	2961	1853	1979	2118	2398	2893	3414	3160	4298	5539
z_{PC}	18.1	17.8	17.8	17.8	17.4	17.4	17.4	17.5	17.4	17.3
σ_{PC}	2.5	2.5	2.5	2.5	2.5	2.5	2.5	2.5	2.5	2.5
z_{CG}	15.0	14.7	14.7	14.7	14.3	14.3	14.3	14.4	14.4	14.3
σ_{CG}	3.0	3.0	3.0	3.0	3.0	3.0	3.0	3.0	3.0	3.0
z_{HC}	13.7	13.4	13.4	13.4	13.0	13.0	13.0	13.1	13.0	12.9
σ_{HC}	3.0	2.7	2.7	2.7	2.7	2.7	2.7	2.7	2.7	2.7
σ_{CH_3}	3.2	3.1	3.1	3.1	3.6	3.6	3.7	2.6	2.6	2.5
z_{Tat}	16.9	16.8	17.0	16.4	16.5	16.7	16.3	16.6	17.1	
σ_{Tat}	2.5	3.0	3.5	2.5	3.0	3.5	2.5	3.0	3.5	
A_{L}	71.5	73.5	73.5	73.5	75.6	75.6	75.6	75.0	75.4	75.9

Table 2.9: Fitting Results of the bound THG model for DOPC membranes. $z_{\text{PC}} - z_{\text{CG}} = 3.1$ and $z_{\text{CG}} - z_{\text{HC}} = 1.3$ in all fits.

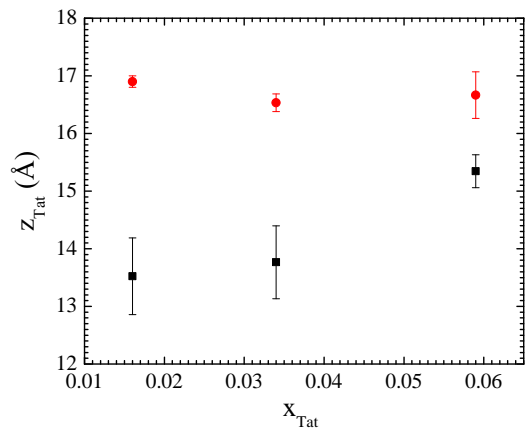


Figure 2.19: z_{Tat} as a function of Tat mole fraction x_{Tat} for fits with lower bounds on the headgroup widths (red circles) and without lower bounds (black squares). Error bars are standard deviations from imposing Tat Gaussian widths, $\sigma_{\text{Tat}} = 2.5, 3.0$ or 3.5 \AA .

2.4.4 Molecular Dynamics Simulations

As emphasized in Sec. 2.4.3, Tat position inside a bilayer was difficult to determine, which is a shortcoming of modeling a complex system with limited data sets. Therefore, we also employed a model independent approach using MD simulations. From simulations of a DOPC bilayer with Tat, X-ray form factors can be calculated. Then, calculated form factors were directly compared to experimental form factors. When a good match between simulated form factors and experimental form factors was obtained, spacial distribution of simulated atoms along the bilayer normal direction was analyzed to obtain the positions of lipid components as well as Tat. The SIMtoEXP software [62] described in Sec. 2.3.1 facilitated the comparison of simulations to experimental form factors.

Due to the slow relaxation in lipid bilayers and limited accuracy of the force field, a good agreement between experimental and MD simulation calculated form factors may be difficult to reach. Consequently, we carried out several constrained simulations at various A_L and z_{Tat} as described in Sec. 2.2.8. We then compared the simulated form factor $F(q_z)$ with the experimentally measured one. Figure 2.20 shows such comparison for a DOPC bilayer. As discussed in Sec. 2.4.3, the simulated form factor shifted to larger q_z as the area per lipid was increased. From this comparison, we found the simulation at $A_L = 70 \text{ \AA}^2$ to be the best match with the experimental form factor, yielding the lowest χ^2 . However, the form factor for $A_L = 72 \text{ \AA}^2$ matched the experiment better than that for 70 \AA^2 near $q_z = 0.3 \text{ \AA}^{-1}$, which suggests that a better match might lie between 70 and 72 \AA^2 . This case was not investigated further. The electron density profile for the best fit is shown in Fig. 2.21. The comparison for DOPC with $x_{\text{Tat}} = 0.015$ where there is one Tat in each monolayer is shown in Fig. 2.22. The comparison for DOPC with $x_{\text{Tat}} = 0.03$ is shown in Fig. 2.23.

The best match for DOPC/Tat (128:4) was found when the Tats were constrained at 18 \AA away from the bilayer center (Fig. 2.25). The other best fit results were: DOPC $A_L = 70 \text{ \AA}^2$ and DOPC/Tat(128:2) $A_L = 72 \text{ \AA}^2$, $z_{\text{Tat}} = 18 \text{ \AA}$. It clearly indicates that with increasing Tat concentration, A_L increases. The agreement worsened as Tat was constrained to be closer to the center of the bilayer. When Tats were constrained at 5 \AA away from the bilayer center, we observed a spontaneous formation of water pores in the MD simulation. However, as shown in Fig. 2.25 the corresponding form factor calculated from MD simulations does not match well with experiments.

We summarize our results for how Tat affects the lipid bilayer in Fig. 2.26. The

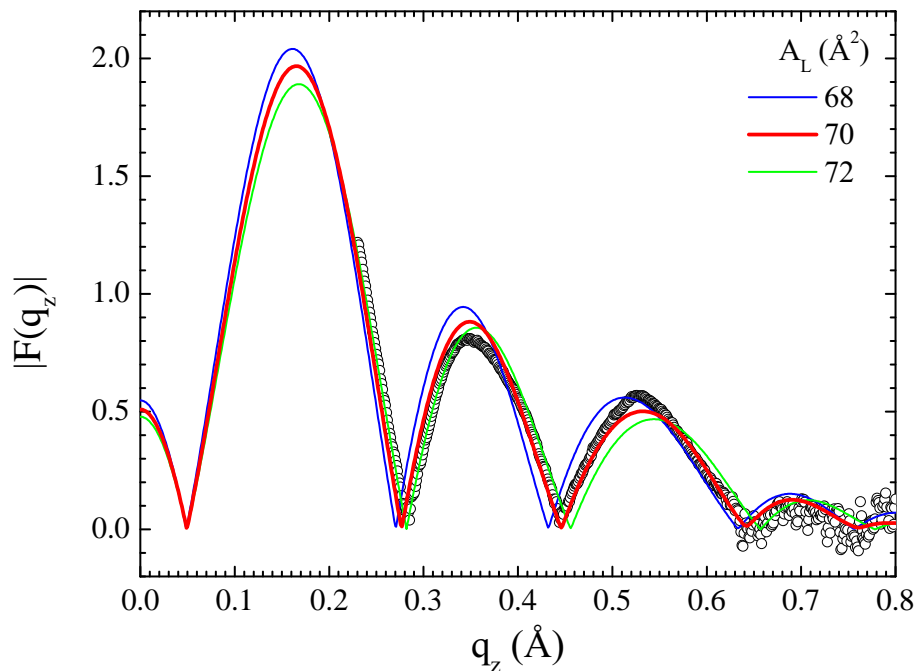


Figure 2.20: MD simulated form factors for DOPC at $A_L = 68 \text{ \AA}^2$ (blue solid line), 70 \AA^2 (red solid line), and 72 \AA^2 (green solid line) compared to the experimental form factor (open circles) scaled vertically to best match the form factor for 70 \AA^2 .

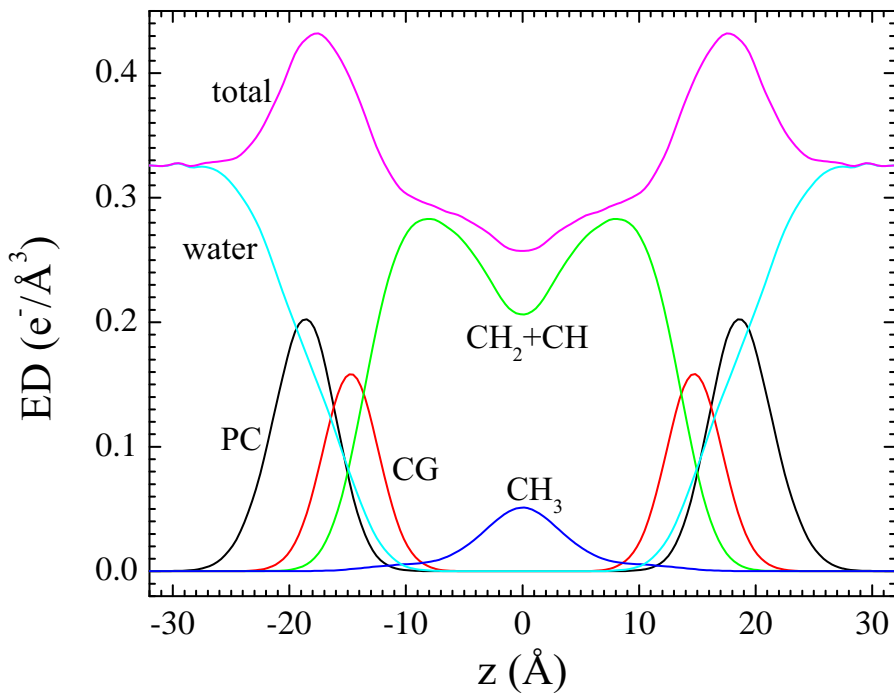


Figure 2.21: The simulated, symmetrized electron density profile for DOPC at $A_L = 70 \text{ \AA}^2$ as a function of the distance away from the bilayer center. Each component profile is labeled with its name: PC (phosphate-choline), CG (carbonyl-glycerol), CH_2+CH (methylene-methine combination), CH_3 (terminal methyl). The sum of all the components is labeled as total.

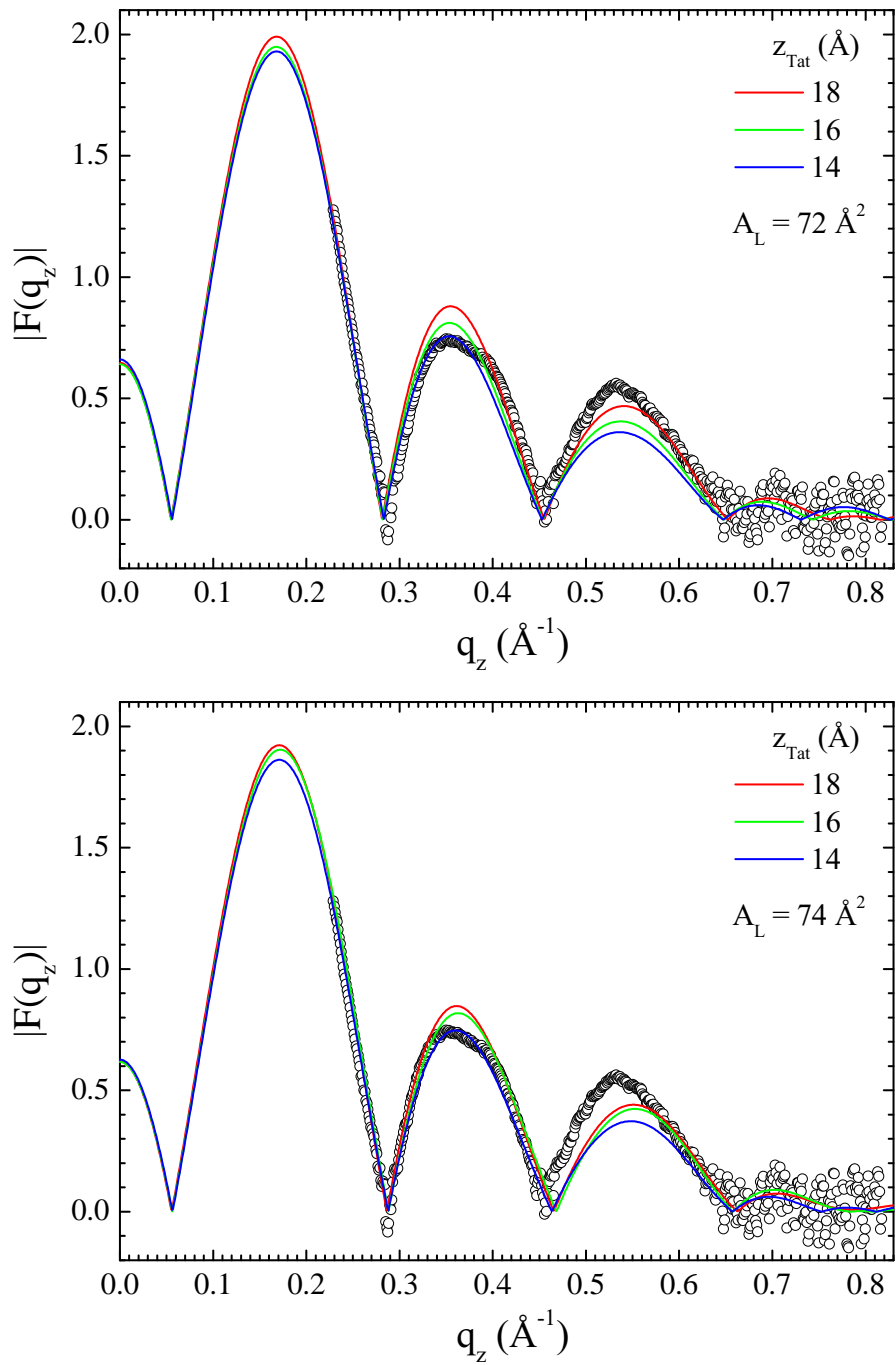


Figure 2.22: MD simulated form factors for DOPC with $x_{\text{Tat}} = 0.015$ at $A_L = 72 \text{ \AA}^2$ (top) and 74 \AA^2 (bottom), with $z_{\text{Tat}} = 18 \text{ \AA}$ (red solid lines), 16 \AA (green solid lines), and 14 \AA (blue solid lines) compared to the experimental form factor (open circles) scaled vertically to best match the form factor for $z_{\text{Tat}} = 18 \text{ \AA}$.

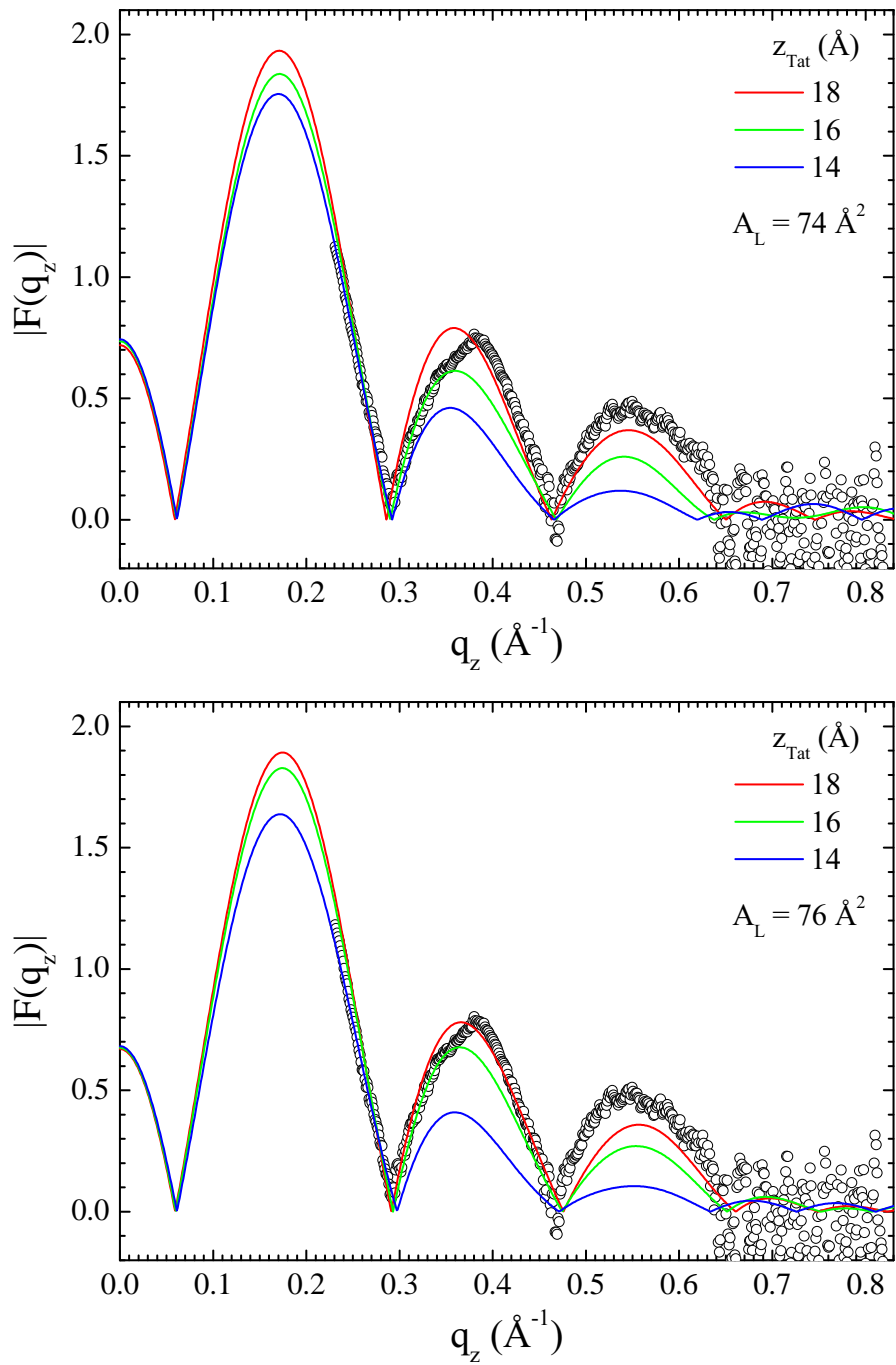


Figure 2.23: MD simulated form factors for DOPC with $x_{\text{Tat}} = 0.030$ at $A_L = 74 \text{ \AA}^2$ (top) and 76 \AA^2 (bottom), with $z_{\text{Tat}} = 18 \text{ \AA}$ (red solid lines), 16 \AA (green solid lines), and 14 \AA (blue solid lines) compared to the experimental form factor (open circles) scaled vertically to best match the form factor for $z_{\text{Tat}} = 18 \text{ \AA}$.

$x_{\text{Tat}} = 0.015$				$x_{\text{Tat}} = 0.030$			
$A_L (\text{\AA}^2)$	$z_{\text{Tat}} (\text{\AA})$	a	χ^2	$A_L (\text{\AA}^2)$	$z_{\text{Tat}} (\text{\AA})$	a	χ^2
70	18	0.621	60.1	70	18	0.621	60.1
70	16	0.568	69.1	70	16	0.568	69.1
70	14	0.439	131	70	14	0.439	131
70	12	0.285	391	70	12	0.285	391
70	10	0.199	440	70	10	0.199	440
70	8	0.196	374	70	8	0.196	374
70	5	0.159	527	70	5	0.159	527
72	18	0.72	18.0	72	18	0.72	18.0
72	16	0.65	24.9	72	16	0.65	24.9
72	14	0.6	31.4	72	14	0.6	31.4
72	12	0.426	104	72	12	0.426	104
72	10	0.219	443	72	10	0.219	443
72	8	0.205	336	72	8	0.205	336
72	5	0.165	448	72	5	0.165	448
74	18	0.722	21.3	74	18	0.722	21.3
74	16	0.704	25.9	74	16	0.704	25.9
74	14	0.631	24.7	74	14	0.631	24.7
74	12	0.412	81.9	74	12	0.412	81.9
74	10	0.312	194	74	10	0.312	194
74	8	0.246	351	74	8	0.246	351
74	5	0.177	427	74	5	0.177	427

Table 2.10: Comparison of the simulated form factors to the experimental form factors.

x_{Tat}	A_L	z_{Tat}	$\langle D_{\text{PP}} \rangle$	D_{PP}	x	Δt	H_{Tat}	R_{Tat}	R_2	z_{phos}	z_{guan}	χ^2
0	70		36.3									
0.015	72	18	35.6	32.8	35.8	3.5	9.2	8.1	15.0	14.7	15.5	18
0.015	72	16	36.1	33.0	36.3	3.3	9.4	8.0	9.0	14.9	14.5	24.9
0.015	74	18	35.0	33.0	35.1	3.3	8.6	8.3	23.9	14.9	16.5	21.3
0.015	74	16	35.0	32.1	35.2	4.2	7.6	8.9	20.4	14.0	13.5	25.9
0.030	74	18	35.3	32.6	NA	3.7	7.6	8.9	NA	14.5	15.5	24.3
0.030	74	16	35.3	31.2	NA	5.1	7.7	8.8	NA	13.1	13.5	40.1
0.030	76	18	34.2	32.0	NA	4.3	7.6	8.9	NA	13.9	16.5	14.8
0.030	76	16	34.9	31.4	NA	4.9	7.8	8.7	NA	13.3	14.5	30.4

Table 2.11: Summary of simulation results. $\langle D_{\text{PP}} \rangle$, phosphorus-phosphorus distance averaged over all lipids; D_{PP} , Tat-perturbed phosphorus atoms; x , thickness away from Tat; Δt , $\langle D_{\text{PP}}^{\text{DOPC}} \rangle - D_{\text{PP}}$; H_{Tat} , Tat height; R_{Tat} , radius of Tat cylinder; R_2 , radius of the calculated in-plane Tat-perturbed region; R_3 , effective radius of the simulation box.

x_{Tat}	A_L	z_{Tat}	$\langle D_{\text{PP}} \rangle$	D_{PP}	Δt	H_{Tat}	R_{Tat}	R_2	z_{phos}	z_{guan}
0.015	72.9	17.1	35.4	32.7	3.6	8.7	8.3	17.1	14.6	15.1
0.030	75.2	17.3	34.8	31.9	4.4	7.7	8.8	NA	13.8	15.4

Table 2.12: Summary of weighted average results. The caption is the same as Table 2.11.

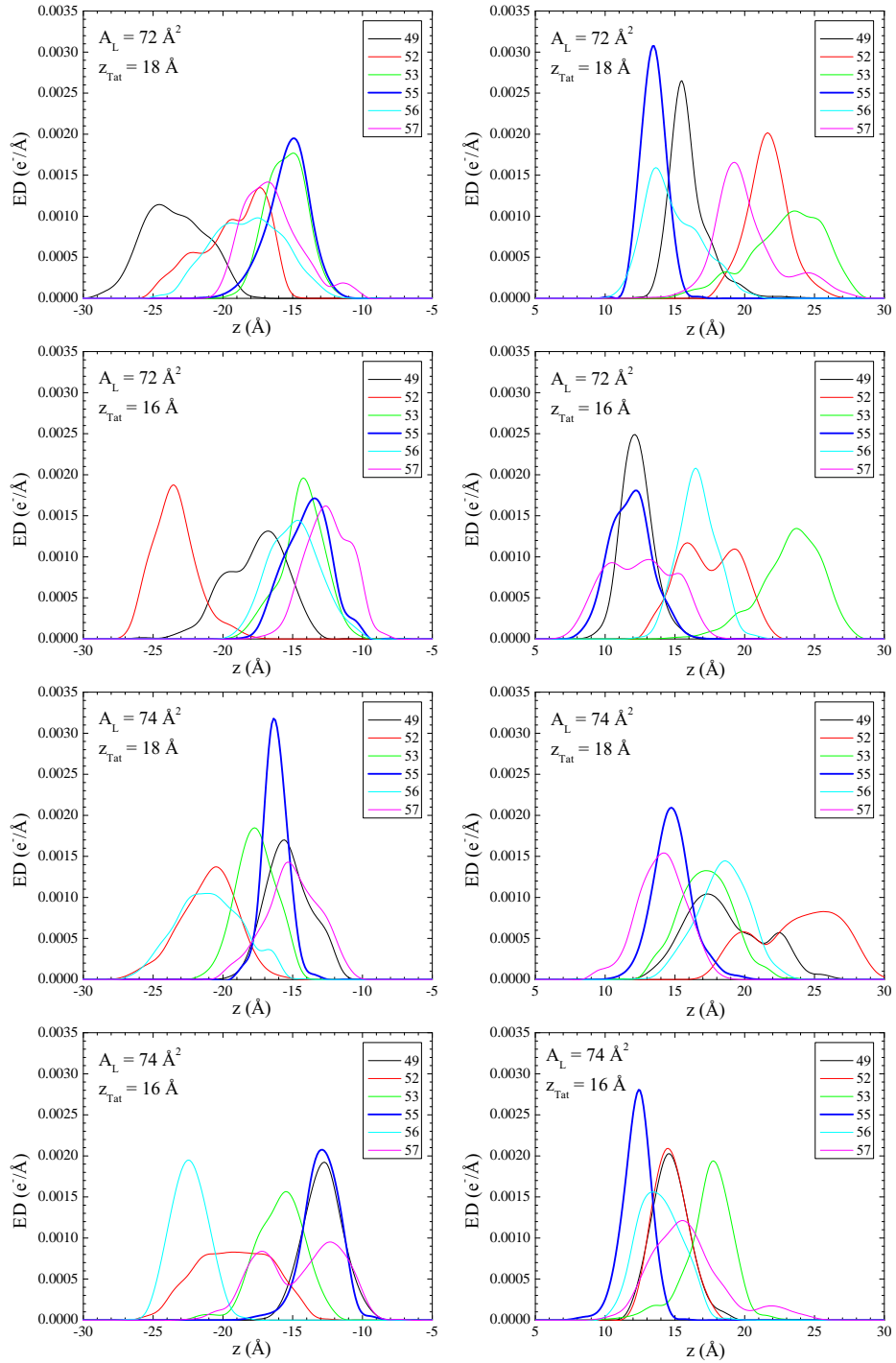


Figure 2.24: Electron density profiles of guanidinium groups from the four best matched simulations for DOPC with $x_{\text{Tat}} = 0.015$ (one Tat on each leaflet). Tat on the lower and upper leaflets are shown on the left and right plots, respectively.

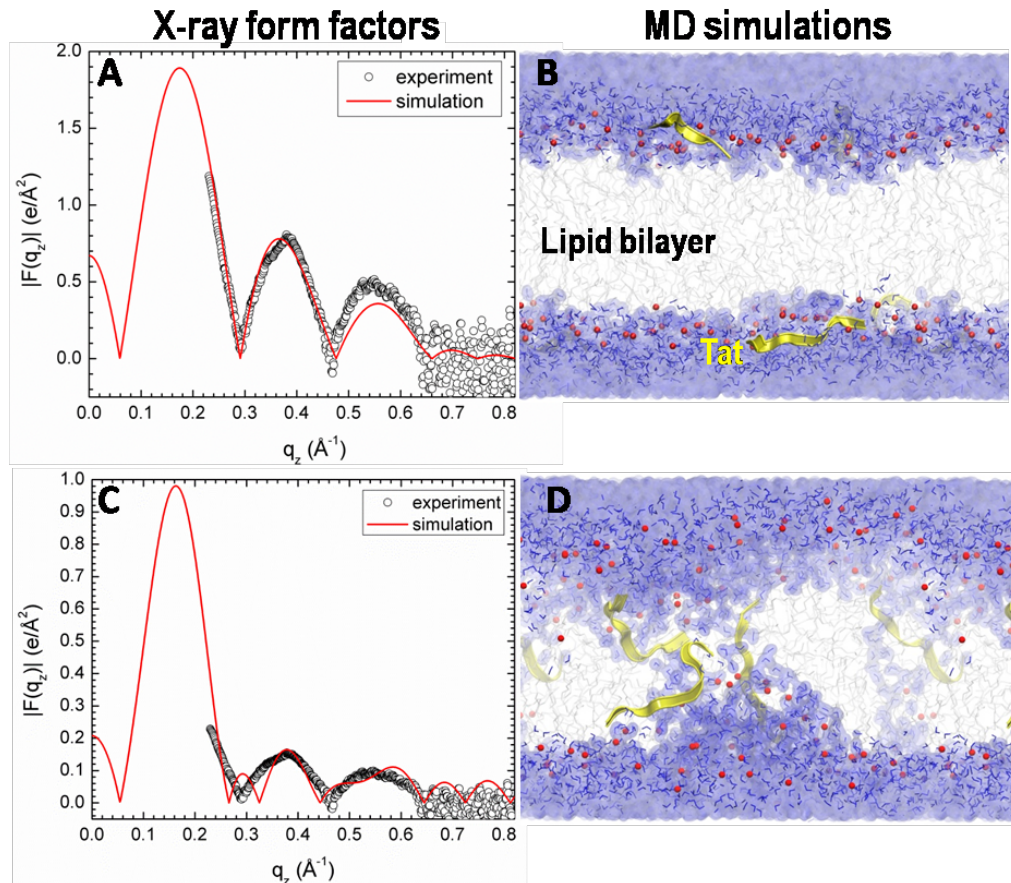


Figure 2.25: MD simulated form factors (red solid lines in A and C) of Tat/(DOPC+Tat), $x_{\text{Tat}}=0.030$, with Tat fixed at $z_{\text{Tat}}=18 \text{\AA}$ (panel A) and 5\AA (panel C) from the bilayer center compared to experimental form factors (open circles) scaled vertically to provide the best fit to the simulations. Corresponding snapshots are shown in Panels B and D in which the lipid chains are represented as grey sticks on a white background, Tats are yellow, phosphate groups are red and water is blue.

height of Tat, $H_{Tat} = 8.7 \text{ \AA}$, was the full width at half maximum of the Tat electron density profiles obtained from simulations and the cylindrical radius, $R_{Tat} = 8.3 \text{ \AA}$, was calculated to give the measured volume. The Z distances from the center of the bilayer were derived from weighted averages of four MD simulations of Tat:DOPC 2:128. The χ^2 obtained by comparison to experiment indicated that the best Z_{Tat} lay between the simulated values of 16 \AA and 18 \AA and the best area/lipid A_L lay between the simulated values of 72 \AA^2 and 74 \AA^2 , so averages were obtained from these four combinations of Z_{Tat} and A_L , weighted inversely with their χ^2 . The average positions, z'_{phos} , of phosphates situated underneath the Tats were calculated by averaging over the phosphates whose in-plane distance, R , from the center of Tat is smaller than R_{Tat} . The simulation cell extended to 38 \AA , far enough to ensure that z_{phos} for most of the lipids is the same as for DOPC. Assuming a simple linear ramp in z_{phos} , Fig. 2.26 then indicates a ring of boundary lipids that extends twice as far in R as Tat itself. Although the guanidinium electron density profile was broad (Fig. not yet included), indicating that some were pointing away from the bilayer relative to the center of Tat, more were pointing towards the bilayer center as indicated in Fig. 2.26.

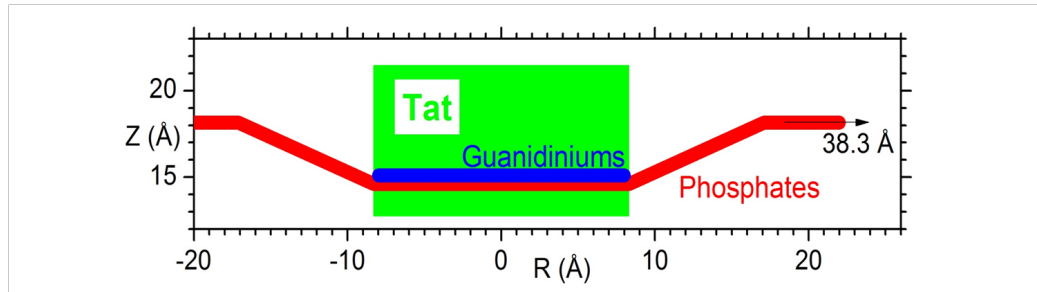


Figure 2.26: Location of Tat in DOPC bilayer. Tat is represented as a cylinder, z is the distance from the bilayer center, and R is the in-plane distance from the center of Tat. The average z of the lipid phosphates as a function of R and the arginine guanidiniums are shown in red and blue, respectively.

2.5 Discussion

Given that 8 of the 11 amino acids in Tat (47-57) are arginines and lysines, one would have suggested 20 years ago that highly charged Tat would partition strongly into solution rather than being associated with lipid bilayers. By contrast, but in agreement with more recent perspectives on arginine partitioning into the interfacial

region [73], we find that Tat interacts with lipid bilayers, even with neutral DOPC and DOPC/DOPE mixtures, as well as with negatively charged DOPC/DOPS and nuclear membrane mimic lipid mixtures. This paper presents multiple lines of evidence for a Tat/membrane interaction. Fig. ?? shows that Tat decreases the bending modulus. Although one could argue that such a decrease is only apparent and could instead be due to local changes in membrane spontaneous curvature [74], either interpretation supports a Tat-bilayer interaction. The changes with increasing Tat concentration in the X-ray membrane form factors in Fig. ?? prove that Tat affects membrane structure, and the shift of the zero positions to higher q_z suggests thinning. Thinning is substantiated by quantitative analysis of the X-ray data and by MD simulations. Fig. 7A shows that the average membrane thickness, as measured by the distance D_{PP} between phosphocholines on opposite surfaces, decreases with increasing Tat concentration. Similar thinning is shown in Fig. 7B for the distance D_{HH} between the maxima in the electron density profiles of opposite surfaces. Compared to D_{PP} , D_{HH} is pulled towards both the carbonyl/glycerol groups and Tat because both have electron densities ($0.4 \text{ e}/\text{\AA}^3$) greater than water ($0.33 \text{ e}/\text{\AA}^3$) or hydrocarbon ($0.3 \text{ e}/\text{\AA}^3$). Although the thinning shown in Figs. 7A and 7B is not large, it obviously requires interaction of Tat with the bilayers. Fig. 7C shows that A_L increases with increasing Tat concentration, by both model fitting and MD simulations.

It is of considerable interest to learn where Tat resides, on average, in the membrane, as this would establish a base position from which translocation would be initiated. We have combined our two main methods, MD simulations and X-ray scattering, to address this question. In general, Tats locate at the bilayer/water interface as indicated in Section 3.2, and they are close to the phosphocholine headgroup region by comparing the simulated 2ZTat in Fig. 7.D with 7.A. Although the SDP modeling of the X-ray data obtains excellent fits to the experimental form factors for a model with Tat deep in the hydrocarbon interior (see Fig. S5), the corresponding MD simulation (shown in Fig. 4.C) eliminates this spurious result. Fig. 7D also shows that modeling gives smaller values for z_{Tat} than the simulation. The modeling result is supportive of the original simulation result of Herce and Garcia that Tat resides closer to the bilayer center than do the phosphocholine groups [45]. That is a base position that would be a possibly important precursor to translocation, as would the larger A_L .

Several groups have carried out calculations and MD simulations showing that

the cost of moving an arginine group from water to the bilayer center is 12-26 kcal/mol [73, 75–77] or 6-7 kcal/mol if side-chain snorkeling to the surface is taken into account [78]. This is not inconsistent with our result that Tat interacts with the membrane because, as is well known, the bilayer is not just a hydrocarbon slab, but has interfacial headgroup regions where Tat can reside. It has been suggested that the free energy cost for charged amino acids entering the headgroup region is similar to that for partitioning into octanol, about an order of magnitude smaller free energy cost than partitioning into cyclohexane [79–81]. Simulations suggest that the free energy is smaller for an arginine residing in the interfacial region than in water, roughly by 3 kcal/mole, depending upon the lipid [73, 81]. Our results therefore appear energetically reasonable.

One concern with diffraction experiments on samples consisting of adjacent bilayers in a stack or in a multilamellar vesicle is that the samples have to be partially dried to obtain conventional diffraction data. But then there is no pure water layer between adjacent bilayers, so a hydrophilic peptide is forced into the interfacial, partially hydrophilic region of the lipid bilayer. In contrast, by using diffuse scattering, we obtained structure from experimental samples that had a range of lamellar D spacings (see Fig. 2 caption) that were considerably larger than the thickness of the bilayer in Fig. 7A, thereby providing an ample pure water space, typically greater than 20Å. The result that $2z_{\text{Tat}}$ shown in Fig. 7D is so much smaller than our repeat spacings shows that Tat preferentially associates with the membrane rather than dissociating into water.

Tat also increases the mosaic spread observed by X-ray and neutron scattering as shown in Figs. S1-3; this is a much larger scale disordering of the stack of bilayers.

We analyzed the secondary structures of Tats from MD simulations using the Define Secondary Structure of Proteins (DSSP) program [82]. Data from the MD simulation which has the best fit to experimental X-ray form factors show that Tat contains neither α -nor β -helix structures. It appears that the membrane does not influence the conformation of solubilized Tat.

Given our structural and elastic moduli results, we now compare to other experiments in the literature. In 2008, the Wong group implicated Tats ability to induce saddle-splay curvature with a potential role of bidentate hydrogen bonding as key [35]. Rhodamine-tagged Tat only entered GUVs when the PE headgroup was included with PS and PC lipids (PS/PC/PE, 20:40:40), indicating that hydrogen-

bonding, and/or curvature-promoting lipids are required for Tat translocation. In PS/PE (20:80) lipids, they found Tat caused a highly curved cubic phase using X-ray diffraction [35]. In our experiments, there was little effect of adding DOPE to DOPC at either a 3:1 or 1:1 mole ratio on decrease in the bending modulus, bilayer thinning, or Tats outward movement with increasing concentration. Our two results are not inconsistent, however, since curvature-promotion appears not to be required for Tats ability to lower the energy required to bend nor to locate Tat in the bilayer, both of which may be important for Tat translocation. Yet Tat does translocate across membranes in their experiments only with PE in the membrane, so the ability to induce saddle-splay curvature may also be required for Tats translocation. An X-ray, neutron and AFM study reported thickening upon initial Tat binding, in contradiction to our result in Fig. 7B that shows thinning [83]. We suggest that this difference was caused by their using stiff gel phase DPPC lipid that did not allow bound Tat to perturb the bilayer. Using a variety of techniques, including high sensitivity isothermal titration calorimetry and ^2H - and ^{31}P -NMR, Ziegler *et al.* [?] presented evidence that the lipid bilayer remains intact upon Tat binding and our results confirm this. Finally, we compare our structural results to those obtained by solid state NMR, although at a lower hydration level than in our sample. Su *et al.* [42] found that Tat lies parallel to the bilayer surface in the headgroup region of DMPC/DMPG (8:7) bilayers, similar to our cartoon in Fig. 9.

2.6 Conclusion

Although a recent MD simulation using umbrella sampling [84] found that the free energy required for R_9C to traverse a membrane was smaller if a water pore was present, we could not directly test the existence of a transient water pore from our X-ray scattering experiment. This is because, even with a water pore, the translocation process still requires crossing a free energy barrier which is a non-equilibrium process. X-ray form factors measure an equilibrium state. If the form factors obtained from water pore structures agreed well with experiments, it would indicate that the pore structure was thermodynamically stable. This may be the case for some antimicrobial peptides, but certainly not for cell-penetrating peptides. Finding a kinetically competent pathway for the interesting phenomenon of translocation of highly charged Tat through hydrophobic membranes is difficult. An energetically passive translocation

likely occurs very seldom on an MD simulation time scale, and it probably happens quickly, so it would not significantly change the average structure of the membrane in which it occurs. Although our results in this paper do not reveal a kinetically competent pathway, they do show that Tat is drawn to the surface of the membrane, and is therefore ready for translocation at a region of local thinning. And they show that these interactions tend to soften (Fig. 2) the membrane and increase the area per lipid A_L , thereby likely reducing the energy barrier for passive translocation.

Chapter 3

Ripple Phase

When the temperature is reduced from the fluid phase, the ripple phase is observed in bilayers consisting of DMPC and DPPC lipids. This chapter discusses X-ray scattering experiments on the ripple phase formed by dimyristolphosphatydylcholine (DMPC) bilayers.

3.1 Introduction

(At some point, do some literature search and write up this section) The ripple phase has been a fascinating thermodynamic phase to many physicists and physical chemists since its discovery. It was originally observed in calorimetry study for alkanes by sturevant. Although this phase has never been reported to occur in a biologically relevant situation, it provides an interesting opportunity to study fundamental lipid interactions and their influence on the bilayer shape. (Let's find some recent papers and see if anyone says anything about biological relevance)

In the first structural study of this phase by Tardieu *et al.*, the X-ray diffraction pattern from DLPC was phased by a pattern recognition technique and the electron density map was calculated. It was shown that the structure corresponds to a 2D oblique unit cell shown in Fig. 3.1. The calculated electron density map showed that DLPC bilayers are height modulated and have a smooth, asymmetric shape. The ripple wavelength λ_r was reported to be 85.3 Å, the lamellar periodicity D 55.3 Å, and the oblique angle γ 110°. The electron density map reported the ripple amplitude $A = 15$ Å in DLPC.

Various experiments have indicated the existence of two types of ripple phases: the

stable asymmetric and the metastable symmetric phase. In the asymmetric phase, a plane of reflection perpendicular to the ripple wave vector is absent. The metastable symmetric phase has been seen in DPPC bilayers, but not in DMPC.

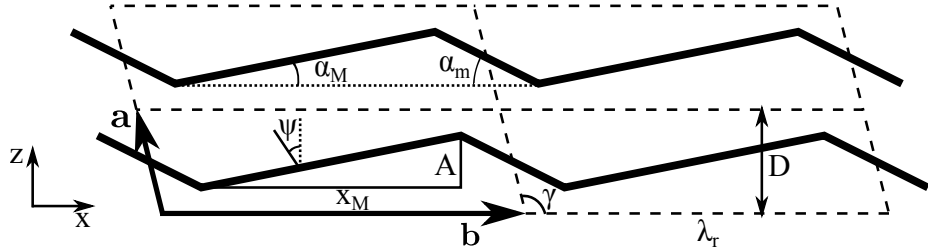


Figure 3.1: Lattice structure of the asymmetric ripple phase. Unit cells are shown in dash lines. Center of bilayers are shown by thick, solid lines. Notations in the figure are (**a** and **b**: lattice unit vectors), (D : D -spacing along z), ($\lambda_r = |\mathbf{b}|$: ripple wavelength), (γ : oblique tilt angle), (A : ripple amplitude), (ψ : chain tilt angle with respect to the z direction), and (x_M : projected length of the major arm).

The equilibrium structure of the ripple phase has been extensively studied by X-ray diffraction [2,8,85–89], neutron diffraction [90,91], AFM [], freeze fracture electron microscopy [92], and freeze fracture scanning tunneling microscopy [] techniques. In the scanning tunneling microscopy experiment [7], the three-dimensional contours of the ripple phase $P_{\beta'}$ of dimyristoylphosphatidylcholine (DMPC) were imaged, and a ripple wavelength of 130 Å and an amplitude of 45 Å were reported.

While many studies used multilamellar samples, the ripple phase was also found in unilamellar vesicles, where a vesicle has only one bilayer [93].

The ripple phase has been detected in phosphatidylcholines (PC) and phosphatidylglycerol (PG), but no ripple phase has been observed in bilayers composed of PE headgroups. These studies suggest that the size of headgroup has something to do with the ripple formation. Indeed, it has been suggested that the size mismatch between the bulky PC headgroup and hydrocarbon chains lead to tilt of the chains.

From X-ray data of the DMPC ripple of unoriented samples, Wack and Webb [8] argued that the ripples have a sawtooth shape, but were unable to phase the observed pattern. Their X-ray form factor data were later phased by employing a modeling and fitting technique by Sun *et al.* [88], and the electron density map was calculated, which indicated that the ripples indeed have a sawtooth shape. The map also showed that the major arm is about twice as long as the minor arm. The bilayer thickness was found to be larger than that of the minor arm. The value of the bilayer thickness

in the major arm was comparable to the thickness of DMPC bilayers in the gel phase.

A structural investigation by X-ray diffraction of the ripple phase of oriented dipalmitoylphosphatidylcholine (DPPC) samples indicated that hydrocarbon chains are packed in a hexagonal lattice with chains tilted in the plane perpendicular to the ripple wave vector [94]. In that study, the oblique angle γ was found to be 90° . It is believed that the resolved structure was for the symmetric ripple, which has been shown to be thermodynamically metastable and whose occurrence depends on the sample history [95]. In [94], only symmetric ripple was observed in the low angle X-ray scattering, which seems to contradict with the metastability of this symmetric ripple.

Sengupta et al. [96] has investigated temperature dependence of the average structure of DMPC and concluded that there is no obvious change in the structure as a function of temperature. On the other hand, the ripple phase composed of POPC showed some variation in the average structure. Based on calculated electron density profiles and model parameters, they argued that chains in both major and minor arms are tilted with respect to the stacking z direction by the same amount and that chains are parallel to the local normal in the major arm. This argument was inconsistent with the findings in [88] that the thickness of major arm is almost identical to that of the gel phase where chains are tilted by $\sim 30^\circ$. To circumvent this discrepancy, Sengupta *et al.* speculated that chains might be titled by some amount into the direction perpendicular to the ripple direction. This type of information , however, is not well captured in low angle scattering data, and wide angle scattering is essential.

In a giant unilamellar vesicle composed of a mixture of DPPC and DOPC, co-existing domains of L'_β and P'_β have been found [97]. The P'_β domain had lower concentration of DPPC than the L'_β domain. Addition of anionic lipids (DOPG?) turned the gel phase domain into the ripple phase domains. The authors concluded that reduction of surface tension drove highly stressed gel phase to less stressed ripple phase.

AFM The ripple phase has also been observed in the top layer of solid supported double layers through atomic force microscopy (AFM). The effect of the bottom layer on the top layer in the ripple phase has not been thoroughly studied. It is not clear whether the structure of these ripple formation top layers is the same as that in a bulk sample such as MLVs and oriented samples.

A few MD (molecular dynamics) simulations have shed light on molecular organi-

zation in the ripple phase as well. de Vrie *et al.* [98] carried out atomistic simulations resulting in an assymetric ripple where chains are gel-like in the major arm and interdigitated in the minor side. Coarse-grain simulations performed later essentially found the same results [99].

A theory developed by Chen *et al.* [100] has been successful in describing some features in the ripple phase. In this theory, the divergence of the tilt field of lipids are coupled to the curvature of the bilayer. Increase in the divergence of the lipid tilt is compensated by increase in the curvature, leading to the observed height modulated ripple phase. This theory predicted ripple phases with different symmetry for chiral and achiral lipids. Later, Katsaras and Raghunathan [101] carried out low angle X-ray scattering experiment on regular DMPC and achiral DMPC and found that there was no structural difference between them.

Raghunathan theory (2011)

Schmidt theory (2013)

D (Å)	λ_r (Å)	γ (deg)
55.0	159.4	99.0
57.0	140.8	97.6
57.3	151.6	97.8
57.4	148.4	97.6
57.5	144.1	97.8
57.5	141.9	98.0
58.0	140.1	98.2
57.8	145.0	98.2
58.0	141.7	98.4
59.8	129.6	97.3
60.6	130.1	97.0
61.5	130.8	96.5
62.4	122.0	95.9
63.9	123.1	94.9
64.9	120.3	92.3

Table 3.1: Lattice constants for DMPC at $T = 18.0$ °C reported by Wack and Webb [8] except the one colored in blue. The data collected and analyzed in this thesis are colored blue.

3.2 Materials and Methods

3.2.1 Sample Preparation

DMPC was purchased from Avanti Polar Lipids. Four mg DMPC powder was dissolved in 140 μl chloroform:methanol (2:1 v:v) mixture. The solution was plated onto silicon wafers following the rock and roll procedure [102]. See also Sec. 2.2.3. For all the ripple phase experiments, the temperature of the hydration chamber was set to 18 °C. In 2011 and 2012 synchrotron experiments, the samples were created and annealed more than a week in advance and stored in a refrigerator. The quality of these samples measured by their mosaic spread was found to worsen over time after the samples were annealed. Therefore, to attempt better quality, the samples were annealed for only about 12 hours just before the X-ray experiment. Figure 3.2 shows a picture of the annealing chamber. Annealing is promoted both by hydration and by elevated temperature. To achieve gentle but efficient hydration of a sample, filter papers were installed that exposed a larger surface for evaporation. The temperature was set to 60 °C. It must be emphasized that the annealing chamber should equilibrate in an annealing oven set to 60 °C, prior to putting a sample in the chamber. When a sample was put in the chamber sitting at a room temperature and then the system was placed inside the oven, warmer water vapor inside the chamber condensed on the cooler sample, causing so called flooding of oriented sample. A small drop of water on an oriented film is detrimental for the orientation quality because the entropy-driven formation of unilamellar vesicles causes oriented bilayers to peel off one by one.

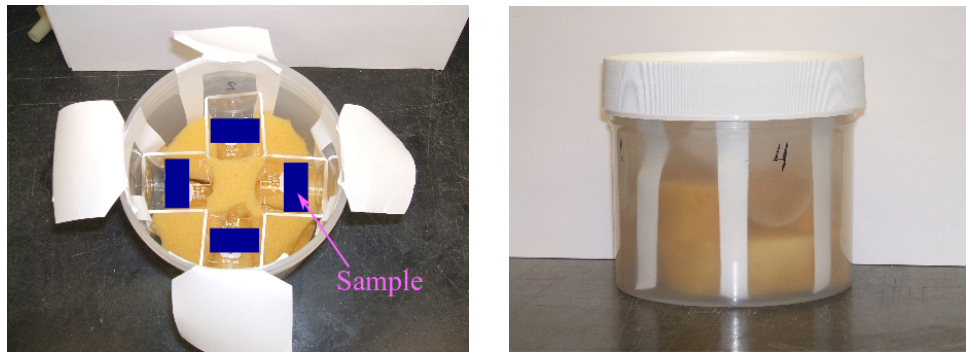


Figure 3.2: Picture of an annealing chamber.

The sample for the grazing incident wide angle study was prepared in the same way as for low angle study. In order to minimize the geometric broadening, the sample

was trimmed to 1 mm in width along the beam direction.

The sample for transmission study was deposited on a thin, 35 micron, silicon wafer, and oriented following the rock and roll procedure [102]. Because the wafer was very fragile, attaching the sample to a sticky thing was impossible. Instead, the sample was attached to a plastic cap on a small vial with a small amount of heat sink compound at a corner of the wafer. The wafer was stable enough for rocking.

3.2.2 Instrumental Resolution

The X-ray scattering experiments were carried out at the Cornell High Energy Synchrotron Source (CHESS) G1 station in three different runs (2011, 2012, and 2013). The low angle X-ray scattering (LAXS) data analyzed in this thesis were collected in 2013. The near grazing incidence wide angle X-ray scattering (nGIWAXS) data were also collected in the 2013 run, but with smaller energy dispersion than in the LAXS experiment. The transmission wide angle X-ray scattering (TWAXS) data were collected in the 2011 run. The ripple phase experiment in the 2012 run was not successful due to low sample quality. The instrumental resolution in these X-ray experiments depended on the beam divergence, energy dispersion, and geometric broadening.

3.2.2.1 Divergence

The beam divergence quantifies an angular spread of the incoming X-ray beam. We estimated the beam divergence by measuring the horizontal and vertical beam widths at two known sample-to-detector S distances with difference ΔS . The beam widths were larger at the further distance, which indicated that the beam was divergent. We calculated the divergence as $\text{div} = \Delta B / \Delta S$, where ΔB is the difference in beam widths at different S distances. Table 3.2 summarizes beam divergence.

year	type of experiment	horizontal (rad.)	vertical (rad.)
2013	LAXS	4.2×10^{-5}	1.6×10^{-4}
2013	nGIWAXS	4.2×10^{-5}	1.6×10^{-4}
2011	TWAXS	2.5×10^{-5}	5×10^{-5}

Table 3.2: Beam divergence

3.2.2.2 Energy dispersion

A W/B₄C multilayer monochromator with energy bandwidth $\Delta E/E$ of 1.3% was used in the LAXS and TWAXS experiments. The energy of the X-ray beam was 10.55 keV, corresponding to a wavelength λ of 1.175 Å, in the LAXS experiment. To achieve a higher instrumental resolution than that for the LAXS experiment, a (111) silicon monochromator was used for the nGIWAXS experiment, which gave $\Delta E/E$ of 0.01%. Due to the geometry of the G1 station, the Si monochromator was placed in the G1 hutch, in series with the multilayer monochromator. Table 3.3 summarizes energy dispersion.

year	type of experiment	$\Delta E/E$ (%)	E (keV)	λ (Å)
2013	LAXS	1.5	10.55	1.175
2013	nGIWAXS	0.01	10.55	1.175
2011	TWAXS	1.5	10.54	1.176

Table 3.3: Energy dispersion

3.2.2.3 Geometric Broadening

The beam footprint on the sample has a finite size and this causes geometric broadening of diffraction peaks on the CCD detector.

LAXS In the LAXS experiment, the geometric broadening in the horizontal x direction is simply the horizontal beam width for $k = 0$ peaks with minor additional broadening for $k \neq 0$ peaks. Geometric broadening in the vertical z direction is due to different heights of the sample along the y direction of the beam at non zero angle of incidence ω . It is given approximately by $w_s \tan \theta$, where w_s is the sample width along the y direction and θ is the scattering angle. The beam shape, measured through a semi-transparent 200 µm thick molybdenum (Mo) beam stop, is shown in Fig. 3.3 and 3.4. The horizontal beam width was 1.7 pixels (0.12 mm). The vertical beam width was approximately 1 mm, tall enough to cover the entire sample if the sample was tilted between 0° and 11.5°. The sample was rocked during X-ray exposure between -1.6° and 7° in order to observe many diffraction peaks in one data collection and keep all the sample in the beam.

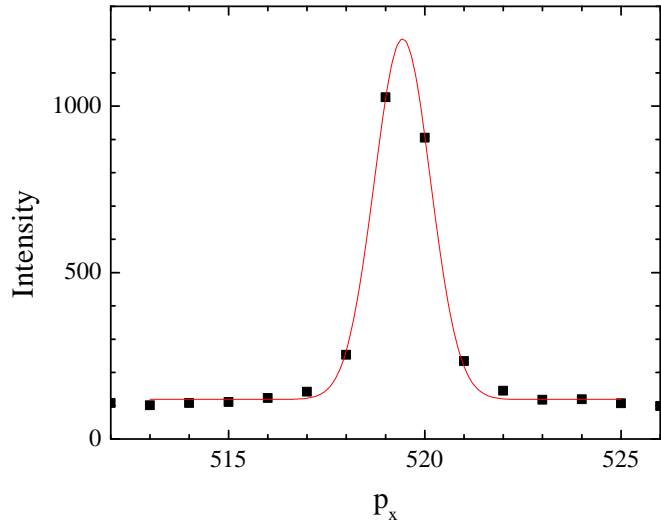


Figure 3.3: The horizontal profile of the beam used in the 2013 low resolution study. Each pixel was 0.07113 mm, which gave a CCD angular resolution $\Delta\theta$ of 0.0057°, corresponding to $\Delta q = 0.0011 \text{ \AA}^{-1}$ at the sample to detector distance of 359.7 mm. The beam FWHM = 1.7 pixels, giving $\Delta\theta = 0.010^\circ$ or $\Delta q = 0.0019 \text{ \AA}^{-1}$.

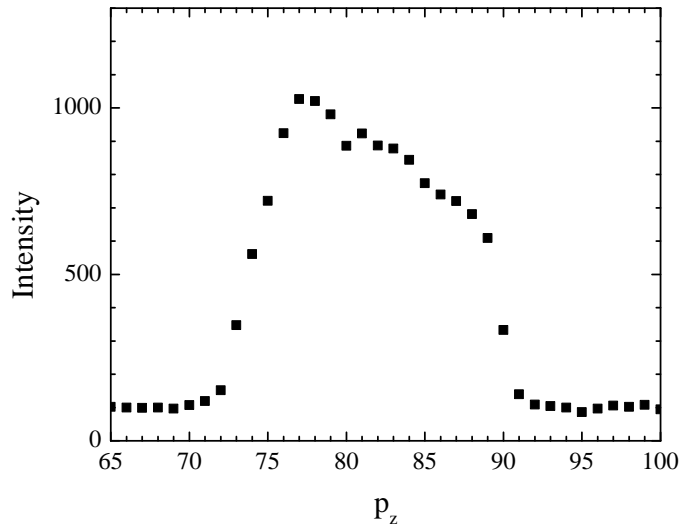


Figure 3.4: The vertical profile of the beam used in the 2013 low resolution study. The beam height = 15 pixels = 1.1 mm.

nGIWAXS In the nGIWAXS experiment, the horizontal geometric broadening was due to the sample width along the beam direction and the horizontal beam width. From the geometry of the experiment shown in Fig. 3.5, the geometric broadening Δx can be estimated, assuming simple additivity,

$$\Delta x = \Delta x_{\text{beam}} + w_s \tan(2\theta),$$

where θ is the in-plane scattering angle. The total scattering angle 2θ for the ripple WAXS was approximately 16° . To minimize the contribution to Δx from the sample, the sample was trimmed to $w_s = 1$ mm along the beam direction. This width was chosen because (1) I could not trim more without a more sophisticated device than a simple razor blade, (2) a very narrow sample would be a weak scattering body, and (3) disordering effect from the sample edge might become too significant to ignore. Given the above reasons and due to limited availability of synchrotron beam time, I considered a 1 mm width to be reasonable. The horizontal beam width was 4 pixels (0.28 mm) as shown in Fig. 3.6. With these experimental parameters, the resolution was estimated to be $\Delta x = 0.57$ mm = 8 pixels, which would be the unresolved width of an intrinsically infinitely sharp wide angle peak. [Comment and refer to the gel phase data shown in the result section of nGIWAXS.](#) The sample to detector distance were 220.6 mm, measured using silver behenate. Then, the minimum peak width measured in q -space would be $\Delta q \approx 0.014 \text{ \AA}^{-1}$. The vertical geometric broadening was negligible because the sample width w_s was narrow and scattering of interest occurred at small q_z .

TWAXS In the TWAXS experiment, geometric broadening in both x and z directions was non-negligible. To calculate the broadening, let us assume that the beam has a rectangular cross section with its height Y_b and width X_b as shown in Figure 3.8. When the sample is tilted by ω , X-rays emerging from the top edge of the sample travel extra distance compared to the distance that X-rays from the bottom edge of the sample travel. This, then, leads to distortion of the scattered beam; namely, the scattered beam will appear on the CCD screen as a parallelogram as shown in Figure 3.8. Figure 3.9 shows the top- and sideview of the projection of the beam on the sample. From simple geometry, it can be shown that $a = Y_b / \tan \omega$, $b = aX/(2S)$, $c = aZ/(2S) + Y_B/2$, and $B = \tan^{-1}(Z/S)$. Since $H = 2c$ and $W = 2b$, H and W in

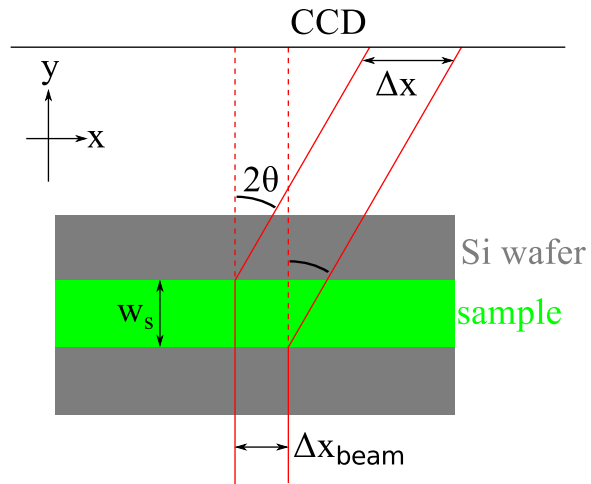


Figure 3.5: In-plane geometric broadening due to the sample width w_s and the beam width Δx_{beam} . A top view of the sample (green) on the Si wafer (gray) and the incoming and diffracted X-rays (bounded by red solid lines) are shown. The total in-plane scattering angle for a lipid chain-chain correlation is labeled as 2θ , and the geometric broadening as Δx .

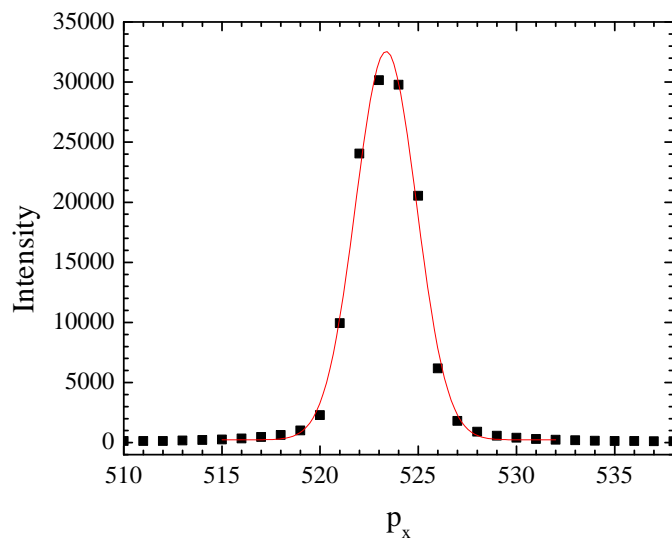


Figure 3.6: The horizontal profile of the beam used in the 2013 high resolution experiment. The CCD angular resolution $\Delta\theta = 0.0092^\circ$ corresponding to $\Delta q = 0.0017 \text{ \AA}^{-1}$, at the sample to detector distance of 220.6 mm. The beam FWHM = 3.7 pixels = 0.26 mm, giving $\Delta\theta = 0.034^\circ$ or $\Delta q = 0.0063 \text{ \AA}^{-1}$.

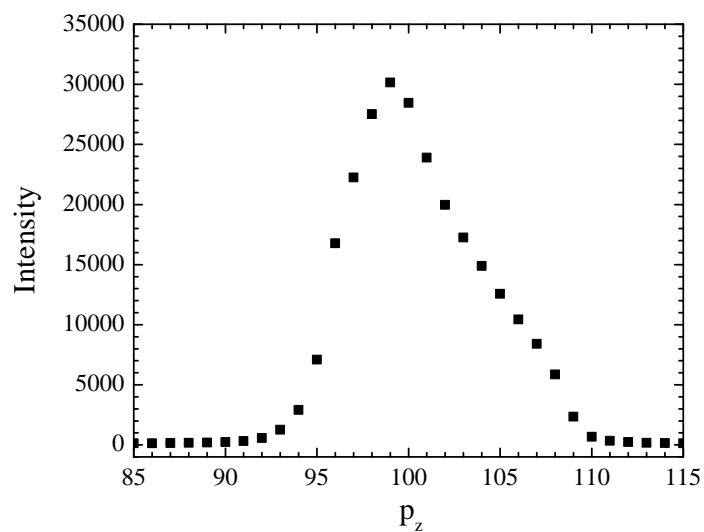


Figure 3.7: The vertical profile of the beam used in the 2013 high resolution experiment. The beam height = 9 pixels = 0.64 mm.

Figure 3.10 are given by

$$H = Y_b \left(1 + \frac{Z}{S \tan \omega} \right) \quad (3.1)$$

$$W = Y_b \frac{X}{S \tan \omega}. \quad (3.2)$$

The sample to detector distance S was 158.6 mm, giving an angular CCD resolution of $0.013^\circ/\text{pixel}$, or $0.0024 \text{ \AA}^{-1}/\text{pixel}$. The observed wide angle peak was at $(X, Z) = (44.0 \text{ mm}, 15.5 \text{ mm})$. The beam width and height were both $0.2 \text{ mm} = 2.8 \text{ pixels}$. With this setup, $W = 0.7 \text{ pixels}$ and $H = 3.1 \text{ pixels}$. Therefore, the distorted shape of the diffraction peak was negligible. Table 3.4 summarizes geometric broadening for our experiments.

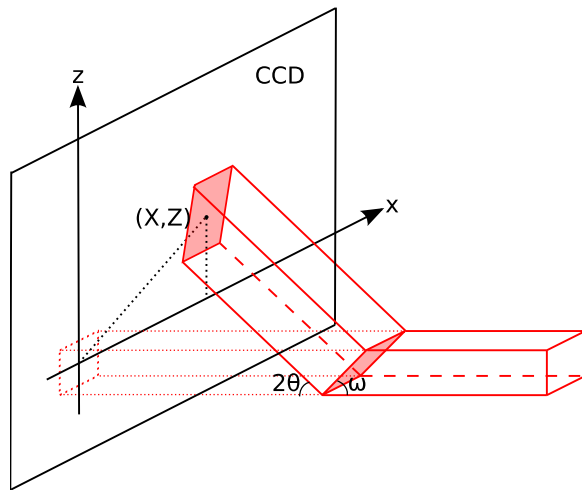


Figure 3.8: Geometric broadening in TWAXS. The cross section of the incoming X-ray with the sample and the CCD detector are both shaded in red. The sample is tilted by ω . The red dots show the transmitted beam. The incoming beam is rectangular but upon scattering appears as a parallelogram on the CCD.

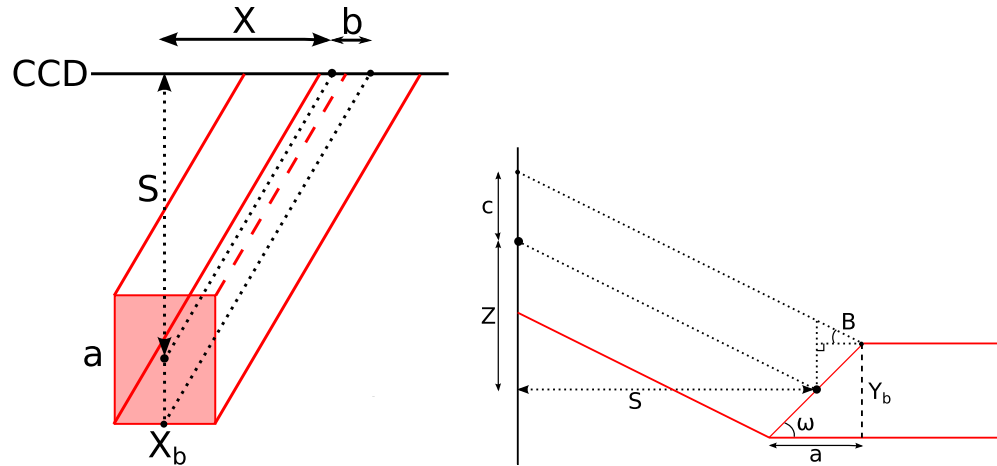


Figure 3.9: Top and side view of the beam on the sample in TWAXS. The cross section of the incoming X-ray with the sample is shaded in red. X_b and Y_b are the beam width and height, respectively. S is the sample to detector distance. (X, Z) is a position of the center of the scattered beam on the detector with respect to the center of the transmitted beam as shown in Figure 3.8.

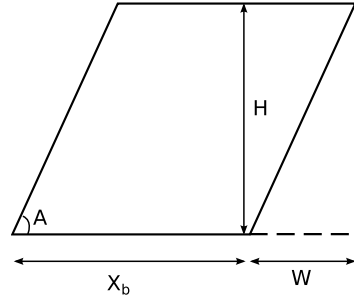


Figure 3.10: Projection of rectangular beam on the detector. Scattered beam appears as a parallelogram on the CCD.

type of experiment	horizontal (pixels)	horizontal (\AA^{-1})	vertical (pixels)	vertical (\AA^{-1})
LAXS	1.7	0.0019	$6.6q_z$	$0.0072q_z$
nGIWAXS	8	0.014		
TWAXS	2.8	0.0067	3.1	0.0074

Table 3.4: Geometric broadening

3.2.3 Low Angle X-ray Scattering Experiment

The X-ray beam for the low angle X-ray scattering (LAXS) experiment was set up by the station scientist, Dr. Arthur Woll. We chose the sample to detector distance to be 359.7 mm, measured by indexing silver behenate Bragg peaks. The D-spacing of silver behenate is known to be 58.367 Å.

Occasionally, sheets of molybdenum (Mo), each nominally 25 μm were used to attenuate the incoming beam. These sheets were installed by Dr. Arthur Woll in the upstream of the sample chamber. The attenuation length μ of 10.55 keV X-ray in Mo is 13.74 μm [103]. For a 25 μm thick Mo attenuator, the attenuation factor is calculated to be $[\exp(-25/13.74)]^{-1} = 6.2$. The exact attenuation factor was determined by comparing X-ray images collected with and without the attenuator, shown in Fig. 3.11. The attenuation factor of the nominally 25 μm thick Mo was found to be 6.9 for the wavelength used (1.175 Å), indicating an actual thickness of 27 μm .

Sheets of Mo were also used as a semi-transparent beam stop downstream of the sample, just outside the hydration chamber, to attenuate the beam and strong orders. 100 and 200 μm were used to attenuate strong orders and either 200 or 225 μm to attenuate the beam. To avoid saturation of CCD pixels by the very intense beam of 10^{11} photons/mm²/second, the beam stop was always set to attenuate the beam.

A few Bragg peaks in the low angle X-ray scattering of the ripple phase were very strong, leading to saturation of CCD pixels for data collection with a long exposure time. In order to probe a wide range of q -space, three images were taken: 1) a short, one second exposure with a nominally 25 micron molybdenum attenuator installed in the upstream of the sample to reduce the intensity of the incoming X-ray beam, 2) one second exposure without the beam attenuator, and 3) 60 second exposure with a beam stop blocking the very intense (1,0) and (2,0) peaks. See Fig. 3.12. Then, the integrated intensity of (1,0) peak was measured from the first image. This value was multiplied by 6.9 to account for the beam attenuation and by 60 to scale with the exposure time. The intensity of (2,0) and (2,-1) were measured from the second image, also multiplied by 60 to account for the shorter exposure time. The intensities of the rest of the observed peaks were measured from the third image.

The integrated intensity of each peak was obtained using the Nagle lab tview software developed by Dr. Yufeng Liu [50] by putting a box around a peak and summing up the intensity in those pixels that fall inside the box. The background

scattering was estimated by measuring the intensity in pixels near the peak but not containing any peak tail. The choice of box size was made according to the width of each peak. Because of mosaic spread in the sample, the peaks were wider for higher orders. Consequently, the box was made wider for higher orders. The box size was chosen so that approximately 80% of the peak intensity was counted toward the integrated intensity.

3.2.4 Near Grazing Incidence Wide Angle X-ray Scattering Experiment

The high resolution wide angle X-ray scattering (WAXS) experiment was also carried out at the G1 station. The instrument was set up by the G1 station scientist, Arthur Woll, and the assistant scientist, Dr. Robin Baur. Wide angle X-ray scattering was collected at an incident angle of 0.2° . The total external reflection from an air-lipid interface occurs approximately at 0.1° and 0.17° for air-silicon interface, so 0.2° is not quite grazing incidence. Grazing incidence usually implies that the incident angle is less than the critical angle for a total external reflection. Therefore, 0.2° is called near grazing incidence (NGI) in this thesis. The background scattering was collected at -0.2° . Subtraction of the negative angle data from the positive angle data resulted in a clean sample scattering image.

3.2.5 Transmission Wide Angle X-ray Scattering Experiment

The transmission wide angle X-ray scattering (TWAXS) experiment was also carried out at the G1 station. The incident angle ω was set to -45° for transmission data collection (see Fig. 3.13). A $35\ \mu\text{m}$ thick silicon substrate absorbs 10.5 keV X-ray by only 20% [103], so most of the incoming X-rays penetrated the thin substrate.

Unfortunately, the axis of the rotation motor did not coincide with the sample axis, so the sample to detector distance varied as ω was varied. To accurately measure the sample to detector distance, low angle scattering from a silver behenate (AgBe) sample was collected at a fixed ω . Due to large mosaic spread of the AgBe sample, many orders were visible. While the relative intensity of each order was inaccurate, the positions of peaks were the same as those observed with a rotating sample. To measure the D-spacing of the sample, ω was set to 1° . The sample to detector distance was measured to be 174.7 mm at $\omega = 0^\circ$. From the sample holder geometry shown in

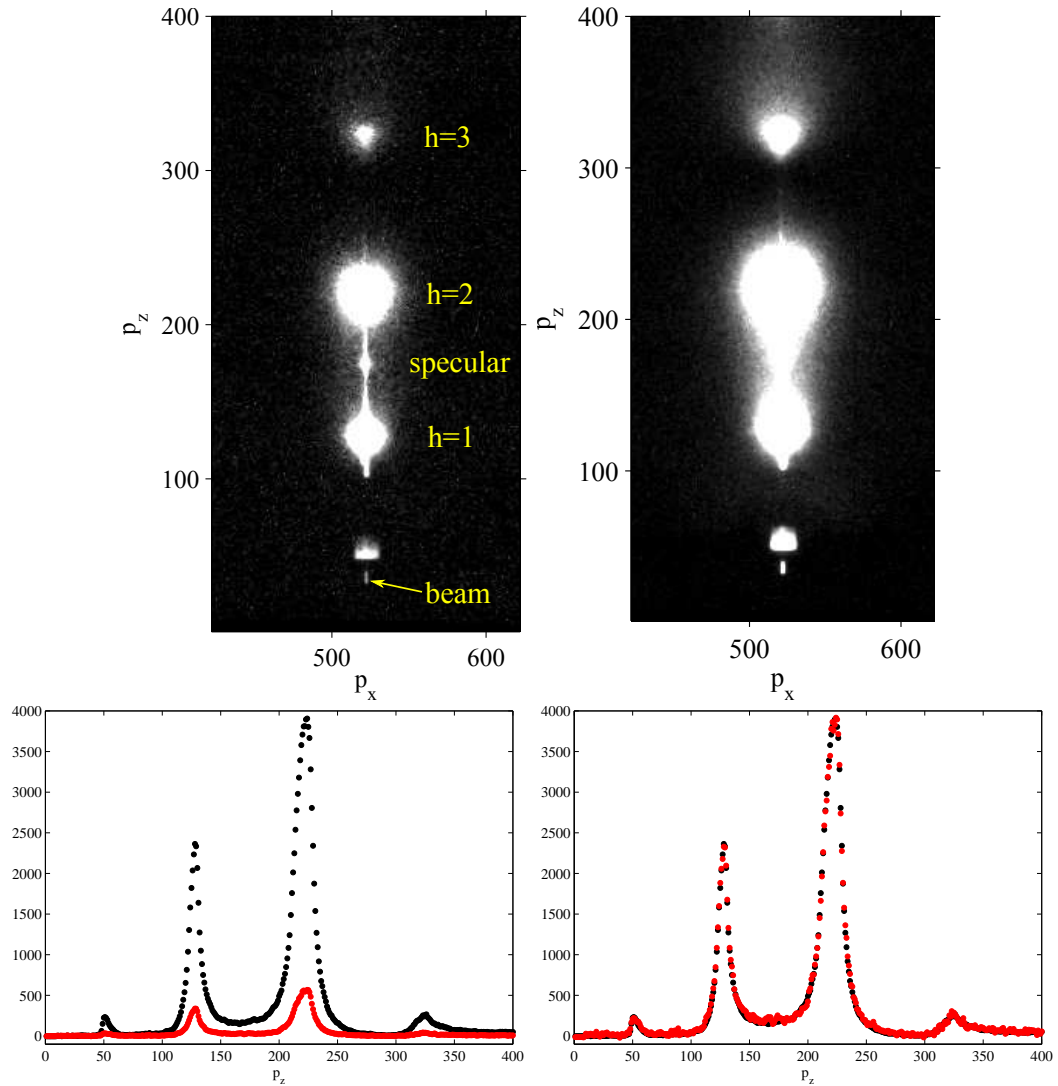


Figure 3.11: (top panels) CCD images of X-ray scattering taken with (left) and without (right) a nominally 25 μm thick Mo attenuator. These data were taken at a fixed angle of incidence $\omega = 0.8^\circ$. The sample was an oriented film of DOPC:DOPE (3:1) in the fluid phase at 37 °C. The wavelength was 1.175 Å, the same as the one used for the ripple phase experiment. The same gray scale is used in both images. 100 pixel = 0.11 Å⁻¹ in q . A small dot located about $(p_x, p_z) = (520, 170)$ between the first and second orders is a specular reflection from the substrate. The exposure times were 1 second. (bottom panels) Vertical p_z slices of the X-ray images shown in the top panels (left). The scattering intensity measured with the attenuator (red solid circles) was multiplied by a factor of 6.9 and compared to the intensity measured without the attenuator (black solid circles, right).

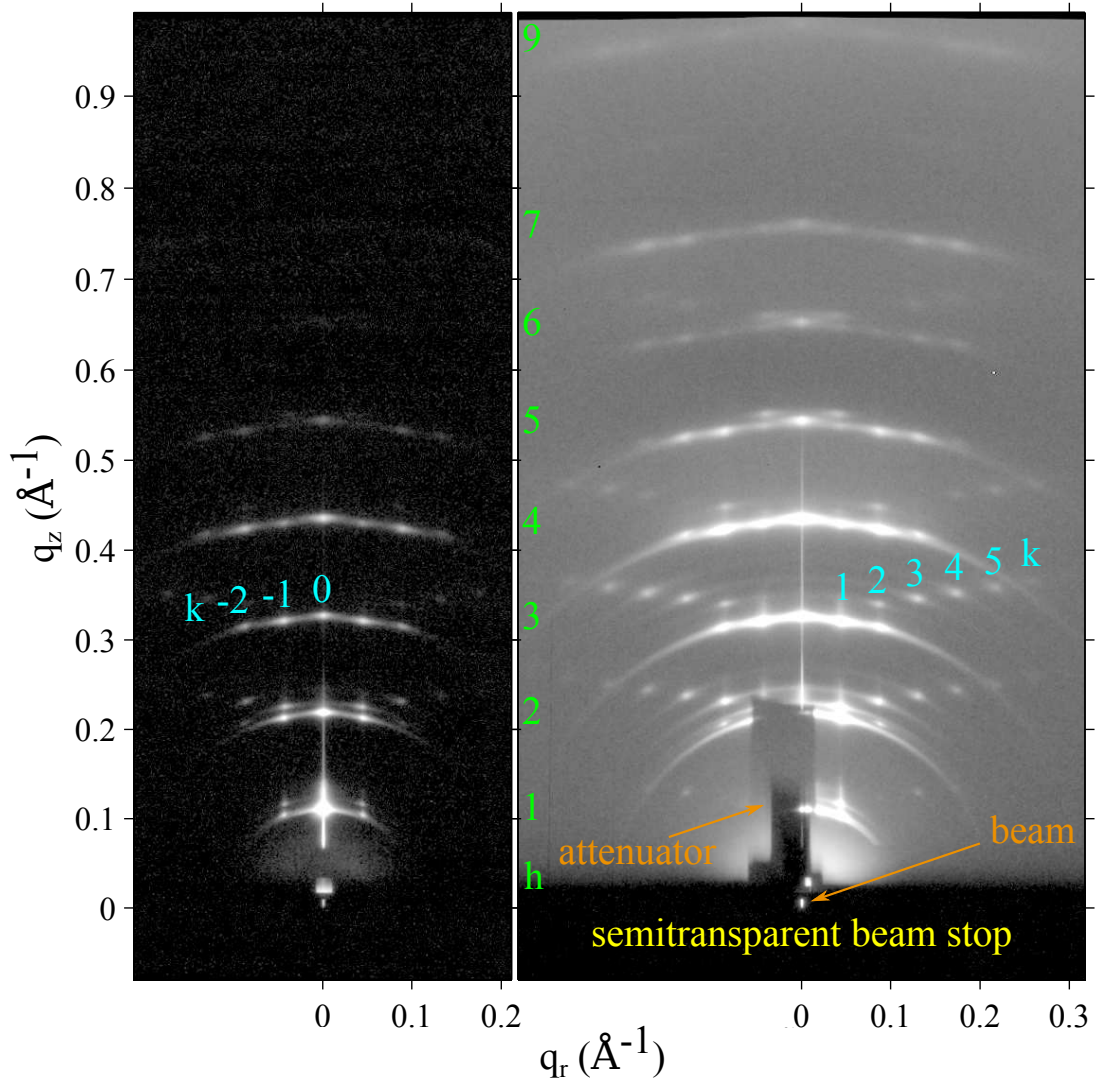


Figure 3.12: 1 second exposure (left) and 60 second exposure (right) of the low angle X-ray scattering from the DMPC ripple phase in gray log scales. The index h is labeled in green. $(3, k)$ reflections are identified in cyan. The shadow cast by 100 μm thick molybdenum attenuator blocking strong $(1, 0)$ and $(2, 0)$ orders in the right image is labeled as attenuator and extends from $q_z = 0 \text{ \AA}^{-1}$ to 0.2 \AA^{-1} . $D = 57.8 \text{ \AA}$, $\lambda_r = 145.0 \text{ \AA}$, and $\gamma = 98.2^\circ$.

Fig. 3.14, the sample to detector distance was estimated to be 158.6 mm at $\omega = 45^\circ$. A picture of the sample holder is shown in Fig. 3.15.

To level the sample, the sample was first leveled coarsely by watching the sample scattering. When ω was negative, much of the incoming beam was absorbed by the flat substrate, yielding weak sample scattering. When ω became positive, sample scattering was strong. With this procedure, we leveled the sample with an uncertainty of $\pm 0.2^\circ$. We then measured the beam intensity at various sample heights as a function of ω . The sample was level when the beam intensity had the narrowest dip as the sample was moved vertically through the beam.

Background scattering was collected by replacing the sample with a bare wafer. The bare wafer was not placed exactly at the same location as the sample, which gave slightly different background scattering. This only affected the background subtraction near the beam. The wide angle scattering was not affected by this inexact placement of the bare wafer.

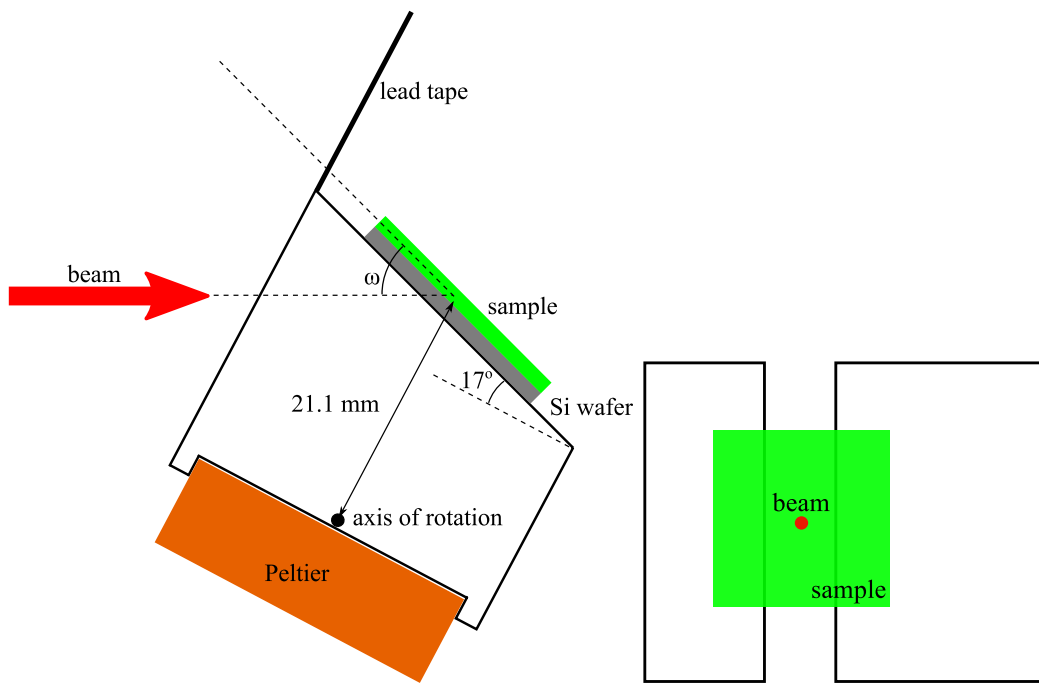


Figure 3.13: Schematics of the sample holder in the transmission mode. Side (left) and top (right) views are shown. The thickness of the Si wafer = $35 \mu\text{m}$. The thickness of the sample $\approx 10 \mu\text{m}$. The distance between the axis of rotation and sample = 21.1 mm.

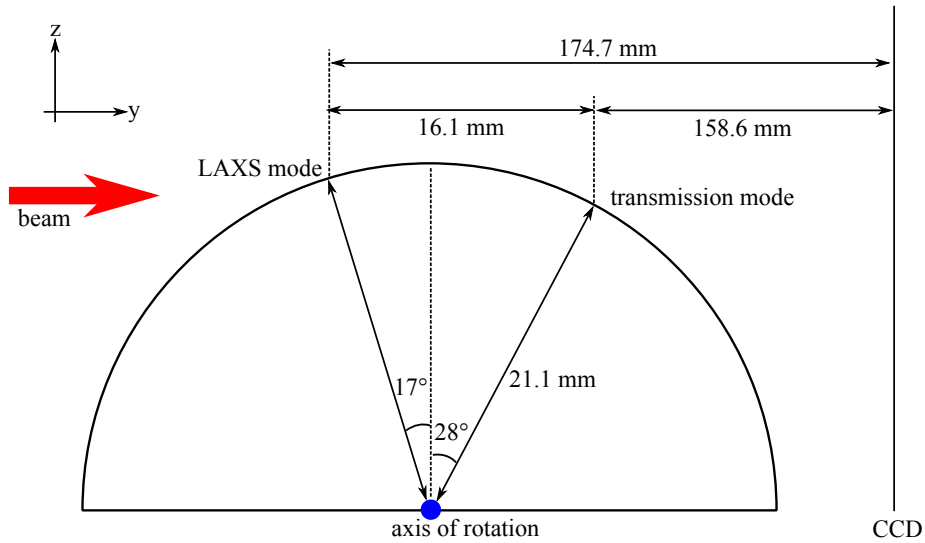


Figure 3.14: Circular path followed by the sample as the angle of incidence ω was changed. The sample to detector distance and D -spacing of the sample were measured in the LAXS mode, where $\omega = 1^\circ$. WAXS images were collected at the transmission mode, where $\omega = -45^\circ$. The z position of the sample was slightly higher at the LAXS mode than at the transmission mode, so the sample holder was vertically shifted for different modes.

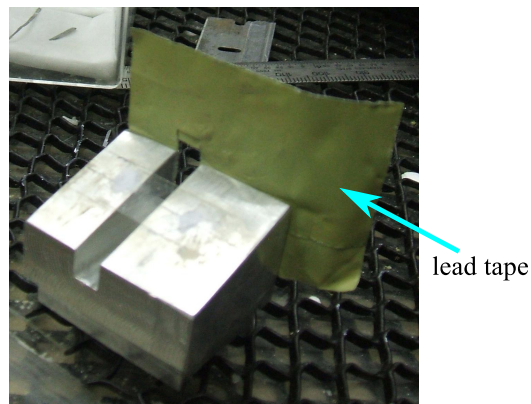


Figure 3.15: Picture of the sample holder looking from above. A lead tape was attached to the back of the sample holder to help reduce the background scattering, typically coming from the air gap between the flightpath snout and the mylar window of the chamber.

3.3 LAXS: analysis

3.3.1 Lattice Structure

The unit cell vectors for the two-dimensional oblique lattice shown in Fig. 3.1 can be expressed as

$$\mathbf{a} = \frac{D}{\tan \gamma} \hat{\mathbf{x}} + D \hat{\mathbf{z}} \quad (3.3)$$

and

$$\mathbf{b} = \lambda_r \hat{\mathbf{x}}. \quad (3.4)$$

The corresponding reciprocal lattice unit cell vectors are

$$\mathbf{A} = \frac{2\pi}{D} \hat{\mathbf{z}} \quad (3.5)$$

and

$$\mathbf{B} = \frac{2\pi}{\lambda_r} \hat{\mathbf{x}} - \frac{2\pi}{\lambda_r \tan \gamma} \hat{\mathbf{z}}. \quad (3.6)$$

The reciprocal lattice vector, \mathbf{q}_{hk} for the Bragg peak with Miller indices (h, k) is

$$\mathbf{q}_{hk} = h\mathbf{A} + k\mathbf{B}, \quad (3.7)$$

so its Cartesian components are

$$\mathbf{q}_{hk} \cdot \hat{\mathbf{x}} = q_{hk}^x = \frac{2\pi k}{\lambda_r} \equiv q_k^x \quad (3.8)$$

$$\mathbf{q}_{hk} \cdot \hat{\mathbf{y}} = q_{hk}^y = 0 \quad (3.9)$$

$$\mathbf{q}_{hk} \cdot \hat{\mathbf{z}} = q_{hk}^z = \frac{2\pi h}{D} - \frac{2\pi k}{\lambda_r \tan \gamma}. \quad (3.10)$$

Our sample consists of many ripple domains with a uniform distribution of in-plane directions of the ripple wave vector, \mathbf{b} in Fig. 3.1. In this case, q_{hk}^x and q_{hk}^y are combined to give $q_{hk}^r = 2\pi k / \lambda_r$.

3.3.2 Sample q-space

The incoming and outgoing wavevectors of the x-ray beam in Fig. 3.16 are given by

$$\mathbf{k}_{\text{in}} = \frac{2\pi}{\lambda} \hat{\mathbf{y}}, \quad \mathbf{k}_{\text{out}} = \frac{2\pi}{\lambda} (\sin 2\theta \cos \phi \hat{\mathbf{x}} + \cos 2\theta \hat{\mathbf{y}} + \sin 2\theta \sin \phi \hat{\mathbf{z}}), \quad (3.11)$$

where λ is the wavelength of x-ray, 2θ is the total scattering angle, and ϕ is the angle measured from the equator on the detector. The scattering vector (also called momentum transfer vector) is the difference between \mathbf{k}_{in} and \mathbf{k}_{out} ,

$$\begin{aligned} \mathbf{q} &= \mathbf{k}_{\text{out}} - \mathbf{k}_{\text{in}} \\ &= q (\cos \theta \cos \phi \hat{\mathbf{x}} - \sin \theta \hat{\mathbf{y}} + \cos \theta \sin \phi \hat{\mathbf{z}}), \end{aligned} \quad (3.12)$$

where $q = 4\pi \sin \theta / \lambda$ is the magnitude of the scattering vector. When the sample is rotated by ω about the lab x-axis in the clockwise direction as shown in Fig. 3.16, the sample q -space also rotates and are given by

$$\hat{\mathbf{e}}_x = \hat{\mathbf{x}}, \quad \hat{\mathbf{e}}_y = \cos \omega \hat{\mathbf{y}} + \sin \omega \hat{\mathbf{z}}, \quad \hat{\mathbf{e}}_z = -\sin \omega \hat{\mathbf{y}} + \cos \omega \hat{\mathbf{z}}. \quad (3.13)$$

From Eq. (3.12) and (3.13), we find Cartesian components of the sample q -space to be

$$\begin{aligned} q_x &= \mathbf{q} \cdot \hat{\mathbf{e}}_x = q \cos \theta \cos \phi, \\ q_y &= \mathbf{q} \cdot \hat{\mathbf{e}}_y = q (-\sin \theta \cos \omega + \cos \theta \sin \phi \sin \omega), \\ q_z &= \mathbf{q} \cdot \hat{\mathbf{e}}_z = q (\sin \theta \sin \omega + \cos \theta \sin \phi \cos \omega). \end{aligned} \quad (3.14)$$

The position, (X, Z) , of a CCD pixel is measured with respect to the beam and given by

$$X = S \tan 2\theta \cos \phi, \quad Z = S \tan 2\theta \sin \phi, \quad (3.15)$$

where S is the distance between the sample and detector.

From a model for the electron density of a lipid bilayer, one calculates the X-ray scattering intensity pattern, $I(\mathbf{q})$. Then, Eq. (3.14) and (3.15) relate $I(\mathbf{q})$ to the experimentally measured intensity pattern, $I(X, Z)$. It is important to remember that a given pixel position, (X, Z) , corresponds to a triplet (q_x, q_y, q_z) . Fully exploring the sample q -space requires changing ω for a fixed wavelength, which was achieved

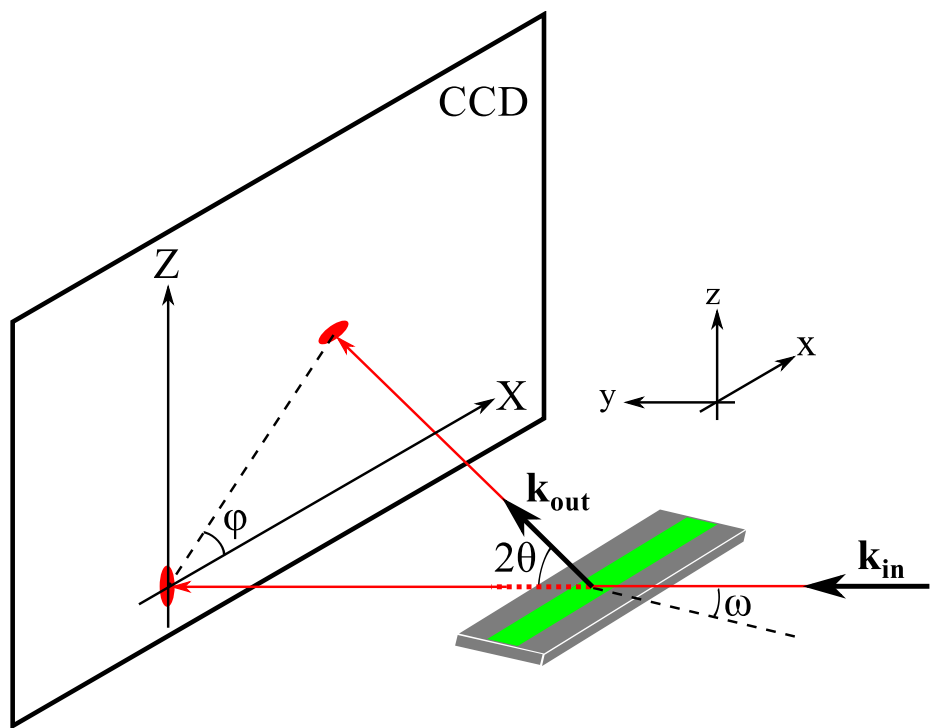


Figure 3.16: Experimental reflectivity geometry.

by continuously rotating the sample with a motor. In the ripple phase, because our sample has in-plane rotational symmetry, the ripple side peaks ($h, k \neq 0$) make up Bragg rings while the main peaks ($h, k = 0$) are still delta function like (see Fig. 3.17) in q -space. In order for the main peak to be observed, ω must be equal to θ_B , but the side peaks are observed at any ω . Those side peaks get slightly smeared due to integration over q_y .

For low angle x-ray scattering (LAXS), it is convenient to linearize the above equations in terms of θ and ω . In the small angle approximation, $\sin \phi \approx Z/(2S\theta)$ and $\cos \phi \approx X/(2S\theta)$, and

$$\begin{aligned} q_x &\approx \frac{4\pi\theta \cos \phi}{\lambda} \approx kX/S \\ q_y &\approx q_z \omega - \frac{4\pi\theta^2}{\lambda} \approx q_z \omega - \frac{\lambda q_z^2}{4\pi} \\ q_z &\approx \frac{4\pi\theta \sin \phi}{\lambda} \approx kZ/S, \end{aligned} \quad (3.16)$$

with $k = 2\pi/\lambda$. For wide angle X-ray scattering, the exact relations given by Eq. (3.14) are necessary. Especially in the transmission experiment, where ω is large, an observed X-ray pattern appears nontrivial and becomes almost impossible to analyze without the use of Eq. (3.14). The transmission experiment is discussed in Sec.3.7.

3.3.3 Lorentz Correction

Our sample has in-plane rotational symmetry about the z -axis. Ignoring mosaic spread to which we will come back later, this means that the sample consists of many domains with differing ripple directions, all domains being parallel to the substrate. In sample q -space, ripple ($h, k \neq 0$) side peaks are represented as rings centered at the meridian, or q_z -axis, while ($h, k = 0$) main peaks are still points on the meridian (see Fig. 3.17). Then, for an arbitrary incident angle ω , ($h, 0$) peaks are not observed while side peaks are observed for a range of ω as will now be explained.

In order to capture all (h, k) peaks in one X-ray exposure, the sample was continuously rotated over a range of $\omega, \Delta\omega$, about the x -axis. As a result of this rotation, the ($h, 0$) main peaks become arcs that subtend an angle $\Delta\omega$, as shown in Fig. 3.18, with its length equal to $\Delta\omega q_{h0}$. The detector records the intersections of these arcs

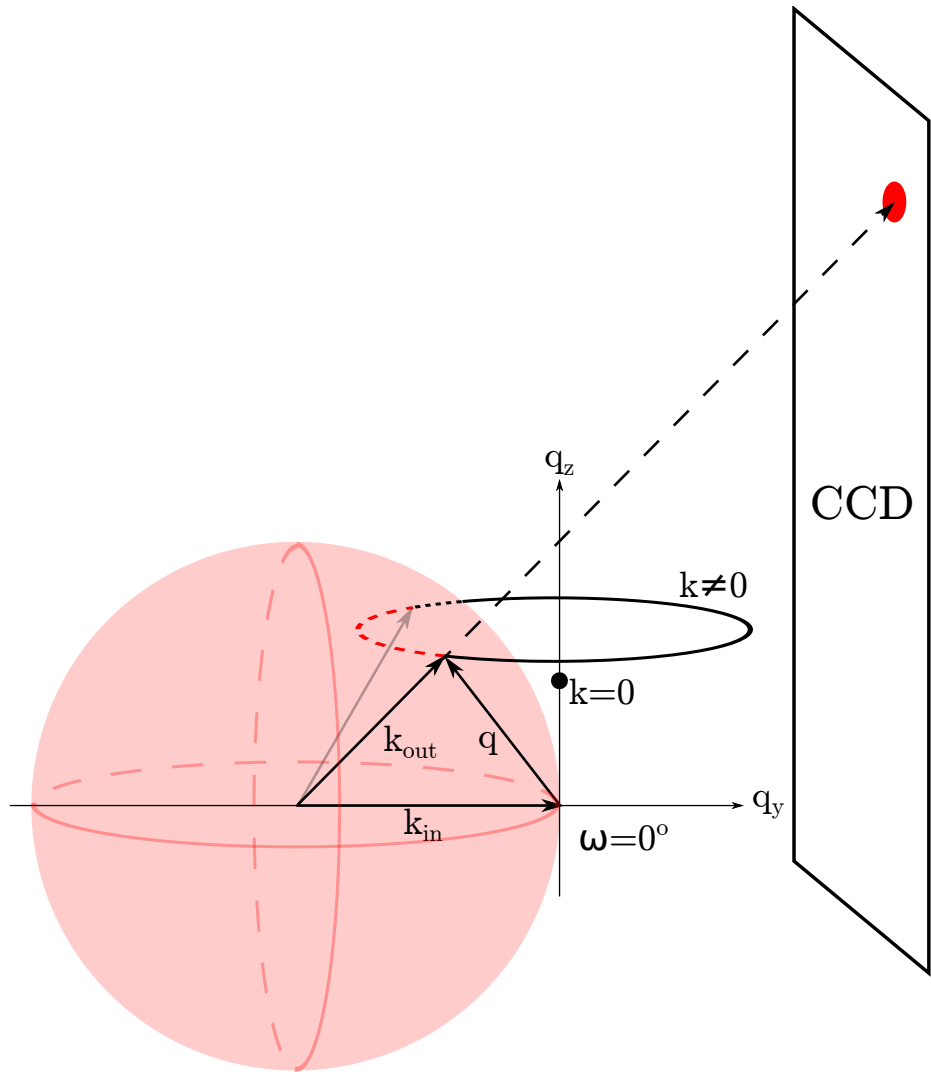


Figure 3.17: Ewald sphere construction for the ripple phase diffraction in the low angle regime. A ripple $k = 0$ peak is the solid, black circle on the q_z -axis. A ripple $k \neq 0$ ring is the black ring centered about the q_z -axis. The portion of the ring that is inside the Ewald sphere is shown as a red dashed line and the portion of the ring that is outside but behind the Ewald sphere is shown as a black dotted line. The magnitude of the total scattering angle is exaggerated. With a wavelength of 1.175 \AA , the magnitude $|k_{in}| = 5.35 \text{ \AA}^{-1}$. For a $h = 5$ peak, $q_{50}^z = 0.54 \text{ \AA}^{-1}$, one tenth of k_{in} .

with the Ewald sphere, so the intrinsic scattering intensity of the $(h, k = 0)$ reflections is the product of the observed intensity, I_{hk}^{obs} with the arc length, that is,

$$I_{h0} = \Delta\omega q_{h0}^z I_{h0}^{\text{obs}}. \quad (3.17)$$

This is the usual Lorentz correction for lamellar orders.

Now, we consider relative intensity of side peaks for a given order h . As described earlier, $(h, k \neq 0)$ side peaks are represented as rings whose radius is q_{hk}^r in the sample q -space. Because only the domains with the right ripple direction can satisfy the Bragg's condition at a given fixed angle ω , the intrinsic scattering intensity in this ring is reduced by a factor of $2\pi q_k^r$ compared to the $(h, 0)$ reflections. This reduction of intensity can be nicely visualized by the Ewald sphere construction shown in Fig. 3.17, which shows that the entire rings are not intersected by the Ewald sphere at a fixed angle. Then, the intrinsic scattering intensity in a ring is

$$I_{hk \neq 0} \propto 2\pi q_{hk}^r I_{hk}^{\text{obs}}. \quad (3.18)$$

During an X-ray exposure, the sample q -space rotates and the rings are intersected by the Ewald sphere at all our experimental incident angles ω . However, as Fig. 3.19 shows, only small parts of the rings are actually intersected with the Ewald sphere. To obtain the full expression for $(h, k \neq 0)$ reflections, we now turn to a more rigorous calculation.

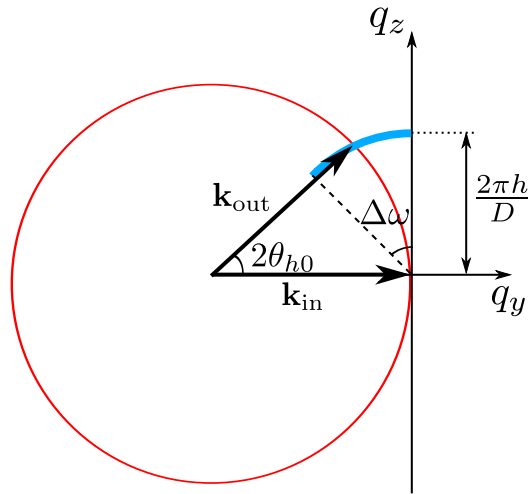


Figure 3.18: Side view of an arc of $k = 0$ peak shown as a thick blue line.

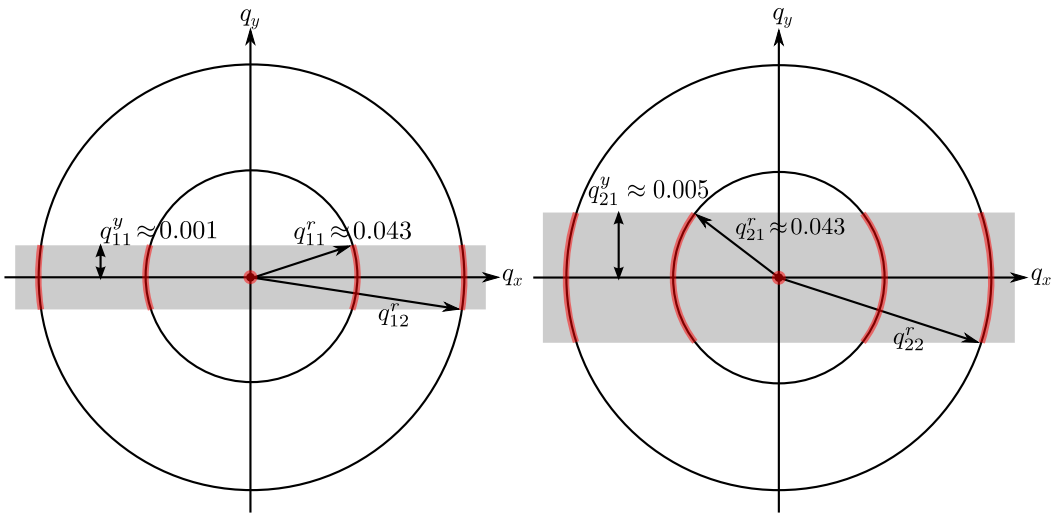


Figure 3.19: q -space representations of Bragg peaks and Bragg rings for $h = 1$ and 2 and $k = 0, 1$, and 2 in q_{hk}^z planes. The intersection between the Ewald sphere and a Bragg peak/ring is indicated in red. The observed intensity for the $k \neq 0$ orders is proportional to the fraction of the length of red arcs in the circumference. This fraction is equal to one for $k = 0$ reflections. Because the reflections are not in the same q_z plane, the range of q_y integration indicated by the height of the gray rectangle is different for different h orders. For $\gamma \neq 90^\circ$, the range of q_y integration is slightly different for different k reflections with the same h . The values shown are for $D = 58$ Å, $\lambda_r = 145$ Å, $\gamma = 90^\circ$, and $\lambda = 1.175$ Å. The magnitude of curvature of arcs is exaggerated.

Mathematically, the rotation is equivalent to an integration over ω . In low angle X-ray scattering, q_z is nearly constant at a given pixel as ω is changed, which can be seen from Eq. (3.16). As Eq. (3.16) shows, ω dependence appears only through q_y , so rotating the sample is realized by integrating over q_y ; formally, we write $d\omega = dq_y/q_z$. To derive the integration limits on q_y , let us consider two cases: (1) When $\omega \leq 0$, the incoming X-ray beam is blocked by the back of the substrate. This sets the lower limit of ω to 0. Plugging $\omega = 0$ in Eq. 3.16), we find the lower limit of the q_y integration to be $-\lambda q_z^2/(4\pi)$. (2) When $\omega \geq 2\theta$, the substrate blocks the outgoing X-ray, so the maximum $\omega = 2\theta$. Within the small angle approximation, $q_z \approx 4\pi\theta/\lambda$. Then, the maximum ω can be expressed as $\lambda q_z/(2\pi)$. Plugging this expression for ω in Eq. (3.16), we find the upper limit of the q_y integration to be $\lambda q_z^2/(4\pi)$. Also integrating over the detector pixels X and Z to obtain integrated intensity, we write the observed intensity as

$$\begin{aligned} I_{hk}^{\text{obs}} &\propto \int dX \int dZ \int d\omega I_{hk} \\ &\propto \int dq_x \int dq_z \int_{-\frac{\lambda q_z^2}{4\pi}}^{\frac{\lambda q_z^2}{4\pi}} \frac{dq_y}{q_z} I_{hk}(\mathbf{q}), \end{aligned} \quad (3.19)$$

where $1/q_z$ factor in q_y integration is the usual Lorentz polarization factor in the small angle approximation.

For a crystalline sample with in-plane rotational symmetry, the structure factor of a ripple Bragg peak is

$$S_{hk}(\mathbf{q}) = S_{hk}(q_r, q_z) = \frac{1}{2\pi q_r} \delta(q_r - q_{hk}^r) \delta(q_z - q_{hk}^z), \quad (3.20)$$

where $q_{hk}^r = 2\pi|k|/\lambda_r$. Thus, the scattering pattern in the ripple phase is a collection of Bragg rings for $k \neq 0$ centered at the meridian and the Bragg peaks for $k = 0$ located along the meridian. The scattering intensity is $I(\mathbf{q}) = |F(\mathbf{q})|^2 S(\mathbf{q})$, where $F(\mathbf{q})$ is the form factor. After the q_z integration, the observed, integrated intensity of (h, k) peak is proportional to

$$I_{hk}^{\text{obs}} \propto \frac{|F_{hk}|^2}{q_{hk}^z} \int dq_x \int_{-q_{hk}^{y0}}^{q_{hk}^{y0}} dq_y \frac{\delta(q_r - q_{hk}^r)}{2\pi q_r}, \quad (3.21)$$

where $q_{hk}^{y0} = \lambda(q_{hk}^z)^2/(4\pi)$. For side peaks ($k \neq 0$), we have

$$\begin{aligned} \int dq_x \int_{-q_{hk}^{y0}}^{q_{hk}^{y0}} dq_y \frac{\delta(q_r - q_{hk}^r)}{2\pi q_r} &\approx \int_{-q_{hk}^{y0}/q_{hk}^r}^{q_{hk}^{y0}/q_{hk}^r} d\phi \int dq_r q_r \frac{\delta(q_r - q_{hk}^r)}{2\pi q_r} \\ &= \frac{q_{hk}^{y0}}{\pi q_{hk}^r}. \end{aligned} \quad (3.22)$$

For main peaks ($k = 0$), we have

$$\begin{aligned} \int dq_x \int_{-q_{hk}^{y0}}^{q_{hk}^{y0}} dq_y \frac{\delta(q_r - q_{hk}^r)}{2\pi q_r} &= \int_0^{2\pi} d\phi \int dq_r q_r \frac{\delta(q_r - q_{hk}^r)}{2\pi q_r} \\ &= 1 \end{aligned} \quad (3.23)$$

Using Eq. (3.21 – 3.23), we write the observed integrated intensity as

$$I_{h0}^{\text{obs}} \propto \frac{|F_{h0}|^2}{q_{h0}^z} \quad (3.24)$$

$$I_{hk}^{\text{obs}} \propto \frac{|F_{hk}|^2}{q_{hk}^z} \frac{q_{hk}^{y0}}{\pi q_{hk}^r} = |F_{hk}|^2 \frac{\lambda q_{hk}^z}{2\pi} \frac{1}{2\pi q_{hk}^r} = |F_{hk}|^2 \frac{2\theta_{hk}}{2\pi q_{hk}^r}, \quad (3.25)$$

where $2\theta_{hk} = \lambda q_{hk}^z/(2\pi)$ is the incident angle at which the outgoing X-ray for the peak (h, k) is blocked by the substrate. Eq. (3.24) and (3.25) relate the form factor calculated from a model to the experimentally observed intensity, and are partially equivalent to Eq. (3.17) and (3.18).

In non-linear least squares fitting procedure, we fitted the observed integrated intensity to the calculated intensity from a bilayer model using these Lorentz corrections. This is because we can determine experimental uncertainties on observed intensity rather than the Lorentz-corrected form factors. We avoid propagating the uncertainties by fitting a model to observed intensity.

3.3.4 Absorption Correction for LAXS

In this section, we derive the absorption correction for an oriented sample. The calculation involves an explicit integration over the incident angle, ω , which is necessitated by the sample rotation during an X-ray exposure. The procedure is to write down an absorption factor, $A(\omega, \theta)$, for a given scattering angle at a given incident angle,

and then integrate over ω . We ignore q_x dependence because the X-ray path inside the sample is nearly within the y - z plane for low angle scattering. The correction for wide angle scattering is described in a later section.

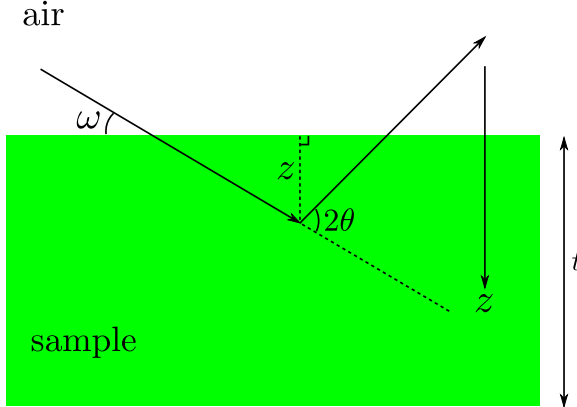


Figure 3.20: The path of X-rays within the sample. The incident angle is ω and the total scattering angle is 2θ . An X-ray with a penetration depth of z is shown. The total thickness of the sample is t . Refraction correction is smaller than what? for $\theta > 0.5^\circ$ ($h = 1$).

Assume that all the X-rays enter the sample from the top surface. The total scattering angle is given by 2θ (see Fig. 3.20). Let the z -axis point downward. At the top surface (air-sample interface), $z = 0$. For X-rays that travel to z and then scatter, the total path length within the sample is

$$L(z, \omega, \theta) = \frac{z}{\sin \omega} + \frac{z}{\sin(2\theta - \omega)} = z g(\omega, \theta), \quad (3.26)$$

where $g(\omega, \theta) = (\sin \omega)^{-1} + (\sin(2\theta - \omega))^{-1}$. For each ray, the intensity is attenuated by the sample absorption. If non-attenuated intensity is equal to I_0 , then the attenuated intensity is

$$I(z, \omega, \theta) = I_0 \exp\left(-\frac{L}{\mu}\right), \quad (3.27)$$

where μ is the absorption length of an X-ray. μ is about 2.6 mm for 10.5 keV for both water and lipids in all phases [103]. The observed intensity of scattering from a sample fixed at an angle ω is equal to the integration of Eq. (3.27) over the total

thickness of the sample and given by

$$\begin{aligned} I(\omega, \theta) &= \int_0^t dz I(z, \omega, \theta) = I_0 \int_0^t dz \exp\left(-\frac{g(\omega, \theta)}{\mu} z\right) \\ &= I_0 \mu \frac{1 - \exp\left(-\frac{t}{\mu} g(\omega, \theta)\right)}{g(\omega, \theta)}. \end{aligned} \quad (3.28)$$

Defining the absorption factor at a fixed angle to be $A(\omega, \theta)$, the observed intensity can also be written as

$$I(\omega, \theta) = A(\omega, \theta) t I_0, \quad (3.29)$$

where $t I_0$ is the intensity we would observe for non-absorbed X-rays. Equating Eq. (3.28) and (3.29), we get

$$A(\omega, \theta) = \frac{\mu}{t} \frac{1 - \exp\left(-\frac{t}{\mu} g(\omega, \theta)\right)}{g(\omega, \theta)}. \quad (3.30)$$

If μ is taken to infinity (no absorption), $A(\omega, \theta)$ goes to 1 as expected. The absorption factor A_{h0} for the $k = 0$ peaks is given by $A(\omega = \theta = \theta_B)$, plotted in Fig. 3.21. As shown, this factor is about 20 % for $h = 1$ peak relative to $h = 4$, so it is not negligible.

For $k \neq 0$ side peaks, an integration over the incident angle ω is necessary because these peaks are observable at all our experimental incident angles as described in section 3.3.3. The observed intensity for side peaks from a rotating sample is simply

$$I_{\text{obs}}(\theta) = \int_0^{2\theta} d\omega I(\omega, \theta). \quad (3.31)$$

The upper integration limit is equal to 2θ because the substrate completely blocks the scattered X-rays above this angle as discussed in section 3.3.3. Eq. (3.30), which is essentially the integrand in Eq. (3.31), is plotted in Fig. 3.22. It is maximum when $\omega = \theta$, meaning that the path length is shortest at the Bragg condition. The non-attenuated observed intensity is equal to $2\theta t I_0$. We, then, define the absorption factor $A(\theta)$ to be the ratio of the total observed intensity to the total non-attenuated intensity,

$$A(\theta) \equiv \frac{I_{\text{obs}}(\theta)}{2\theta t I_0}. \quad (3.32)$$

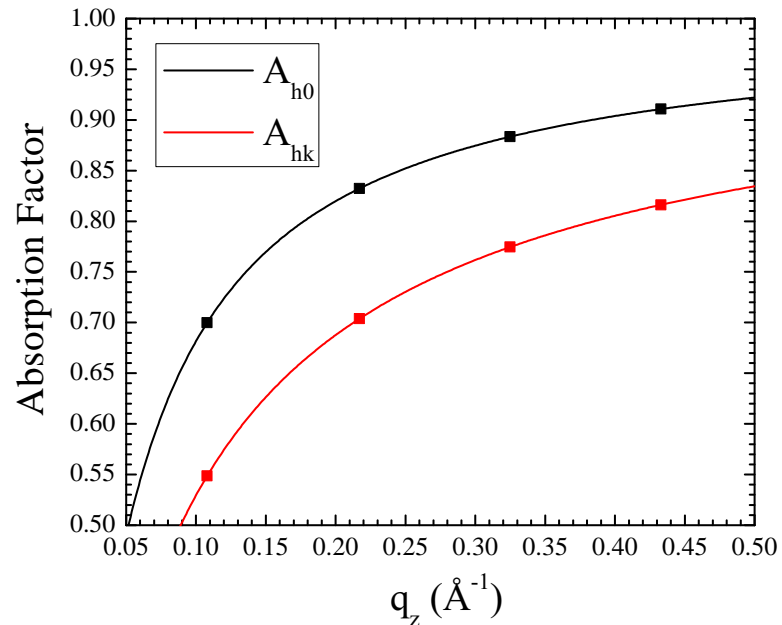


Figure 3.21: Absorption factors as a function of $q_z \approx 4\pi\theta/\lambda$. Values at $q_z = 2\pi h/D$ corresponding to $D = 57.8 \text{ \AA}$ are shown as squares. $\mu = 2600 \mu\text{m}$, $t = 10 \mu\text{m}$, and $\lambda = 1.175 \text{ \AA}$.

Using Eq. (3.30) and (3.31) in (3.32), we arrive at the final absorption factor

$$A(\theta) = \frac{1}{2\theta} \int_0^{2\theta} d\omega A(\omega, \theta) = \frac{\mu}{2\theta t} \int_0^{2\theta} d\omega \frac{1 - \exp\left(-\frac{t}{\mu}g(\omega, \theta)\right)}{g(\omega, \theta)}. \quad (3.33)$$

$A_{hk} = A(\theta)$ is plotted in Fig. 3.21. The absorption correction $A_c(\theta)$ is the inverse of Eq. (3.33).

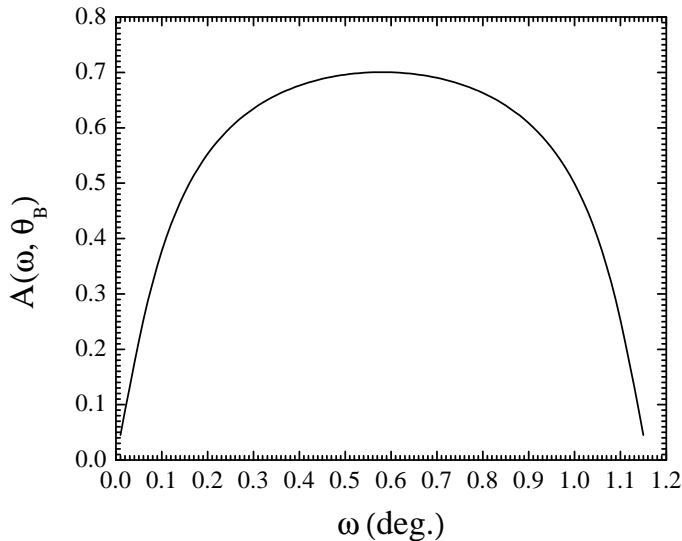


Figure 3.22: Eq. (3.30) plotted as a function of ω for $\theta = \theta_B = 0.58^\circ$, corresponding to a Bragg angle for $D = 57.8 \text{ \AA}$.

3.3.5 Correction due to mosaic spread

Integrated intensity needs to be corrected for mosaic spread. During an X-ray exposure, the sample was continuously rotated. Due to this rotation, each pixel integrates intensity over a range of incident angles ω . As described in appendix A.2.2, a mosaic spread distribution can be probed by changing ω , so rotating the sample is essentially equivalent to integrating a mosaic spread distribution. Because the range of the distribution probed is approximately given by $\omega = [0, 2\theta_{hk}]$ where θ_{hk} is the Bragg angle for a (h, k) reflection, this range is larger for higher h orders. This effect is illustrated in Fig. 3.23.

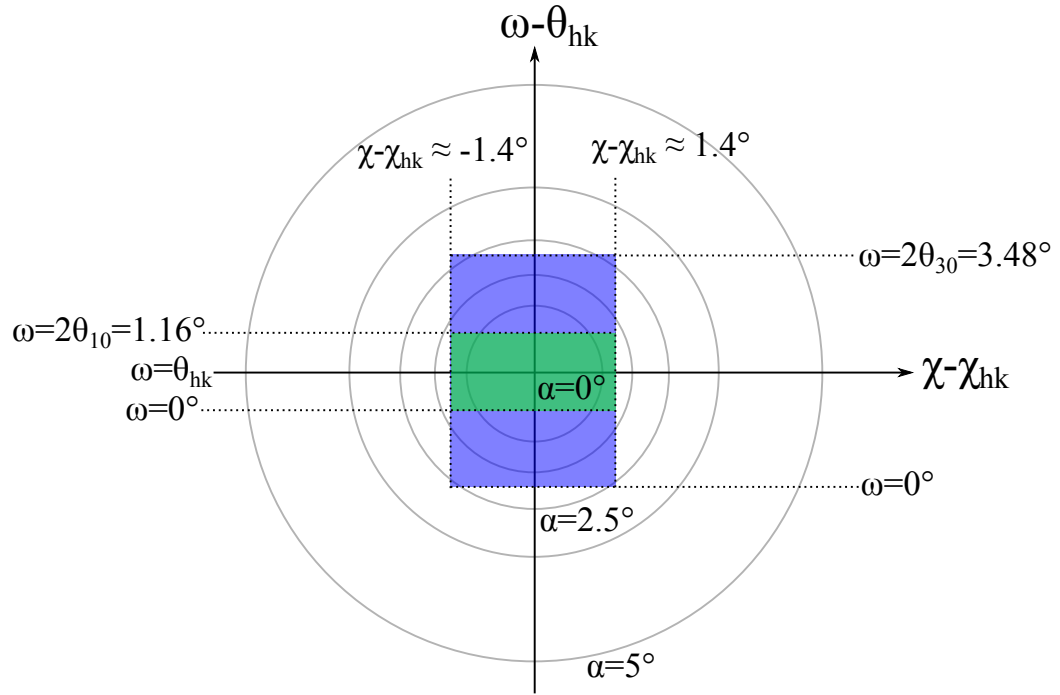


Figure 3.23: Contours of a mosaic spread distribution projected on the $\omega\chi$ -plane, where $\chi - \chi_{hk}$ is an angle measured from a (h, k) reflection on the detector ($\chi = \pi/2 - \phi$ in Fig. 3.16) and θ_{hk} is the Bragg angle for a (h, k) reflection. The distribution function takes a form of Lorentzian centered at $\alpha = 0$. Domains with $\alpha = 0$ are probed at $\omega = \theta_{hk}$ and $\chi = \chi_{hk}$. Integrated intensity of $(1, k)$ reflection arises from domains in the green shaded area while that of $(3, k)$ reflection is from the blue shaded area, which is three times larger.

We limit $\chi - \chi_{hk}$ to go from -1.4° to 1.4° . The effect of cutoff on $\chi - \chi_{hk}$ is not very important because most of observed intensity was included in integration boxes. In contrast, cutoff on ω due to substrate blocking the scattering is important, especially for lower h orders.

We take the distribution to be Lorentzian, which has been experimentally observed (REF, Dr. Nagle),

$$P(\alpha) = \frac{N}{\alpha^2 + \alpha_M^2}, \quad (3.34)$$

where N is a normalization constant and α_M is the HWHM of the distribution. N satisfies

$$N \approx \frac{1}{2\pi} \left(\int_0^{\frac{\pi}{2}} d\alpha \frac{\alpha}{\alpha^2 + \alpha_M^2} \right)^{-1}. \quad (3.35)$$

We then consider a two dimensional contour map on a $\omega\chi$ plane. Intensity for a reflection with a Bragg angle of θ_B is given by

$$I = \int_{-\theta_B}^{\theta_B} d\omega \int_{-\chi_0}^{\chi_0} d\chi P(\alpha) = \int_{-\theta_B}^{\theta_B} d\omega \int_{-\chi_0}^{\chi_0} d\chi \frac{N}{\omega^2 + \chi^2 + \alpha_M^2} \quad (3.36)$$

After the integration over χ , Eq. (3.36) is

$$I = 4N \int_0^{\theta_B} \frac{d\omega}{\sqrt{\omega^2 + \alpha_M^2}} \arctan\left(\frac{\chi_0}{\sqrt{\omega^2 + \alpha_M^2}}\right). \quad (3.37)$$

Eq. (3.37) is plotted in Fig. 3.24.

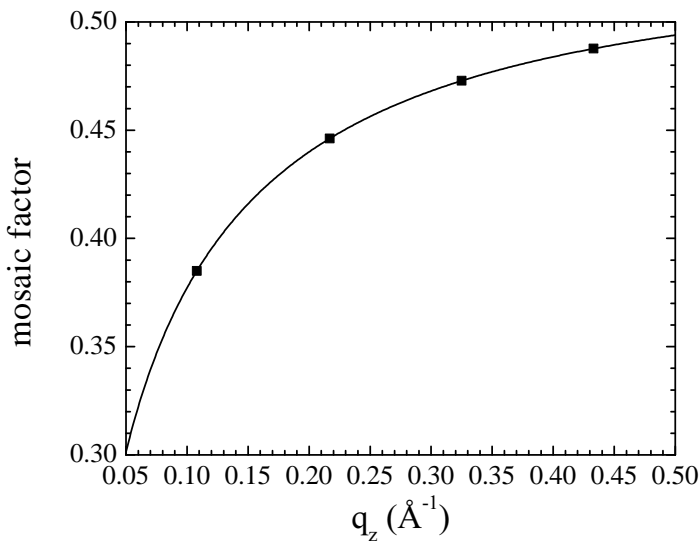


Figure 3.24: Mosaic factor given by Eq. (3.37) as a function of $q_z \approx 4\pi\theta/\lambda$. Values at $q_z = 2\pi h/D$ corresponding to $D = 57.8 \text{ \AA}$ are shown as squares. $\alpha_M = 0.05^\circ$ and $\chi_0 = 1.4^\circ$. Eq. (3.37) reaches ~ 0.54 at $\theta_B = \pi/2$ and $\chi_0 = 1.4^\circ$ and reaches ~ 1 at $\theta_B = \pi/2$ and $\chi_0 = 1.4^\circ$ as expected.

h	k	Absorption	Mosaicity	Lorentz
1	-1	1.96	2.63	14.16
1	0	1.41	2.56	0.11
1	1	1.79	2.56	12.67
1	2	1.74	2.53	25.00
1	3	1.69	2.50	34.12
2	-2	1.45	2.27	14.19
2	-1	1.43	2.27	6.97
2	0	1.19	2.22	0.22
2	1	1.41	2.22	6.45
2	2	1.39	2.22	12.51
2	3	1.39	2.22	18.29
2	4	1.39	2.22	23.92
2	5	1.39	2.17	28.76
2	6	1.37	2.17	33.73
3	-2	1.30	2.13	9.31
3	-1	1.30	2.13	4.50
3	0	1.14	2.13	0.33
3	1	1.28	2.08	4.35
3	2	1.28	2.08	8.52
3	3	1.28	2.08	12.56
3	4	1.27	2.08	16.42
3	5	1.27	2.08	20.18
3	6	1.27	2.08	23.81
4	-3	1.23	2.04	10.54
4	-2	1.22	2.04	6.94
4	-1	1.22	2.04	3.40
4	0	1.10	2.04	0.44
4	1	1.22	2.04	3.28
4	2	1.22	2.04	6.39
4	3	1.21	2.04	9.50
4	4	1.20	2.04	12.60
4	5	1.20	2.04	15.49
4	6	1.20	2.04	18.35

Table 3.5: Correction for the ripple LAXS peaks

h	k	Absorption	Mosaicity	Lorentz
5	-3	1.19	2.00	8.44
5	-2	1.19	2.00	5.49
5	-1	1.19	2.00	2.64
5	0	1.08	2.00	0.54
5	1	1.19	2.00	2.43
6	-4	1.16	2.00	9.36
6	-3	1.16	2.00	6.92
6	-2	1.16	2.00	4.47
6	-1	1.16	2.00	2.23
6	0	1.06	2.00	0.65
6	1	1.16	2.00	2.24
6	2	1.16	2.00	4.40
6	3	1.15	2.00	6.38
6	4	1.15	2.00	8.40
7	-4	1.14	1.96	7.94
7	-3	1.14	1.96	5.86
7	-2	1.14	1.96	3.82
7	-1	1.14	1.96	1.86
7	0	1.05	1.96	0.76
8	0	1.04	1.96	0.87
9	-5	1.11	1.96	7.60
9	-4	1.11	1.96	6.07
9	-3	1.11	1.96	4.50
9	-2	1.11	1.96	2.98
9	-1	1.11	1.96	1.50
9	0	1.04	1.96	0.98

Table 3.6: Correction for the ripple LAXS peaks

3.4 LAXS: model

3.4.1 Contour Part of the Form Factor

As in Ref. [88], we take the ripple profile to have a sawtooth profile. Its amplitude is A and the projection of the major arm on the ripple direction is x_M as shown in Fig. 3.1. Then, we write the ripple profile as

$$u(x) = \begin{cases} -\frac{A}{\lambda_r - x_0} \left(x + \frac{\lambda_r}{2} \right) & \text{for } -\frac{\lambda_r}{2} \leq x < -\frac{x_0}{2}, \\ \frac{A}{x_0} x & \text{for } -\frac{x_0}{2} \leq x \leq \frac{x_0}{2}, \\ -\frac{A}{\lambda_r - x_0} \left(x - \frac{\lambda_r}{2} \right) & \text{for } \frac{x_0}{2} < x \leq \frac{\lambda_r}{2}. \end{cases} \quad (3.38)$$

The ripple profile has inversion symmetry, so that the resulting form factor is real. A and x_M are fitting parameters that depend on the integrated intensity of each peak while D , λ_r , and γ are determined from measuring the positions of the Bragg peaks.

In order to allow the electron density along the ripple direction to modulate, we include two additional parameters, one to allow for the electron density across the minor side to be different by a ratio f_1 from the electron density across the major side and a second parameter f_2 , which is multiplied by δ functions $\delta(x \pm x_M/2)$ to allow for a different electron density near the kink between the major and the minor sides. The full expression for the contour part of the form factor $F_C(\mathbf{q})$, which is a two dimensional Fourier transform of Eq. 3.38, is found in Appendix A.4.

3.4.2 Transbilayer Part of the Form Factor

The hybrid model developed by Wiener *et al.* [104] has been successful in modeling the electron density profile in the gel phase. The hybrid model with two Gaussian functions each representing the headgroup and terminal methyl group was employed by Sun et al. [88] for phasing the ripple phase X-ray data published by Wack and Webb [8]. We employed the same model for fitting our data since it was shown to be very successful in fitting the ripple X-ray data. Because our data contain more data points at larger q , we also used a model that has three Gaussian functions, two of which represent the headgroup and the other one represents the terminal methyl group.

In the hybrid model, the terminal methyl region of the bilayer is represented as a Gaussian function [104]. The headgroups are represented by one and two Gaussian

functions in 1G and 2G hybrid model, respectively. The methylene and water regions are each treated as a constant. The gap between the two constants is represented by a sine function. Then, for half of the bilayer, $0 \leq z \leq D/2$, the electron density has the form,

$$\rho(z) = \rho_G(z) + \rho_S(z) + \rho_B(z), \quad (3.39)$$

where the Gaussian part is given by

$$\rho_G(z) = \sum_{i=1}^{1 \text{ or } 2} \rho_{H_i} e^{-(z-Z_{H_i})^2/(2\sigma_{H_i}^2)} + \rho_M e^{-z^2/(2\sigma_M^2)}, \quad (3.40)$$

the strip part is given by

$$\rho_S(z) = \begin{cases} \rho_{CH_2} & \text{for } 0 \leq z < Z_{CH_2}, \\ \rho_W & \text{for } Z_W \leq z \leq D/2, \end{cases} \quad (3.41)$$

and the bridging part is given by

$$\rho_B(z) = \frac{\rho_W - \rho_{CH_2}}{2} \cos\left[\frac{-\pi}{\Delta Z_H}(z - Z_W)\right] + \frac{\rho_W + \rho_{CH_2}}{2} \quad \text{for } Z_{CH_2} < z < Z_W. \quad (3.42)$$

with $\Delta Z_H = Z_W - Z_{CH_2}$. Here, we assume $Z_{H2} > Z_{H1}$. Table 3.6 shows some of the definitions.

	1G	2G
Z_{CH_2}	$Z_{H1} - \sigma_{H1}$	$Z_{H1} - \sigma_{H1}$
Z_W	$Z_{H1} + \sigma_{H1}$	$Z_{H2} + \sigma_{H2}$

Table 3.7: Definitions of Z_{CH_2} and Z_W

The transbilayer profile along $x = -z \tan \psi$ can be obtained by rotating the coordinates x and z by ψ in the clockwise direction and reexpressing $\rho(z)$ in terms of the rotated coordinates. This leads to replacing x with $x' = x \cos \psi + z \sin \psi$ and z with $z' = -x \sin \psi + z \cos \psi$. Then, the rotated transbilayer profile is

$$\rho(x, z) = \delta(x + z \tan \psi)[\rho_G(z') + \rho_S(z') + \rho_B(z')]. \quad (3.43)$$

Taking the two dimensional Fourier transform of Eq. (3.43) leads to the transbi-

layer part of the form factor,

$$F_T = \int_{-\frac{D}{2}}^{\frac{D}{2}} \int_{-\frac{\lambda_r}{2}}^{\frac{\lambda_r}{2}} [\rho(x, z) - \rho_W] e^{i(q_x x + q_z z)} dx dz \quad (3.44)$$

$$= F_G + F_S + F_B. \quad (3.45)$$

The form factor is calculated in the minus fluid convention, where the bilayer electron density is measured with respect to the electron density of the surrounding solvent. The expression for F_T is rather messy, so the derivation and full expression are in Appendix A.6. Here, we note that the fitting parameters in this model are Z_{Hi} , σ_{Hi} , and ρ_{Hi} for each of the two headgroup Gaussian functions, σ_M and ρ_M for the terminal methyl Gaussian, ψ for the lipid tilt, and an overall scaling factor. $rhochtwo$ is absorbed into the overall scaling factor. The contour part of the form factor has four more parameters (A , x_M , f_1 , and f_2). In total, the modified 2G hybrid model implements 13 structural parameters. Generally, we made Z_{Hi} , ψ , A , x_M , f_1 , and f_2 free parameters to guide the nonlinear least square procedure to find a reasonable fit while the rest of the parameters was fixed to the corresponding gel phase values reported in Ref. [104]. The best estimate of the gel phase structure was reported in Ref. [53]. Precise values for the fixed parameters were not important because we set those fixed parameters free to find the best fit once a reasonable fit was obtained.

3.5 LAXS: results

We measured scattering on oriented samples in almost identical conditions as the best unoriented sample of Wack and Webb. As discussed earlier, these two types of samples have different Lorentz corrections, so this allowed us to check our data obtained on oriented samples against an unoriented sample. As Table 3.9 shows, agreement between our oriented data and the unoriented data was good, but form factor from our oriented sample was in many cases slightly larger than that from the unoriented sample. We attribute this discrepancy to the way intensity was extracted. In X-ray data from an oriented sample, each peak was well separated, so integrating a peak intensity was trivial. In contrast, some reflections in unoriented data were overlapping with each other (three pairs of overlapping peaks are highlighted in Table 3.9), making separation of intensity difficult. If the $(1, 0)$ peak in the unoriented data had been overestimated, that would account for the observed discrepancy. Indeed, the microdensitometer trace in [8] suggests that the $(1, 0)$ and $(1, -1)$ reflections could have similar intensity as we observed in our oriented sample. Table 3.7 and 3.8 summarize observed intensity from our data shown in Fig. 3.12. q_z values for observed peaks were corrected for index of refraction (Appendix A.7).

Table 3.10 summarizes representative fits obtained by a nonlinear least square fitting procedure. Fit1 and Fit2 were fits using the 1G hybrid model, and Fit3-Fit7 were with the 2G hybrid model. As Table 3.10 shows, Fit5 produced the smallest χ^2 value. This fit was arrived by first getting Fit3, then freeing the widths of the three Gaussian (Fit4), and finally freeing the amplitudes of the Gaussian. We also tried a different route; from Fit3, we freed up the amplitudes of the Gaussian (Fit6) and then set the widths of the Gaussian free, arriving at Fit7. While the χ^2 values of fit5 and fit7 were not very different, they resulted in $h = 6$ orders having the opposite phases as shown in Table A.2. We consistently obtained model form factors that were too small compared to the experimental ones for $(h, k) = (3, 0)$, $(6, k)$, and $(9, 0)$. This can be understood by inspecting the contour part of the form factor $F_C(\mathbf{q})$ given by Eq. A.29. The model form factor $F(\mathbf{q})$ is a product of $F_C(\mathbf{q})$ and $F_T(\mathbf{q})$. Figure 3.25 plots a two dimensional map of $|F_C(\mathbf{q})|$ for $\lambda_r = 145 \text{ \AA}$, $A = 21.5 \text{ \AA}$, $x_M = 103 \text{ \AA}$, $f_1 = 0.5$, and $f_2 = -3$, values of which are taken from Fit5. It shows that $|F_C(\mathbf{q})|$ takes very small values at $(h, k) = (3, 0)$, $(6, 0)-(6, 4)$, and $(9, 0)$, leading to small values of the model $F(\mathbf{q})$ for those peaks as well. These weak spots in $|F_C(\mathbf{q})|$

h	k	q_z (Å $^{-1}$)	q_r (Å $^{-1}$)	box size (pixels)	I_{hk}^{obs}	σ_I	correction	$ F_{hk} $	σ_F
1	-1	0.102	-0.043	10 × 7	726.0	63.0	73.086	86.3	3.7
1	0	0.109	0.000	10 × 7	180818.0	1759.0	0.394	100.0	0.5
1	1	0.114	0.043	10 × 7	228.0	28.0	58.027	43.1	2.6
1	2				0.0	1.0	110.055	0.0	3.9
1	3	0.128	0.130	10 × 7	3.8	0.2	144.592	8.8	0.2
2	-2	0.206	-0.087	10 × 7	49.2	3.5	46.738	18.0	0.6
2	-1	0.212	-0.044	10 × 7	1818.0	20.0	22.641	76.0	0.4
2	0	0.218	0.000	10 × 7	10200.0	174.0	0.577	28.7	0.2
2	1	0.224	0.043	10 × 7	550.0	10.0	20.187	39.5	0.4
2	2	0.231	0.086	10 × 7	112.0	3.0	38.607	24.6	0.3
2	3	0.237	0.129	10 × 7	27.0	0.2	56.444	14.6	0.1
2	4	0.243	0.173	10 × 7	8.2	0.4	73.827	9.2	0.2
2	5	0.250	0.214	10 × 7	2.6	0.7	86.837	5.6	0.7
2	6	0.256	0.257	10 × 7	1.2	0.2	100.446	4.1	0.3
3	-2	0.314	-0.087	15 × 7	305.0	15.0	25.723	33.2	0.8
3	-1	0.321	-0.043	15 × 7	1205.0	22.0	12.436	45.9	0.4
3	0	0.326	0.000	15 × 7	1566.0	110.0	0.788	13.2	0.5
3	1			15 × 7	0.0	31.0	11.586	0.0	7.1
3	2	0.339	0.086	15 × 7	32.4	1.6	22.766	10.2	0.2
3	3	0.345	0.129	15 × 7	39.1	0.9	33.555	13.6	0.2
3	4	0.352	0.172	15 × 7	27.7	0.7	43.295	13.0	0.2
3	5	0.358	0.215	15 × 7	12.2	0.3	53.212	9.6	0.1
3	6	0.364	0.258	15 × 7	3.5	0.5	62.802	5.6	0.4
4	-3	0.417	-0.131	20 × 8	142.0	8.0	26.557	23.0	0.6
4	-2	0.423	-0.087	20 × 8	755.4	19.0	17.265	42.8	0.5
4	-1	0.429	-0.043	20 × 8	429.6	34.0	8.454	22.6	0.9
4	0	0.435	0.000	20 × 8	1917.0	23.0	0.976	16.2	0.1
4	1	0.441	0.043	20 × 8	45.3	7.2	8.153	7.2	0.6
4	2	0.448	0.085	20 × 8	43.6	2.4	15.897	9.9	0.3
4	3			20 × 8	0.0	1.3	23.450	0.0	2.1
4	4	0.461	0.173	20 × 8	2.1	0.4	30.981	3.0	0.3
4	5	0.467	0.215	20 × 8	3.2	0.3	38.076	4.1	0.2
4	6	0.473	0.259	20 × 8	1.0	1.1	45.126	2.5	1.1

Table 3.8: Observed intensity for $h = 1$ to 4 at $D = 57.8$, $\lambda_r = 145$, and $\gamma = 98.2^\circ$.

h	k	q_z (Å $^{-1}$)	q_r (Å $^{-1}$)	box size (pixels)	I_{hk}^{obs}	σ_I	correction	$ F_{hk} $	σ_F
5	-3	0.525	-0.132	25 × 9	86.2	6.8	20.084	15.6	0.6
5	-2	0.532	-0.087	25 × 9	145.0	4.0	13.060	16.3	0.2
5	-1	0.538	-0.042	25 × 9	63.4	3.4	6.291	7.5	0.2
5	0	0.544	0.000	25 × 9	260.0	4.0	1.169	6.5	0.1
5	1	0.550	0.040	25 × 9	50.0	2.8	5.774	6.4	0.2
6	-4	0.628	-0.175	30 × 10	11.4	0.8	21.778	5.9	0.2
6	-3	0.635	-0.131	30 × 10	15.6	0.9	16.094	5.9	0.2
6	-2	0.641	-0.085	30 × 10	10.1	1.8	10.389	3.8	0.3
6	-1	0.647	0.043	30 × 10	16.3	3.0	5.193	3.4	0.3
6	0	0.653	0.000	30 × 10	60.2	4.7	1.389	3.4	0.1
6	1	0.659	0.044	30 × 10	20.4	1.5	5.217	3.9	0.1
6	2			30 × 10	0.0	0.6	10.208	0.0	0.9
6	3	0.672	0.128	30 × 10	5.9	0.3	14.657	3.5	0.1
6	4	0.679	0.170	30 × 10	4.2	0.3	19.309	3.4	0.1
7	-4	0.737	-0.174	35 × 10	40.0	1.1	17.682	10.0	0.1
7	-3	0.743	-0.130	35 × 10	36.0	1.8	13.060	8.1	0.2
7	-2	0.749	-0.085	35 × 10	15.0	7.3	8.512	4.2	0.9
7	-1	0.755	-0.042	35 × 10	22.0	2.3	4.145	3.6	0.2
7	0	0.760	0.000	35 × 10	36.0	1.8	1.569	2.8	0.1
8	0				0.0	3.0	1.773	0.0	0.9
9	-5	0.951	-0.215	35 × 10	16.0	3.0	16.549	6.1	0.5
9	-4	0.957	-0.173	35 × 10	16.9	3.0	13.233	5.6	0.5
9	-3			35 × 10	0.0	8.0	9.790	0.0	3.3
9	-2	0.969	-0.086	35 × 10	10.0	2.9	6.497	3.0	0.4
9	-1			35 × 10	0.0	6.0	3.263	0.0	1.7
9	0	0.981	0.000	35 × 10	17.0	10.0	2.000	2.2	0.6

Table 3.9: Observed intensity for $h = 5$ to 9 at $D = 57.8$, $\lambda_r = 145$, and $\gamma = 98.2^\circ$ (continued from Table 3.7).

h	k	q^* (Å $^{-1}$)	unoriented $ F_{hk} ^*$	oriented $ F_{hk} $	error
1	-1	0.111	60.8	86.3	3.7
1	0	0.108	100.0	100.0	0.5
1	1	0.123	26.9	43.1	2.6
1	2			0.0	3.9
1	3	0.185	7.6	8.8	0.2
2	-2	0.224	15.1	18.0	0.6
2	-1	0.215	71.2	76.0	0.4
2	0	0.217	39.7	28.7	0.2
2	1	0.228	33.9	39.5	0.4
2	2	0.246	22.7	24.6	0.3
2	3	0.271	14.2	14.6	0.1
2	4	0.301	7.8	9.2	0.2
2	5	0.329		5.6	0.7
2	6			4.1	0.3
3	-2	0.325	29.3	33.2	0.8
3	-1	0.322	44.2	45.9	0.4
3	0	0.325	12.0	13.2	0.5
3	1			0.0	7.1
3	2	0.350	10.5	10.2	0.2
3	3	0.370	14.9	13.6	0.2
3	4	0.394	10.0	13.0	0.2
3	5			9.6	0.1
3	6			5.6	0.4

Table 3.10: Comparison of form factor obtained in two different methods.
 *Unoriented data are from Wack and Webb [8].

can be moved by varying A and x_M . However, A and x_M are very sensitive to strong peaks that are on the white streak in Fig. 3.25: namely, $(h, k) = (1, 0), (1, -1), (2, 0), (2, -1), (3, -1), (3, -2)$, and so on. Then, for our data set, minima in the χ^2 space are normally found with values of A and x_M that result in $F_C(\mathbf{q})$ similar to the one shown in Fig. 3.25. This analysis suggests that to fit those underestimated orders better may require a different model for the contour part of the form factor rather than trying various models for the transbilayer part of the form factor $F_T(\mathbf{q})$. Since the sawtooth profile is a very reasonable assumption, an improvement should be made in modeling the kink regions. For example, introducing a short plateau parallel to the ripple x -axis instead of the sharp turn in the kink region of the current model would lead to a band of intensity along the q_z axis, which could bring about larger values of $|F_C(\mathbf{q})|$ at those underestimated peak positions. We did not consider improving our models because we were only interested in the predicted phases for calculating an electron density profile.

	Fit1	Fit2	Fit3	Fit4	Fit5	Fit6	Fit7
model	M1G	M1G	M2G	M2G	M2G	M2G	M2G
χ^2	11996	9664	19458	8827	8525	8905	8883
A	20.4	24.2	22.1	21.5	21.5	21.4	21.5
x_M	98.5	118.8	92.6	104.0	102.9	102.1	102.7
f_1	0.489	0.726	0.776	0.515	0.538	0.516	0.511
f_2	0*	-11.3	-6.06	-2.77	-2.81	-2.62	-2.63
ψ	15.2°	14.3°	10.5°	14.4°	14.4°	15.1°	14.8°
Z_{H1}	19.8	19.7	18.1	19.5	18.7	19.1	19.0
σ_{H1}	3.43*	3.43*	2.94*	3.06	2.51	2.94*	2.97
ρ_{H1}	10.77*	10.77*	9.91*	9.91*	7.03	8.38	8.45
Z_{H2}	NA	NA	20.0	20.4	22.4	23.2	23.0
σ_{H2}	NA	NA	1.47*	3.17	1.38	1.47*	1.72
ρ_{H2}	NA	NA	7.27*	7.27*	3.75	2.83	3.00
σ_M	1.67*	1.67*	1.83*	2.47	2.53	1.83*	1.87
ρ_M	9.23*	9.23*	10.9*	10.9*	5.15	6.87	6.97

Table 3.11: Model parameters. Fit1 and Fit2 were performed with the M1G model while Fit3 to 7 were with the M2G model.

*Parameters were fixed to the values shown.

Figure 3.26 plots a two dimensional electron density profile calculated using the phases obtained from Fit5 and our experimental form factors. The density profile shows the same sawtooth profile that has been observed by previous X-ray diffraction

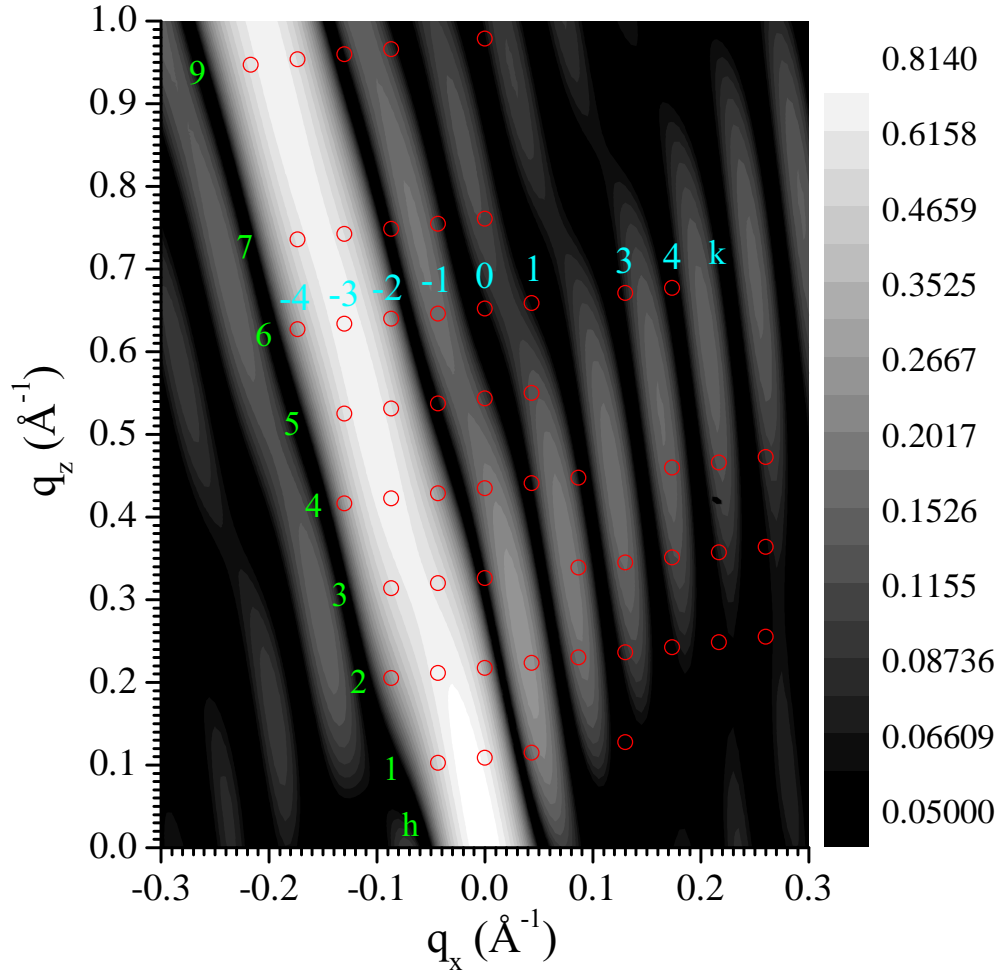


Figure 3.25: Two dimensional map of the contour part of the form factor $|F_C(\mathbf{q})|$ given by Eq. A.29. The color is in a log scale shown by the color bar. Red circles are the positions of the observed peaks. The actual experimental data (Fig. 3.12) had left-right symmetry because of in-plane powder of the sample. h and k indices are labeled for some of the peaks in green and cyan, respectively. The experimentally observed form factors are given by the product $|F_C(\mathbf{q})||F_T(\mathbf{q})|$.

studies as well [?, 88, 96], confirming the notion of height modulation in the ripple phase. Another distinct feature seen in Fig. 3.26 is the presence of the methyl trough in the major arm, manifested by a black band along the bilayer center extending from $x \approx -50 \text{ \AA}$ to 50 \AA . This feature was not observed in the minor arm. To obtain the thickness of the bilayer in the major arm, electron density profiles calculated using the phases from various fits are plotted in Fig. 3.27 along the slice shown by the straight dashed line in Fig. 3.26 (Slice A). Slice A is along the normal of the major arm and is centered in the middle of the hydrocarbon region. It indicates that the bilayer head-head spacing $D_{\text{HH}}^{\text{major}}$ is $40.0\text{--}42.0 \text{ \AA}$ in the major arm (see also Table 3.11). Electron density profiles are also plotted along Slice B in Fig. 3.28. Slice B is along the normal to the minor arm and is centered in the middle of the hydrocarbon region. It indicates that $D_{\text{HH}}^{\text{minor}}$ is $29.2\text{--}31.0 \text{ \AA}$ in the minor arm. Table 3.11 summarizes these results along with calculated tilt angles of the major and minor arms, α_M and α_m , respectively, where $\alpha_M = \arctan(A/x_M)$ and $\alpha_m = \arctan(A/x_m) = \arctan(A/(\lambda_r - x_M))$ (see Fig. 3.1). Table 3.10 and 3.11 imply that the amplitude and lengths of the sawtooth profile in Fit2 are quite different from other fits. However, as Fig. 3.29 shows, the calculated density profile is overall similar to the one obtained from Fit5 shown in Fig. 3.26. In fact, electron density profiles calculated using Fit1–7 all indicate that $\alpha_M \approx 12^\circ$ and $\alpha_m \approx 27^\circ$.

	Fit1	Fit2	Fit3	Fit4	Fit5	Fit6	Fit7	I	II	III
χ^2	11996	9664	19458	8827	8525	8905	8883		1364	8131
$D_{\text{HH}}^{\text{major}}$	42.0	41.0	40.0	40.6	40.6	41.8	41.8	38	38.0	41.8
$D_{\text{HH}}^{\text{minor}}$	30.8	31.0	29.2	29.2	29.2	31.0	31.0	31	28.6	30.6
α_M	11.7°	11.5°	13.4°	11.7°	11.8°	11.8°	11.8°	10.5°	11.5°	11.5°
α_m	23.7°	42.7°	22.9°	27.7°	27.1°	26.5°	26.9°	26.1°	28.1°	25.1°

Table 3.12: Ripple structural quantities.

I: Results from Sun *et al.*

II: Used only up to $(h, k) = (3, 4)$

III: Replaced lower order $|F(h, k)|$ with those from Wack and Webb, keeping the same relative error

As noted in a previous paragraph, fits to $(h, k) = (3, 0)$, $(6, 0)\text{--}(6, 4)$, and $(9, 0)$ were not great. We also noticed that the phase of $(1, 3)$ was unstable. To study how the electron density profile varies as we vary the phases of those peaks, we deliberately flipped the sign of the phases. Figure 3.30 and 3.31 show the effect of such operations

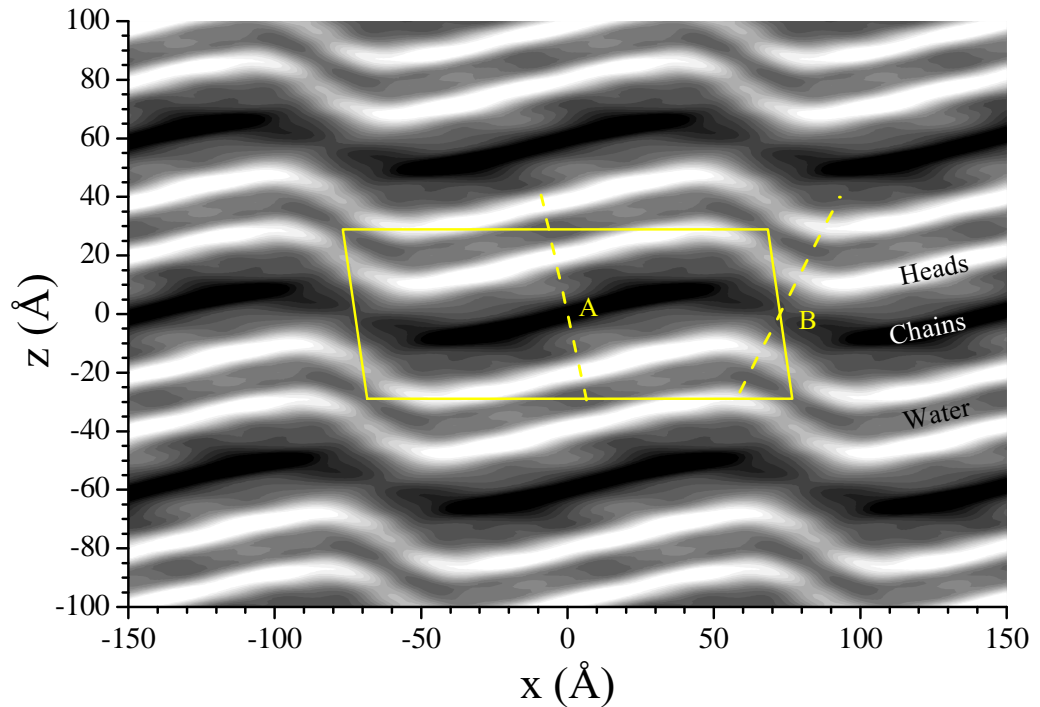


Figure 3.26: Two dimensional electron density profile calculated using the phases predicted by the 2G hybrid model (Fit5). White is most electron dense and black is least electron dense. A unit cell is shown with a solid yellow line. Dash lines A and B are the slices plotted in Fig. 3.27 and Fig. 3.28, respectively.

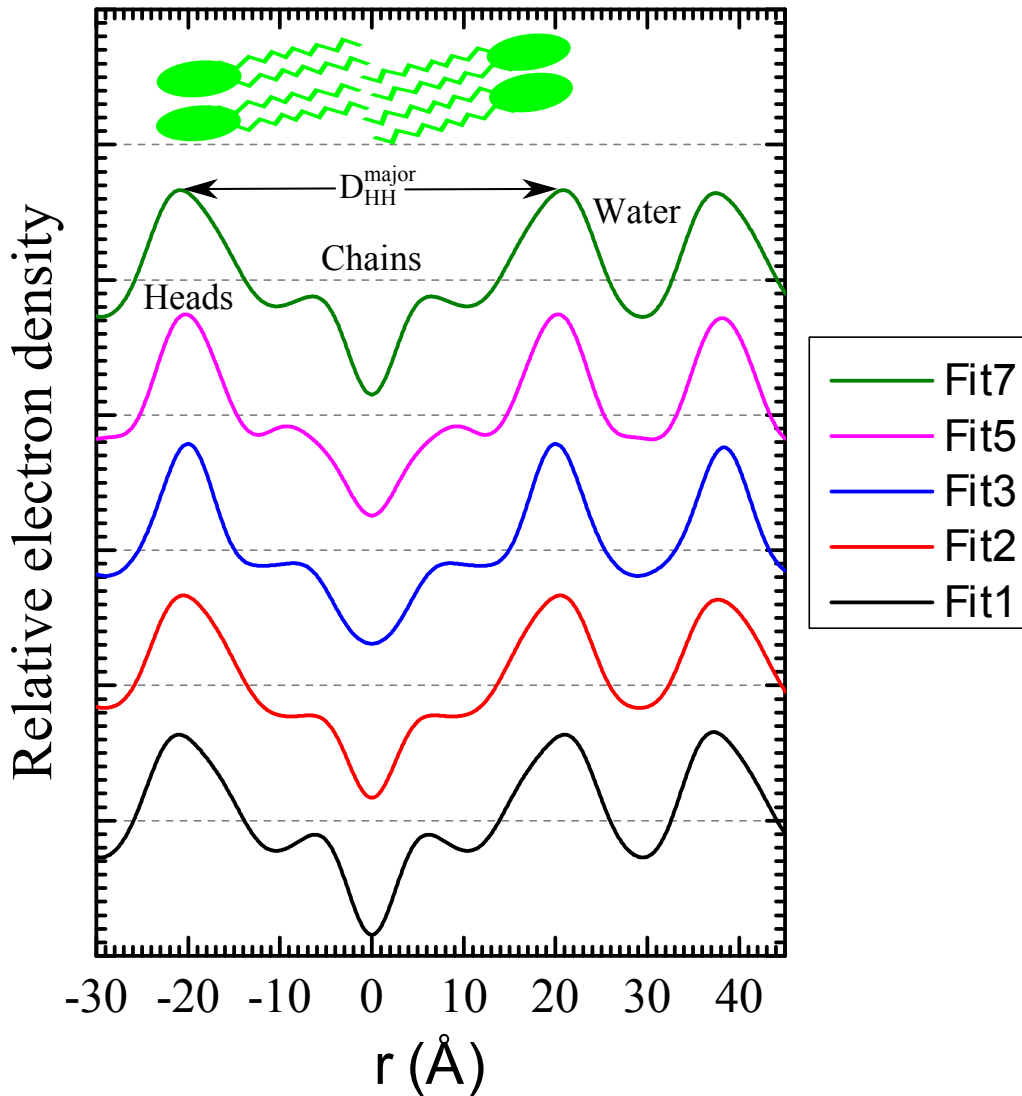


Figure 3.27: Electron density profiles along Slice A shown in Fig. 3.26, calculated using the phases predicted by different fits. The distance r is measured from the bilayer center. A cartoon of lipids is shown at the top, designating different parts of the profile as the lipid headgroup and chains. The fit from which each profile was calculated is shown in the figure legend.

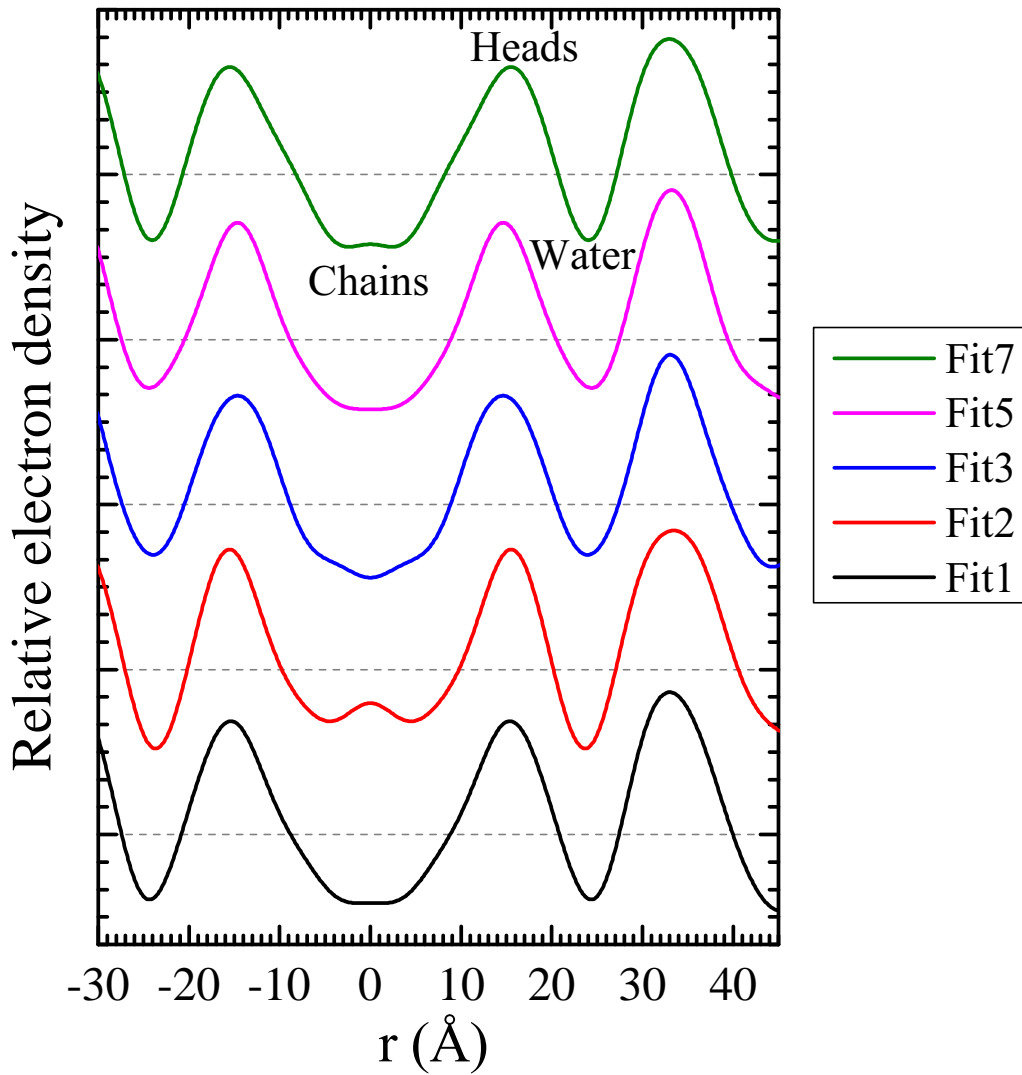


Figure 3.28: Electron density profiles along Slice B shown in Fig. 3.26, calculated using the phases predicted by different fits. The distance r is measured from the bilayer center. The fit from which each profile was calculated is shown in the figure legend.

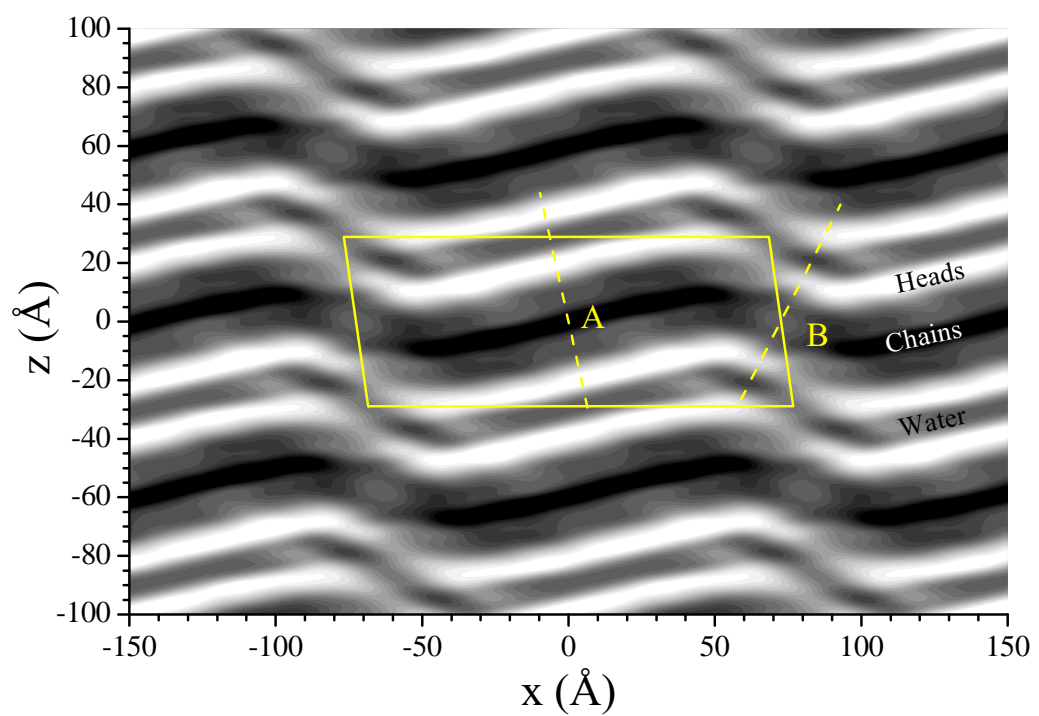


Figure 3.29: Two dimensional electron density profile calculated using the phases predicted by Fit2.

using the phases obtained by Fit5. In Fit5a, we inverted the phase of (3, 0) and in Fit5b, the phases of (1, 3), (3, 0), (6, 0), and (9, 0) were inverted. Essentially, we obtained approximately the same $D_{\text{HH}}^{\text{major}}$ among three cases while the variation in $D_{\text{HH}}^{\text{minor}}$ is about the same as observed with various fits (Fit1–7). Also, presence of the terminal methyl trough in the major arm was robust, but the profile of the chain regions in the minor arm was less robust. Other combination and variations including (6, 1), (6, 2), (6, 3), and (6, 4) resulted in similar variations of the density profile.

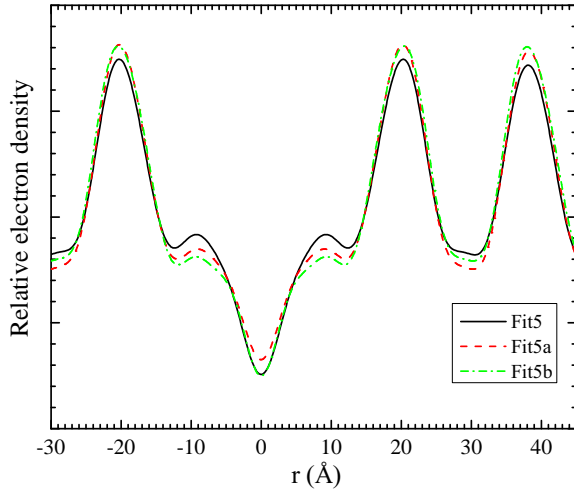


Figure 3.30: Variation in the electron density profile along Slice A. Reversing the sign of the (3, 0) phase in Fit5 resulted in the red dashed profile (Fit5a). Reversing the sign of the (1, 3), (3, 0), (6, 0), and (9, 0) resulted in the green dash-dotted profile (Fit5b). The distance r is measured from the bilayer center.

In summary, we observed that the thickness of the minor arm was smaller than that of the major arm and these thicknesses did not vary much among different models and fits. The electron density profile in the major arm showed clear separation of the headgroup and chains while that in the minor arm did not. Furthermore, the terminal methyl trough like feature in the major arm was quite robust, but whether the minor arm has a small dip or rise in the density at the bilayer center could not be determined. Obtaining a robust electron density profile in the minor arm may require an improved model. Table 3.12 summarizes the final structural results.

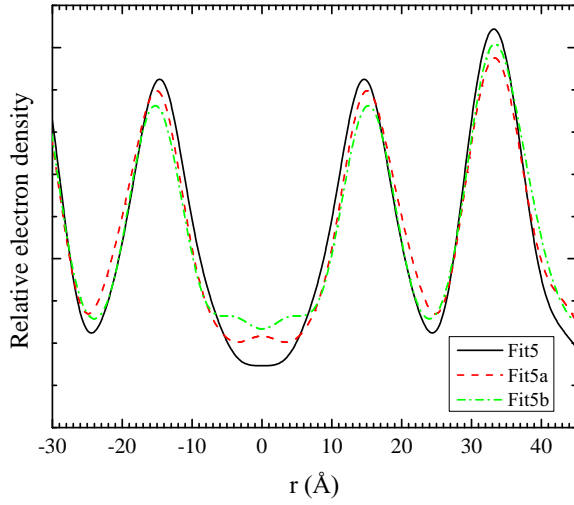


Figure 3.31: Variation in the electron density profile along Slice B. Reversing the sign of the (3, 0) phase in Fit5 resulted in the red dashed profile (Fit5a). Reversing the sign of the (1, 3), (3, 0), (6, 0), and (9, 0) resulted in the green dash-dotted profile (Fit5b). The distance r is measured from the bilayer center.

x_M	$101 \pm 2 \text{ \AA}$
A	$21 \pm 1 \text{ \AA}$
$D_{\text{HH}}^{\text{major}}$	$41 \pm 1 \text{ \AA}$
$D_{\text{HH}}^{\text{minor}}$	$30 \pm 1 \text{ \AA}$
α_M	$12^\circ \pm 1^\circ$
α_m	$27^\circ \pm 1^\circ$
D	57.8 \AA
λ_r	145.0 \AA
γ	98.2°

Table 3.13: Estimated structural quantities

3.6 nGIWAXS: results

3.6.1 Fluid and gel phase

Figure 3.32 shows the data reduction of near grazing incidence wide angle X-ray scattering (nGIWAXS) data of the DMPC fluid phase at $T = 30\text{ }^{\circ}\text{C}$. The original scattering image taken at $\omega = 0.5^\circ$ had unwanted scattering due to mylar windows in the hydration chamber which overlapped with the fluid phase WAXS. Subtracting background scattering data taken at incident angle $-\omega$ removed these unwanted features in the scattering data, resulting in a sample scattering image (Fig. 3.32(bottom, left panel)). This sample scattering image was then transformed to the sample q -space using the relationship between the CCD pixel positions and the sample q -space given by Eq. 3.14 and Eq. 3.15. The nonlinearity of this relationship is not negligible and must be taken into account for wide angle scattering data. The black regions in the sample q -space image (Fig. 3.32(bottom, right panel)) are the regions of q -space that were not probed by the detector. Because of the nonlinearity in the transformation, straight detector edges were turned into curves, the effect of which was most visible near the meridian $q_r = 0$. All nGIWAXS data in this chapter were reduced in the same manner.

Because of chain disordering in the fluid phase, chain-chain scattering gives rise to intensity along an arc [105] with a broad width in q . Scattering of the fluid phase WAXS is most intense at the equator. However, scattering near the equator was strongly absorbed by the sample and substrate, so observing the peak in the fluid phase WAXS would require a different experimental geometry. The data were collected with a low resolution setup to maximize intensity. The low resolution did not pose a problem for analysis of the data because observed features were broad. Figure 3.33 plots intensity along q_r showing that the fluid phase WAXS was centered at $q \approx 1.41\text{ \AA}^{-1}$. This corresponds to an average chain-chain distance of 4.5 \AA . A Lorentzian fit to the profile resulted in the full width half maximum (FWHM) $\Delta q_r = 0.288\text{ \AA}^{-1}$.

Figure 3.34 shows nGIWAXS of the the DMPC $L_{\beta I}$ gel phase that occurs at the highest hydration [11,53], collected with the high resolution setup. Because exposure time was short, the data did not have much intensity, but the (2,0) peak was clearly visible on the equator. When the peak profile of the (2,0) peak in q_r was fitted to a Lorentzian, we obtained an excellent fit with its FWHM $\Delta q_r = 0.014\text{ \AA}^{-1}$, centered

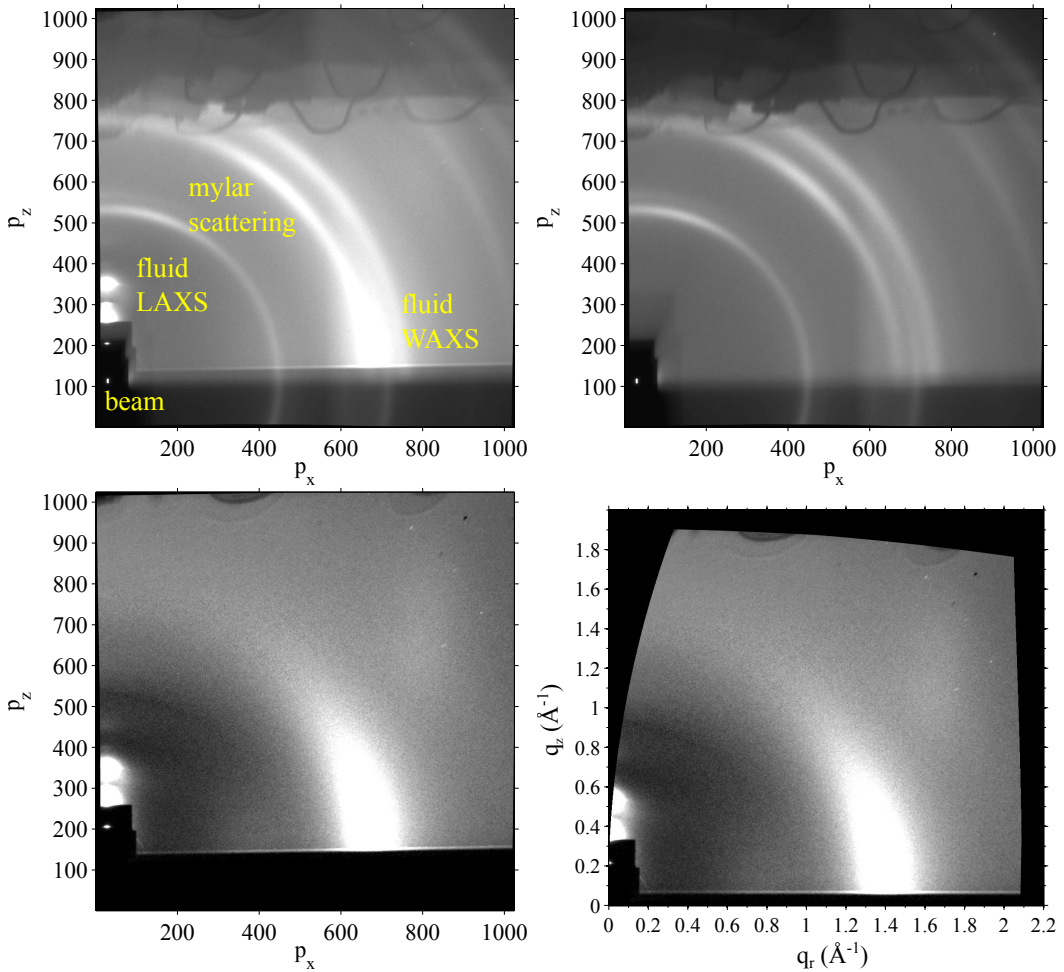


Figure 3.32: Data reduction of nGIWAXS data. (top) Fluid phase scattering at 30 °C taken at $\omega = 0.5^\circ$ (left) and at -0.5° (right) with the low resolution setup at the 2011 run. The sample width $w_s = 2$ mm. The fluid phase LAXS is also visible near the beam. The darker region below the equator defined by the beam vertical position p_z was due to the substrate. The beam was visible through the semitransparent beam stop. Scattering at $p_z > 750$ was the shadow cast by the electrical wires and thermal shielding in the hydration chamber. (bottom) The background subtracted image (left) and corresponding image in the sample q -space (right). Except some minor left over scattering, all the background scattering was removed very nicely. Because the meridian was not exactly along the vertical pixels, the background subtracted image was rotated by $\sim 1^\circ$ in the clockwise direction before the q -space transformation. The data reduction was done using MATLAB.

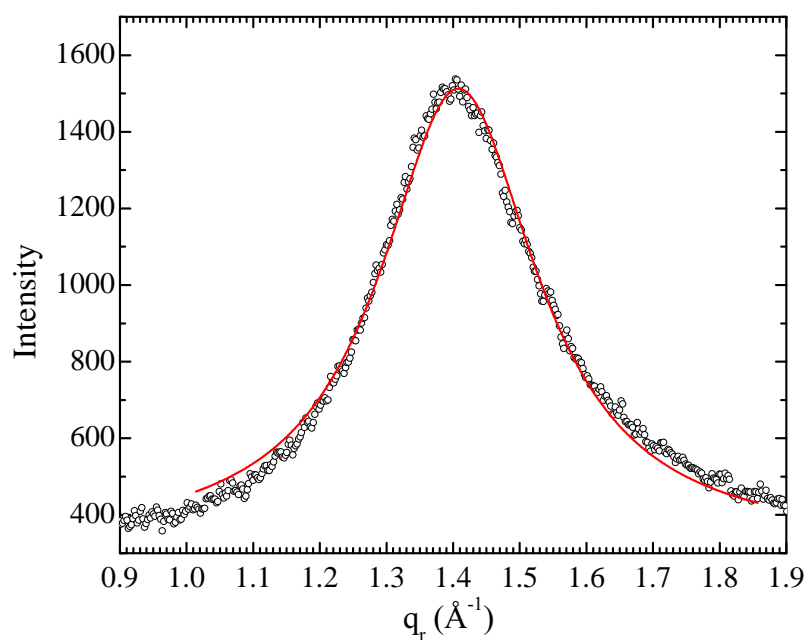


Figure 3.33: Fluid phase WAXS plotted along q_r at $q_z = 0.012 \text{ \AA}^{-1}$. The red solid line is a Lorentzian fit with its FWHM equal to 0.288 \AA^{-1} , centered at $q_r = 1.408$. Extra intensity at larger q_r was due to water scattering, which led to a slightly asymmetric profile.

at $q_r = 1.479 \text{ \AA}^{-1}$. This is the instrumental resolution as discussed in Sec. 3.2.2.3.

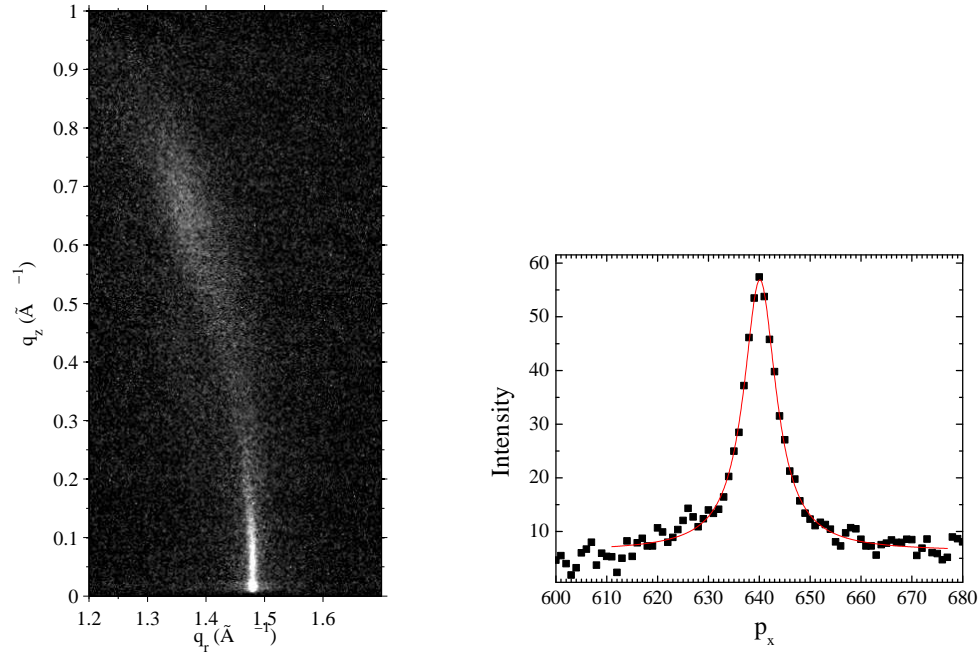


Figure 3.34: (left) nGIWAXS image of the DMPC gel phase at $10 \text{ }^\circ\text{C}$ for $D = 57.7 \text{ \AA}$ where the sample was in the $L_{\beta I}$ phase. The $(2,0)$ peak was at $q_r = 1.479 \text{ \AA}^{-1}$, corresponding to $d_{20} = 4.25 \text{ \AA}$. (right) The $(2,0)$ peak plotted along horizontal pixels p_x . The solid red line is a Lorentzian fit to the data, resulting in the FWHM of ~ 8 pixels, corresponding to $\Delta q = 0.014 \text{ \AA}^{-1}$, which is an unresolved width of intrinsically infinitely sharp peak estimated in Sec. 3.2.2.

3.6.2 Ripple phase

Figure 3.35 shows nGIWAXS from an oriented DMPC film in the ripple phase for $D = 60.8 \text{ \AA}$, collected with the high resolution setup. We observed a stronger peak and a weaker one off the equator. The maximum intensity of the stronger peak was at $(q_r, q_z) \approx (1.478 \text{ \AA}^{-1}, 0.20 \text{ \AA}^{-1})$ as shown in Fig. 3.36. The weaker peak was observed closer to the equator, and separation of this peak from the stronger one was most visible at $q_z = 0.12 \text{ \AA}^{-1}$, indicating that the center of this peak was near $(q_r, q_z) \approx (1.457 \text{ \AA}^{-1}, 0.12 \text{ \AA}^{-1})$. Because of absorption of X-rays due to the sample, intensity became attenuated as one approaches the equator. Very close to the equator, there is Vineyard-Yoneda peak that is due to constructive interference with scattering

from the substrate, which we will not consider. Absorption and Vineyard-Yoneda peak did not affect determination of the ripple peak positions as the ripple peaks were located at sufficiently large q_z . The positions of the peaks were confirmed by transmission wide angle X-ray scattering, which is discussed in the next section.

We also investigated dependence of the ripple WAXS on the interbilayer D -spacing. Figure 3.37 compares nGIWAXS at two different D -spacing, showing that chain scattering did not depend on the D -spacing in this range. A weak feature that looks like an arc coming from the chain peak was observed. This feature extended from $\phi = 0^\circ$ to at least 70° . This feature is perhaps mosaic spread scattering.

We estimated the width of the stronger peak by fitting the intensity profile in q_r to double Lorentzian as shown in Fig. 3.38. The fit resulted in the FWHM $\Delta q_r = 0.025 \text{ \AA}^{-1}$ centered at 1.478 \AA^{-1} and $\Delta q_r = 0.140 \text{ \AA}^{-1}$ centered at 1.464 \AA^{-1} . A fit with a single Lorentzian was not very good, and a broader Lorentzian was necessary to produce a reasonable fit. We also fitted the peak profile in q_r at $q_z = 0.12 \text{ \AA}^{-1}$, where two distinct peaks were observed (Fig.3.39). The two sharp peaks fitted with Lorentzian yielded the FWHM of about 0.025 \AA^{-1} , consistent with the FWHM obtained for the stronger peak. The widths and positions of the observed peaks are summarized in Table 3.13.

As Fig. 3.39 shows, the double Lorentzian fit was only successful within a limited range in q_r . This could be due to an underlining broad peak like the one shown in Fig. 3.38. To investigate this possibility, we fitted the same peak profile to triple Lorentzian with fixed widths. Two of the Lorentzian had fixed widths of 0.025 \AA^{-1} representing the sharp peaks and the last one had a fixed width of 0.14 \AA^{-1} representing the broad peak. Figure 3.39 shows an excellent fit obtained over a large range in q_r , suggesting that the estimated peak widths are not unreasonable. Curiously, the center of the stronger peak was different at the two different q_z : $(q_r, q_z) = (1.485 \text{ \AA}^{-1}, 0.12 \text{ \AA}^{-1})$ and $(1.478 \text{ \AA}^{-1}, 0.2 \text{ \AA}^{-1})$, while the total q was about the same, $\sim 1.49 \text{ \AA}^{-1}$.

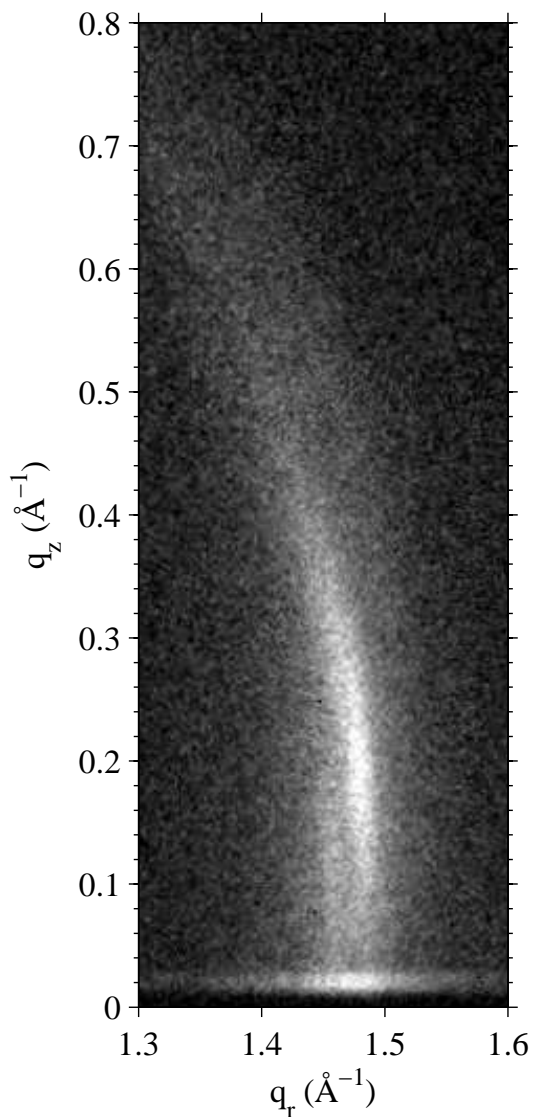


Figure 3.35: High resolution nGIWAXS of the DMPC ripple phase for $D = 60.8 \text{ \AA}$. The angle of incidence ω was 0.2° . The stronger peak was at $(q_r, q_z) \approx (1.478 \text{ \AA}^{-1}, 0.20 \text{ \AA}^{-1})$. The weaker peak was at $(q_r, q_z) \approx (1.452 \text{ \AA}^{-1}, 0.12 \text{ \AA}^{-1})$. The scattered intensity along the line slightly above $q_z = 0 \text{ \AA}^{-1}$ is the Vineyard-Yoneda peak [106, 107].

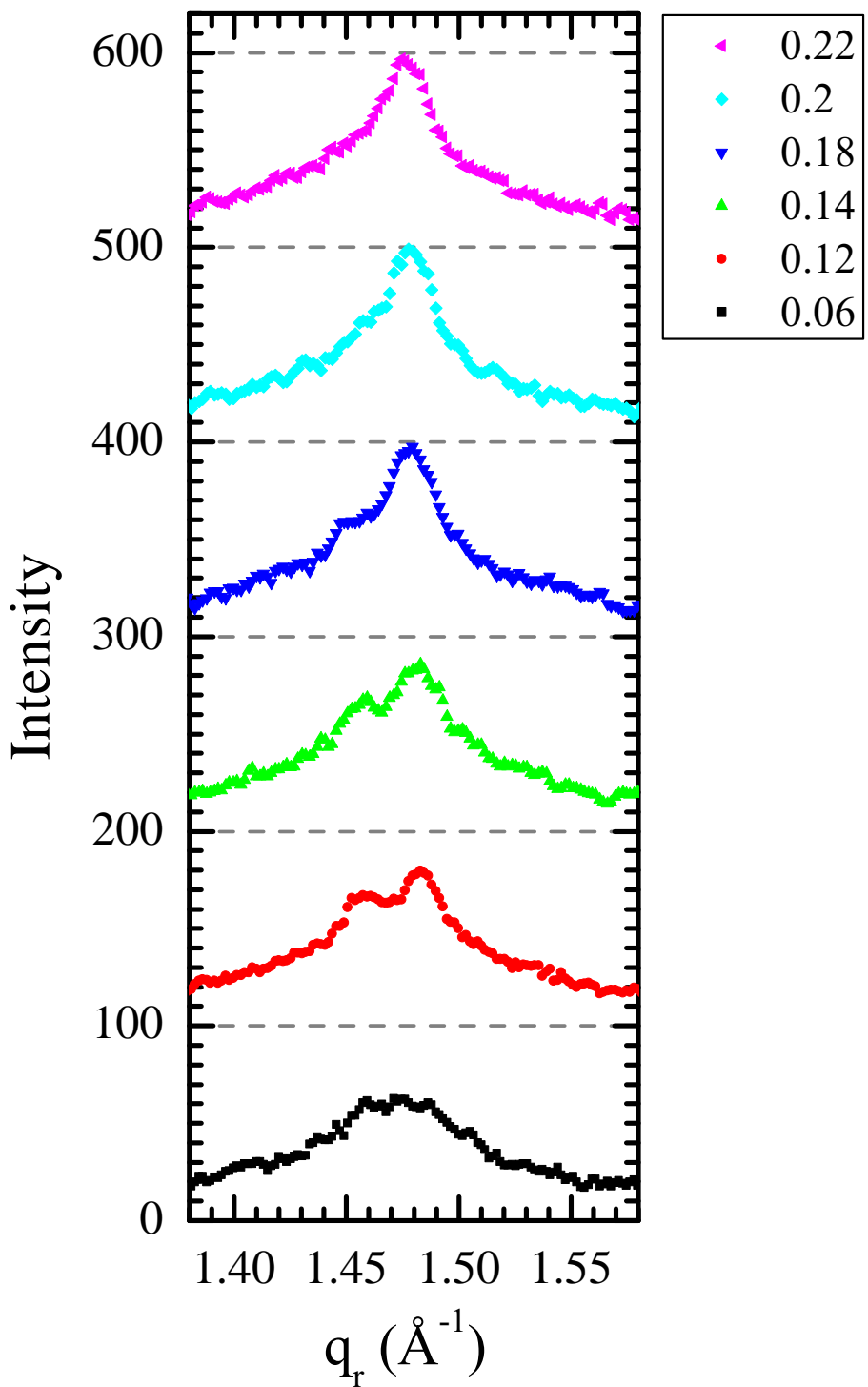


Figure 3.36: q_r swaths of the ripple WAXS, each averaged over 0.02 \AA^{-1} in q_z . Each curve is shifted by 100 vertically. The central q_z values of swaths are shown in the figure legend.

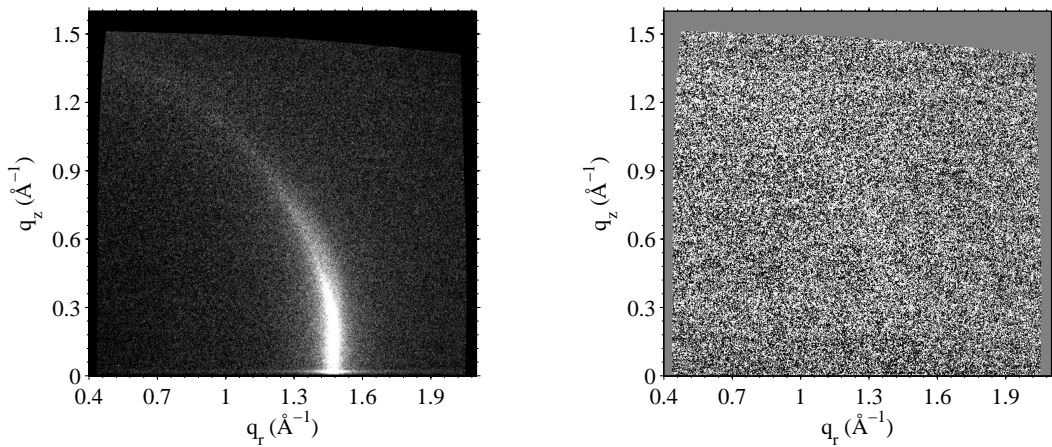


Figure 3.37: nGIWAXS of the DMPC ripple phase for $D = 59.2 \text{ \AA}$ (left) and difference between $D = 59.2 \text{ \AA}$ and 60.8 \AA (right). The difference shows no obvious feature, indicating that the ripple WAXS patterns at the two D-spacing were identical within an error. The angle of incidence ω was 0.2° . The data were taken with the high resolution setup.

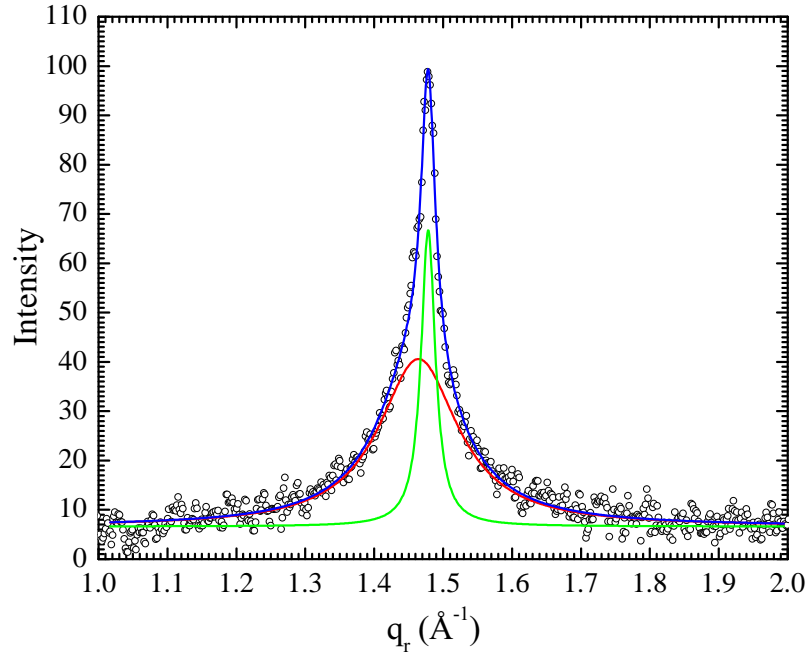


Figure 3.38: Peak profile in q_r at $q_z = 0.2 \text{ \AA}^{-1}$ fitted to double Lorentzian functions. The FWHM and center obtained were 0.025 \AA^{-1} and 1.478 \AA^{-1} (green) and 0.140 \AA^{-1} and 1.464 \AA^{-1} (red), respectively. The solid blue line is a sum of the two Lorentzian fits.

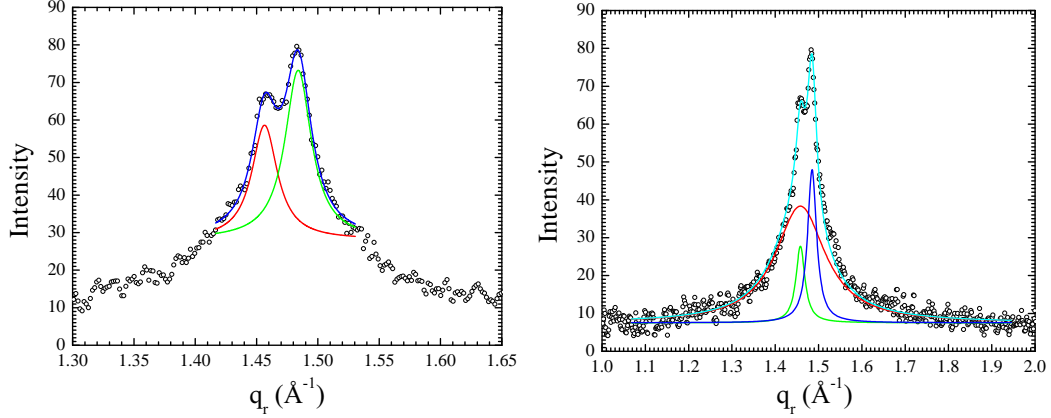


Figure 3.39: (left) Peak profile in q_r at $q_z = 0.12 \text{ \AA}^{-1}$ fitted to double Lorentzian functions. The FWHM and center obtained were 0.025 \AA^{-1} and 1.457 \AA^{-1} (red) and 0.026 \AA^{-1} and 1.484 \AA^{-1} (green), respectively. The fit was limited within a range in which fits were reasonable. (right) The same peak profile fitted to triple Lorentzian. The FWHM was constrained to 0.025 \AA^{-1} (blue), 0.025 \AA^{-1} (green), and 0.14 \AA^{-1} (red). The center was found to be 1.485 \AA^{-1} (blue), 1.458 \AA^{-1} (green), and 1.458 \AA^{-1} (red).

peaks	q (\AA^{-1})	q_r (\AA^{-1})	q_z (\AA^{-1})	Δq_r (\AA^{-1})	Δq_z (\AA^{-1})	$\hat{\theta}$
stronger	1.491	1.478	0.20	0.025	0.4	7.7°
weaker	1.462	1.457	0.12	0.025		4.7°
broader	1.463-1.478	1.458-1.464	0.12-0.20	0.140		
gel (2,0)	1.479	1.479	0	0.014	0.4	0°
fluid	1.41				0.288	

Table 3.14: Summary of measured peak properties. The values of Δq_z are from Sec. 3.7. $\hat{\theta} = \arctan(q_z/q_r)$. $R = I_{\text{strong}}/I_{\text{weak}} \approx 1.5-1.85$.

3.7 TWAXS: results

Figure 3.40(left) shows background subtracted transmission wide angle X-ray scattering (TWAXS) of the DMPC gel $L_{\beta I}$ phase obtained at $\omega = 45^\circ$. The background scattering image was collected by replacing the sample with a bare Si wafer. Imperfect subtraction of mylar scattering can be seen in the background subtracted image. This was most likely due to slight displacement of mylar windows when the sample was replaced with a bare wafer. Three main reflections whose Miller indices are (2,0), (1,1), and (1,-1) were observed along with the (1, ± 1) satellite peaks. Because the data were taken at $\omega = 45^\circ$, the WAXS pattern appeared on the CCD detector very differently from the respective pattern in the sample q -space. Therefore, the CCD to q -space transformation shown in Fig 3.40(right) was important in analyzing the TWAXS data.

Figure 3.41 shows the TWAXS pattern of the ripple phase after the CCD to q transformation. The stronger peak observed in nGIWAXS was also observed at approximately the same location. Because of a lower instrumental resolution than in the nGIWAXS experiment, the weaker peak was not as well separated. Figure 3.42 shows a hint of the weak peak at $q_z = 0.12 \text{ \AA}^{-1}$. This data set taken in the 2011 run motivated me to try an experiment with a higher instrumental resolution, which led to the nGIWAXS experiment in the 2013 run.

The length L of scattering entities in the z direction can be estimated by measuring the full length Δq_z of the (2,0) Bragg rod in q_z in the $L_{\beta I}$ phase [108], the relation between them being $\Delta q_z = 4\pi/L$. Figure 3.43 shows intensity of observed Bragg rods along q_z averaged in q_r for the gel and ripple phases. The full length Δq_z for the (2,0) gel phase peak was measured to be about 0.4 \AA^{-1} , corresponding to $L \approx 31 \text{ \AA}$. This value of L indicates that chains in the upper and lower monolayers scatter coherently, which has been shown to be the case for DPPC previously [108]. Figure 3.43(right) compares Δq_z in the ripple and gel phases, showing that Δq_z was about the same in both phases. Therefore, chains in the major arm are also coupled between the monolayers. We note that mosaic spread of the sample would make the apparent Δq_z larger, so that $L \approx 31 \text{ \AA}$ might be the lower bound on the true L .

Finally, Fig. 3.44 plots q_z swath along the weaker Bragg rod and along the entire ripple WAXS pattern. We found no obvious intensity maxima below $q_z = 0.12 \text{ \AA}^{-1}$, asserting that the weaker peak was also off the equator as discussed in Sec. 3.6. We

also found no sign of a third peak.

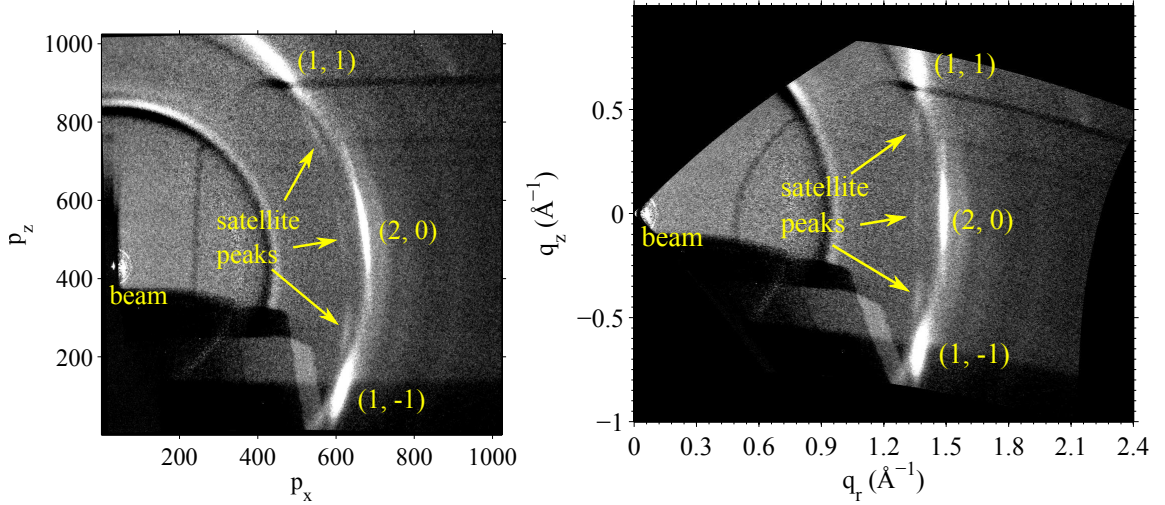


Figure 3.40: Transmission WAXS of the DMPC gel $L_{\beta I}$ phase observed on the CCD detector (left) and its corresponding pattern in the sample q -space (right). Bragg rods were indexed as $(2,0)$, $(1,1)$ and $(1,-1)$. The satellite peaks of $(1,\pm 1)$ reflections were also labeled. The black region in the right image corresponds to q -space that was not probed. The edges of the sample q -space image were distorted due to the nonlinear relation between the detector pixels and the sample q -space as discussed in Sec. 3.6. A ring of intensity at $q \approx 0.9 \text{ \AA}^{-1}$ is due to imperfect subtraction of the mylar scattering. Residual mylar scattering is also visible near the $(2,0)$ Bragg rod.

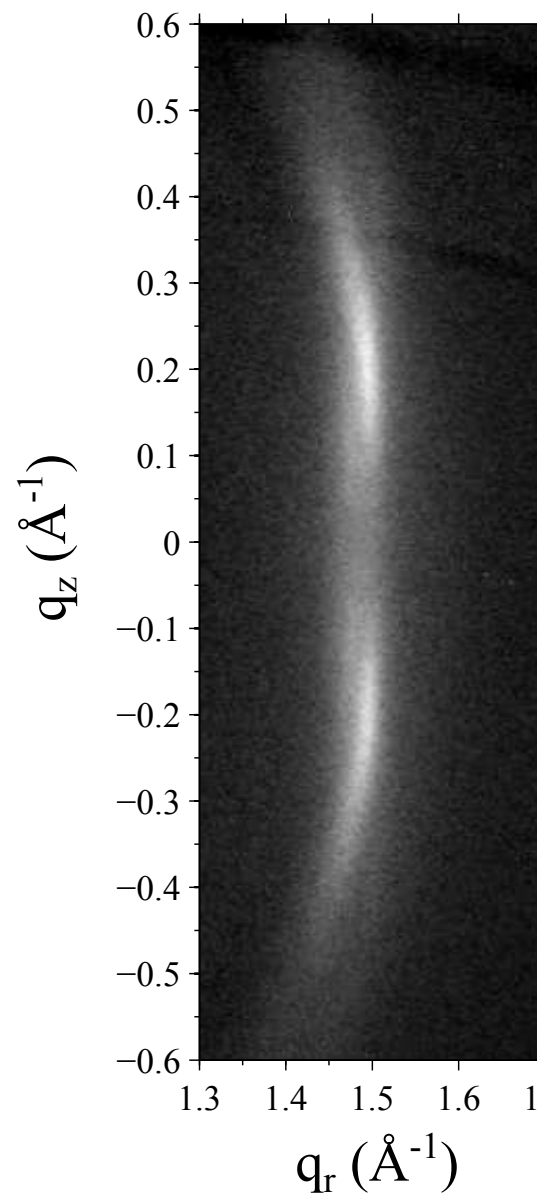


Figure 3.41: TWAXS image of the DMPC ripple phase at 18 °C and $D = 60.3 \text{ \AA}$.

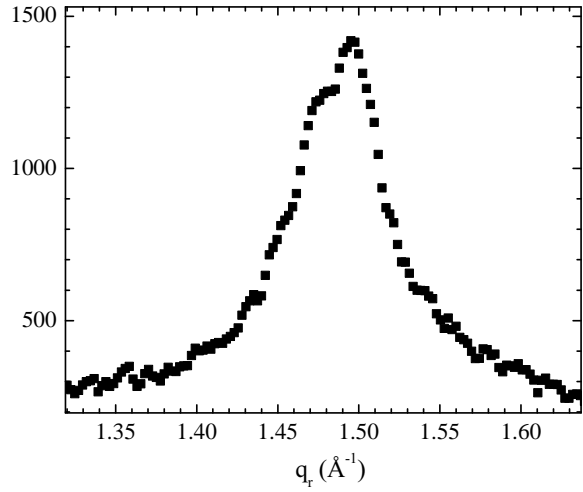


Figure 3.42: q_r swath of the ripple TWAXS averaged between 0.11 \AA^{-1} and 0.13 \AA^{-1} in q_z . Asymmetric shape of the profile is due to two Bragg rods centered at different q_r values as discussed in Sec. 3.6.

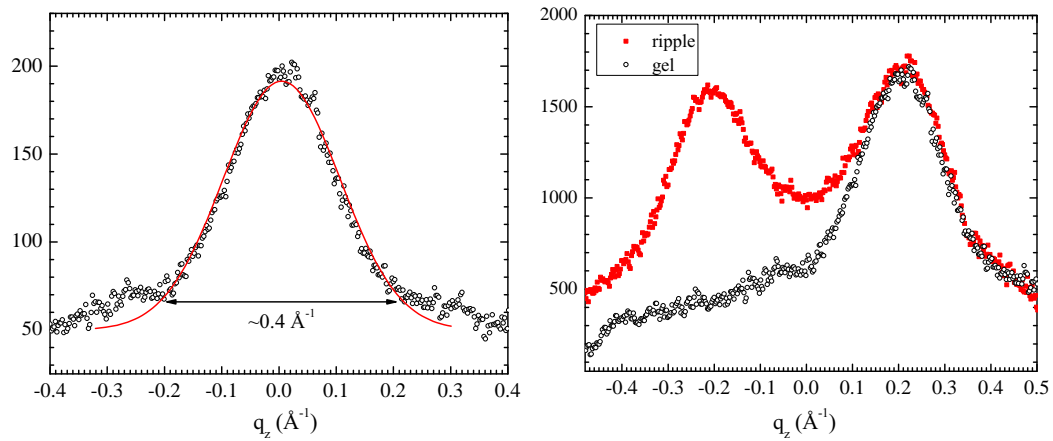


Figure 3.43: (left) q_z swath of the gel (2,0) Bragg rod. The solid line is a Gaussian fit with the FWHM of 0.23 \AA^{-1} . (right) q_z swath of the ripple peak averaged between 1.465 \AA^{-1} and 1.481 \AA^{-1} in q_r (red solid squares) and the gel (2,0) peak scaled and shifted to guide visual comparison (open black circles).

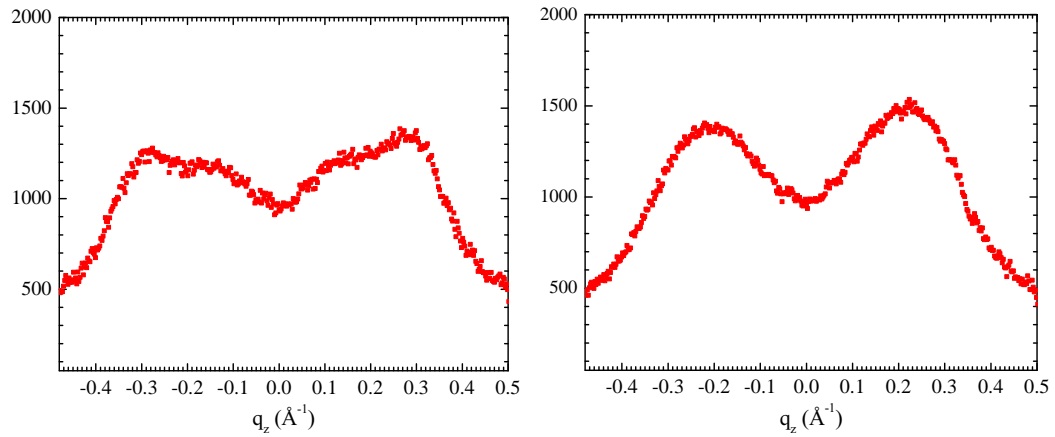


Figure 3.44: q_z swath averaged between 1.465 \AA^{-1} and 1.481 \AA^{-1} (left) and between 1.465 \AA^{-1} and 1.51 \AA^{-1} (right) in q_r . The left plot is approximately the q_z profile along the weaker peak while the right profile extends over the entire ripple WAXS pattern.

3.8 Discussion

3.8.1 Major arm

There has been a number of evidence to suggest that the major arm is like the gel phase. Figure 3.45 compares our electron density profile in the major arm to the DMPC gel phase profile reported by Tristram-Nagle *et al.* [53]. It shows that the density profile of the major arm is similar to that of the gel phase and the thickness is comparable between the two phases although the ripple profile does not show distinction between the phosphate and carbonyl-glycerol headgroups as in the gel phase. Also, the terminal methyl trough appears to be wider in the ripple major arm, which could be a sign that the terminal methyl is slightly more disordered in the ripple phase than in the gel phase. As discussed in Sec. 3.5, however, small features in the ripple profile were not reliable because they depended on which fitting results were used to produce the electron density profile. An important point we can make based on Fig. 3.45 is that chains must be tilted by some amount with respect to the local bilayer normal. If we use the distance between the centers of the headgroups as the bilayer thickness, we have about 38 Å for the gel phase and 40 Å for the ripple phase. Because chains are tilted by 30° in the L_{βI} phase, the chain tilt angle θ_t in the ripple major arm is roughly estimated to be 25° ± 1°. This constraint on θ_t and the measured α_M are important in understanding the nGIWAXS data.

While the electron density profile derived from the LAXS data indicates that chains are gel-like in the major arm, it does not show whether or not chains in different leaflets are coupled. To answer this question, we turned to transmission WAXS where we were able to carefully measure the width of observed Bragg rods. Figure 3.43 shows that the widths of the Bragg rods in the ripple and gel phases are approximately the same, indicating that chains in different leaflets in the ripple major arm also scatter coherently. This point can be contrasted with the chain packing in the major arm observed in atomistic MD simulations by de Vries *et al.* [98]. In their simulations, while chains were straightened out (all-trans) like in the case of the gel phase, their chain tilt angles $\hat{\theta}$ were modulated along the ripple direction. It was also clearly seen in their simulations that chains in the different leaflets were decoupled and tilted in the opposite direction. Our TWAXS data are inconsistent with this picture and instead consistent with normal gel phase packing where chains in different leaflets constitute long coherently scattering entities.

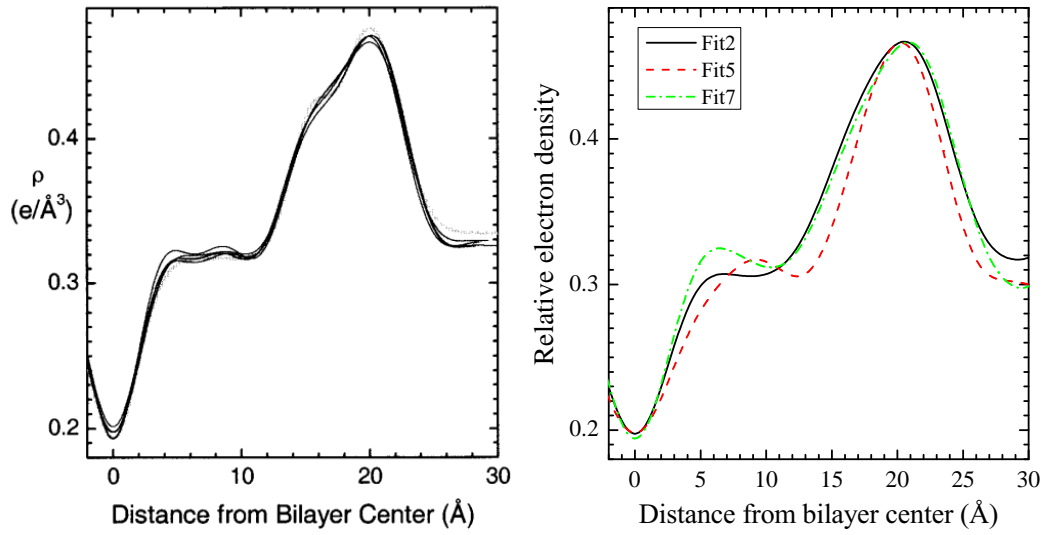


Figure 3.45: Comparison of the electron density profiles of the DMPC gel phase (left) and the major arm in the ripple phase (right). The DMPC profile is taken from Ref. [53]. The ripple major arm profiles were calculated using the phases predicted by Fit2, 5, and 7 (black, red, and green, respectively). The ripple profiles are scaled to match with the gel phase profile.

Regarding indexing the wide angle peaks

The chain-chain correlation length can be estimated by using the Scherrer equation [109],

$$B = \frac{0.94\lambda}{L \cos \theta},$$

where B is the observed FWHM of a Bragg peak, λ is the wavelength, L is the length over which chains are positionally correlated, and θ is the Bragg angle. For the (2, 0) Bragg peak in the gel $L_{\beta I}$ phase, we obtained the FWHM $\Delta q = 0.014 \text{ \AA}^{-1}$ and the position of the peak $q = 1.479 \text{ \AA}^{-1}$. For our X-ray wavelength $\lambda = 1.175 \text{ \AA}$, the Scherrer equation yields $L = 426 \text{ \AA}$. Because the width of the (2,0) gel phase peak was not instrumentally resolved, the correlation length of chains was greater than 426 \AA . The width of similar lipid, DPPC, was resolved and had a correlation length of 2900 \AA [110].

In contrast, the observed peaks in the ripple phase were instrumentally resolved (Fig. 3.38). The FWHM of the stronger peak was estimated to be 0.025 \AA^{-1} , corresponding to the correlation length of $\sim 240 \text{ \AA}$, indicating that the correlation length in the ripple phase is shorter than that in the gel phase. This observation can be qualitatively understood by supposing that chains in the major and minor arms are not correlated, so that gel phase like chains in the major arm are only correlated within the major arm, limiting the correlation length along the ripple direction to be less than the length of the major arm, $\sim 100 \text{ \AA}$. Although it is possible that chains are correlated over a much longer distance along the direction perpendicular to the ripple direction leading to a sharp reflection along q_y , what is observed in our in-plane powder sample is a convolution of a broad width along q_x and sharp one along q_y . Such convolution would result in a broad Bragg rod as observed in our nGIWAXS data. To quantitatively understand the observed peak widths would require to model the finite size effect rigorously. This could lead to a prediction for the peak shape that is not Gaussian assumed by the Scherrer equation [109], which we did not consider.

3.8.2 Minor arm

Some previous work have suggested that chains in the minor arm are disordered and fluid as in the L_{α} fluid phase. Figure 3.46 compares our electron density profiles in the minor arm to the DMPC fluid phase profile reported by Kucerka *et al.* [68]. Unlike in the case for the major arm, the density profile in the minor arm does not

resemble that of the fluid phase at all. This radically different profile of the minor arm is not an artifact as we successfully obtained a typical bilayer profile for the major arm. Inconsistency of the minor arm being like the fluid phase is also seen in our nGIWAXS data. Figure 3.47 compares observed WAXS patterns of the ripple and fluid phase. The fluid phase pattern was centered at $q_r = 1.4 \text{ \AA}^{-1}$, where there is no obvious feature in the WAXS pattern of the ripple phase. While one could argue that the fluid phase pattern can be scaled down to match the tail of the ripple Bragg peaks, thereby making the two consistent with each other, as previously argued in Ref. [89], subtraction of the fluid phase pattern from the ripple pattern would result in an asymmetric shape of the ripple Bragg peaks, which is not very reasonable.

Another type of chain packing, possibly with atypical bilayer profile, for the minor arm is the chain interdigititation proposed by de Vries *et al.* [98]. Figure 3.48 compares the electron density profiles in the minor arm with that of the DHPC $L_\beta I$ interdigitated phase reported by [?]. Absence of the methyl trough can be seen in both $L_\beta I$ phase and the ripple minor arm, but the widths of the headgroups are much narrower in the DHPC $L_\beta I$ phase. The widths of the "headgroups" in the minor arm profile are about 10 Å, comparable with those in the major arm profile. While Fig. 3.48 suggests that interdigitated chains are not completely inconsistent with our results in terms of an overall shape of the density profile, our nGIWAXS pattern clearly eliminates the packing proposed in Ref. [98]. Figure 3.49 compares the calculated wide angle pattern from their atomistic MD simulations to our measured nGIWAXS pattern from the ripple phase. As noted in Ref. [98], interdigitated chains in the minor arm scatter coherently, giving rise to a Bragg peak centered at $q_z \approx 0.4 \text{ \AA}^{-1}$. This off-equator Bragg peak is due to chains being tilted by about 20° with respect to the stacking z direction though they are essentially parallel to the local bilayer normal. We saw no sign of a Bragg peak at such large q_z in our nGIWAXS data, so our wide angle data do not support the structure proposed by de Vries *et al.* [98].

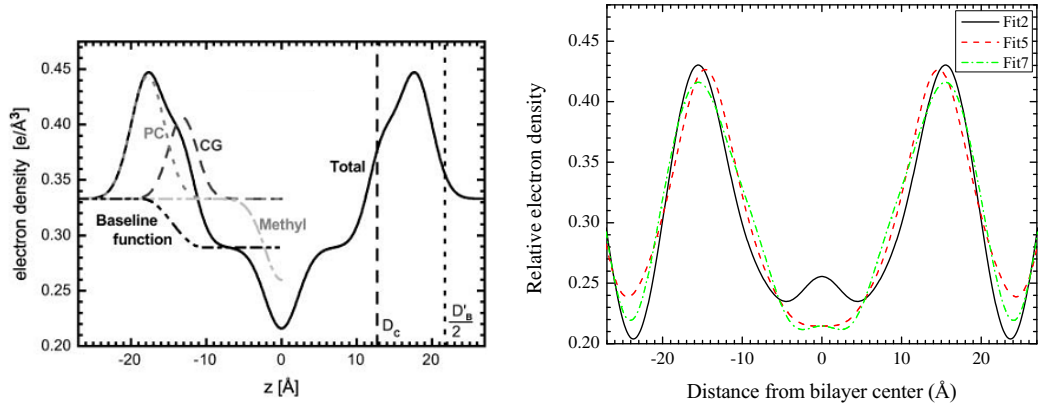


Figure 3.46: Comparison of the electron density profiles of the DMPC fluid phase (left) and the minor arm in the ripple phase (right). The DMPC profile is taken from Ref. [68]. The ripple minor arm profiles were calculated using the phases predicted by Fit2, 5, and 7 (black, red, and green, respectively). The ripple profiles are scaled to match approximately with the fluid phase profile.

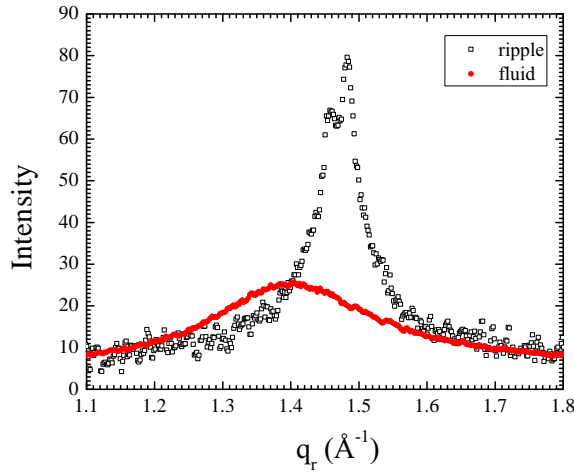


Figure 3.47: Comparison of the ripple (black) and fluid (red) phase WAXS at $q_z = 0.012 \text{ \AA}^{-1}$. The fluid phase data were taken with the low resolution setup and scaled vertically to enable visual comparison.

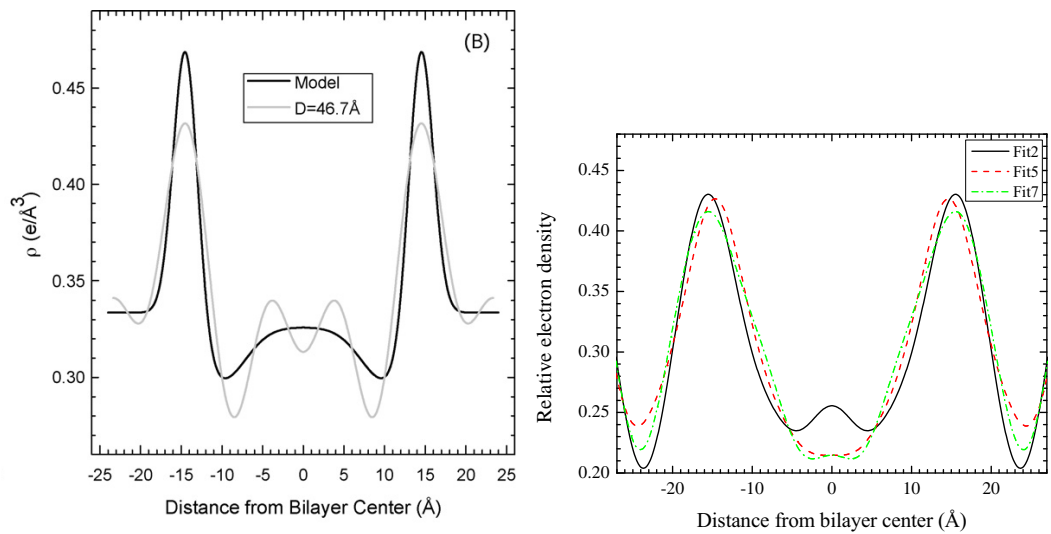


Figure 3.48: Comparison of the electron density profiles of the DHPC L_β I interdigitated phase (left) and the minor arm in the ripple phase (right). The DHPC profile is taken from Ref. [?]. The ripple minor arm profiles were calculated using the phases predicted by Fit2, 5, and 7 (black, red, and green, respectively). The ripple profiles are scaled to match approximately with the L_β I phase profile.

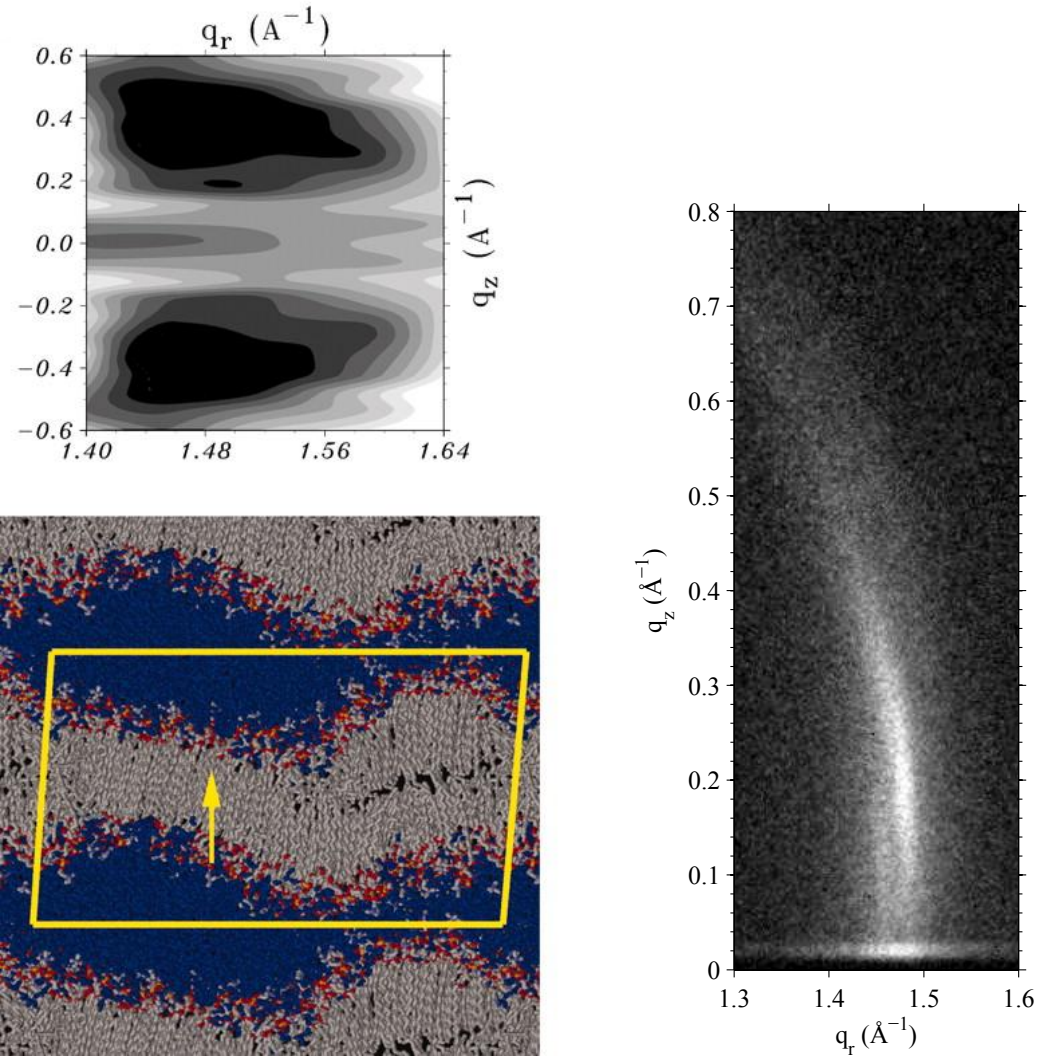


Figure 3.49: Comparison of the wide angle (WAXS) pattern predicted by the ripple phase structure proposed in Ref. [98] (left) and our measured WAXS (right). In the left, the interdigitated chains scatter coherently, giving rise to a Bragg peak at $q_z \approx 0.4 \text{ \AA}^{-1}$, while q_z values of the observed peaks in our data were 0.12 \AA^{-1} and 0.2 \AA^{-1} .

3.9 Conclusion

The ripple phase has attracted many researchers since its discovery in 1967, and extensive study on average structural properties such as the ripple wavelength, oblique angle, D -spacing, and electron density profiles have been reported. From those experimental measurements, many theoretical models to explain the origin of the ripple phase have been considered. Yet, molecular packing in the asymmetric ripple has only been elusive. Several work have suggested various molecular packing in this phase. Based on the diffusion measurements that showed a fast component and slow component, the idea of micro phase separation that the major arm is gel like while the minor arm is fluid like was proposed. This idea was supported by a later low angle X-ray study that showed the thickness of the major arm is comparable to that of the gel phase while the thickness of the minor arm is smaller. This work was then followed by a wide angle X-ray study on unoriented samples, arguing that the micro phase separation is consistent with the wide angle data. Another proposed molecular packing was based on the electron density profile derived from X-ray form factors. Given that the model parameter that represents the chain tilt was constant throughout the ripple bilayer, it was argued that chains were gel like in both major and minor arms with the same chain tilt angle with respect to the stacking z direction. More recently, a MD simulation proposed interdigitated chains in the minor arm while chains are gel like in the major arm but with decoupled leaflets.

Previous predictions and suggestions for molecular packing in the asymmetric ripple so far have not been directly tested because of lack of a high quality electron density profile and quantitative wide angle scattering data from an oriented sample. Therefore, we sought to fill the gap with synchrotron X-ray techniques. Our strength were three fold: 1) brilliant synchrotron beam that allowed use of Si monochromator with a very small energy dispersion, 2) stacks of ~ 2000 bilayers oriented on the substrate that scattered strongly and anisotropically, and 3) hydration chamber that allowed us to control the hydration of the sample with minimum background scattering. While we could not calculate the electron density profile with high precision unambiguously or solve the chain packing in the minor arm based on the measured wide angle scattering data, we were able to test the aforementioned proposed molecular packing. Our new data sets should also facilitate testing variations of those proposed structure as well as new structures that will come forth in a future. For

example, Monte Carlo simulations based on a model free energy can be tuned to obtain a good fit to our measured wide angle data. One could also consider some exotic packing such as swirling pattern observed in Ref. [?]. Predicting the scattering intensity pattern from these structures might lead to a different way to analyze our LAXS and nGIWAXS data and possibly more improved study of the ripple phase.

Future possible experiments include a high resolution transmission experiment, where both geometric broadening and energy dispersion are minimized. The expected resolution is the width of the X-ray beam, which is about 3 pixels. This experiment doubles the best resolution achieved in this work. Another slightly different high resolution experiment is to use silicon crystal analyzer downstream of the sample, which completely remove geometric broadening. The downside of this type of high resolution experiment is that only one point in q-space is probed at any given exposure, so getting a full 2D map of wide angle scattering is time consuming.

Also highly speculative, but the ripple phase might be an interesting phase to study curvature sensing peptides. The description of curvature in the ripple phase has been around for a while. Those curvature sensing peptides may accumulate at the kink regions. Then, the electron density profile can be calculated with the analysis detailed in this work. It would be very interesting if peptide-lipid interactions also significantly modify the wide angle pattern. With a known perturbation property of a peptide on lipids, it could shed light on the structure of the minor arm. For example, if indeed chains are fluid like in the minor, some peptides might have tendency to accumulate in the minor arm because of ease of insertion compared to the gel-like major arm. Then, the ripple phase might be used to study biologically relevant problems.

Appendices

Appendix A

A.1 More results from chapter 2

A.2 Mosaic Spread for NFIT analysis

First we calculate how mosaic spread affects the structure factor $S(q)$. Next we discuss two experimental methods. Third, we discuss the updated NFIT program. Fourth, we show the results.

A.2.1 Mosaic Spread: Calculation

In this section, an analytical framework for dealing with mosaic spread is developed. A sample of oriented stacks of bilayers consists of many small domains, within which layers are registered in an array. An ideal domain is a domain where the layers are parallel to the substrate, whose surface is in the sample xy -plane, so the orientation \mathbf{n} of an ideal domain is perpendicular to the substrate as shown in Fig. A.3. In general, the orientation \mathbf{n}' of a domain is tilted from that of an ideal domain by some angle α . Then, we consider a mosaic spread distribution function, $P(\alpha)$, representing a probability of finding a domain with a tilt α . We assume that the sample is symmetric about the substrate normal, so that the distribution $P(\alpha)$ does not depend on the azimuthal angle, β . The normalization condition on $P(\alpha)$ is

$$1 = \int_0^{2\pi} d\beta \int_0^{\frac{\pi}{2}} d\alpha \sin \alpha P(\alpha). \quad (\text{A.1})$$

The object of this section is to derive the X-ray scattering structure factor including the distribution function $P(\alpha)$.

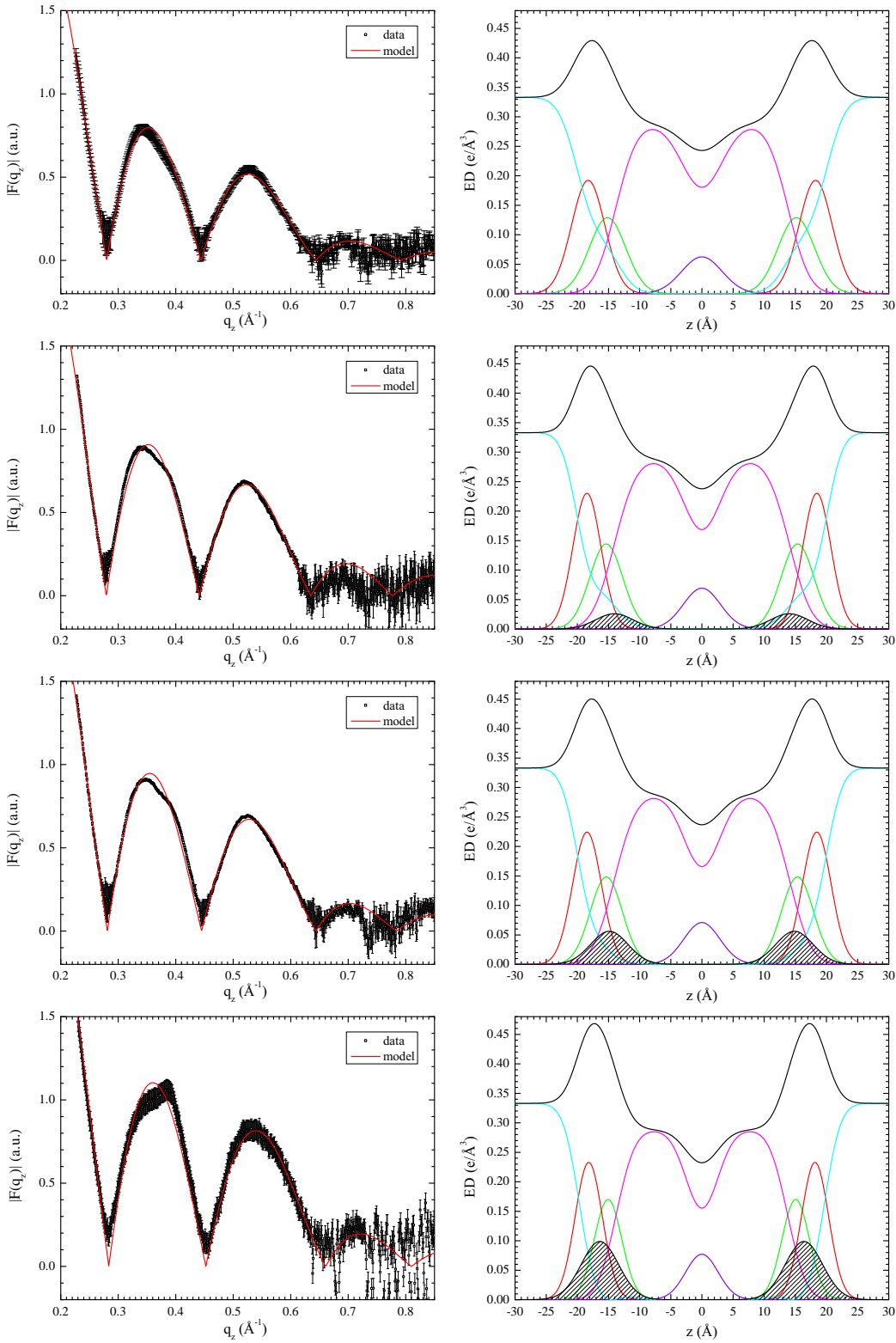


Figure A.1: The best fits to DOPC:DOPE (3:1) form factors (left) and the corresponding electron density profiles (right) with $x_{\text{Tat}} = 0, 0.016, 0.034$, and 0.059 (from top to bottom).

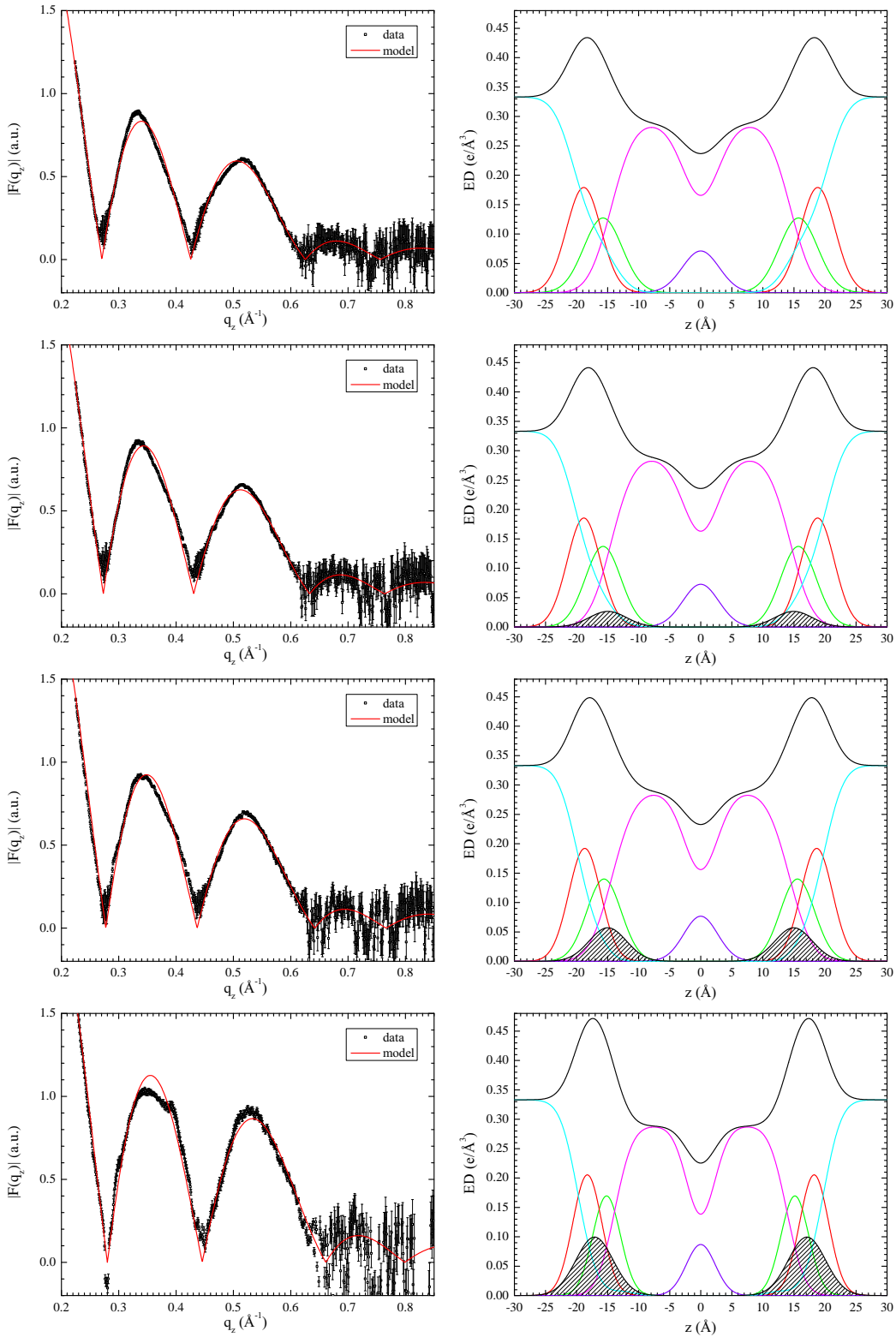


Figure A.2: The best fits to DOPC:DOPE (1:1) form factors (left) and the corresponding electron density profiles (right) with $x_{\text{Tat}} = 0, 0.016, 0.034$, and 0.059 (from top to bottom).

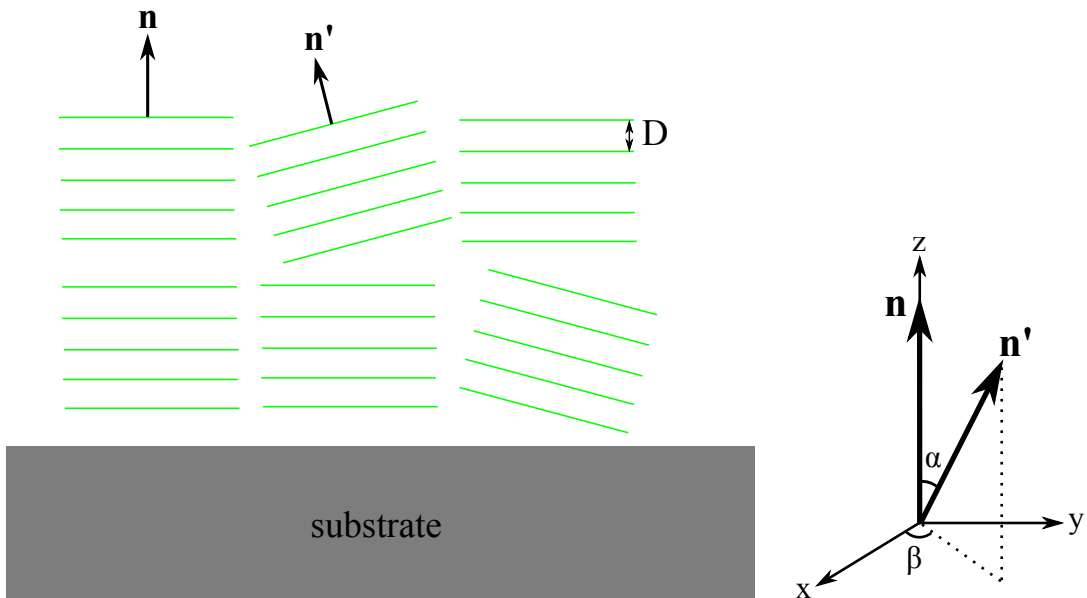


Figure A.3: Two dimensional view of mosaic spread (left) and notations used in this section (right). The stacking direction of an ideal domain is \mathbf{n} and that of a tilted domain \mathbf{n}' . The deviation of \mathbf{n}' from \mathbf{n} denoted as α quantifies the degree of misorientation of a domain. The x , y , and z -axes are the sample coordinates.

First, let us consider a two dimensional example. Our sample consists of two identical domains except a tilt α shown in Fig. A.4. Then, the sample structure factor $S^{\text{sam}}(\mathbf{q})$ is a superposition of the structure factor $S(\mathbf{q})$ of the ideal domain and $S(\mathbf{q}')$ of the tilted domain,

$$S^{\text{sam}}(\mathbf{q}) = S(q_x, q_z) + S(q'_x, q'_z). \quad (\text{A.2})$$

To express $S(q'_x, q'_z)$ in terms of the sample q -space (q_x, q_z) , we write q'_x and q'_z in terms of q_x , q_z , and α ,

$$\begin{aligned} q'_x &= \mathbf{q} \cdot \hat{\mathbf{x}}' = q \cos\left(\frac{\pi}{2} - \theta + \alpha\right) \\ q'_z &= \mathbf{q} \cdot \hat{\mathbf{z}}' = q \sin\left(\frac{\pi}{2} - \theta + \alpha\right) \\ q_x &= q \cos(\pi/2 - \theta) \\ q_z &= q \sin(\pi/2 - \theta) \end{aligned} \quad (\text{A.3})$$

where $q = |\mathbf{q}|$. Eq. (A.2) and (A.3) give the structure factor of a sample consisting of the two domains. With a continuous distribution of \mathbf{n}' , we integrate over the angle α with each structure factor modulated by the distribution function $P(\alpha)$,

$$S_M(\mathbf{q}) = S_M(q, \theta) = \int_{-\frac{\pi}{2}}^{\frac{\pi}{2}} d\alpha S(q'_x, q'_z) P(\alpha), \quad (\text{A.4})$$

Variables q and θ are used in the above equation to make a connection with the three dimensional case, where the spherical coordinates are convenient, which we discuss now.

For a three dimensional sample, the basic idea is the same as the two dimensional case. In the three dimensional case, we also rotate the vector \mathbf{n}' about the z -axis by an angle β after the rotation about the y -axis by an angle α , so all we need to do is to apply appropriate rotation matrices to the sample xyz -axes which define the domain coordinates $x'y'z'$.

The rotation matrix for rotating a vector about the y -axis is given by

$$R_y = \begin{pmatrix} \cos \alpha & 0 & \sin \alpha \\ 0 & 1 & 0 \\ -\sin \alpha & 0 & \cos \alpha \end{pmatrix} \quad (\text{A.5})$$

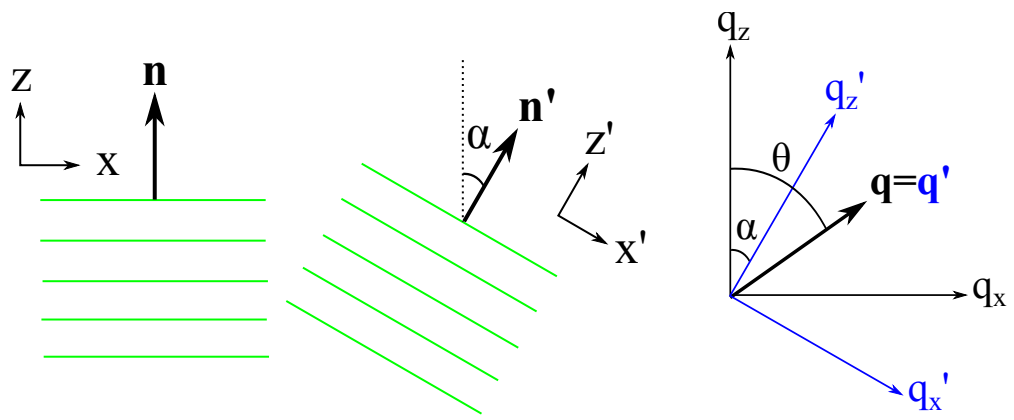


Figure A.4: Example of a two dimensional sample consisting of an ideal and tilted domains. $\mathbf{q} = (q_x, q_z)$ is the sample q -space and $\mathbf{q}' = (q'_x, q'_z)$ is the domain q -space. The two q -spaces are related by a rotation of α about the y -axis, which is into the page.

and for rotating about the z -axis

$$R_z = \begin{pmatrix} \cos \beta & -\sin \beta & 0 \\ \sin \beta & \cos \beta & 0 \\ 0 & 0 & 1 \end{pmatrix}. \quad (\text{A.6})$$

Then, what we want is

$$\hat{\mathbf{x}}' = R_z R_y \begin{pmatrix} 1 \\ 0 \\ 0 \end{pmatrix} = \begin{pmatrix} \cos \alpha \cos \beta \\ \cos \alpha \sin \beta \\ -\sin \alpha \end{pmatrix} \quad (\text{A.7})$$

$$\hat{\mathbf{y}}' = R_z R_y \begin{pmatrix} 0 \\ 1 \\ 0 \end{pmatrix} = \begin{pmatrix} -\sin \beta \\ \cos \beta \\ 0 \end{pmatrix} \quad (\text{A.8})$$

$$\hat{\mathbf{z}}' = R_z R_y \begin{pmatrix} 0 \\ 0 \\ 1 \end{pmatrix} = \begin{pmatrix} \sin \alpha \cos \beta \\ \sin \alpha \sin \beta \\ \cos \alpha \end{pmatrix}. \quad (\text{A.9})$$

The domain q -space, (q'_x, q'_y, q'_z) , in terms of the sample q -space (q_x, q_y, q_z) is given by

$$q'_x = \mathbf{q} \cdot \hat{\mathbf{x}}' = q_x \cos \alpha \cos \beta + q_y \cos \alpha \sin \beta - q_z \sin \alpha, \quad (\text{A.10})$$

$$q'_y = \mathbf{q} \cdot \hat{\mathbf{y}}' = -q_x \sin \beta + q_y \cos \beta, \quad (\text{A.11})$$

$$q'_z = \mathbf{q} \cdot \hat{\mathbf{z}}' = q_x \sin \alpha \cos \beta + q_y \sin \alpha \sin \beta + q_z \cos \alpha. \quad (\text{A.12})$$

The transformation expressed in the spherical coordinates is

$$\cos \theta' = \frac{q'_z}{q} = \sin \theta \sin \alpha \cos(\phi - \beta) + \cos \theta \cos \alpha, \quad (\text{A.13})$$

$$\tan \phi' = \frac{q'_y}{q'_x} = \frac{\sin \theta \sin(\phi - \beta)}{\sin \theta \cos \alpha \cos(\phi - \beta) - \cos \theta \sin \alpha}. \quad (\text{A.14})$$

Summing over all the domains, we get for the mosaic spread modified structure factor

$$S_M(q, \theta, \phi) = \int_0^{2\pi} d\beta \int_0^{\frac{\pi}{2}} d\alpha S(q, \theta', \phi') P(\alpha) \quad (\text{A.15})$$

with Eq. (A.13) and Eq. (A.14).

To test these equations, let us apply them to the simple case of a stack of rigid layers with their normals parallel to the z -axis in spherical coordinates. The structure factor is then

$$S(q, \theta, \phi) = \frac{\delta(q - \frac{2\pi h}{D})}{q^2} \delta(\cos \theta - 1) \delta(\phi) \quad (\text{A.16})$$

where $\delta(x)$ is the Dirac delta function. From Eq. (A.14), $\delta(\phi')$ is equivalent to $\delta(\beta - \phi)$. Setting $\beta = \phi$ in Eq. (A.13) gives $\cos \theta' = \cos(\alpha - \theta)$. Then, the mosaic spread modified structure factor $S_M(\mathbf{q})$ is

$$\begin{aligned} S_M(q, \theta, \phi) &= \int d\alpha \int d\beta \frac{\delta(q - \frac{2\pi h}{D})}{q^2} \delta(\cos \theta' - 1) \delta(\beta - \phi) P(\alpha) \\ &= \frac{\delta(q - \frac{2\pi h}{D})}{q^2} \int d\alpha \delta(\cos[\alpha - \theta] - 1) P(\alpha) \\ &= \frac{\delta(q - \frac{2\pi h}{D})}{q^2} P(\theta). \end{aligned} \quad (\text{A.17})$$

Eq. (A.17) describes hemispherical shells with radii of $2\pi h/D$ in the sample q -space. As will be described in the next section, a 2D detector records cross sections of these shells, which give rise to mosaic arcs along $q = 2\pi h/D$.

The structure factor of thermally fluctuating layers is not simple delta functions and gives rise to diffuse scattering. Analysis of the diffuse scattering from a sample with mosaic spread requires Eq. (A.15).

A.2.2 Mosaic Spread: Near Equivalence of Two Methods

In this section, we discuss experimental procedures to probe appropriate q -space to measure the mosaic spread distribution, $P(\alpha)$. In our setup, the angle of incidence between the beam and substrate, denoted by ω , can be varied. A conventional method to measure $P(\alpha)$ is a rocking scan, where one measures the integrated intensity of a given Bragg peak as a function of ω with a fixed detector position. Another method that takes an advantage of an area detector [111] measures the intensity as a function of χ on a two dimensional detector (see Fig. A.5). This method has been used to quantify complete pole figures for thin films with fiber texture (isotropic in-plane orientation) [112]. First, we want to compare the two methods mentioned above and determine their relationship.

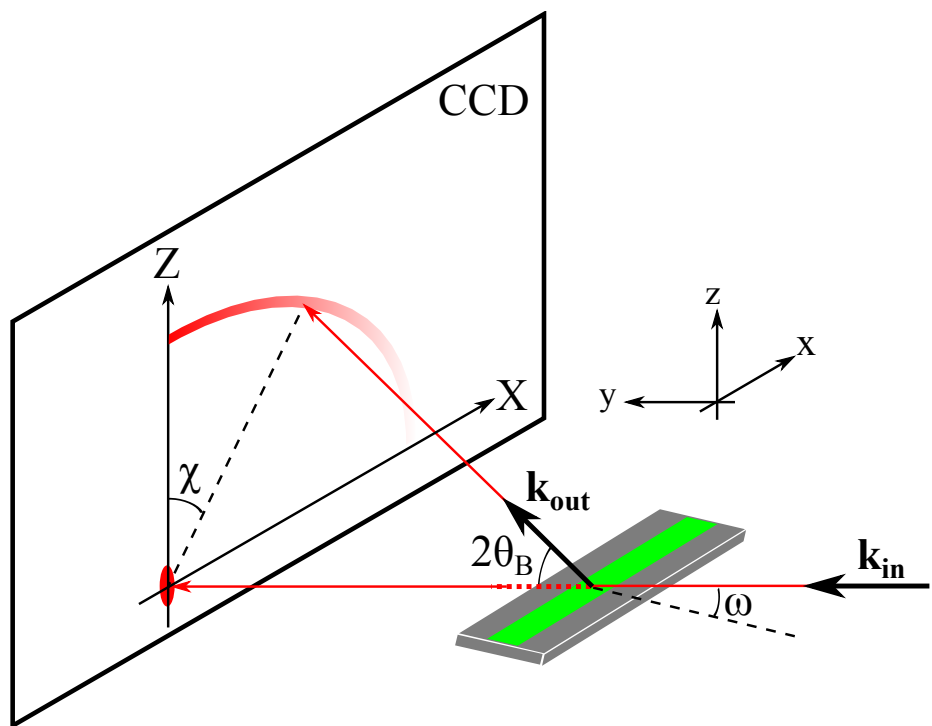


Figure A.5: Notations used in this section. The arc originating from the Z -axis is the mosaic arc due to the mosaic spread distribution.

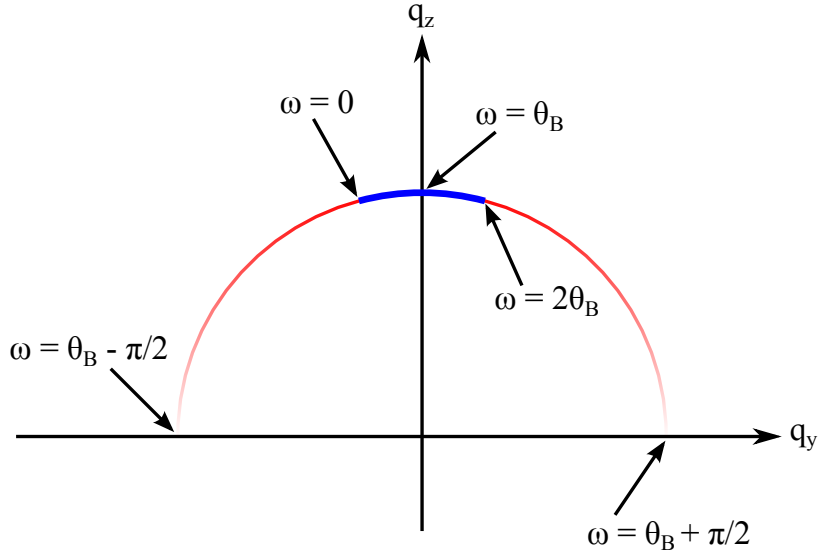


Figure A.6: Rocking scan trace in q -space.

Eq. (3.14) expressed in terms of the coordinates defined in Fig. A.5 is

$$\begin{aligned} q_x &= q \cos \theta \sin \chi \\ q_y &= q (-\sin \theta \cos \omega + \cos \theta \cos \chi \sin \omega) \\ q_z &= q (\sin \theta \sin \omega + \cos \theta \cos \chi \cos \omega). \end{aligned} \quad (\text{A.18})$$

For a rocking scan focused on a particular order, $\chi = 0$ and $\theta = \theta_B$ while ω is varied about θ_B , where θ_B is the Bragg angle. Then,

$$\begin{aligned} q_x &= 0 \\ q_y &= q_B \sin(\omega - \theta_B) \\ q_z &= q_B \cos(\omega - \theta_B), \end{aligned} \quad (\text{A.19})$$

which shows that this scan traces a part of the circular path in the $q_x = 0$ plane as shown in Fig. A.6. As Fig. A.6 shows, however, the rocking scan only probes a small fraction of the entire distribution, limited by $2\theta_B$. As discussed in section 3.3.3, beyond $\omega = 2\theta_B$, the substrate blocks scattering. On the other hand, the ring analysis takes advantage of a two dimensional detector and can probe a substantially wider range of the distribution in principle: approximately $\pm 45^\circ$ at $\omega = \theta_B$. This method is now described.

In the ring method, we set $\omega = \theta_B$ and scan on the detector along $\theta = \theta_B$ as a function of χ . Then, Eq. (A.18) becomes

$$\begin{aligned} q_x &= q \cos \theta_B \sin \chi \\ q_y &= q \sin \theta_B \cos \theta_B (\cos \chi - 1) \\ q_z &= q(\sin^2 \theta_B + \cos^2 \theta_B \cos \chi), \end{aligned} \quad (\text{A.20})$$

where $q = 4\pi \sin \theta_B / \lambda$. For small θ_B , Eq. (A.20) reduces to

$$\begin{aligned} q_x &\approx q \sin \chi \\ q_y &\approx 0 \\ q_z &\approx q \cos \chi. \end{aligned} \quad (\text{A.21})$$

For a sharp Bragg peak, this ring method gives the same mosaic intensity $I(\chi, \theta_B)$ in Eq. (A.21) as the rocking method mosaic intensity $I(\omega - \theta_B)$ in Eq. (A.19) because the mosaic distribution $P(\alpha)$ is in-plane isotropic. Differences occur when diffuse scattering is added. The diffuse scattering intensity is much broader and weaker than the Bragg peaks. In the ring method, it can be estimated as the average from two rings offset on either side from θ_B and subtracted from the θ_B ring.

A.2.3 NFIT

The original NFIT program was written by Dr. Yufeng Liu and described in his thesis. It was used in the Nagle lab, with small updates for data handling, from 2003 until recently. A newer version has been implemented by Michael Jablin that calculates the theoretical structure factor using cylindrical domains appropriate for in-plane correlations [48] rather than rectangular domains appropriate for coherence domains. All these versions approximated the effect of mosaic spread roughly by averaging only in the q_r direction at fixed q_z which means that mosaic rings are approximated as mosaic lines or spikes. The subsequent development described here and not yet adopted by the Nagle lab calculates the structure factor $S(q_r, q_z)$ with rotational symmetry about the z -axis, which eliminates the ϕ' dependence in Eq. (A.15). The program interpolates $S(q_r, q_z)$ in terms of the spherical coordinates q and θ with $\phi = 0$ to perform the double integration in Eq. (A.15). After the mosaic spread

integration, the program performs the q_y integration described in section 2.2.6. For this integration, the calculated S_M is interpolated in terms of q_x , q_y , and q_z .

Note: if the structure factor defined in the Cartesian coordinates is desired (for a case of square domains instead of circular ones), Eq. (A.10 – A.12) can be used instead of Eq. (A.13) and (A.14).

While it is an improvement, the new program also is an approximation because it does not include the unknown form factor $|F(q_z)|$. The mosaic spread integration mixes up intensity at different q_z values, so the separation of $|F(q_z)|$ from $S(\mathbf{q})$ is in principle impossible. One way to deal with this issue would be to combine the SDP program, which determines $|F(q_z)|$, with the NFIT program, but that will end up with too many non-linear parameters. Another possibility is to limit the fitting range to regions close to the meridian. For a small range of integration, it is not unreasonable to assume that the form factor is approximately constant as can be seen from Eq. (A.12) with small q_x , q_y , and α . Therefore, the analysis developed in this appendix ignores the form factor.

A.3 More results from LAXS models

h	k	Model $F(h, k)$							Data $ F(h, k) $	σ_F
		Fit1	Fit2	Fit3	Fit4	Fit5	Fit6	Fit7		
1	-1	-74.0	-71.6	-39.4	-78.4	-77.1	-79.1	-79.8	86.3	3.7
1	0	-94.3	-89.2	-63.1	-98.6	-100.0	-99.6	-100.1	100.0	0.5
1	1	23.7	19.9	19.9	23.9	25.2	24.1	24.2	43.1	2.6
1	2	-6.0	-2.3	-8.3	-6.0	-6.9	-5.9	-6.0	0.0	3.9
1	3	0.3	-3.7	6.9	1.4	2.0	1.5	1.4	8.8	0.2
2	-2	-17.2	-20.2	-28.5	-19.7	-20.4	-20.1	-20.1	18.0	0.6
2	-1	-62.2	-59.1	-53.9	-67.9	-66.5	-65.7	-66.9	76.0	0.4
2	0	-32.1	-31.9	-30.8	-33.2	-33.0	-33.0	-33.1	28.7	0.2
2	1	31.8	30.2	32.3	31.5	31.5	32.1	32.0	39.5	0.4
2	2	-25.0	-24.2	-22.9	-24.0	-23.9	-24.3	-24.3	24.6	0.3
2	3	15.0	15.0	14.8	14.9	14.9	14.9	14.9	14.6	0.1
2	4	-6.1	-5.2	-12.0	-8.6	-8.9	-8.6	-8.5	9.2	0.2
2	5	1.1	-2.4	10.2	6.6	7.0	6.8	6.6	5.6	0.7
2	6	0.1	5.5	-4.0	-7.2	-7.1	-7.0	-7.0	4.1	0.3
3	-2	34.2	33.3	29.9	40.3	40.6	39.9	40.1	33.2	0.8
3	-1	39.4	39.1	27.6	45.5	44.9	44.0	44.4	45.9	0.4
3	0	-3.2	-4.3	-2.3	-4.3	-4.0	-4.1	-4.2	13.2	0.5
3	1	-9.4	-6.9	-11.2	-9.2	-9.6	-9.8	-9.5	0.0	7.1
3	2	14.1	12.4	15.0	14.0	14.3	14.5	14.3	10.2	0.2
3	3	-12.9	-13.7	-12.5	-13.1	-13.1	-13.2	-13.1	13.6	0.2
3	4	8.6	11.7	9.0	9.5	9.4	9.2	9.3	13.0	0.2
3	5	-4.1	-7.9	-7.1	-6.0	-5.9	-5.6	-5.7	9.6	0.1
3	6	1.1	3.6	5.4	3.9	3.9	3.6	3.7	5.6	0.4
4	-3	-18.1	-18.9	-18.0	-20.4	-21.7	-22.6	-21.6	23.0	0.6
4	-2	-48.5	-45.2	-23.9	-53.5	-53.2	-53.5	-53.0	42.8	0.5
4	-1	-17.8	-19.9	-7.8	-19.4	-19.0	-18.7	-18.7	22.6	0.9
4	0	11.3	14.3	7.8	12.7	12.6	12.7	12.6	16.2	0.1
4	1	-2.8	-7.8	-1.0	-4.1	-3.7	-3.7	-3.8	7.2	0.6
4	2	-4.0	1.6	-5.4	-2.9	-3.3	-3.5	-3.3	9.9	0.3
4	3	7.1	3.2	7.8	6.3	6.5	6.7	6.5	0.0	2.1
4	4	-6.5	-5.7	-6.8	-6.4	-6.3	-6.4	-6.4	3.0	0.3
4	5	4.2	6.1	5.0	4.7	4.4	4.3	4.4	4.1	0.2
4	6	-1.8	-4.9	-3.8	-2.8	-2.5	-2.3	-2.5	2.5	1.1

Table A.1: Form factors for $h = 1$ to 4

h	k	Model $F(h, k)$							Data $ F(h, k) $	σ_F
		Fit1	Fit2	Fit3	Fit4	Fit5	Fit6	Fit7		
5	-3	-18.2	-17.8	-26.6	-16.2	-16.4	-17.7	-17.3	15.6	0.6
5	-2	-21.1	-21.4	-19.3	-19.3	-19.3	-19.6	-19.4	16.3	0.2
5	-1	1.8	1.9	4.4	2.0	2.0	2.2	2.2	7.5	0.2
5	0	4.7	4.8	6.4	4.3	4.6	4.5	4.3	6.5	0.1
5	1	-6.1	-8.3	-8.2	-6.1	-6.4	-6.3	-6.1	6.4	0.2
6	-4	-1.9	-1.8	6.9	2.2	2.2	-3.0	-2.8	5.9	0.2
6	-3	-4.3	-4.0	7.8	6.6	6.7	-5.9	-5.9	5.9	0.2
6	-2	-1.4	-1.7	1.5	2.7	2.8	-1.7	-1.8	3.8	0.3
6	-1	0.8	1.1	-2.7	-2.0	-2.2	1.1	1.1	3.4	0.3
6	0	-0.2	-0.5	0.8	0.7	0.7	-0.3	-0.3	3.4	0.1
6	1	-0.2	0.1	1.5	0.6	0.8	-0.2	-0.2	3.9	0.1
6	2	0.3	0.3	-2.0	-1.2	-1.5	0.3	0.3	0.0	0.9
6	3	-0.2	-0.5	0.5	1.0	1.2	-0.2	-0.2	3.5	0.1
6	4	-0.1	0.6	1.5	-0.2	-0.1	0.0	0.0	3.4	0.1
7	-4	-12.8	-12.0	-13.9	-9.8	-9.7	-9.6	-9.6	10.0	0.1
7	-3	-12.8	-13.0	-7.5	-9.6	-9.6	-9.2	-9.4	8.1	0.2
7	-2	1.1	0.9	3.0	0.9	1.0	1.1	1.1	4.2	0.9
7	-1	2.2	2.5	1.8	1.5	1.7	1.7	1.7	3.6	0.2
7	0	-2.4	-3.8	-3.1	-1.8	-2.1	-2.2	-2.2	2.8	0.1
8	0	-0.8	0.1	-1.0	-0.4	0.1	-0.4	-0.4	0.0	0.9
9	-5	-5.6	-5.2	2.5	-0.7	-7.3	-8.7	-8.0	6.1	0.5
9	-4	-5.5	-5.6	1.1	-0.6	-6.6	-8.0	-7.4	5.6	0.5
9	-3	0.5	0.3	-0.7	0.1	0.7	1.1	1.0	0.0	3.3
9	-2	0.9	1.2	-0.2	0.1	1.0	1.4	1.2	3.0	0.4
9	-1	-1.0	-1.7	0.7	-0.1	-1.3	-1.9	-1.7	0.0	1.7
9	0	0.4	1.7	-0.4	0.1	0.6	1.0	0.9	2.2	0.6

Table A.2: Form factors for $h = 5$ to 9

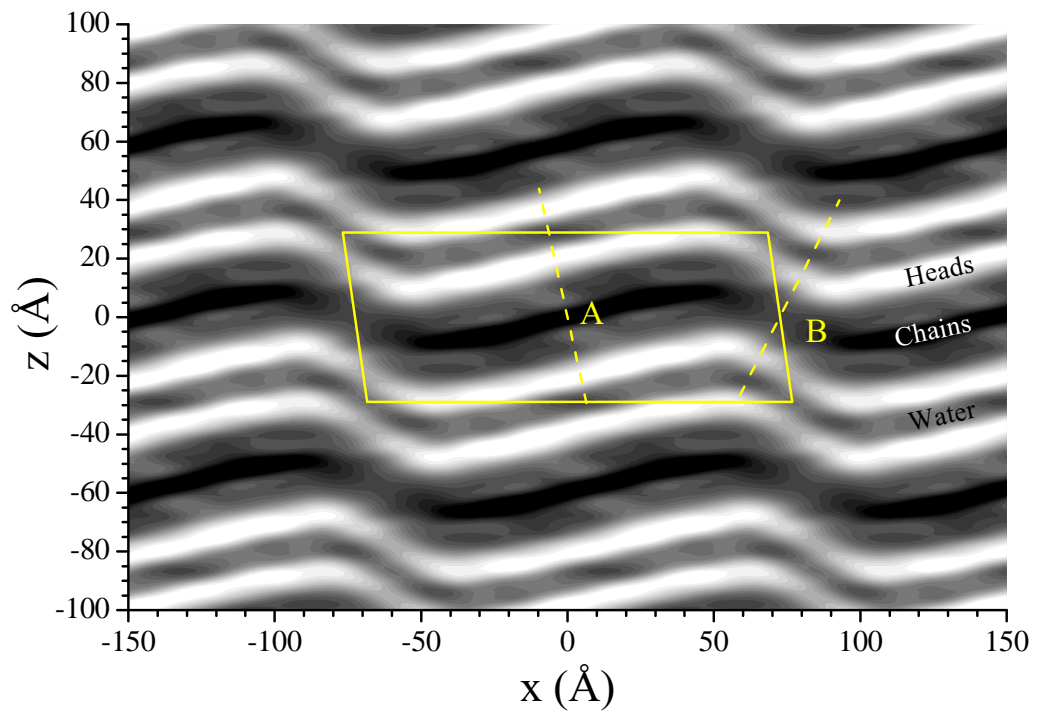


Figure A.7: Two dimensional electron density profile from Fit1.

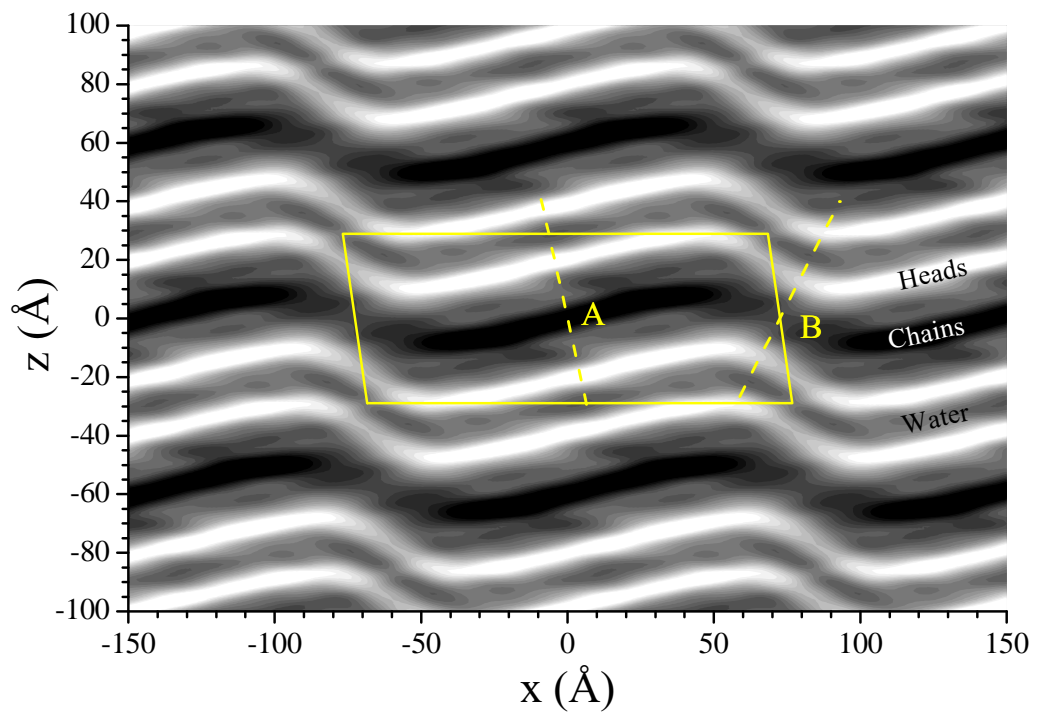


Figure A.8: Two dimensional electron density profile from Fit3.

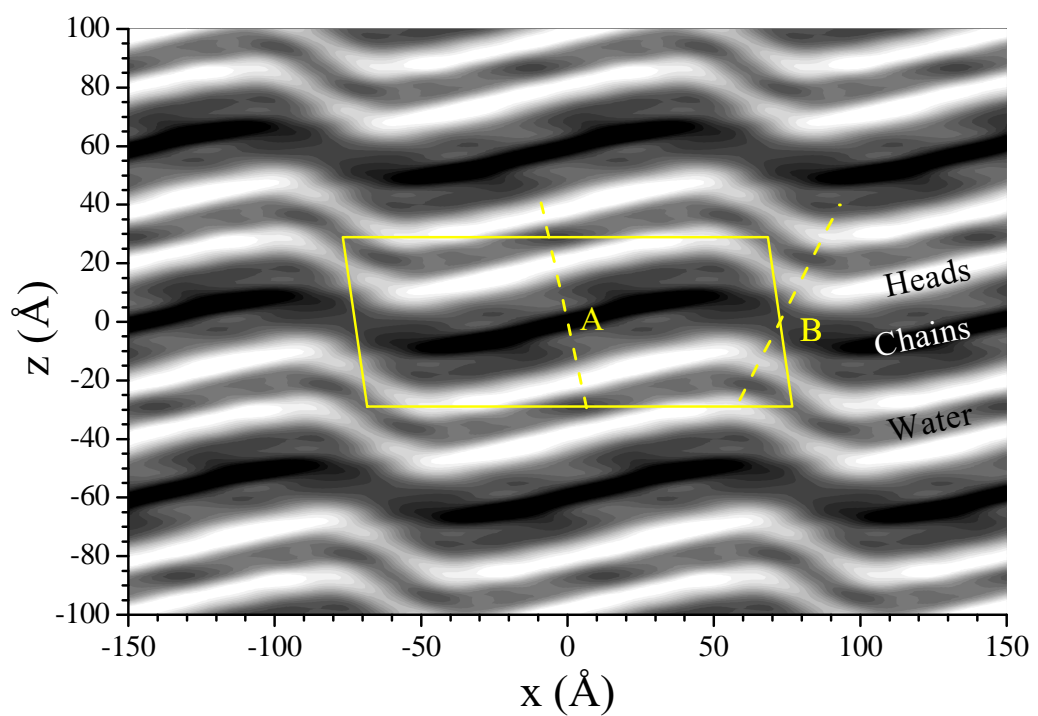


Figure A.9: Two dimensional electron density profile from Fit7.

A.4 Derivation of the contour part of the form factor

In this section, we derive F_C . The ripple profile, $u(x)$ is given by

$$u(x) = \begin{cases} -\frac{A}{\lambda_r - x_0} \left(x + \frac{\lambda_r}{2} \right) & \text{for } -\frac{\lambda_r}{2} \leq x < -\frac{x_0}{2} \\ \frac{A}{x_0} x & \text{for } -\frac{x_0}{2} \leq x \leq \frac{x_0}{2} \\ -\frac{A}{\lambda_r - x_0} \left(x - \frac{\lambda_r}{2} \right) & \text{for } \frac{x_0}{2} < x \leq \frac{\lambda_r}{2} \end{cases} \quad (\text{A.22})$$

The contour part of the form factor is the Fourier transform of the contour function, $C(x, z)$,

$$F_C(\mathbf{q}) = \frac{1}{\lambda_r} \int_{-\frac{\lambda_r}{2}}^{\frac{\lambda_r}{2}} dx \int_{-\frac{D}{2}}^{\frac{D}{2}} dz C(x, z) e^{iq_z z} e^{iq_x x}$$

As discussed in section X, the modulated models allow the electron density to modulate along the ripple direction, x . This means

$$C(x, z) = \begin{cases} f_1 \delta[z - u(x)] & \text{for } -\frac{\lambda_r}{2} \leq x < -\frac{x_0}{2} \\ \delta[z - u(x)] & \text{for } -\frac{x_0}{2} < x < \frac{x_0}{2} \\ f_1 \delta[z - u(x)] & \text{for } \frac{x_0}{2} \leq x < \frac{\lambda_r}{2} \\ + f_2 \delta\left(x + \frac{x_0}{2}\right) \delta\left(z + \frac{A}{2}\right) + f_2 \delta\left(x - \frac{x_0}{2}\right) \delta\left(z - \frac{A}{2}\right). \end{cases} \quad (\text{A.23})$$

The contribution from the minor arm is

$$\begin{aligned} & \frac{1}{\lambda_r} \int_{-\frac{\lambda_r}{2}}^{-\frac{x_0}{2}} dx e^{iq_x x} e^{iq_z u(x)} + \int_{\frac{x_0}{2}}^{\frac{\lambda_r}{2}} dx e^{iq_x x} e^{iq_z u(x)} \\ &= \frac{1}{\lambda_r} \int_{\frac{x_0}{2}}^{\frac{\lambda_r}{2}} dx e^{-i[q_x x - q_z \frac{A}{\lambda_r - x_0} (x - \frac{\lambda_r}{2})]} + \int_{\frac{x_0}{2}}^{\frac{\lambda_r}{2}} dx e^{i[q_x x - q_z \frac{A}{\lambda_r - x_0} (x - \frac{\lambda_r}{2})]} \\ &= \frac{2}{\lambda_r} \int_{\frac{x_0}{2}}^{\frac{\lambda_r}{2}} \cos \left[\left(q_x - q_z \frac{A}{\lambda_r - x_0} \right) x + q_z \frac{A}{\lambda_r - x_0} \frac{\lambda_r}{2} \right] \end{aligned} \quad (\text{A.24})$$

Using a trigonometric identity,

$$\sin u - \sin v = 2 \cos[(u + v)/2] \sin[(u - v)/2],$$

and defining

$$\omega(\mathbf{q}) = \frac{1}{2} (q_x x_0 + q_z A), \quad (\text{A.25})$$

we further simplify Eq. (A.24),

$$\begin{aligned} &= \frac{2}{\lambda_r} \frac{\lambda_r - x_0}{\frac{1}{2} q_x \lambda_r - \omega} \cos \left[\frac{1}{2} \left(\frac{1}{2} q_x \lambda_r + \omega \right) \right] \sin \left[\frac{1}{2} \left(\frac{1}{2} q_x \lambda_r - \omega \right) \right] \\ &= \frac{1}{\lambda_r} \frac{\lambda_r - x_0}{\frac{1}{2} q_x \lambda_r - \omega} \cos \left[\frac{1}{2} \left(\frac{1}{2} q_x \lambda_r + \omega \right) \right] \frac{\sin \left(\frac{1}{2} q_x \lambda_r - \omega \right)}{\cos \left[\frac{1}{2} \left(\frac{1}{2} q_x \lambda_r - \omega \right) \right]} \\ &= \frac{\lambda_r - x_0}{\lambda_r} \frac{\cos \left[\frac{1}{2} \left(\frac{1}{2} q_x \lambda_r + \omega \right) \right]}{\cos \left[\frac{1}{2} \left(\frac{1}{2} q_x \lambda_r - \omega \right) \right]} \frac{\sin \left(\frac{1}{2} q_x \lambda_r - \omega \right)}{\frac{1}{2} q_x \lambda_r - \omega}. \end{aligned} \quad (\text{A.26})$$

Similarly, we calculate the contribution from the major arm,

$$\begin{aligned} \frac{1}{\lambda_r} \int_{-\frac{x_0}{2}}^{\frac{x_0}{2}} dx e^{i \left(\frac{q_z A}{x_0} + q_x \right) x} &= \frac{2}{\lambda_r} \int_0^{\frac{x_0}{2}} dx \cos \left(\frac{q_z A}{x_0} + q_x \right) x \\ &= \frac{x_0 \sin \omega}{\lambda_r \omega} \end{aligned} \quad (\text{A.27})$$

The contribution from the kink region is

$$\begin{aligned} &\frac{1}{\lambda_r} \iint dx dz \left[\delta \left(x + \frac{x_0}{2} \right) \delta \left(z + \frac{A}{2} \right) + \delta \left(x - \frac{x_0}{2} \right) \delta \left(z - \frac{A}{2} \right) \right] e^{iq_x x} e^{iq_z z} \\ &= \frac{2}{\lambda_r} \cos \omega. \end{aligned} \quad (\text{A.28})$$

Therefore,

$$\begin{aligned} F_C(\mathbf{q}) &= \frac{x_0 \sin \omega}{\lambda_r \omega} + f_1 \frac{\lambda_r - x_0}{\lambda_r} \frac{\cos \left[\frac{1}{2} \left(\frac{1}{2} q_x \lambda_r + \omega \right) \right]}{\cos \left[\frac{1}{2} \left(\frac{1}{2} q_x \lambda_r - \omega \right) \right]} \frac{\sin \left(\frac{1}{2} q_x \lambda_r - \omega \right)}{\frac{1}{2} q_x \lambda_r - \omega} \\ &\quad + \frac{2f_2}{\lambda_r} \cos \omega \end{aligned} \quad (\text{A.29})$$

some additional models. We write the form factor as

$$F(\mathbf{q}) = F_C^M(\mathbf{q}) F_T^M(\mathbf{q}) + f_1 F_C^m(\mathbf{q}) F_T^m(\mathbf{q}) + f_2 F_C^k(\mathbf{q}) F_T^k(\mathbf{q}) \quad (\text{A.30})$$

such that

$$F_C^M = \frac{x_0}{\lambda_r} \frac{\sin \omega}{\omega} \quad (\text{A.31})$$

$$F_C^m = \frac{\lambda_r - x_0}{\lambda_r} \frac{\cos \left[\frac{1}{2} \left(\frac{1}{2} q_x \lambda_r + \omega \right) \right]}{\cos \left[\frac{1}{2} \left(\frac{1}{2} q_x \lambda_r - \omega \right) \right]} \frac{\sin \left(\frac{1}{2} q_x \lambda_r - \omega \right)}{\frac{1}{2} q_x \lambda_r - \omega} \quad (\text{A.32})$$

$$F_C^k = \frac{2}{\lambda_r} \cos \omega. \quad (\text{A.33})$$

A.5 Rotation of a Two-Dimensional Function

Let us consider rotating a function, $f(x, z)$ in two dimensions by an angle, ψ , in the counterclockwise direction (see Fig. X). This is easily achieved by rotating the coordinate system by ψ in the clockwise direction. Let rotated coordinates be x' and z' . A point in the original coordinates, (x, z) , is written as (x', z') in the new coordinates. More specifically, the point P is written as $\mathbf{P} = x\hat{\mathbf{x}} + z\hat{\mathbf{z}} = x'\hat{\mathbf{x}}' + z'\hat{\mathbf{z}}'$. $\hat{\mathbf{x}}$ and $\hat{\mathbf{z}}$ in the $x'z'$ coordinate system are written as

$$\hat{\mathbf{x}} = \cos \psi \hat{\mathbf{x}}' + \sin \psi \hat{\mathbf{z}}' \quad (\text{A.34})$$

$$\hat{\mathbf{z}} = -\sin \psi \hat{\mathbf{x}}' + \cos \psi \hat{\mathbf{z}}'. \quad (\text{A.35})$$

Pluggin these in $\mathbf{P} = x\hat{\mathbf{x}} + z\hat{\mathbf{z}}$ leads to

$$x' = x \cos \psi - z \sin \psi \quad (\text{A.36})$$

$$z' = z \cos \psi + x \sin \psi, \quad (\text{A.37})$$

the inverse of which is

$$x = x' \cos \psi + z' \sin \psi \quad (\text{A.38})$$

$$z = -x' \sin \psi + z' \cos \psi. \quad (\text{A.39})$$

Using the latter equations, $f(x, z)$ can be expressed in terms of x' and z' . The resulting function $f(x', z')$ is the rotated version of $f(x, z)$.

As an example, let us consider a Dirac delta function located at $(x, z) = (0, Z_{\text{H}})$, that is, $f(x, z) = \delta(x)\delta(z - Z_{\text{H}})$. After the rotation by ψ , it becomes

$$\begin{aligned} f(x, z) &\rightarrow \delta(x \cos \psi + z \sin \psi)\delta(-x \sin \psi + z \cos \psi - Z_{\text{H}}) \\ &= \frac{\delta(x + z \tan \psi)}{|\cos \psi|} \frac{\delta(-x \sin \psi \cos \psi + z \cos^2 \psi - Z_{\text{H}} \cos \psi)}{1/|\cos \psi|} \\ &= \delta(x + z \tan \psi)\delta(z \tan \psi \sin \psi \cos \psi + z \cos^2 \psi - Z_{\text{H}} \cos \psi) \\ &= \delta(x + z \tan \psi)\delta(z - Z_{\text{H}} \cos \psi), \end{aligned}$$

which is a part of the expression for $T_{\psi}(x, z)$ in the simple delta function model.

A.6 Derivation of the transbilayer part of the form factor in the 2G hybrid model

In this section, we derive the trasbilayer part of the form factor calculated from the 2G hybrid model discussed in section X. Defining $z' = -x \sin \psi + z \cos \psi$, the Fourier transform of a Gaussian function along the line tilted from z -axis by ψ is

$$\begin{aligned} & \iint dz dx \rho_{\text{Hi}} \exp \left\{ -\frac{(z' - Z_{\text{Hi}})^2}{2\sigma_{\text{Hi}}^2} \right\} \delta(x \cos \psi + z \sin \psi) e^{iq_x x} e^{iq_z z} \\ &= \frac{1}{\cos \psi} \int_{-\frac{D}{2}}^{\frac{D}{2}} dz \rho_{\text{Hi}} \exp \left\{ -\frac{(z - Z_{\text{Hi}} \cos \psi)^2}{2\sigma_{\text{Hi}}^2 \cos^2 \psi} + i(q_z - q_x \tan \psi) z \right\} \\ & \approx \rho_{\text{Hi}} \sqrt{2\pi} \sigma_{\text{Hi}} \exp \left\{ i\alpha Z_{\text{Hi}} - \frac{1}{2} \alpha^2 \sigma_{\text{Hi}}^2 \right\} \end{aligned} \quad (\text{A.40})$$

with $\alpha = q_z \cos \psi - q_x \sin \psi$. Using Eq. (A.40) and adding the other side of the bilayer and the terminal methyl term, we get

$$F_{\text{G}} = \sqrt{2\pi} \left[-\rho_{\text{M}} \sigma_{\text{M}} \exp \left\{ -\frac{1}{2} \alpha^2 \sigma_{\text{M}}^2 \right\} + \sum_{i=1}^{\text{1 or 2}} 2\rho_{\text{Hi}} \sigma_{\text{Hi}} \cos(\alpha Z_{\text{Hi}}) \exp \left\{ -\frac{1}{2} \alpha^2 \sigma_{\text{Hi}}^2 \right\} \right]. \quad (\text{A.41})$$

The strip part of the model in the minus fluid convention is

$$\rho_{\text{S}}(z) = \begin{cases} -\Delta\rho & \text{for } 0 \leq z < Z_{\text{CH}_2} \cos \psi, \\ 0 & \text{for } Z_{\text{W}} \cos \psi \leq z \leq D/2, \end{cases} \quad (\text{A.42})$$

where $\Delta\rho = \rho_{\text{W}} - \rho_{\text{CH}_2}$. Then, the corresponding Fourier transform is

$$\begin{aligned} F_{\text{S}} &= \iint dz dx e^{iq_x x} e^{iq_z z} \rho_{\text{S}}(z) \delta(x \cos \psi + z \sin \psi) \\ &= \frac{2}{\cos \psi} \int_0^{Z_{\text{CH}_2} \cos \psi} dz \cos \left(\frac{\alpha}{\cos \psi} z \right) (-\Delta\rho) \\ &= -2\Delta\rho \frac{\sin(\alpha Z_{\text{CH}_2})}{\alpha}. \end{aligned} \quad (\text{A.43})$$

The bridging part of the model in the minus fluid convention is

$$\rho_B(x, z) = \frac{\Delta\rho}{2} \cos\left[\frac{-\pi}{\Delta Z_H}(z' - Z_W)\right] - \frac{\Delta\rho}{2} \quad (\text{A.44})$$

for $Z_{CH_2} \cos \psi < z < Z_W \cos \psi$, and 0 otherwise. Here, $\Delta Z_H = Z_W - Z_{CH_2}$. Then, for the strip part of the form factor, we have

$$\begin{aligned} F_B &= \iint dz dx e^{iq_x x} e^{iq_z z} \delta(x \cos \psi + z \sin \psi) \rho_B(x, z) \\ &= \frac{\Delta\rho}{\cos \psi} \int_{Z_{CH_2} \cos \psi}^{Z_W \cos \psi} dz \cos\left(\alpha \frac{z}{\cos \psi}\right) \left\{ \cos\left[-\frac{\pi}{\Delta Z_H} \left(\frac{z}{\cos \psi} - Z_W\right)\right] - 1 \right\} \\ &= \Delta\rho \left\{ \frac{\Delta Z_H \sin\left[\frac{\pi(-u+Z_W)}{\Delta Z_H} + \alpha u\right]}{-2\pi + 2\alpha\Delta Z_H} + \frac{\Delta Z_H \sin\left[\frac{\pi(u-Z_W)}{\Delta Z_H} + \alpha u\right]}{2\pi + 2\alpha\Delta Z_H} - \frac{\sin(\alpha u)}{\alpha} \right\} \Big|_{Z_{CH_2}}^{Z_W} \\ &= -\frac{\Delta\rho}{\alpha} [\sin(\alpha Z_W) - \sin(\alpha Z_{CH_2})] \\ &\quad + \frac{\Delta\rho}{2} \left(\frac{1}{\alpha + \frac{\pi}{\Delta Z_H}} + \frac{1}{\alpha - \frac{\pi}{\Delta Z_H}} \right) [\sin(\alpha Z_W) + \sin(\alpha Z_{CH_2})]. \end{aligned} \quad (\text{A.45})$$

Because our X-ray scattering intensity was measured in a relative scale, an overall scaling factor was necessary for a non linear least square fitting procedure. This means that $\Delta\rho$ can be absorbed in the scaling factor. Doing so means that the values of ρ_{Hi} and ρ_M resulting from a fitting procedure are relative to $\Delta\rho$. One way to have these parameters in the absolute scale is to integrate the bilayer electron density over the lipid volume and equate the result to the total number of electrons in the lipid, which can easily be calculated from the chemical formula. For the ripple phase study in this thesis, the absolute values of the electron density were not of importance, so the discussion was omitted in the main text.

A.7 Correction due to refractive index

q_z needs to be corrected for index of refraction [50].

Let θ' and λ' be the true scattering angle and wavelength within the sample. The wavelength by an energy analyzer, λ , and the scattering angle calculated from a position on a CCD detector, θ are apparent. The correction is not necessary in the horizontal direction. The Snell's law in Fig. X gives

$$n \cos \theta = n' \cos \theta' \quad (\text{A.46})$$

$$n\lambda = n'\lambda'. \quad (\text{A.47})$$

For low angle X-ray scattering, the momentum transfer along z direction is

$$q_z = \frac{4\pi \sin \theta'}{\lambda'} \quad (\text{A.48})$$

$$= \frac{4\pi n'}{n\lambda} \sin \theta' \quad (\text{A.49})$$

$$= \frac{4\pi n'}{n\lambda} \sqrt{1 - \cos^2 \theta'} \quad (\text{A.50})$$

$$= \frac{4\pi n'}{n\lambda} \sqrt{1 - \left(\frac{n}{n'} \cos \theta\right)^2}. \quad (\text{A.51})$$

The apparent scattering angle, θ , is directly related to the vertical pixel position, p_z , by

$$\theta = \frac{1}{2} \tan^{-1} \left(\frac{p_z}{S} \right), \quad (\text{A.52})$$

where S is the sample-to-detector distance. The typical units of S and p_z are in mm. In our experimental setup, $n = 1$ and $n' = 0.9999978$ for lipids at $\lambda = 1.18 \text{ \AA}$. $S = 359.7 \text{ mm}$.

A.8 Thin Rod Model of the ripple phase

The thin rod model will be applied to the ripple phase WAXS. In this model, electron density of lipid chains are described as delta functions and lipid head groups are assumed not to contribute to scattering. Since the molecular packing of the major side of ripple phase is hypothesized to be gel-like, the model may be adequate. First, we will study diffraction from chains packed in gel phase manner whose system size is infinite but whose packing plane make an angle ξ with the xy plane. This infinite case is adequate for indexing the ripple Bragg peaks while it ignores the peak broadening effect. The system will later be truncated along the ripple direction to see the effect of the finite size on peak broadening. Finally, in-plane powder will be taken into account to derive a peak intensity pattern.

First, let us calculate the positions of the diffraction peaks from a two dimensional orthorhombic lattice whose plane makes an angle ξ with respect to the xy plane and extends to infinity. As a unit cell, we will take a parallelepipedon containing two rods, one located at the origin and the other located at the center (Fig. A.10). The lattice vectors are $\mathbf{a}_1 = a_1 \cos \xi \hat{\mathbf{x}} + a_1 \sin \xi \hat{\mathbf{z}}$ and $\mathbf{a}_2 = a_2 \hat{\mathbf{y}}$. There are other choices for how the lattice is oriented with respect to the ripple direction, which should be considered as well. Then, the Laue conditions are given by

$$2\pi h = \mathbf{q} \cdot \mathbf{a}_1 = (a_1 \cos \xi) q_x + (a_1 \sin \xi) q_z \quad (\text{A.53})$$

$$2\pi k = \mathbf{q} \cdot \mathbf{a}_2 = a_2 q_y, \quad (\text{A.54})$$

with h and k being zero or integer. Let us define the chain tilt angle θ to be the angle between the stacking z direction and the chain direction. We also define ϕ to represent the direction into which chains are tilted. In other words, θ and ϕ are usual spherical coordinates with respect to the ripple x , y , and z axes, not the local bilayer Cartesian axes. With this choice of coordinates, chains are tilted with respect to the local bilayer normal if $\theta = 0$. $\theta = \xi$ and $\phi = \pi$ gives chains parallel to the local bilayer normal, or $\theta_t = 0$. It would be good to work out the relation between θ and θ_t , θ_t being the chain tilt with respect to the local bilayer normal.

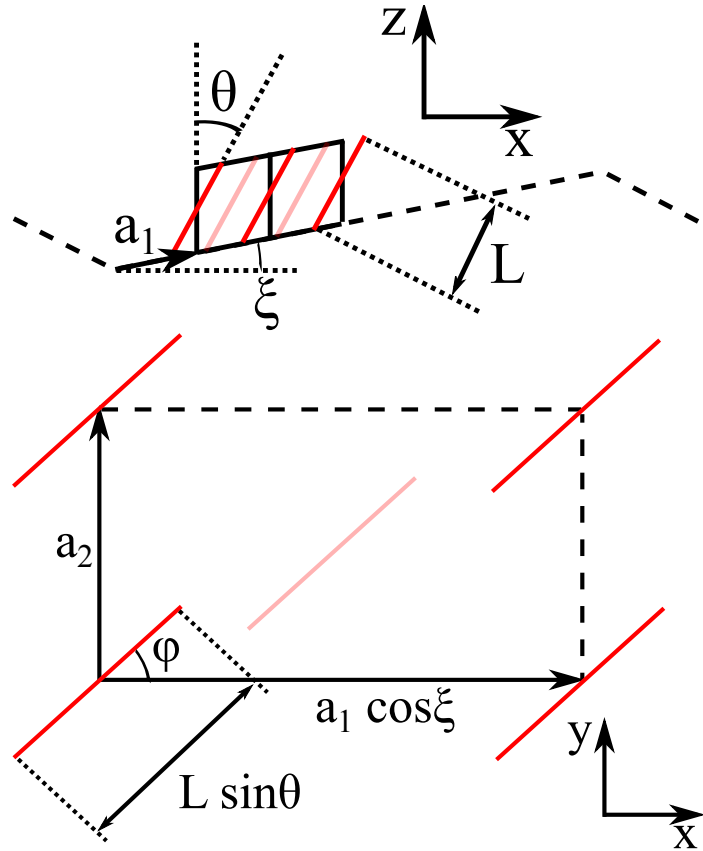


Figure A.10: Unit cell for chain packing in the major arm. (top) Projection of the unit cell in the xz -plane. The unit cell is taken as a parallelepipedon shown by black solid lines, each unit cell containing two chains. Chains located at the center of the unit cell are drawn as opaque red lines while chains at the lattice points are drawn as solid red lines. The dash line indicates the mid-plane of a rippling bilayer. Chains are tilted with respect to the stacking z direction by θ and the major arm is tilted with respect to the ripple x direction by ξ . The chain length is denoted by L . \mathbf{a}_1 and \mathbf{a}_2 are orthorhombic unit cell vectors. (bottom) Projection of the unit cell in the xy -plane. $\phi = 0$ means chains are tilted in the xz plane and $\phi = \pi/2$ means chains are titled into the direction perpendicular to the ripple direction.

The electron density, assuming a delta function for each chain, is given by

$$\rho(\mathbf{r}) = \delta(x - \alpha z, y - \beta z) + \quad (\text{A.55})$$

$$\delta \left[x - \frac{a_1 \cos \xi}{2} - \alpha \left(z - \frac{a_1 \sin \xi}{2} \right), y - \frac{a_2}{2} - \beta \left(z - \frac{a_1 \sin \xi}{2} \right) \right], \quad (\text{A.56})$$

where $\alpha = \tan \theta \cos \phi$ and $\beta = \tan \theta \sin \phi$. The first rod extends for

$$-L/2 \sin \theta \cos \phi \leq x \leq L/2 \sin \theta \cos \phi \quad (\text{A.57})$$

$$-L/2 \sin \theta \sin \phi \leq y \leq L/2 \sin \theta \sin \phi \quad (\text{A.58})$$

$$-L/2 \cos \theta \leq z \leq L/2 \cos \theta, \quad (\text{A.59})$$

and the second rod for

$$-L/2 \sin \theta \cos \phi + a_1/2 \cos \xi \leq x \leq L/2 \sin \theta \cos \phi + a_1/2 \cos \xi \quad (\text{A.60})$$

$$-L/2 \sin \theta \sin \phi + a_2/2 \leq y \leq L/2 \sin \theta \sin \phi + a_2/2 \quad (\text{A.61})$$

$$-L/2 \cos \theta + a_1/2 \sin \xi \leq z \leq L/2 \cos \theta + a_1/2 \sin \xi. \quad (\text{A.62})$$

Then, the form factor is given by

$$F(\mathbf{q}) = \int dx \int dy \int dz \rho(\mathbf{r}) e^{i\mathbf{q}\cdot\mathbf{r}} \quad (\text{A.63})$$

$$\begin{aligned} &= \int_{-\frac{L}{2} \cos \theta}^{\frac{L}{2} \sin \theta} dz e^{i(\alpha q_x + \beta q_y + q_z)z} + \\ &\int_{-\frac{L}{2} \cos \theta + \frac{a_1}{2} \sin \xi}^{\frac{L}{2} \cos \theta + \frac{a_1}{2} \sin \xi} dz e^{\frac{i}{2}[q_x(a_1 \cos \xi - \alpha a_1 \sin \xi) + q_y(a_2 - \beta a_1 \sin \xi)]} e^{i(\alpha q_x + \beta q_y + q_z)z} \\ &= \left[1 + e^{\frac{i}{2}(a_1 \cos \xi q_x + a_1 \sin \xi q_z + a_2 q_y)} \right] \frac{2}{\gamma} \sin \left(\frac{\gamma L \cos \theta}{2} \right) \\ &= [1 + e^{i\pi(h+k)}] \frac{2}{\gamma} \sin \left(\frac{\gamma L \cos \theta}{2} \right), \end{aligned} \quad (\text{A.64})$$

where $\gamma = \alpha q_x + \beta q_y + q_z$. Eq. A.64 shows that peaks with $h+k$ being odd is extinct. For $h+k$ even, we have

$$F(\mathbf{q}) = \frac{4}{\gamma} \sin \left(\frac{\gamma L \cos \theta}{2} \right). \quad (\text{A.65})$$

For (20) peak, $q_y = 0$ and $4\pi = a_1 \cos \xi q_x + a_1 \sin \xi q_z$. The second equation can be rewritten to give

$$q_z = -\frac{1}{\tan \xi} q_x + \frac{4\pi}{a_1 \sin \xi} \quad (\text{A.66})$$

which defines a straight line in $q_x q_z$ -plane along which (20) Bragg rod appears. Eq. A.65 has a peak at $\gamma = 0$. Hence, the maximum intensity of (20) peak is at q_x and q_z that satisfy Laue conditions and $\gamma = 0$. This gives three equations and three unknowns. Explicitly written, we have

$$q_y = 0 \quad (\text{A.67})$$

$$4\pi = a_1 \cos \xi q_x + a_1 \sin \xi q_z \quad (\text{A.68})$$

$$0 = \tan \theta \cos \phi q_x + q_z \quad (\text{A.69})$$

Solving these, we get

$$q_x = \frac{4\pi}{a_1 \cos \xi (1 - \tan \theta_t \cos \phi \tan \xi)} \quad (\text{A.70})$$

$$q_z = \frac{-4\pi \tan \theta_t \cos \phi}{a_1 \cos \xi (1 - \tan \theta_t \cos \phi \tan \xi)} \quad (\text{A.71})$$

For $\phi = \pi/2$, we have $q_x = 4\pi/(a_1 \cos \xi)$ and $q_z = 0$, so one would expect to see a peak on the equator, the case of which is similar to $L_{\beta I}$ phase in gel phase. To get back to ordinary gel phase, ξ should be set equal to zero.

For any (hk) line, we again have three equations and three unknowns as

$$2\pi h = q_x a_1 \cos \xi + q_z a_1 \sin \xi \quad (\text{A.72})$$

$$2\pi k = q_y a_2 \quad (\text{A.73})$$

$$0 = q_x \tan \theta_t \cos \phi + \frac{2\pi k}{a_2} \tan \theta_t \sin \phi + q_z \quad (\text{A.74})$$

Solving for q_x , q_y , and q_z , we obtain

$$q_x = \frac{2\pi(h + ka\beta \sin \xi)}{a_1 \cos \xi(1 - \alpha \tan \xi)} \quad (\text{A.75})$$

$$q_y = \frac{2\pi k}{a_2} \quad (\text{A.76})$$

$$q_z = \frac{-2\pi(h\alpha + ka\beta \cos \xi)}{a_1 \cos \xi(1 - \alpha \tan \xi)}, \quad (\text{A.77})$$

where $a = a_1/a_2$.

Bibliography

- [1] PF Fahey and WW Webb. Lateral diffusion in phospholipid bilayer membranes and multilamellar liquid crystals. *Biochemistry*, 17(15):3046–3053, 1978.
- [2] A. Tardieu, Vittorio Luzzati, and F.C. Reman. Structure and polymorphism of the hydrocarbon chains of lipids: A study of lecithin-water phases. *Journal of Molecular Biology*, 75(4):711 – 733, 1973.
- [3] Elizabeth J Luna and Harden M McConnell. The intermediate monoclinic phase of phosphatidylcholines. *Biochimica et Biophysica Acta (BBA)-Biomembranes*, 466(3):381–392, 1977.
- [4] Bruce R. Copeland and Harden M. McConnel. The rippled structure in bi-layer membranes of phosphatidylcholine and binary mixtures of phosphatidyl-choline and cholesterol. *Biochimica et Biophysica Acta (BBA) - Biomembranes*, 599(1):95 – 109, 1980.
- [5] D Ruppel and E Sackmann. On defects in different phases of two-dimensional lipid bilayers. *Journal de Physique*, 44(9):1025–1034, 1983.
- [6] JAN Zasadzinski and MB Schneider. Ripple wavelength, amplitude, and configuration in lyotropic liquid crystals as a function of effective headgroup size. *Journal de Physique*, 48(11):2001–2011, 1987.
- [7] JA Zasadzinski, J Schneir, J Gurley, V Elings, and PK Hansma. Scanning tunneling microscopy of freeze-fracture replicas of biomembranes. *Science*, 239(4843):1013–1015, 1988.
- [8] Daniel C. Wack and Watt W. Webb. Synchrotron x-ray study of the modulated lamellar phase $p\beta'$ in the lecithin-water system. *Phys. Rev. A*, 40:2712–2730, Sep 1989.

- [9] RJ Wittebort, CF Schmidt, and RG Griffin. Solid-state carbon-13 nuclear magnetic resonance of the lecithin gel to liquid-crystalline phase transition. *Biochemistry*, 20(14):4223–4228, 1981.
- [10] Marilyn B Schneider, WINSTON K Chan, and Watt W Webb. Fast diffusion along defects and corrugations in phospholipid p beta, liquid crystals. *Biophysical journal*, 43(2):157–165, 1983.
- [11] GS Smith, EB Sirota, CR Safinya, and Noel A Clark. Structure of the 1 β phases in a hydrated phosphatidylcholine multimembrane. *Physical review letters*, 60(9):813, 1988.
- [12] Rainer Fischer, Mariola Fotin-Mleczek, Hansjrg Hufnagel, and Roland Brock. Break on through to the other sidebiophysics and cell biology shed light on cell-penetrating peptides. *ChemBioChem*, 6(12):2126–2142, 2005.
- [13] Alain Joliot and Alain Prochiantz. Transduction peptides: from technology to physiology. *Nat Cell Biol*, 6(3), 2004.
- [14] Maria Lindgren, Mattias Hillbrink, Alain Prochiantz, and lo Langel. Cell-penetrating peptides. *Trends in Pharmacological Sciences*, 21(3):99 – 103, 2000.
- [15] Alan D. Frankel and Carl O. Pabo. Cellular uptake of the tat protein from human immunodeficiency virus. *Cell*, 55(6):1189 – 1193, 1988.
- [16] Maurice Green and Paul M. Loewenstein. Autonomous functional domains of chemically synthesized human immunodeficiency virus tat trans-activator protein. *Cell*, 55(6):1179 – 1188, 1988.
- [17] Eric Viks, Priscille Brodin, and Bernard Lebleu. Hiv-1 tat protein basic domain rapidly translocates through the plasma membrane and accumulates in the cell nucleus. *Journal of Biological Chemistry*, 272(25):16010–16017, 1997.
- [18] Gohar Ter-Avetisyan, Gisela Tnnemann, Danny Nowak, Matthias Nitschke, Andreas Herrmann, Marek Drab, and M. Cristina Cardoso. Cell entry of arginine-rich peptides is independent of endocytosis. *Journal of Biological Chemistry*, 284(6):3370–3378, 2009.

- [19] Gisela Tnnemann, Robert M. Martin, Simone Haupt, Christoph Patsch, Frank Edenhofer, and M. Cristina Cardoso. Cargo-dependent mode of uptake and bioavailability of tat-containing proteins and peptides in living cells. *The FASEB Journal*, 20(11):1775–1784, 2006.
- [20] Andr Ziegler, Pierluigi Nervi, Markus Drrenberger, and Joachim Seelig. The cationic cell-penetrating peptide cpptat derived from the hiv-1 protein tat is rapidly transported into living fibroblasts: optical, biophysical, and metabolic evidence. *Biochemistry*, 44(1):138–148, 2005. PMID: 15628854.
- [21] J. S. Wadia, R. V. Stan, and S. F. Dowdy. Transducible tat-ha fusogenic peptide enhances escape of tat-fusion proteins after lipid raft macropinocytosis. *Nature Medicine*, 10(3):310–315, 2004.
- [22] I. M. Kaplan, J. S. Wadia, and S. F. Dowdy. Cationic tat peptide transduction domain enters cells by macropinocytosis. *Journal of Controlled Release*, 102(1):247–253, 2005.
- [23] David A Mann and Alan D Frankel. Endocytosis and targeting of exogenous hiv-1 tat protein. *The EMBO journal*, 10(7):1733, 1991.
- [24] Jean Philippe Richard, Kamran Melikov, Hilary Brooks, Paul Prevot, Bernard Lebleu, and Leonid V Chernomordik. Cellular uptake of unconjugated tat peptide involves clathrin-dependent endocytosis and heparan sulfate receptors. *Journal of Biological Chemistry*, 280(15):15300–15306, 2005.
- [25] Simon W Jones, Richard Christison, Ken Bundell, Catherine J Voyce, Sarah Brockbank, Peter Newham, and Mark A Lindsay. Characterisation of cell-penetrating peptide-mediated peptide delivery. *British journal of pharmacology*, 145(8):1093–1102, 2005.
- [26] Agnès Vendeville, Fabienne Rayne, Anne Bonhoure, Nadir Bettache, Philippe Montcourrier, and Bruno Beaumelle. Hiv-1 tat enters t cells using coated pits before translocating from acidified endosomes and eliciting biological responses. *Molecular biology of the cell*, 15(5):2347–2360, 2004.
- [27] Christina Foerg, Urs Ziegler, Jimena Fernandez-Carneado, Ernest Giralt, Robert Rennert, Annette G Beck-Sickinger, and Hans P Merkle. Decoding the

- entry of two novel cell-penetrating peptides in hela cells: lipid raft-mediated endocytosis and endosomal escape. *Biochemistry*, 44(1):72–81, 2005.
- [28] Antonio Fittipaldi and Mauro Giacca. Transcellular protein transduction using the tat protein of hiv-1. *Advanced drug delivery reviews*, 57(4):597–608, 2005.
- [29] Ying Liu, Melina Jones, Cynthia M Hingtgen, Guojun Bu, Nick Laribee, Rudolph E Tanzi, Robert D Moir, Avindra Nath, and Johnny J He. Uptake of hiv-1 tat protein mediated by low-density lipoprotein receptor-related protein disrupts the neuronal metabolic balance of the receptor ligands. *Nature medicine*, 6(12):1380–1387, 2000.
- [30] Vladimir P Torchilin, Ram Rammohan, Volkmar Weissig, and Tatyana S Levchenko. Tat peptide on the surface of liposomes affords their efficient intracellular delivery even at low temperature and in the presence of metabolic inhibitors. *Proceedings of the National Academy of Sciences*, 98(15):8786–8791, 2001.
- [31] Vladimir P Torchilin, Tatyana S Levchenko, Ram Rammohan, Natalia Volodina, Brigitte Papahadjopoulos-Sternberg, and Gerard GM D’Souza. Cell transfection in vitro and in vivo with nontoxic tat peptide-liposome–dna complexes. *Proceedings of the National Academy of Sciences*, 100(4):1972–1977, 2003.
- [32] Carsten Rudolph, Christian Plank, James Lausier, Ulrike Schillinger, Rainer H Müller, and Joseph Rosenecker. Oligomers of the arginine-rich motif of the hiv-1 tat protein are capable of transferring plasmid dna into cells. *Journal of Biological Chemistry*, 278(13):11411–11418, 2003.
- [33] Ashok Chauhan, Akshay Tikoo, Arvinder K Kapur, and Mahavir Singh. The taming of the cell penetrating domain of the hiv tat: myths and realities. *Journal of Controlled Release*, 117(2):148–162, 2007.
- [34] JM Sabatier, E Vives, K Mabrouk, ABDELAZIZ Benjouad, H Rochat, A Duval, B Hue, and ELMOSTAFA Bahraoui. Evidence for neurotoxic activity of tat from human immunodeficiency virus type 1. *Journal of virology*, 65(2):961–967, 1991.

- [35] A. Mishra, V. D. Gordon, L. H. Yang, R. Coridan, and G. C. L. Wong. Hiv tat forms pores in membranes by inducing saddle-splay curvature: Potential role of bidentate hydrogen bonding. *Angewandte Chemie-International Edition*, 47(16):2986–2989, 2008.
- [36] S. T. Yang, E. Zaitseva, L. V. Chernomordik, and K. Melikov. Cell-penetrating peptide induces leaky fusion of liposomes containing late endosome-specific anionic lipid. *Biophysical Journal*, 99(8):2525–2533, 2010.
- [37] P. E. G. Thoren, D. Persson, E. K. Esbjorner, M. Goksor, P. Lincoln, and B. Norden. Membrane binding and translocation of cell-penetrating peptides. *Biochemistry*, 43(12):3471–3489, 2004.
- [38] SD Krämer and H Wunderli-Allenspach. No entry for tat (44–57) into liposomes and intact mdck cells: novel approach to study membrane permeation of cell-penetrating peptides. *Biochimica et Biophysica Acta (BBA)-Biomembranes*, 1609(2):161–169, 2003.
- [39] C. Ciobanasu, J. P. Siebrasse, and U. Kubitscheck. Cell-penetrating hiv1 tat peptides can generate pores in model membranes. *Biophysical Journal*, 99(1):153–62, 2010.
- [40] Philip A Gurnev, Sung-Tae Yang, Kamran C Melikov, Leonid V Chernomordik, and Sergey M Bezrukov. Cationic cell-penetrating peptide binds to planar lipid bilayers containing negatively charged lipids but does not induce conductive pores. *Biophysical journal*, 104(9):1933–1939, 2013.
- [41] H. D. Herce, A. E. Garcia, J. Litt, R. S. Kane, P. Martin, N. Enrique, A. Rebolledo, and V. Milesi. Arginine-rich peptides destabilize the plasma membrane, consistent with a pore formation translocation mechanism of cell-penetrating peptides. *Biophysical Journal*, 97(7):1917–1925, 2009.
- [42] Y. C. Su, A. J. Waring, P. Ruchala, and M. Hong. Membrane-bound dynamic structure of an arginine-rich cell-penetrating peptide, the protein transduction domain of hiv tat, from solid-state nmr. *Biochemistry*, 49(29):6009–6020, 2010.

- [43] S. Shojania and J. D. O’Neil. Hiv-1 tat is a natively unfolded protein - the solution conformation and dynamics of reduced hiv-1 tat-(1-72) by nmr spectroscopy. *Journal of Biological Chemistry*, 281(13):8347–8356, 2006.
- [44] P. Bayer, M. Kraft, A. Ejchart, M. Westendorp, R. Frank, and P. Rosch. Structural studies of hiv-1 tat protein. *Journal of Molecular Biology*, 247(4):529–535, 1995.
- [45] H. D. Herce and A. E. Garcia. Molecular dynamics simulations suggest a mechanism for translocation of the hiv-1 tat peptide across lipid membranes. *Proceedings of the National Academy of Sciences of the United States of America*, 104(52):20805–20810, 2007.
- [46] S. Yesylevskyy, S. J. Marrink, and A. E. Mark. Alternative mechanisms for the interaction of the cell-penetrating peptides penetratin and the tat peptide with lipid bilayers. *Biophysical Journal*, 97(1):40–49, 2009.
- [47] SL Barna, MW Tate, SM Gruner, and EF Eikenberry. Calibration procedures for charge-coupled device x-ray detectors. *Review of Scientific Instruments*, 70(7):2927–2934, 1999.
- [48] Y. Lyatskaya, Y. F. Liu, S. Tristram-Nagle, J. Katsaras, and J. F. Nagle. Method for obtaining structure and interactions from oriented lipid bilayers. *Physical Review E*, 63(1):0119071–0119079, 2001.
- [49] Y. F. Liu and J. F. Nagle. Diffuse scattering provides material parameters and electron density profiles of biomembranes. *Physical Review E*, 69(4):040901–040904(R), 2004.
- [50] Yufeng Liu. *NEW METHOD TO OBTAIN STRUCTURE OF BIOMEMBRANES USING DIFFUSE -RAY SCATTERING: APPLICATION TO FLUID PHASE DOPC LIPID BILAYERS*. PhD thesis, Carnegie Mellon University, 2003.
- [51] John F Nagle and Stephanie Tristram-Nagle. Structure of lipid bilayers. *Biochimica et Biophysica Acta (BBA)-Reviews on Biomembranes*, 1469(3):159–195, 2000.

- [52] Norbert Kuerka, John F. Nagle, Jonathan N. Sachs, Scott E. Feller, Jeremy Pencer, Andrew Jackson, and John Katsaras. Lipid bilayer structure determined by the simultaneous analysis of neutron and x-ray scattering data. *Biophysical Journal*, 95(5):2356 – 2367, 2008.
- [53] Stephanie Tristram-Nagle, Yufeng Liu, Justin Legleiter, and John F. Nagle. Structure of gel phase DMPC determined by x-ray diffraction. *Biophysical Journal*, 83(6):3324 – 3335, 2002.
- [54] Anthony R. Braun, Jonathan N. Sachs, and John F. Nagle. Comparing simulations of lipid bilayers to scattering data: The gromos 43a1-s3 force field. *The Journal of Physical Chemistry B*, 117(17):5065–5072, 2013.
- [55] <http://seal.web.cern.ch/seal/documents/minuit/mnusersguide.pdf>.
- [56] <http://lcgapp.cern.ch/project/cls/work-packages/mathlibs/minuit/index.html>.
- [57] Berk Hess, Carsten Kutzner, David van der Spoel, and Erik Lindahl. Gromacs 4: Algorithms for highly efficient, load-balanced, and scalable molecular simulation. *Journal of Chemical Theory and Computation*, 4(3):435–447, 2008.
- [58] Joakim P. M. Jmbeck and Alexander P. Lyubartsev. Derivation and systematic validation of a refined all-atom force field for phosphatidylcholine lipids. *The Journal of Physical Chemistry B*, 116(10):3164–3179, 2012.
- [59] Joakim P. M. Jmbeck and Alexander P. Lyubartsev. An extension and further validation of an all-atomistic force field for biological membranes. *Journal of Chemical Theory and Computation*, 8(8):2938–2948, 2012.
- [60] Viktor Hornak, Robert Abel, Asim Okur, Bentley Strockbine, Adrian Roitberg, and Carlos Simmerling. Comparison of multiple amber force fields and development of improved protein backbone parameters. *Proteins: Structure, Function, and Bioinformatics*, 65(3):712–725, 2006.
- [61] W. L. Jorgensen, J. Chandrasekhar, J. D. Madura, R. W. Impey, and M. L. Klein. Comparison of simple potential functions for simulating liquid water. *Journal of Chemical Physics*, 79(2):926–935, 1983.

- [62] Norbert Kuerka, John Katsaras, and JohnF. Nagle. Comparing membrane simulations to scattering experiments: Introducing the simtoexp software. *Journal of Membrane Biology*, 235(1):43–50, 2010.
- [63] Shuichi Miyamoto and Peter A Kollman. Settle: an analytical version of the shake and rattle algorithm for rigid water models. *Journal of computational chemistry*, 13(8):952–962, 1992.
- [64] B. Hess, H. Bekker, H. J. C. Berendsen, and J. G. E. M. Fraaije. Lincs: A linear constraint solver for molecular simulations. *J Comput Chem*, 18(12):1463–1472, 1997.
- [65] Tom Darden, Darrin York, and Lee Pedersen. Particle mesh ewald: An $n \log(n)$ method for ewald sums in large systems. *The Journal of chemical physics*, 98(12):10089–10092, 1993.
- [66] Giovanni Bussi, Davide Donadio, and Michele Parrinello. Canonical sampling through velocity rescaling. *The Journal of chemical physics*, 126(1):014101, 2007.
- [67] Michele Parrinello and Aneesur Rahman. Polymorphic transitions in single crystals: A new molecular dynamics method. *Journal of Applied physics*, 52(12):7182–7190, 1981.
- [68] Norbert Kučerka, Yufeng Liu, Nanjun Chu, Horia I Petrache, Stephanie Tristram-Nagle, and John F Nagle. Structure of fully hydrated fluid phase DMPC and DLPC lipid bilayers using X-ray scattering from oriented multilamellar arrays and from unilamellar vesicles. *Biophysical journal*, 88(4):2626–2637, 2005.
- [69] Norbert Kučerka, Stephanie Tristram-Nagle, and John F Nagle. Closer look at structure of fully hydrated fluid phase dppc bilayers. *Biophysical journal*, 90(11):L83–L85, 2006.
- [70] Norbert Kučerka, Stephanie Tristram-Nagle, and John F Nagle. Structure of fully hydrated fluid phase lipid bilayers with monounsaturated chains. *The Journal of membrane biology*, 208(3):193–202, 2005.

- [71] Stephanie Tristram-Nagle, Chao-Ping Yang, and John F Nagle. Thermodynamic studies of purple membrane. *Biochimica et Biophysica Acta (BBA)-Biomembranes*, 854(1):58–66, 1986.
- [72] <http://www.basic.northwestern.edu/biotools/proteinCalc.html>.
- [73] A. C. V. Johansson and E. Lindahl. The role of lipid composition for insertion and stabilization of amino acids in membranes. *Journal of Chemical Physics*, 130(18), 2009.
- [74] S. Tristram-Nagle and J. F. Nagle. Hiv-1 fusion peptide decreases bending energy and promotes curved fusion intermediates. *Biophysical Journal*, 93(6):2048–2055, 2007.
- [75] L. B. Li, I. Vorobyov, and T. W. Allen. Potential of mean force and pk(a) profile calculation for a lipid membrane-exposed arginine side chain. *Journal of Physical Chemistry B*, 112(32):9574–9587, 2008.
- [76] I. Vorobyov, L. B. Li, and T. W. Allen. Assessing atomistic and coarse-grained force fields for protein-lipid interactions: The formidable challenge of an ionizable side chain in a membrane. *Journal of Physical Chemistry B*, 112(32):9588–9602, 2008.
- [77] J. L. MacCallum, W. F. D. Bennett, and D. P. Tieleman. Distribution of amino acids in a lipid bilayer from computer simulations. *Biophysical Journal*, 94(9):3393–3404, 2008.
- [78] E. V. Schow, J. A. Freites, P. Cheng, A. Bernsel, G. von Heijne, S. H. White, and D. J. Tobias. Arginine in membranes: The connection between molecular dynamics simulations and translocon-mediated insertion experiments. *Journal of Membrane Biology*, 239(1-2):35–48, 2011.
- [79] W. C. Wimley, T. P. Creamer, and S. H. White. Solvation energies of amino acid side chains and backbone in a family of host-guest pentapeptides. *Biochemistry*, 35(16):5109–5124, 1996.
- [80] W. C. Wimley and S. H. White. Experimentally determined hydrophobicity scale for proteins at membrane interfaces. *Nature Structural Biology*, 3(10):842–848, 1996.

- [81] B. Roux. Lonely arginine seeks friendly environment. *Journal of General Physiology*, 130(2):233–236, 2007.
- [82] W. Kabsch and C. Sander. Dictionary of protein secondary structure: pattern recognition of hydrogen-bonded and geometrical features. *Biopolymers*, 22(12):2577–637, 1983.
- [83] D. Choi, J. H. Moon, H. Kim, B. J. Sung, M. W. Kim, G. Y. Tae, S. K. Satija, B. Akgun, C. J. Yu, H. W. Lee, D. R. Lee, J. M. Henderson, J. W. Kwong, K. L. Lam, K. Y. C. Lee, and K. Shin. Insertion mechanism of cell-penetrating peptides into supported phospholipid membranes revealed by x-ray and neutron reflection. *Soft Matter*, 8(32):8294–8297, 2012.
- [84] K. Huang and A. E. Garcia. Free energy of translocating an arginine-rich cell-penetrating peptide across a lipid bilayer suggests pore formation. *Biophysical Journal*, 104(2):412–420, 2013.
- [85] Martin J. Janiak, Donald M. Small, and G. Graham Shipley. Nature of the thermal pretransition of synthetic phospholipids: dimyristoyl- and dipalmitoyl-lecithin. *Biochemistry*, 15(21):4575–4580, 1976.
- [86] Martin J Janiak, Donald M Small, and G Graham Shipley. Temperature and compositional dependence of the structure of hydrated dimyristoyl lecithin. *Journal of Biological Chemistry*, 254(13):6068–6078, 1979.
- [87] Haruhiko Yao, Sinzi Matuoka, Boris Tenchov, and Ichiro Hatta. Metastable ripple phase of fully hydrated dipalmitoylphosphatidylcholine as studied by small angle x-ray scattering. *Biophysical journal*, 59(1):252–255, 1991.
- [88] W J Sun, S Tristram-Nagle, R M Suter, and J F Nagle. Structure of the ripple phase in lecithin bilayers. *Proceedings of the National Academy of Sciences*, 93(14):7008–7012, 1996.
- [89] Beth A Cunningham, Ari-David Brown, David H Wolfe, W Patrick Williams, and Anthony Brain. Ripple phase formation in phosphatidylcholine: Effect of acyl chain relative length, position, and unsaturation. *Physical Review E*, 58(3):3662, 1998.

- [90] Kell Mortensen, Walter Pfeiffer, Erich Sackmann, and Wolfgang Knoll. Structural properties of a phosphatidylcholine-cholesterol system as studied by small-angle neutron scattering: ripple structure and phase diagram. *Biochimica et Biophysica Acta (BBA)-Biomembranes*, 945(2):221–245, 1988.
- [91] Jeremy P Bradshaw, Michael S Edenborough, Philip JH Sizer, and Anthony Watts. Observation of rippled dioleoylphosphatidylcholine bilayers by neutron diffraction. *Biochimica et Biophysica Acta (BBA)-Biomembranes*, 987(1):111–114, 1989.
- [92] JT Woodward IV and JA Zasadzinski. Amplitude, wave form, and temperature dependence of bilayer ripples in the p β phase. *Physical Review E*, 53(4):R3044, 1996.
- [93] PC Mason, BD Gaulin, RM Epand, GD Wignall, and JS Lin. Small angle neutron scattering and calorimetric studies of large unilamellar vesicles of the phospholipid dipalmitoylphosphatidylcholine. *Physical Review E*, 59(3):3361, 1999.
- [94] M. P. Hentschel and F. Rustichelli. Structure of the ripple phase P'_β in hydrated phosphatidylcholine multimembranes. *Phys. Rev. Lett.*, 66:903–906, Feb 1991.
- [95] John Katsaras, Stephanie Tristram-Nagle, Yufeng Liu, RL Headrick, E Fontes, PC Mason, and John F Nagle. Clarification of the ripple phase of lecithin bilayers using fully hydrated, aligned samples. *Physical Review E*, 61(5):5668, 2000.
- [96] Kheya Sengupta, V. A. Raghunathan, and John Katsaras. Structure of the ripple phase of phospholipid multibilayers. *Phys. Rev. E*, 68:031710, Sep 2003.
- [97] Li Li and Ji-Xin Cheng. Coexisting stripe-and patch-shaped domains in giant unilamellar vesicles. *Biochemistry*, 45(39):11819–11826, 2006.
- [98] Alex H. de Vries, Serge Yefimov, Alan E. Mark, and Siewert J. Marrink. Molecular structure of the lecithin ripple phase. *Proceedings of the National Academy of Sciences of the United States of America*, 102(15):5392–5396, 2005.
- [99] Olaf Lenz and Friederike Schmid. Structure of symmetric and asymmetric “ripple” phases in lipid bilayers. *Phys. Rev. Lett.*, 98:058104, Jan 2007.

- [100] C-M Chen, TC Lubensky, and FC MacKintosh. Phase transitions and modulated phases in lipid bilayers. *Physical Review E*, 51(1):504, 1995.
- [101] J. Katsaras and V. A. Raghunathan. Molecular chirality and the ripple phase of phosphatidylcholine multibilayers. *Phys. Rev. Lett.*, 74:2022–2025, Mar 1995.
- [102] S. A. Tristram-Nagle. Preparation of oriented, fully hydrated lipid samples for structure determination using x-ray scattering. *Methods Mol Biol*, 400:63–75, 2007.
- [103] http://henke.lbl.gov/optical_constants.
- [104] M.C. Wiener, R.M. Suter, and J.F. Nagle. Structure of the fully hydrated gel phase of dipalmitoylphosphatidylcholine. *Biophysical Journal*, 55(2):315 – 325, 1989.
- [105] Thalia T Mills, Gilman ES Toombes, Stephanie Tristram-Nagle, Detlef-M Smilgies, Gerald W Feigenson, and John F Nagle. Order parameters and areas in fluid-phase oriented lipid membranes using wide angle x-ray scattering. *Biophysical journal*, 95(2):669–681, 2008.
- [106] George H Vineyard. Grazing-incidence diffraction and the distorted-wave approximation for the study of surfaces. *Physical Review B*, 26(8):4146, 1982.
- [107] CE Miller, J Majewski, EB Watkins, DJ Mulder, T Gog, and TL Kuhl. Probing the local order of single phospholipid membranes using grazing incidence x-ray diffraction. *Physical review letters*, 100(5):058103, 2008.
- [108] S Tristram-Nagle, R Zhang, RM Suter, CR Worthington, WJ Sun, and JF Nagle. Measurement of chain tilt angle in fully hydrated bilayers of gel phase lecithins. *Biophysical journal*, 64(4):1097–1109, 1993.
- [109] Bertram Eugene Warren. *X-ray Diffraction*. Courier Dover Publications, 1969.
- [110] W-J Sun, RM Suter, MA Knewton, CR Worthington, S Tristram-Nagle, R Zhang, and JF Nagle. Order and disorder in fully hydrated unoriented bilayers of gel-phase dipalmitoylphosphatidylcholine. *Physical Review E*, 49(5):4665, 1994.

- [111] Alejandro B. Rodriguez-Navarro. Registering pole figures using an X-ray single-crystal diffractometer equipped with an area detector. *Journal of Applied Crystallography*, 40(3):631–634, Jun 2007.
- [112] Jessy L. Baker, Leslie H. Jimison, Stefan Mannsfeld, Steven Volkman, Shong Yin, Vivek Subramanian, Alberto Salleo, A. Paul Alivisatos, and Michael F. Toney. Quantification of thin film crystallographic orientation using x-ray diffraction with an area detector. *Langmuir*, 26(11):9146–9151, 2010. PMID: 20361783.